United States Nuclear Regulatory Commission

Protecting People and the Environment

NUREG/CR-7103
PNNL-24647
Volume 3

Pacific Northwest National Laboratory Investigation of Stress Corrosion Cracking in Nickel-Base Alloys: Stress Corrosion Cracking of Cold Worked Alloy 690

Office of Nuclear Regulatory Research

AVAILABILITY OF REFERENCE MATERIALS IN NRC PUBLICATIONS

NRC Reference Material

As of November 1999, you may electronically access NUREG-series publications and other NRC records at NRC's Library at www.nrc.gov/reading-rm.html. Publicly released records include, to name a few, NUREG-series publications; *Federal Register* notices; applicant, licensee, and vendor documents and correspondence; NRC correspondence and internal memoranda; bulletins and information notices; inspection and investigative reports; licensee event reports; and Commission papers and their attachments.

NRC publications in the NUREG series, NRC regulations, and Title 10, "Energy," in the *Code of Federal Regulations* may also be purchased from one of these two sources.

1. **The Superintendent of Documents**
   U.S. Government Publishing Office
   Mail Stop IDCC
   Washington, DC 20402-0001
   Internet: bookstore.gpo.gov
   Telephone: (202) 512-1800
   Fax: (202) 512-2104

2. **The National Technical Information Service**
   5301 Shawnee Rd., Alexandria, VA 22312-0002
   www.ntis.gov
   1-800-553-6847 or, locally, (703) 605-6000

A single copy of each NRC draft report for comment is available free, to the extent of supply, upon written request as follows:

Address: **U.S. Nuclear Regulatory Commission**
Office of Administration
Publications Branch
Washington, DC 20555-0001
E-mail: distribution.resource@nrc.gov
Facsimile: (301) 415-2289

Some publications in the NUREG series that are posted at NRC's Web site address www.nrc.gov/reading-rm/doc-collections/nuregs are updated periodically and may differ from the last printed version. Although references to material found on a Web site bear the date the material was accessed, the material available on the date cited may subsequently be removed from the site.

Non-NRC Reference Material

Documents available from public and special technical libraries include all open literature items, such as books, journal articles, transactions, *Federal Register* notices, Federal and State legislation, and congressional reports. Such documents as theses, dissertations, foreign reports and translations, and non-NRC conference proceedings may be purchased from their sponsoring organization.

Copies of industry codes and standards used in a substantive manner in the NRC regulatory process are maintained at—

The NRC Technical Library
Two White Flint North
11545 Rockville Pike
Rockville, MD 20852-2738

These standards are available in the library for reference use by the public. Codes and standards are usually copyrighted and may be purchased from the originating organization or, if they are American National Standards, from—

American National Standards Institute
11 West 42nd Street
New York, NY 10036-8002
www.ansi.org
(212) 642-4900

Legally binding regulatory requirements are stated only in laws; NRC regulations; licenses, including technical specifications; or orders, not in NUREG-series publications. The views expressed in contractorprepared publications in this series are not necessarily those of the NRC.

The NUREG series comprises (1) technical and administrative reports and books prepared by the staff (NUREG–XXXX) or agency contractors (NUREG/CR–XXXX), (2) proceedings of conferences (NUREG/CP–XXXX), (3) reports resulting from international agreements (NUREG/IA–XXXX), (4) brochures (NUREG/BR–XXXX), and (5) compilations of legal decisions and orders of the Commission and Atomic and Safety Licensing Boards and of Directors' decisions under Section 2.206 of NRC's regulations (NUREG–0750).

U.S.NRC
United States Nuclear Regulatory Commission
Protecting People and the Environment

NUREG/CR-7103
PNNL-24647
Volume 3

Pacific Northwest National Laboratory Investigation of Stress Corrosion Cracking in Nickel-Base Alloys: Stress Corrosion Cracking of Cold Worked Alloy 690

Manuscript Completed: September 2015
Date Published: July 2016

Prepared by:
M.B. Toloczko, N.R. Overman, M.J. Olszta, and S.M. Bruemmer

Pacific Northwest National Laboratory
902 Battelle Boulevard
Richland, Washington 99352

Greg Oberson
NRC Contracting Officer’s Representative

NRC Job Code Number N6925

Office of Nuclear Regulatory Research

ABSTRACT

The report summarizes the results of a testing program to evaluate the effects of cold work, including rolling, forging, and tensile straining, on the primary water stress corrosion cracking (PWSCC) susceptibility of alloy 690. Alloy 690 is a high-chromium, nickel-base material used in reactor pressure vessel head penetration nozzles, steam generator divider plates, and other components. Prior testing indicated that an increase in the amount of cold work increases the crack growth rate in alloy 690, but the relationships between the degree of cold work, the material microstructure, and the cracking behavior were not systematically investigated. For this study, PWSCC growth rates were measured for a total of 37 different alloy 690 specimens in simulated primary water reactor environments. The alloy 690 test materials included six different heats of extruded control-rod-drive mechanism (CRDM) tubing and five plate/bar heats with variations in the degree of cold work, from no cold work to cold work greater than 30%. In addition, different thermo-mechanical treatments were applied to some heats of material before cold working, thereby altering properties such as the grain boundary carbide morphology, to assess how this would affect the PWSCC response. Materials were examined by optical microscopy, electron microscopy, electron backscatter diffraction, and other characterization techniques to devise a mechanistic explanation for the test results and to identify the key parameters that control the PWSCC susceptibility.

FOREWORD

This report describes a study sponsored by the NRC Office of Nuclear Regulatory Research (RES) to investigate the effect of cold work on primary water stress corrosion cracking (PWSCC) susceptibility in Alloy 690. PWSCC in primary pressure boundary components fabricated from nickel-based alloys, such as reactor vessel head penetration nozzles, is a degradation mechanism that can affect the operational safety of pressurized water reactors (PWRs), for instance by allowing the leakage of reactor coolant. Such a scenario in an Alloy 600 control rod drive mechanism (CRDM) nozzle led to boric acid corrosion and wastage of the low alloy steel pressure vessel head at the Davis Besse plant in 2002. Alloy 690 is thought to be more resistant to PWSCC than Alloy 600 because of higher chromium content, and there is no operational experience of its cracking in service. In light of the positive Alloy 690 service history and low crack growth rates measured in laboratory testing sponsored by the industry, utilities have submitted requests to the Office of Nuclear Reactor Regulation (NRR) for relief from the inspection requirements found in Title 10 of the Code of Federal Regulations, Part 50.55a, including a 10 year interval for volumetric examination of pressure vessel head nozzles.

To support the evaluation of these relief requests by NRR and confirm the test results from industry-sponsored research, RES undertook an investigation at Pacific Northwest National Laboratory (PNNL) to measure the crack growth rates in Alloy 690 as a function of cold work. Prior testing described in Volumes 1 and 2 of this report, published in 2011 and 2012 respectively, indicated that increasing the cold work increases the crack growth rate, but the relationships between the degree of cold work, the material microstructure, and the cracking behavior were not systematically investigated. For this study, PWSCC growth rates were measured in specimens from heats of extruded CRDM tube and plate/bar with cold work up to 30%. Different thermo-mechanical treatments were applied to some heats of material to alter properties such as the grain boundary carbide morphology and assess how these treatments affect the PWSCC response. Tests were also performed on Alloy 690 specimens from the weld heat affected zone (HAZ) to determine if this region is particularly susceptible to cracking.

The test results indicated that Alloy 690 with no cold work is very resistant to PWSCC as most crack growth rates are less than 10^{-9} mm/s. The crack growth rate generally increases with increasing cold work. Rates can be greater than 10^{-9} mm/s when the cold work is greater than 10% and approach 10^{-7} mm/s when the cold work is above 30%. Detailed characterization of the materials by microscopy and electron backscatter diffraction indicates that PWSCC susceptibility is dependent on both the heat treatment of the material and the level of plastic deformation at the grain boundaries. Stronger effects are observed when grain boundary carbides are present, as in the mill annealed or thermally treated condition. With respect to the HAZ, the measured crack growth rates were similar to those of non-cold worked Alloy 690.

These data generally confirm the results from prior industry-sponsored research and suggest that PWSCC in an Alloy 690 component with less than 15% global cold work should not result in significant cracking over the current licensing period. However, the cracking rate of components with global cold work levels greater than 15% may be significant depending on the heat treatment of the material. Finally, localized regions with cold work of greater than 15% may promote high crack growth rates within those regions. These results should impact the technical basis for NRR to determine with reasonable assurance that inspection requirements for these materials are appropriate.

CONTENTS

FIGURES

TABLES

EXECUTIVE SUMMARY

The subject of this report, entitled NUREG/CR-7103, Volume 3, “Stress Corrosion Cracking of Cold Worked Alloy 690” is the effect of cold work on the primary water stress corrosion cracking (PWSCC) susceptibility alloy 690, a high-chromium, nickel-base material. Volume 1 of this report, published in 2011, describes the design and operating principles of the systems used to simulate primary water reactor (PWR) conditions and measure the crack growth rate in test specimens, as well as initial data from alloy 690 and weld metals. Volume 2, published in 2012, presents the first crack growth rate measurements for cold worked alloy 690, again in addition to other data from weld metals. The effects of cold work were selected as the focus for Volume 3 because they have been shown to substantially increase the crack growth rate in alloy 690. The prior studies, however, did not systematically investigate the relationships between the degree of cold work, the material microstructure, and the PWSCC behavior.

Alloy 690 is used in pressurized water reactors (PWRs) for reactor pressure vessel head penetration nozzles, steam generator divider plates, and certain other components. PWSCC could cause the leakage of primary water, as in the case at Davis-Besse in 2002 where significant boric acid corrosion of the low alloy steel head was enabled by a through-thickness crack in a lower chromium, nickel-base alloy weld for a control rod drive mechanism (CRDM) nozzle. Alloy 690 is being used by industry in replacement parts to mitigate PWSCC. Some components in plant service may experience cold work (i.e., deformation at near-ambient temperature) during fabrication and installation. The research presented in this report represents the most comprehensive examination of cold work effects conducted to date and quantitatively establishes alloy 690 behavior. PWSCC growth rates have been determined for 37 different alloy 690 specimens with varying degrees of cold work in simulated PWR primary water environments. The amount of cold work ranged from none to greater than 30%. The alloy 690 test materials included six different heats of extruded CRDM tubing and five plate/bar heats. Selected heats were evaluated over a full range of cold work including a CRDM heat in the 0, 12, 17, 21 and 31% cold worked conditions. In addition, the initial material condition was altered before cold work for three heats to assess its effect on PWSCC response. In all cases, crack extension was monitored in situ by direct current potential drop (DCPD) with a noise resolution of about ±1 µm, making it possible to measure extremely low growth rates approaching $5\text{x}10^{-10}$ mm/s. Most SCC tests were performed at 360°C with a dissolved hydrogen concentration of 25 cc/kg. Environmental conditions were modified during a few tests to evaluate the influence of temperature, stress intensity, and electrochemical potential (ECP) on propagation rates.

To assist in understanding the relationship between PWSCC response and material properties, all materials were characterized by optical metallography, scanning electron microscopy (SEM) and electron backscatter diffraction (EBSD) to document the starting microstructure. In addition, EBSD integrated misorientation density (IMD) mapping was used to estimate residual plastic strains, and hardness mapping was employed to indicate strength levels. These measurements assessed the material response over a region of many grains and were performed on the PWSCC test specimens in the crack-growth plane. This approach provides a more representative description of the material properties than the overall level of cold work, which is an average value across the thickness of the material. The hardness and IMD measurements were performed using modern equipment that included an automated hardness tester and a state-of-the-art field emission gun SEM. In order to assess how well the IMD measurements tracked with the level of plastic strain, the IMD was plotted against the hardness (a representation of the stress required to produce plastic strain in a specimen) to see whether it follows the well-established power law strain hardening relationship for alloy 690. An excellent fit was observed with an exponent of ~0.41, a value that is quite reasonable for alloy 690.

Important results have been obtained for alloy 690, establishing PWSCC response as a function of material and environmental parameters. As expected, the plant representative, thermally treated (TT) alloy 690 CRDM tubing heats in the as-received condition were resistant to PWSCC. Under extended constant stress intensity (K) testing, steady but very low propagation rates ($\leq 3 \times 10^{-9}$ mm/s) were observed with very little intergranular (IG) cracking. Similar results were also documented for several mill-annealed (MA) and TT plate and bar heats when tested in the as-received condition. The consistently low PWSCC growth rates measured in a total of seven different heats, even with quite different starting microstructures, established confidence that as-received alloy 690 materials are extremely resistant to cracking.

Low-to-moderate levels of cold work introduced by rolling, forging or tensile straining at room temperature was found to promote IG cracking and higher PWSCC growth rates, particularly when specimens were oriented so that cracking took place in the deformation plane. This is true even for extruded alloy 690 CRDM tubing with an excellent microstructure. Plate and bar materials in the as-received condition and with added cold work exhibited PWSCC growth rates that were generally similar to the CRDM materials. Some alloy 690 heats were examined with cold work in the range of 12-17%CW. These showed PWSCC growth rates between 1 and 5×10^{-9} mm/s at moderate stress intensity levels. These rates were definitely higher than those measured for the as-received materials, but still reflect rather low susceptibility. In order to further evaluate alloy 690 materials with a low level of plastic strain, experiments were conducted on three weld heat affected zone specimens. Measured PWSCC growth rates were below 2×10^{-9} mm/s. In general, it was found that alloy 690 heats cold worked to 20% or greater are susceptible to IG cracking with growth rates typically greater than 1×10^{-8} mm/s and approaching 1×10^{-7} mm/s for cold work levels reaching ~30%. These results clearly demonstrate that the material is not immune to PWSCC, and that the reasons for enhanced susceptibility should be understood to ensure component integrity.

Comparison of PWSCC growth rates to material strength and strain levels revealed a linear dependence on strength (quantified by hardness) and a power law relationship with strain quantified by IMD) for the majority of the alloy 690 materials for the full range of applied cold work level (0-32%). While the fit to IMD was nonlinear, scatter in the trend was similar to the fit to hardness, indicating that for one method of changing strength (cold work), PWSCC growth rates track equally well with both parameters for a given material starting condition. Materials that underwent heat treatments to reduce or remove grain boundary carbides were found to have substantially lower PWSCC growth rates than would be expected from their corresponding hardness and IMD values. In addition, the application of a moderate temperature heat treatment to relax dislocation structures in cold worked materials containing grain boundary carbides was also found to substantially reduce PWSCC growth rates. These results suggest that high localized strains are associated with grain boundary carbides, thereby enhancing the effect of cold work on PWSCC growth in alloy 690. Dislocations structures in the matrix and localized at grain boundaries appear to play a key role in the PWSCC response and additional research may be needed to isolate mechanisms controlling cracking susceptibility.

Subsets of the alloy 690 heats were also used to assess the dependence of PWSCC on applied K level, test temperature and dissolved hydrogen content (quantified by ECP). Highly cold worked alloy 690 was found to have a steep reduction in PWSCC growth as K was reduced below 30 MPa√m with propagation rates dropping to ~2×10^{-9} mm/s for a stress intensity of ~20 MPa√m. However, there was often little or no dependence on stress intensity for values above

30 MPa√m. An Arrhenius temperature dependence was observed for five different combinations of material, heat treatment and cold work with an average activation energy 130 kJ/mol, similar to what has been previously measured for alloy 600. Finally, PWSCC susceptibility was found to decrease for dissolved hydrogen contents that reduce the ECP below the Ni/NiO stability line, while PWSCC growth rates were not obviously affected by dissolved hydrogen contents corresponding to ECP above the Ni/NiO stability line. This latter trend is different than alloy 600 where the SCC susceptibility is reduced at high ECP levels.

ACKNOWLEDGMENTS

The authors recognize support from PNNL staff for the research performed including Rob Seffens for crack-growth system maintenance and testing, Anthony Guzman for general support and Clyde Chamberlin for optical metallography. Important collaborative research has been performed with a project funded by Rolls Royce that has enabled detailed characterizations of cold worked alloy 690 materials greatly expanding hardness and electron backscatter diffraction measurements. Critical interactions with Peter Andresen of General Electric Global Research are also acknowledged. The work was sponsored by the Office of Nuclear Regulatory Research, U.S. Nuclear Regulatory Commission (NRC) under job codes N6925 and N6782 with Greg Oberson as the current project manager. Many helpful discussions with NRC staff are recognized including Darrell Dunn, Rob Tregoning, Dave Alley and Jay Collins. Pacific Northwest National Laboratory is operated by Battelle Memorial Institute for the U.S. Department of Energy.

ABBREVIATIONS AND ACRONYMS

ANL	Argonne National Laboratory
APT	atom probe tomography
AR	as received
ASTM	American Society for Testing and Materials
ATEM	analytical transmission electron microscopy
BSE	backscatter electron
BWR	boiling-water reactor
CGR	crack-growth rate
CF	cold forged
CM	carbide modified
CR	cold rolled
CRDM	control rod drive mechanism
CT	compact tension
CW	cold worked
DCPD	direct current potential drop
DH	dissolved hydrogen
DOE	Department of Energy
EBSD	electron backscatter diffraction
ECP	electrochemical potential
EDS	energy-dispersive x-ray spectroscopy
ENSA	Spanish nuclear power utility
EPRI	Electric Power Research Institute
FIB	focused ion beam
GEG	General Electric Global
GTAW	gas tungsten arc weld
H	hydrogen
HWC	hydrogen water chemistry
IG	intergranular
IGSCC	intergranular stress corrosion cracking
INSS	Institute of Nuclear Safety Systems, Incorporated
K	stress intensity factor
KAPL	Knolls Atomic Power Laboratory
LAS	low alloy steel
LOCA	loss of coolant accident
LWR	light water reactor
MA	mill annealed

MHI	Mitsubishi Heavy Industries
MRP	Materials Reliability Program
NRC	U.S. Nuclear Regulatory Commission
PEELS	parallel detection electron energy loss spectrometer
PNNL	Pacific Northwest National Laboratory
PWR	pressurized water reactor
PWSCC	primary water stress corrosion cracking
R	load ratio (minimum/maximum)
RPV	reactor pressure vessel
SA	solution annealed
SCC	stress corrosion cracking
SE	secondary electron
SEM	scanning electron microscopy
SMAW	shielded metal arc weld
SS	stainless steel
STEM	scanning transmission electron microscopy
TEM	transmission electron microscopy
TG	transgranular
TT	thermally treated
TTZ	transformation toughened zirconia

1 INTRODUCTION

Primary water stress corrosion cracking (PWSCC) in nickel-base alloys is a degradation mechanism that can affect pressure boundary components in pressurized water reactors (PWRs). PWSCC preferentially occurs in components that operate at high temperatures and pressures. Fabrication and welding processes and especially weld repairs leave residual stresses that promote cracking in susceptible materials. The narrow cracks, which are often located in complex structures either within or adjacent to welds, are difficult to detect and characterize during in service inspections. At the time of construction, PWRs used alloy 600 for the base metal along with alloy 82 and 182 weld metals. PWSCC of these materials led to reactor pressure boundary leaks and subsequent boric acid corrosion of low alloy steels at Arkansas Nuclear One-1 in 2001 and Davis-Besse in 2002. Extensive wastage of the Davis-Besse reactor head could have resulted in a loss of coolant accident (LOCA) had reactor operation continued and the damage gone undetected. Circumferential cracks discovered in the V.C. Summer reactor coolant system piping welds in 2000 and in pressurizer nozzle welds at Wolf Creek in 2006 have raised concerns that PWSCC in PWR piping could result in a LOCA.

Increasingly, industry utilizes high chromium alloy 690 and associated weld metals, alloy 52 and 152, in replacements for alloy 600, 82, and 182 components and for mitigation methods including weld onlays and overlays. Alloy 690 has been used in steam generators since 1989 and more than 40 PWR replacement heads using alloys 690/152/52 have been placed into service. The high chromium nickel-base alloys have also been used in RCS piping, nozzles, and instrument penetrations. While the service history has been favorable [1-2], significant industry and international efforts are underway to characterize the PWSCC susceptibility of alloys 690/152/52. Initial results have been reported in MRP-237 Rev. 1 [2] and Rev. 2 [3].

Questions concerning the inherent resistance of alloy 690 to PWSCC were raised after data from Bettis on cold worked alloy 690 plate heats were released [4]. Extremely high propagation rates were observed for certain heats in the highly cold worked condition. These data are summarized in Figure 1.1 and are compared to the SCC growth rate disposition curve for alloy 600 from MRP-55 [5]. Clearly alloy 690 is not immune to PWSCC, and systematic SCC testing has been employed to establish its behavior under a range of material and environmental conditions. Although the issue of PWSCC susceptibility is being addressed by industry, the U.S. Nuclear Regulatory Commission (NRC) has sought to obtain PWSCC growth rates of these resistant alloys and assess mitigation methods to determine the validity and acceptability of licensee flaw analyses, and to support regulatory inspection requirements. To meet these objectives, an improved understanding of the interrelations between component stresses, material microstructure, and the aggressive nature of the PWR environment is necessary.

In the prior programs at Pacific Northwest National Laboratory (PNNL) that began in 2004, SCC test systems were built, vetted using materials and test conditions that would produce known SCC response, and then a testing program was instituted. The effects of stress, cold work, electrochemical potential, temperature, and microstructure were broadly assessed for alloy 690/152/52 materials in Volumes 1 [6] and 2 [7] in this series of reports. The outcome of this research was that the single most important factor affecting the PWSCC susceptibility of alloy 690 was the degree of plastic strain in the material. Highly cold worked alloy 690 (e.g., 30% reduction) was widely found to be very susceptible to PWSCC, not only at PNNL, but worldwide. Lower degrees of cold work, such as in the 20% range, tended to produce a wider range of response from heat to heat. With the exception of the Bettis work [4], cold work levels in the 10-

15% range that are thought to possibly represent maximum possible strain levels in heat affected zones (HAZs) had not been examined. In order to better understand the effects of cold work on PWSCC of alloy 690, the testing program at PNNL was shifted to systematically investigate effects in a large number of alloy 690 control road drive mechanism (CRDM) and plate heats. The current report combines and presents all tests on alloy 690 conducted at PNNL that are related to cold work effects. Results include not only PWSCC growth-rate testing, but also detailed characterization of material microstructures, strain distributions and hardness for direct comparisons to PWSCC response.

This report covers testing of 37 crack growth rate specimens representing 12 different heats of alloy 690 in various thermomechanical conditions as shown in Table 1.1. CRDM product forms, which generally have more uniform microstructures in the as-received thermally treated (TT) condition, were tested along with plate, billet and bar materials in the mill-annealed (MA) or TT conditions. Cold work levels from 12% to 31%, and the effect of different thermal treatments before and after cold working were investigated. One heat of material, the Valinox CRDM heat RE243, was SCC tested in 12 unique thermomechanical conditions. All specimens were subjected to post-test examinations that included crack surface observations and crack profile observations plus electron backscatter diffraction (EBSD) and hardness measurements in the SCC growth plane. Chapter 3 contains information on base microstructures and the effect of cold work on microstructure. Grain boundary microstructures, strains distributions and hardness were measured on all PNNL SCC test specimens and on several additional specimens from other programs. SCC growth rate and crack morphology results on CRDM and plate/billet/bar materials are covered in Chapters 4 and 5, respectively. HAZ SCC test results, all of which were on plate materials, are reported in Chapter 5. Correlations among microstructure, properties and SCC growth rates are described in Chapter 6.

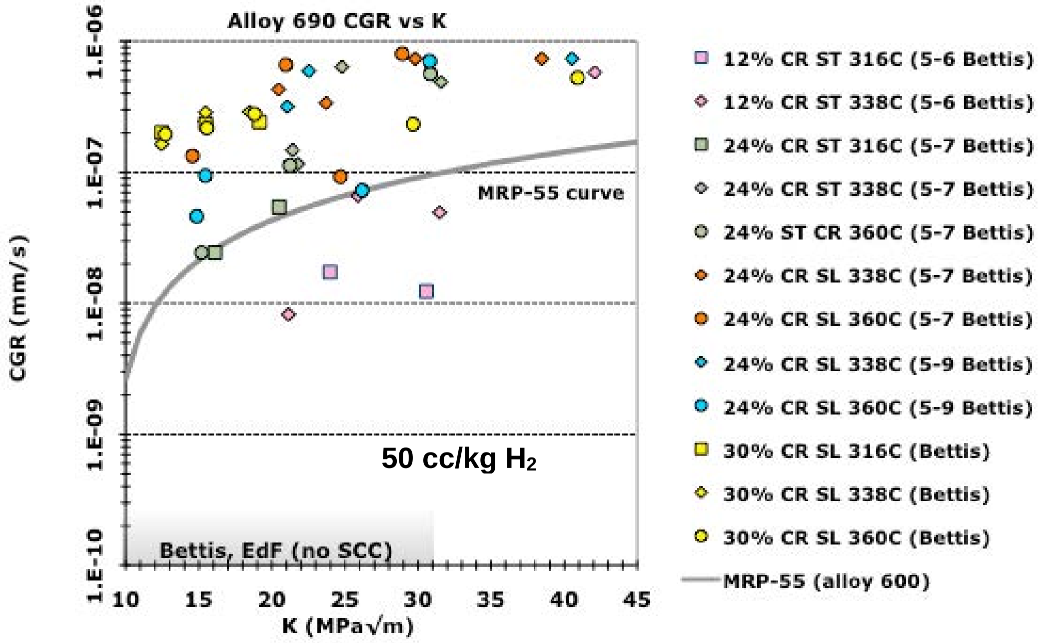

Figure 1.1 **Summary of SCC growth rate data from Bettis [4] on cold rolled alloy 690 plate teats. Test temperatures ranged from 316 to 360°C with a constant dissolved hydrogen content of 50 cc/kg**

Table 1.1 Table of Alloy 690 crack growth specimens discussed in this report

ID	Source/Producer	Heat #	Form	Treatment
CT026	Valinox/Valinox	WP142	CRDM	TT*
CT027	Valinox/Valinox	WP140	CRDM	TT*
CT015	Valinox/Valinox	RE243	CRDM	TT*
CT104	Valinox/Valinox	RE243	CRDM	TT*+11.6%CF S-L/S-T
CT020	Valinox/Valinox	RE243	CRDM	TT*+17%CR S-L
CT054	Valinox/Valinox	RE243	CRDM	TT*+17%CR S-L
CT100	Valinox/Valinox	RE243	CRDM	TT*+21%CF S-L/S-T
CT022	Valinox/Valinox	RE243	CRDM	TT*+30%CR T-L
CT038	Valinox/Valinox	RE243	CRDM	TT*+31%CR S-L
CT099	Valinox/Valinox	RE243	CRDM	TT*+31%CF S-L/S-T
CT053	Valinox/Valinox	RE243	CRDM	TT*+31%CR S-L+RT[‡]
CT014	Valinox/Valinox	RE243	CRDM	TT*+SA†
CT019	Valinox/Valinox	RE243	CRDM	TT*+SA+17%CR S-L
CT068	Valinox/Valinox	RE243	CRDM	TT*+SA+17%CR S-L
CT023	Valinox/Valinox	RE243	CRDM	TT*+SA+30%CR T-L
CT039	Valinox/Valinox	RE243	CRDM	TT*+SA+31%CR S-L
CT093	Ciemat/Valinox	WP787	CRDM	TT*+20%TS
CT103	EPRI/Sumitomo	E67074C	CRDM	TT*+12.7%CF S-L/S-T
CT098	EPRI/Sumitomo	E67074C	CRDM	TT*+31%CF S-L/S-T
CT108	EPRI-Doosan/TK-VDM	133454	CRDM bar	TT*
CT102	EPRI-Doosan/TK-VDM	133454	CRDM bar	TT*+21%CF S-L/S-T
CT084	ANL/Special Metals	NX3297HK12	Plate	MA*
CT036	ANL/Special Metals	NX3297HK12	Plate	MA*+26%CR S-L
CT073	ANL-GE/Special Metals	NX3297HK12	Plate	MA*+30%CF SL/ST
CT074	ANL-GE/Special Metals	NX3297HK12	Plate	HTA[§]+30%CF S-L/S-T
CT085	GE/Allvac	B25K-2	Plate	MA*
CT037	GE/Allvac	B25K-2	Plate	MA*+20%CR S-L
CT070	GE/Allvac	B25K-2	Plate	HTA[§]+20%CR S-L
CT107	EPRI/TK-VDM	114092	Plate	TT*
CT094	GE/TK-VDM	114092	Plate	TT*+32%CF S-L/S-T
CT059	GE-ENSA/Aubert&Duval	WP547	Plate	TT*+32%CF S-L/S-T
CT060	GE-ENSA/Aubert&Duval	WP547	Plate	TT*+22%CR S-L
CT101	EPRI/Allvac	X87N-1	Billet	TT*+21%CF S-L/S-T
CT067	EPRI-ENSA/Aubert&Duval	WP547	Plate	TT* HAZ
CT086	ANL/Special Metals	NX3297HK12	Plate	MA* HAZ
CT087	KAPL/Unknown	Unknown	Plate	AR HAZ

* As-received condition of the material: Thermally Treated (TT) or Mill Annealed (MA)

† Solution Annealed (SA): 1100°C/1h + Water Quench (complete removal of carbides)

‡ Recovery Treatment (RT): 700°C/1h + Air Cool

§ High Temperature Anneal (HTA): Also 1100°C/1h + Water Quench (Higher carbon content in these materials resulted in only partial removal of the carbide population.)

2 SCC CRACK-GROWTH TEST SYSTEMS AND TESTING APPROACH

The purposes of the crack-growth systems are to develop, control and measure stress corrosion cracks under well-defined material and environmental conditions, and ensure that the SCC growth rate response is reproducible and characteristic of the test conditions. Features expected in a good crack-growth system include active constant K load control, active temperature control, a sensitive crack length measurement apparatus, a recirculating high-temperature water system that allows control over all relevant aspects of water chemistry, and continuous monitoring of all pertinent test parameters. The PNNL crack growth systems are based on the test systems at General Electric Global Research (GEG) that were built by Peter Andresen. These crack-growth systems have been copied to various degrees by research institutes and commercial companies throughout the world. In the process of building the systems at PNNL, some design aspects were improved and more up-to-date parts were chosen when advantageous.

2.1 Overview of SCC Crack-Growth Test Systems

The key components of these systems are: (1) a servo-electric load control system capable of holding constant load for very long periods of time, (2) a high-pressure piston pump to pressurize and flow water through the high-temperature loop, (3) an autoclave, (4) a custom-made water mixing loop for chemistry control, (5) a reversing direct current potential drop (DCPD) system for crack length estimation, and (6) software that controls load and provides continuous data acquisition. Careful consideration went into the selection of each piece of equipment to optimize either test system control or test environment. Some of the most important optimizations were to: (1) make sure that all wetted components release no contamination into the water, (2) have a sufficiently high water flow rate through the autoclave to ensure consistent water chemistry, (3) have uniform temperature through a large volume of the autoclave, (4) have consistent water pressure, (5) have highly accurate measurements of test environment (temperature, conductivity, pH, load, dissolved gas content), and (6) have a sensitive DCPD measurement system. Each of the subsystems will be discussed in further detail below.

The water flow design contains two connected loops shown in Figure 2.1. One loop is at low pressure, and its purpose is to flow water through a water column where selected gases and ionic impurities are injected into the water. A side stream is taken off this low-pressure loop and fed into a high-pressure piston pump. The large pressure pulses and flow surges created by the piston pump are dampened by the use of pulsation dampers both at the inlet and outlet of the pump. The high-pressure water flows into a regenerative heat exchanger where hot water leaving the autoclave is used to heat the incoming water. Just prior to the water entering the autoclave, the partially heated water is brought up to test temperature using a preheater. After the water flows through the heated autoclave, it goes back through the regenerative heat exchanger and then through a water cooler that brings the water back down to room temperature. The cooled water then passes through a back-pressure regulator and emerges at low pressure. The water flows through a flow meter, a conductivity sensor, a mixed resin bed demineralizer, and is finally dumped back into the low-pressure chemistry mixing control loop.

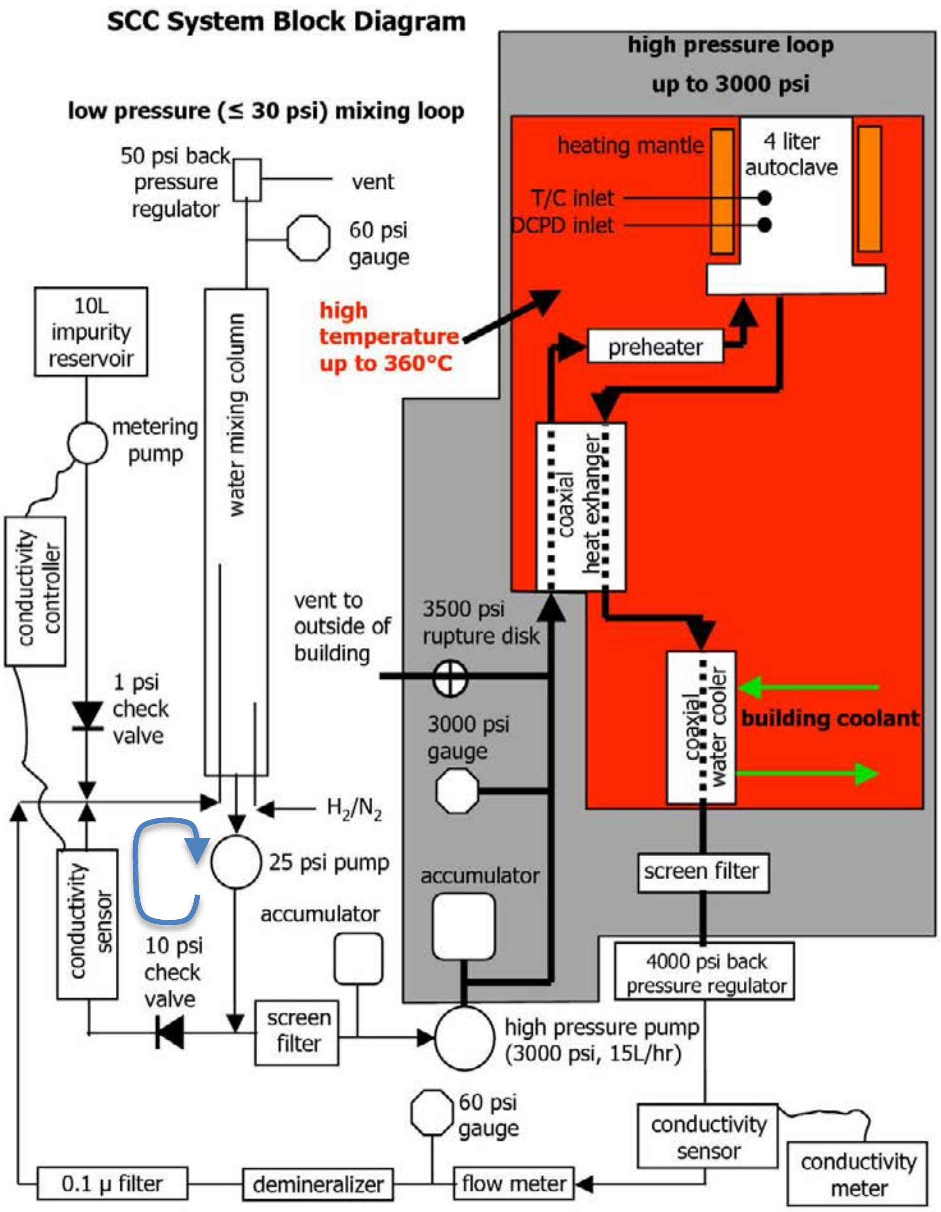

Figure 2.1 Water flow diagram for PNNL SCC crack-growth test systems

Boron (B) and lithium (Li) levels for PWR water testing are controlled by pre-saturating the mixed resin bed demineralizer with boric acid and lithium hydroxide to specific levels that will result in tailored near-constant B and Li content in the water. There is some drift in the Li level in the water because it is singly ionized and is easily displaced from the demineralizer by more highly positively ionized species coming off the autoclave such as chromate. The displaced Li is removed by periodic partial replacement of water in the mixing loop with water having little or no Li (and some B). Boron and Li levels in the mixing loop are determined from measurements of water conductivity, pH, and temperature using pHSC4 software (obtained from Rick Eaker of Duke Power). Autoclave flow rate is held to at approximately 125 cc/min (~2 autoclave exchanges per hour) to provide a consistent chemistry environment within the autoclave.

Load is applied to a sample using a servo-electric motor attached to the test frame. The servo-electric motor is controlled using proprietary software written by Peter Andresen at GEG. The servo-electric motor can provide a smooth cyclic loading sine wave up to about 3 Hz, allowing in-situ pre-cracking of a test sample if desired. Using DCPD data, the GEG software continuously estimates the crack length and adjusts the servo-electric motor to provide constant K loading conditions. As shown in Figure 2.2, the load from the servo-electric motor is transmitted into the autoclave with a pullrod, and the sample is braced from above by a top plate and 4-bar linkage that transmits load to the baseplate of the autoclave which is bolted to the test frame.

Crack length is estimated using a reversing DCPD system also developed by Peter Andresen of GEG. A sketch of the system is shown in Figure 2.3. As with all DC potential drop measurement systems, a constant current is run though the sample, and the voltage across the crack plane is

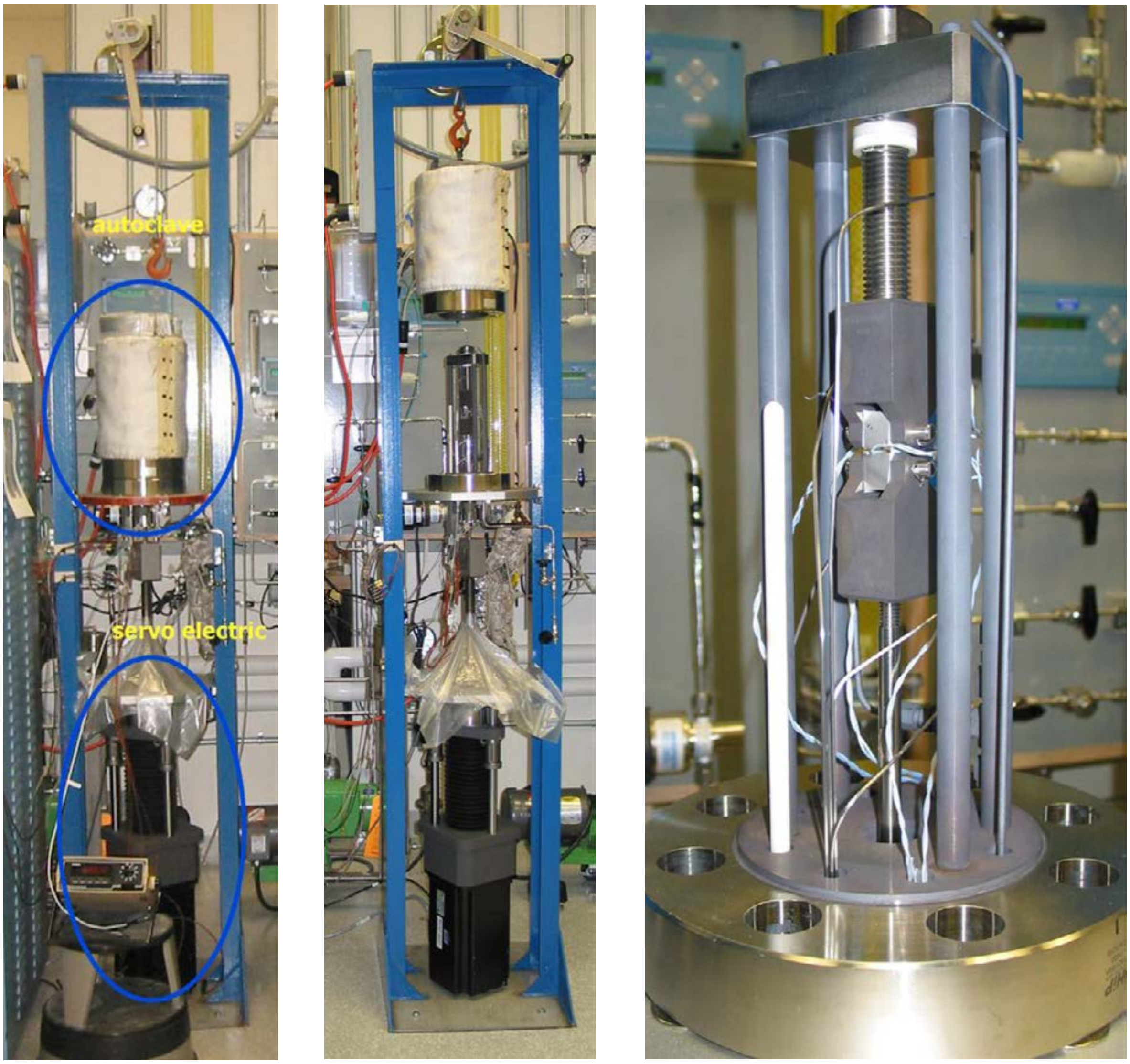

Figure 2.2 Typical crack-growth-rate test frame loading system used at PNNL

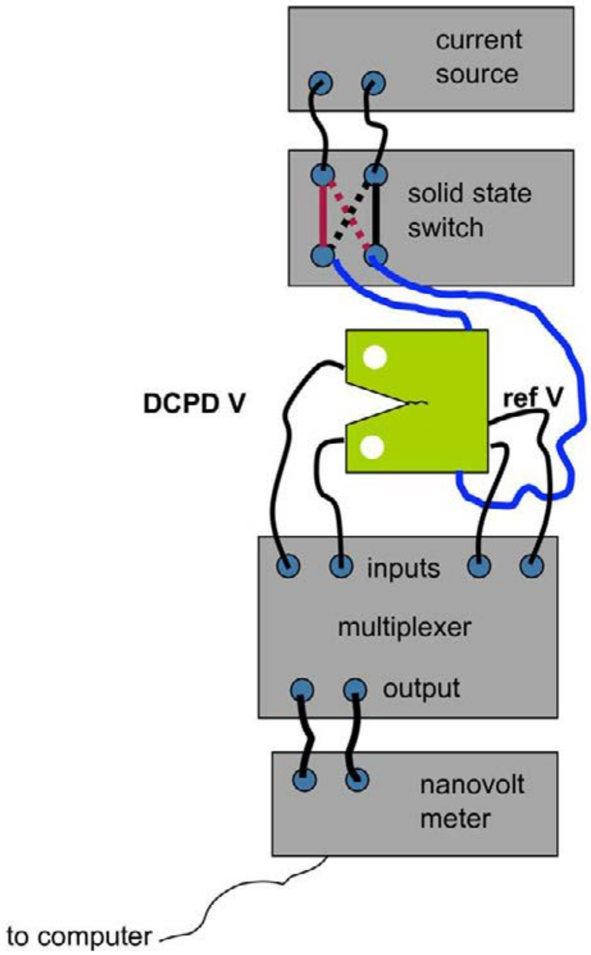

Figure 2.3 Schematic diagram illustrating the DCPD system to measure crack length in situ

measured and converted into a crack length by means of an empirically derived formula relating voltage to crack length. A referenced DCPD resistivity is monitored directly on the test specimen using a “back face” potential method developed at GEG. The algorithm accounts for the fact that the back face potential is also affected by crack length. Using a solid-state polarity-reversing switch built into the current path, potential drop is measured in both a forward and reverse current flow condition. By measuring in both directions, the system eliminates contact voltages from the measurement.

The GEG software also controls the operation of the DCPD system and aggregates the data. Platinum wire is used for current and voltage feeds into the autoclave. For PWR water testing, segmented transformation toughened zirconia (TTZ) tubing is used to help prevent shorting of the Pt wires against other wires or any metal surfaces in the autoclave. Some crosstalk in the voltage wires occurs and is minimized by keeping the wires separated as far as reasonably possible from each other. In addition, the current wires are kept away from the voltage measurement wires. The sample is electrically insulated from the load train through a combination of ceramic spacers and sleeves. Spot welding is used to attach the Pt wires to a specimen. The spot weld locations are marked on the sample prior to inserting the sample into the load train.

The PNNL systems have the capability to monitor autoclave water outlet conductivity, mixing loop water conductivity, autoclave temperature, autoclave water flow rate, sample corrosion potential (via a ZrO_2 insulated Cu/Cu_2O reference electrode in the autoclave), dissolved oxygen, water pressure, DCPD current, and DCPD voltage. With the exception of water pressure and flow rate, these parameters are recorded in the test data file. Statistical information on temperature and current fluctuations are also recorded. Additionally, messages describing changes in test conditions and other issues are a permanent part of the data record.

2.2 General SCC Crack-Growth Testing Approach and Issues

Although systems have been designed for both 1T and 0.5T compact tension (CT) specimens, the primary specimen geometry used in this project is the 0.5T CT with side grooves. The details of this geometry are shown in Figure 2.4. Prior to loading a specimen in the autoclave, the specimen thickness (B), notch depth (a_0), and the width (W) values are all measured and recorded into the data record for the test. During a test, the crack length is defined as "a". Using the specimen dimensions and the strength at the test temperature, in accordance with American Society for Testing and Materials (ASTM) E-1681 [8], an upper limit on K_{EAC} value is calculated using the formula:

$$K_{EAC_{\mathbf{max}}} = \sigma_{ys}\sqrt{D/1.27} \tag{2.1}$$

where σ_{ys} is the yield strength at the test temperature and D is the smaller of B, W-a, and a. For materials with large amounts of work hardening (defined as $\sigma_{UTS}/\sigma_{ys} > 1.3$) such as annealed 300-series stainless steels and nickel-base alloys, the average of the yield and ultimate stress is used in place of the yield stress as per ASTM guidelines. This value is not considered a strict limit but rather provides a reference point for what may be considered a high stress intensity.

After the sample dimensions are measured and spot-weld locations are marked on the sample, it is cleaned and inserted into a test system. Precracking of a sample is done in-situ at the test temperature when a single specimen is being tested. When two or more specimens are mounted in-series, in-situ precracking is not possible because the length of time needed to nucleate a precrack is not consistent and would likely lead to specimens with different precrack lengths. The differing precrack lengths would make it more challenging to maintain and control the K level in both specimens. Thus, our approach is to nucleate a crack individually on each of the two specimens under fatigue in air, and this is followed by continued precracking in-situ for two samples loaded together. Crack transitioning steps are selected to grow the precrack in high-temperature water using the following stages: (1) fatigue, (2) corrosion fatigue and (3) SCC. Typically, this means producing initial pre-cracks of ~1 mm in air followed by an additional ~0.5 mm by cycling in-situ before transitioning to slow cyclic loading plus hold times to promote SCC. An Instron servohydraulic test frame is used to precrack CT specimens in air. The same DCPD electronics and system control software used for the crack-growth systems are also used for precracking in the Instron test frame.

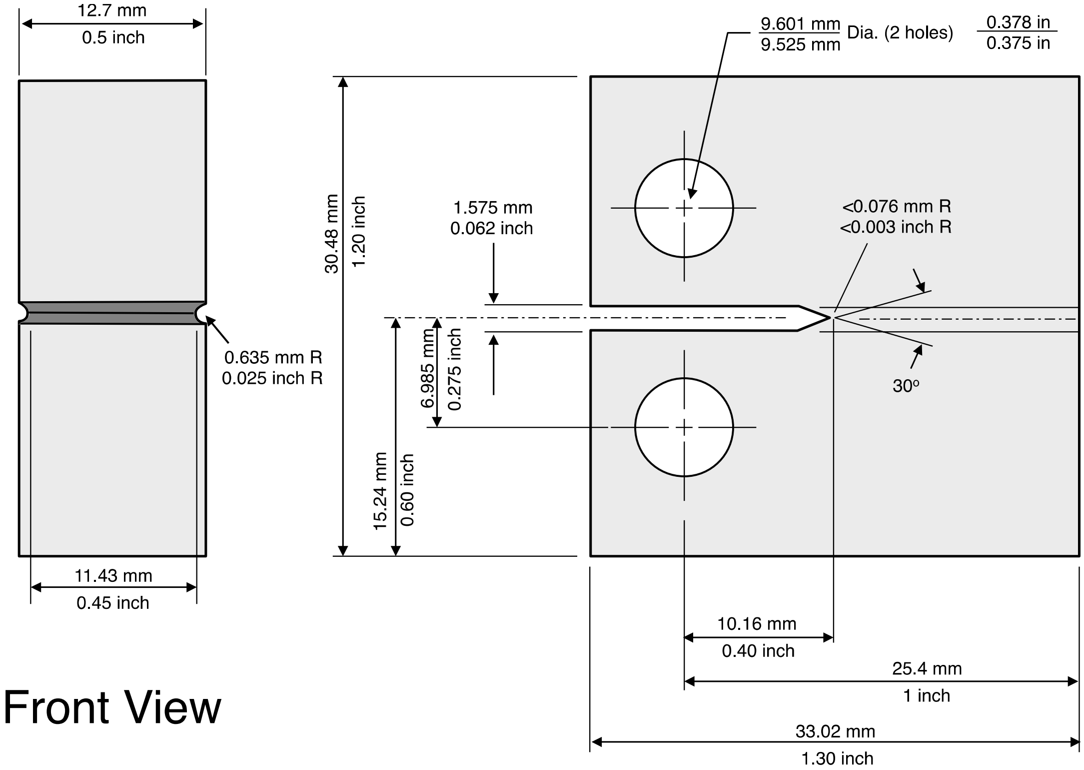

Figure 2.4 **Schematic drawing of a 0.5T CT specimen. Oversized loading holes (~9.5 mm diameter) are used to accommodate ceramic inserts that provide electrical isolation between the CT specimen and clevises. Dimensions for 1T CT specimens are approximately double.**

The first step in precracking is to cycle the sample at a relatively high frequency (2-10 Hz) with a large load ratio and K_{max} less than the K level chosen for constant K. As the crack begins to grow from the notch, the load ratio and frequency are reduced while the K_{max} value is increased. By precracking in this way, each pre-crack segment can grow beyond the plastic zone created by the previous segment. For all samples, cyclic loading steps at frequencies of 0.1 Hz down to 0.001 Hz are performed in high-temperature water. The final phase involves crack transitioning by very slow cycling with a hold time ranging from 1 h to 24 h. This grows the crack beyond the pre-cracking plastic zone and allows the crack to transition from transgranular (TG) fatigue to the crack growth morphology that occurs under constant K conditions. Depending on the material susceptibility, this may be either TG or intergranular (IG) cracking.

For materials such as MA alloy 600 that crack readily in light water reactor (LWR) environments, obtaining a steady crack growth rate after transitioning to constant K can easily be accomplished by following a standard procedure. However, determining a constant K crack growth rate in highly SCC-resistant materials such as alloy 690 and its welds is more challenging with the main focus on giving the crack adequate opportunity to become an engaged IGSCC crack. For these materials, the use of alternate cyclic and cycle+hold loading conditions (including R values and modified rise/fall times) are often employed prior to reaching constant K. Tests conducted at PNNL have shown that an R of 0.5 usually produces the best engagement response, and in base metal materials, efforts are made to run the specimen under slow continuous cycling for at least several grain dimensions prior to the onset of cycle+hold loading. The much larger grain dimensions and more irregular shape of the grain boundaries in weld metal specimens makes transitioning to an engaged crack front even more challenging. If extremely slow or inconsistent crack growth rates are observed, cyclic loading is typically restarted to move the crack forward (ten to several hundred micrometers) and then retransition to constant K. This retransitioning procedure may be performed several times. The constant K SCC response is judged on the response of the material to these multiple observations at constant K. Assessment of the propagation rate under selected cyclic loading and hold time conditions is also used to judge the environment-assisted crack growth resistance of the material.

The ideal increment of crack length over which to measure a steady crack growth rate (CGR) would be several grain diameters. However, this is often an impractical goal for the high Cr alloys that could take more than two years for a single observation, and so it is necessary to choose an increment based on factors related accuracy and resolution in the DCPD crack length data trend. The most easily quantifiable factor is noise or scatter in the DCPD crack length data. Each PNNL crack growth system has slightly different noise levels. Our best system has a noise level of <1.5 µm peak-to-peak, while our “worst” system has <3 µm peak-to-peak noise. Noise creates uncertainty in the measurement that is greatest when only a few measurements are performed, but as the number of measurements is increased, an average value can be resolved along with statistics on the goodness of fit. This is equivalent to fitting a trend line through the data. As long as the noise remains random (e.g., the residuals in the curve fit remain random), trends in the data down to the noise level can be resolved. Other factors contributing to the uncertainty in trends in the data are related to environment, crack morphology effects, and resistivity drift of the material. Environmental parameters such as water temperature, conductivity and dissolved hydrogen have been found to affect the measured crack length, and it is important to limit deviations in these parameters. All environmental parameters on PNNL crack growth systems that can lead to phantom changes in crack length are continuously monitored and tightly controlled.

The factor affecting crack length accuracy and resolution that is most difficult to control is crack morphology. DCPD measurement is founded on the premise that there is no electrical current conduction behind the crack front. However in SCC testing, it has been found that there is almost always some feature in the crack morphology that allows current conduction behind the crack front. The most easily identifiable feature is an uncracked ligament in the wake of a crack front as shown in Figure 2.5. Electric current bridging across very closely spaced crack walls via Ni filaments is also thought to contribute to conduction behind the crack front. Uneven growth along the crack front also causes crack length under-prediction and reduced sensitivity in the same way as ligaments behind the crack front. When using empirical correlations developed from idealized finite element modeling or from air fatigue testing, these features cause under prediction of DCPD-measured crack length and reduce the sensitivity of the DCPD system to detecting movement of the crack front. Since the formation of these features during a test cannot be systematically predicted, there is no way to predictably alter the correlation. Instead, a user-adjustable anticipatory correction factor has been added to the correlation formula. Historical trends in past tests have been used to develop estimated anticipatory correction factors that are applied to current tests. Different materials or different material treatments have been found to require different anticipatory correction factors.

Figure 2.5 **Example of large uncracked ligament detected in the wake of a crack**

Another way exists to compensate for the effect that ligament/contact formation or uneven crack growth has on masking crack extension. During constant K assessments, the crack propagates without any fatigue cycling to break ligaments/contacts and keep the crack front straight. If ligaments/contacts are forming during this constant K crack extension, or if uneven crack extension is occurring, the CGR during load cycling immediately after the constant K observation will be accelerated as the fatigue cycling wipes out some or all of the ligaments/ contacts and straightens the crack front. PNNL routinely applies the exact same cyclic loading conditions before and after a constant K observation to help account for untracked crack extension. When the crack front undergoes little or no shape change or when there is no ligament/contact formation, the propagation rates before and after constant K are very similar as shown in the test data in Figure 2.6. The test trace in Figure 2.7 shows much higher CGRs after constant K that point to untracked crack extension. The amount of untracked crack extension is determined by tracing a slope back from the point where the cycle+hold propagation rate stabilizes to a value that is close to the value observed before constant K. The distance that line sits above the DCPD test trace at the conclusion of the constant K observation is the estimated amount of untracked crack extension. An adjusted constant K CGR is then calculated using this value as shown in the plot.

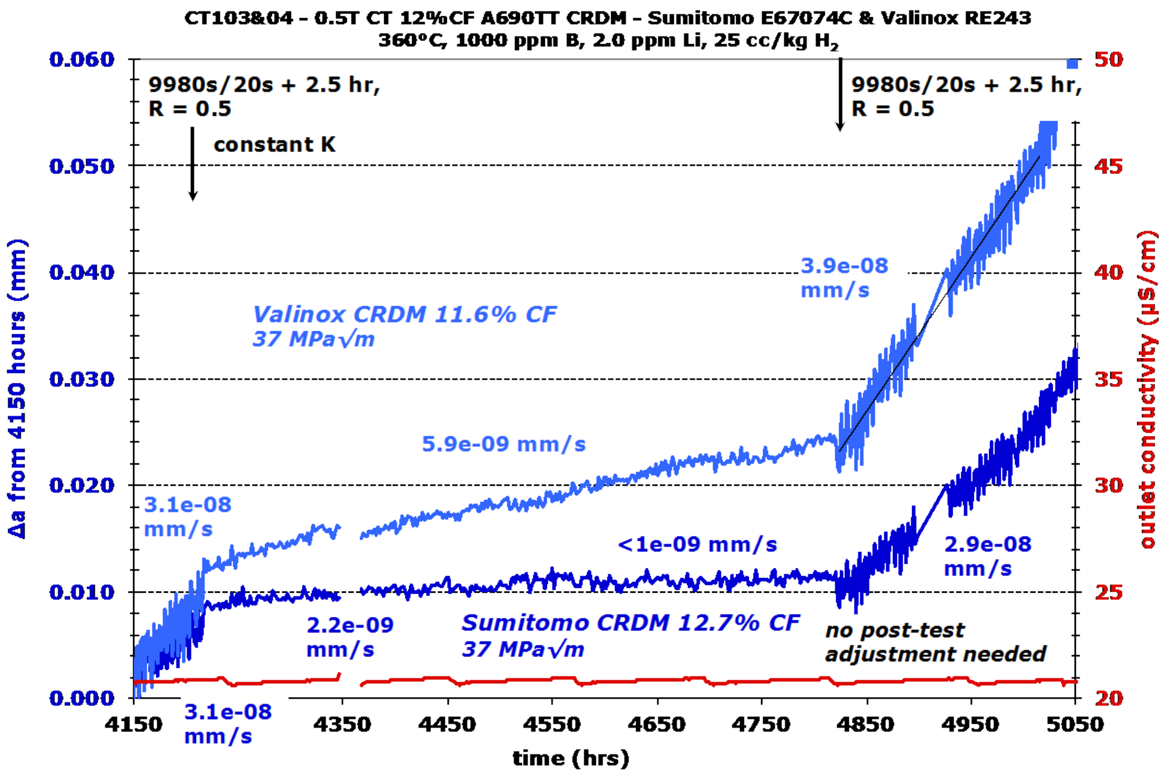

Figure 2.6 Two examples of when the same cyclic loading conditions before and after a constant K observation produce similar crack-growth rates

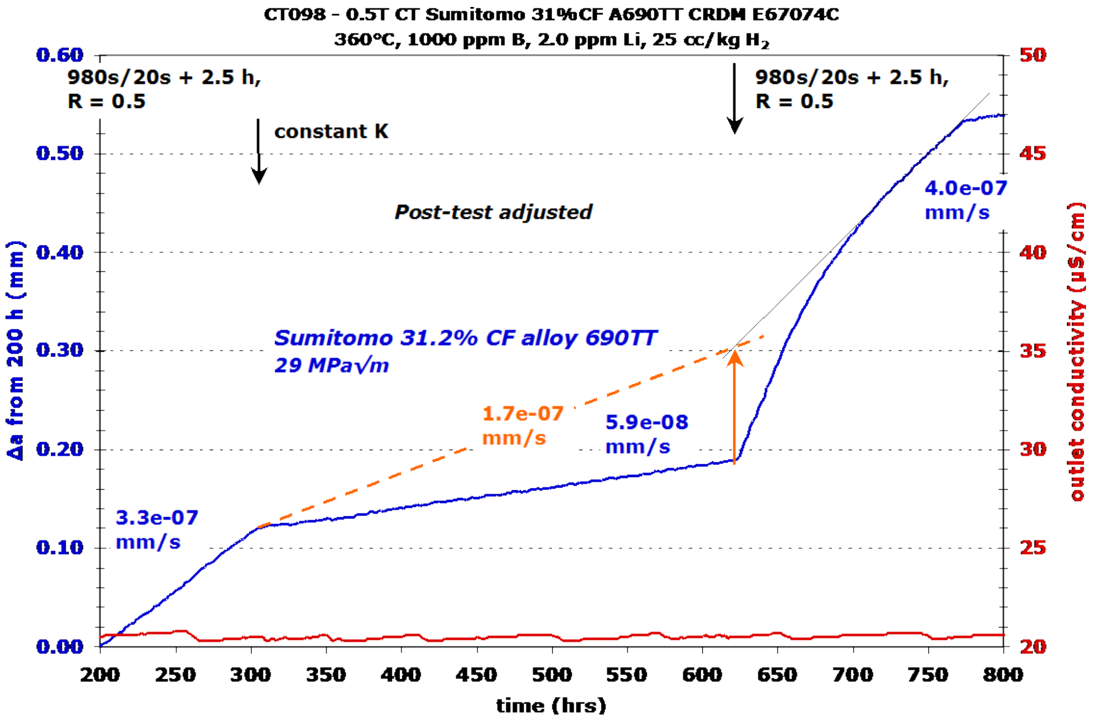

Figure 2.7 Example of accelerated propagation rate after a constant K observation and how it is used to estimate the untracked crack extension and revised constant K crack-growth rate

Besides causing an under prediction in crack length, crack ligaments can also cause large steps in crack extension when they break. Another aspect that leads to falsely high CGR is the resistivity change that occurs in Ni-base alloys such as alloy 600 and alloy 690. It is a well-known phenomenon that the resistivity of these alloys will slowly increase with time when testing at PWSCC temperatures. Without compensation, resistivity drift will give the appearance of a slowly increasing crack length. It is typical to compensate for resistivity drift by monitoring the resistivity of a piece of unstressed reference coupon placed in the autoclave environment. The resistivity change of the test specimen is normalized to the resistivity of the reference coupon. Our approach has been to monitor the resistivity change on a portion of the test specimen itself in a region that is not significantly affected by crack extension. This is a more elegant solution that is easier to implement in the tight confines of the autoclave.

Looking at all these factors in aggregate, the test systems at PNNL are designed with a sufficiently high data acquisition rate to allow trends in crack extension to be detected down to the noise level of the DCPD system as long as test conditions are tightly controlled, resistivity drift is properly factored into the crack length correlation, and a suitable anticipatory correction has been applied.

2.3 Specific SCC Crack-Growth Testing Approach

Unless noted otherwise, experiments were conducted in simulated PWR primary water with 2000 ppm B and 2 ppm Li. A prototypic simulated PWR primary water environment is considered to be 325°C with 29 cc/kg H_2. Tests conducted early in the program were often done at this temperature and hydrogen concentration, however the desire to better understand the SCC CGR response of alloy 690 and its welds eventually led to testing at 350°C, and then later at 360°C. Testing now is routinely conducted at 360°C. Dissolved hydrogen (DH) concentrations employed also changed over the course of the program with most testing now done at DH levels that place the corrosion potential of the material on the Ni/NiO stability line where crack growth response is known to be greatest in alloy 600 and its weld metals [9,10]. The stress intensity (K) was typically controlled to a value of 30 MPa√m under most conditions, however high K values were evaluated up to ~45 MPa√m later in several tests and as low as 18 MPa√m to evaluate K effects. Crack growth tests were performed with two specimens in series allowing a greater range of material conditions to be examined in a shorter period of time.

Specimens were first precracked in air followed by further crack extension using aggressive cycling in high temperature water. A variety of loading conditions were used to attempt to transition from the TG precrack to an IGSCC crack front. Loading conditions included R values ranging from 0.3 to 0.5, the addition of hold times up to 24 h, and various “periodic unload” schemes with a symmetric or a sawtooth wave form (e.g., slow loading followed by rapid unloading). A final cycling step of 980 s rise followed by a 20 s fall (0.001 Hz) with R = 0.5 was often used and followed by the addition of hold times (at K_{max}) before determining crack growth rates at constant K.

The response of the material during transitioning was assessed continuously by comparing current propagation rates to results from earlier tests. As the database of observed crack growth rates and accompanying crack surface morphologies from previous tests grew, higher crack growth rates during transitioning (particularly during cycle+hold loading) could be identified. If a crack growth rate was indicative of a non-engaged crack front during transitioning, then the crack would often be re-transitioned in an attempt to improve SCC engagement. For these SCC resistant alloys, several transitioning attempts were typically made before documenting crack-growth response at constant K.

The general philosophy for assessing SCC behavior of alloy 690 and its weld metals is to first obtain baseline crack growth response with the material in the expected plant thermo-mechanical condition and then follow with tests on material in more aggressive conditions not expected in plant components. Testing begins in either simulated PWR primary water or in an aggressive PWR primary water environment (elevated temperature, testing at the Ni/NiO line). In some tests, these conditions would eventually be followed by systematic variations in environmental conditions to assess the effects of parameters such as temperature, K and corrosion potential on the crack growth rate of these materials.

A variety of post-test examinations are performed on the specimens. Rather than fatigue open the entire CT specimen, it is standard practice at PNNL to cut the CT specimen in the thickness (B) direction into a 2/3 and 1/3 slice. The 2/3 slice is fatigued open for crack surface observations while the 1/3 slice is given an ultrafine polish (colloidal silica as the last step) in cross section to provide an alternate observation of crack morphology and to allow for performing hardness and EBSD strain mapping in representative material. These latter measurements are performed in the geometric crack plane of the specimen ~3 mm ahead of the final crack front. This is well out in front of any plastic strain produced from the applied load during the test. Specimens for other characterizations can also easily be removed for bulk microstructures, from the crack-tip region, or from the crack wall behind the crack front. The one disadvantage of this method is that the entire crack surface cannot be observed. This is felt to be relatively minor compared to the numerous advantages for microstructural characterizations.

2.4 Uncertainties in Crack-Growth Data Measurements

While the noise resolution of the DCPD test method is in the range of ±1 μm and allows establishing trends in the crack growth rate down to ~$5x10^{-10}$ mm/s, the accuracy of these rates depends on some factors that cannot be fully assessed. This is particularly true for resistant materials where SCC engagement is limited and low growth rates are measured. For example, crack front irregularity can have an effect on the DCPD-measured growth rate, but there is no way to document the shape of the crack front as the crack grows, and therefore, this effect cannot be accurately included into post-test crack length corrections. Another issue is that it is often not possible to uniquely identify each phase of a test on a crack surface after the test has ended. As a result, the post-test correction is typically based on the entire in-situ portion of the test. An additional complication is the effect of ligament or contact formation on constant K crack growth. Even though attempts are made during the test to assess these effects, there are no post-test means to assess exactly how well this method works. Crack-growth testing experience and interactions with the international expert community has produced many insights into issues, however many uncertainties cannot be effectively quantified. Based on our experience, state-of-the-art testing methods and data analysis approach, we believe overall uncertainties for crack-growth-rate measurements on SCC-susceptible materials are on the order of ±50%. As noted above, the degree of uncertainty increases for the measurement of low crack-growth rates in SCC-resistant materials where it is difficult to obtain SCC engagement and stable growth. Uncertainty in reported stress intensity is smaller because the application of a post-test correction based on the observed overall crack length gives a good measure of the final stress intensity, and the uncertainties in the small crack length increments for each portion of the test have a small effect of the corrected stress intensity during each step of the test.

3 MICROSTRUCTURE, STRAIN, AND HARDNESS CHARACTERIZATIONS

3.1 Chapter Overview

This chapter covers all aspects of the microstructure of the materials studied for this report. It starts first with an overview of the as-received alloy 690 microstructures. Both CRDM and plate materials are reviewed. This is followed by a review of grain boundary damage microstructures due to cold working. The remaining sections of this chapter are dedicated to hardness and plastic strain characterizations of the materials. The hardness and electron backscatter diffraction (EBSD) integrated misorientation density (IMD) measurement methods are discussed and are followed by the examination results for all the materials. Data tables are used extensively throughout this chapter to summarize observations and measurements.

3.2 Examinations of As-Received Alloy 690 Microstructure

A description is given in Table 3.1 of the six different heats of alloy 690 CRDM material from three different manufacturers that are covered in this report. Four of the heats are from Valinox, one is from Sumitomo, and one is a bar product that was produced by TK-VDM and used by Doosan for CRDM tubing. All materials are in a thermally treated condition with semi-continuous or continuous grain boundary carbide coverage as shown in the scanning electron microscope (SEM) backscatter electron (BSE) images in Figure 3.1. Grain size images in Figure 3.2 show that the Valinox and TK-VDM (Doosan) heats have a grain size of ~90 µm while the extensive twinning not removed by the solution anneal in the Sumitomo CRDM has resulted in a smaller grain size of ~35 µm. Detailed analysis of the general microstructure of the Valinox heats WP140, WP142, and RE243 was reported in the prior NUREG [7].

Table 3.1 Composition, heat treatment, and as-received mechanical properties for the alloy 690 CRDM materials covered in this report

Source/Manufacturer and Heat #	Dim. (mm)	Composition, wt%	Heat Treatments and Room Temp. Mechanical Properties
Valinox/Valinox WP140 Tube 2502	116 OD x 30 wall	Ni-29.0Cr-10.4Fe-0.03C-0.3Mn-0.33Si-0.18Al-0.3Ti-0.005P, <0.001S	1120°C/~1 min, WQ + 716-722°C/10.2 h, Air cool YS = 276 MPa, HV = 163 kgf/mm^2
Valinox/Valinox WP142 Tube 2541	116 OD x 30 wall	Ni-29.0Cr-10.5Fe-0.02C-0.3Mn-0.35Si-0.47Ti-0.01Nb-0.001S-0.003P	1096°C/~1 min, WQ + 716-722°C/10.2 h, Air cool YS = 269 MPa, HV = 163 kgf/mm^2
Valinox/Valinox RE243 Tube 2360	112 OD x 34 wall	Ni-28.9Cr-10.4Fe-0.02C-0.3Mn-0.35Si-0.14Al-0.23Ti-0.024N-0.008P-0.0005S	1122°C/~1 min, WQ + 716-725°C/10.5 h, Air cool YS = 255 MPa, HV = 157 kgf/mm^2
CIEMAT-ENSA/ Valinox WP787	125 OD x 42 wall	Ni-29.1Cr-10.0Fe-0.017C-0.30Mn-0.27Si-0.20Al-0.29Ti-0.007Cu-0.006S-<0.001P	1060°C Anneal + 715°C/6 h/Air Cool YS = 263 MPa, HV not measured
EPRI/ Sumitomo E67074C	127 OD x 33 wall	Ni-29.8Cr-9.8Fe-0.02C-0.29Mn-0.23Si-0.03Cu-0.0002S	Anneal + 725°C/10 h/Air Cool YS and HV not measured
EPRI/ TK-VDM (Doosan) 133454	152 OD solid bar	Ni-29.1Cr-8.9Fe-0.020C-0.26Mn-0.29Si-0.26Al-0.32Ti-0.01Cu-0.02N-0.005P-<0.002S-0.002B	1045°C/4 hr/WQ + 720°C/10 hr/AC YS = 263 MPa, HV = 165 kgf/mm^2

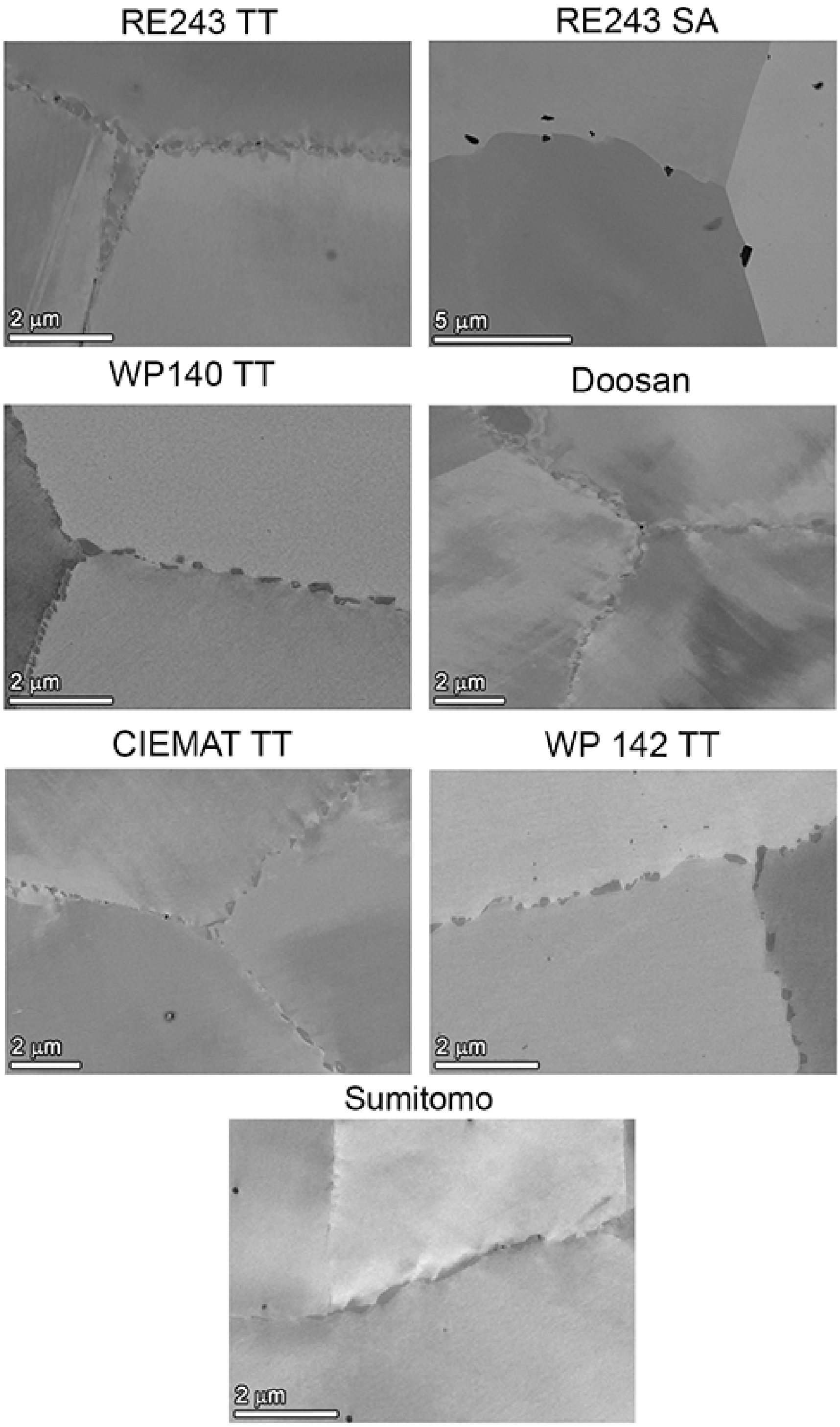

Figure 3.1 SEM BSE summary microstructure images for each of the six different heats of alloy 690 CRDM material

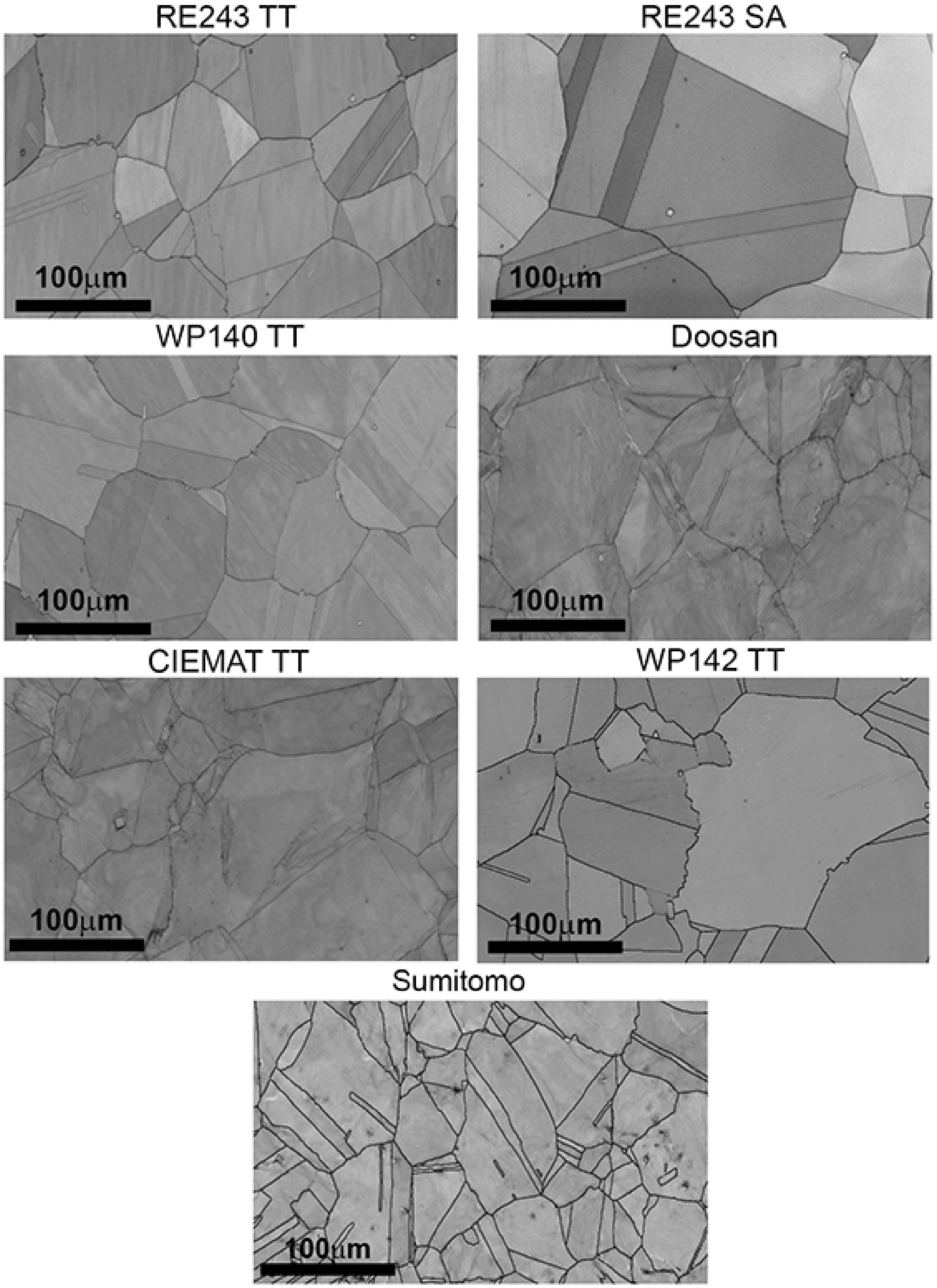

Figure 3.2 Grain size for the six heats of alloy 690 CRDM material. Images were obtained by SEM EBSD pattern quality mapping.

A description is given in Table 3.2 of the five different heats of alloy 690 bar/plate materials from four different manufacturers that are covered in this report. Carbide precipitation was limited to a few isolated grain boundaries in the MA GEG B25K heat, while the MA ANL NX3297HK12 heat exhibited a moderate distribution of IG carbides as shown in Figure 3.3. The Allvac and the TK-VDM plate materials have partial IG carbide coverage, and the ENSA WP547 has almost continuous coverage. Grain size was more variable for the plate materials. SEM-EBSD images in Figure 3.4 show that the grain size for the GEG alloy is ~15 µm and ~50 µm for the ANL alloy. Extensive twinning in the TK-VDM, ENSA and Allvac materials complicates grain size measurement. The TK-VDM and Allvac plate materials appear to have a grain size of ~30 µm, while the ENSA grain size is ~50 µm. This information on the CRDM and bar/plate heats is summarized in Table 3.3.

Table 3.2 Composition, heat treatment, and mechanical properties for the alloy 690 bar/plate materials covered in this report

Source/Manufacturer and Heat #	Composition, wt%	Heat Treatments and Room Temp. Mechanical Properties
ANL/ Special Metals NX3297HK12	Ni-29.5Cr-9.9Fe-0.03C-0.20Mn-0.07Si-0.01Cu-<0.001S	1038°C/2 hr/AC YS not measured, HV = 173 kgf/mm^2
GEG/ Allvac B25K-2†	Ni-29.3Cr-9.2Fe-0.034C-0.22Mn-0.06Si-0.26Al-0.37Ti-<0.01Cu-0.03N-0.006P-<0.0003S-<0.001B	996°C/20 min/AC YS = 294 MPa, HV = 173 kgf/mm^2
EPRI/ TK-VDM 114092	Ni-29.5Cr-9.5Fe-0.020C-0.25Mn-0.26Si-0.32Al-0.36Ti-<0.01Cu-0.003P-<0.002S	1030°C/1 hr/WQ + 715°C/10 hr/AC YS = 285 MPa, HV = 155 kgf/mm^2
ENSA/ Aubert&Duval WP547	Ni-29.4Cr-10.1Fe-0.020C-0.30Mn-0.36Si-0.18Al-0.18Ti-<0.005Cu-0.022N-0.007P-0.0006S-0.0005B	1068°C/20 min/WQ + 715°C/10 hr/AC YS and HV not measured
EPRI/ Allvac X87N-1	Ni-30.0Cr-9.2Fe-0.020C-0.20Mn-0.05Si-<0.01Cu-<0.0003S	1030°C/4 hr/WQ + 727°C/5 hr/AC YS = 265 MPa, HV not measured

† Also referred to as B25K.

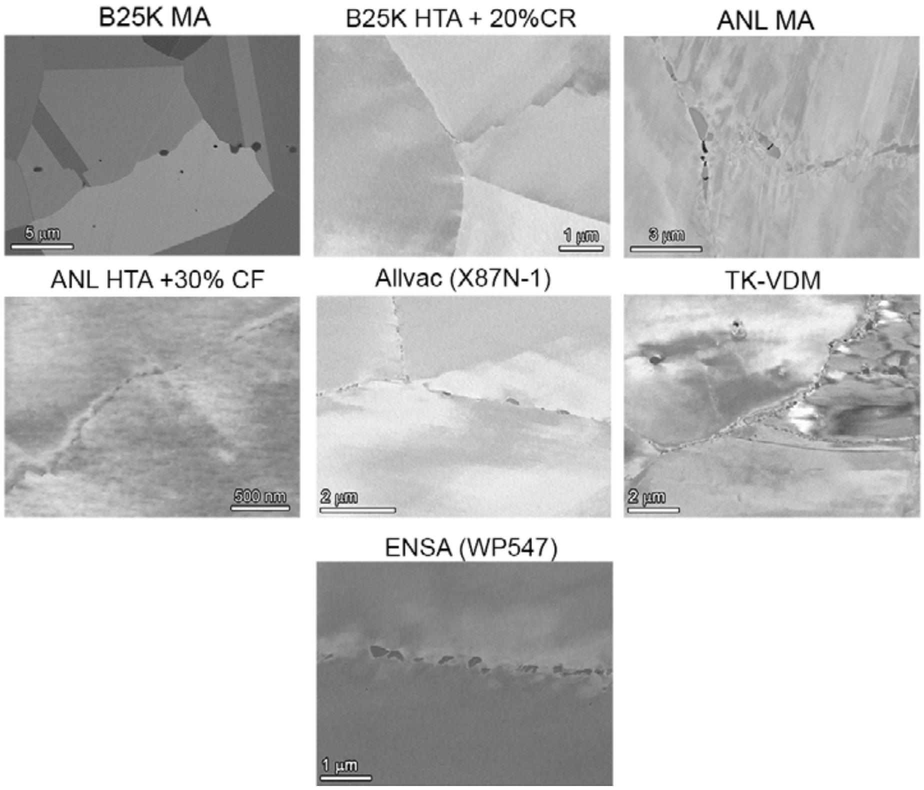

Figure 3.3 SEM BSE summary microstructure images for each of the six different heats of alloy 690 plate materials

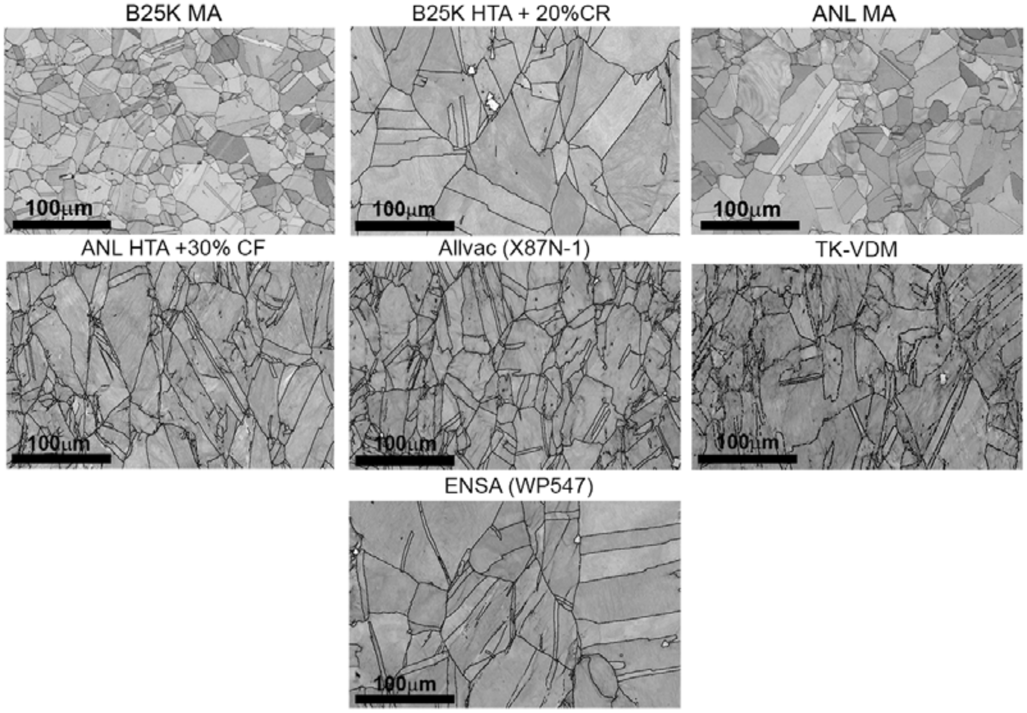

Figure 3.4 Grain size for the six heats of alloy 690 plate material. Images were obtained by SEM EBSD pattern quality mapping

Table 3.3 Summary of grain size and carbide distributions for selected materials

Material	Grain Size (µm)	Carbide Location	Carbide Density
CRDM Materials			
Valinox RE243 TT	~40-50	IG, 50-200 nm	Semi-continuous, spacing ~100 nm
Valinox RE243 SA	~100-120	No carbides	No carbides
Valinox WP140 TT	~75-90	IG, 50-300 nm	Semi-continuous, spacing ~100 nm
TK-VDM 133454 TT	~50-60	IG, 50-200 nm	Semi-continuous, spacing ~100 nm
CIEMAT WP787 TT	~50-60	IG, 50-200 nm	Semi-continuous, spacing ~100 nm
Valinox WP142 TT	~50-60	IG, 50-300 nm	Semi-continuous, spacing ~100 nm
Sumitomo E67074C TT	~35-40	IG, 50-300 nm	Semi-continuous, spacing ~100 nm
Plate Materials			
GEG B25K MA	~10-15	TG and isolated IG, 0.5-1 µm	Low
GEG B25K HTA	~45-50	IG, 20-30 nm	Low, sporadic distribution
GEG B25K HTA + TT	~45-50	IG, 20-30 nm	Low, sporadic distribution
ANL HK3297HK12 MA	~20-25	IG, 0.3-0.5 µm	Semi-continuous Spacing ~100 nm
ANL HK3297HK12 MA + SA	~30-35	IG, 0.01-1 µm	Low, sporadic distribution
Allvac X87N-1 TT	~20-25	IG, 50-200 nm	Semi-continuous Spacing ~200 nm
TK-VDM 114092 TT	~35-40	IG, 50-200 nm	Semi-continuous Spacing ~200 nm
ENSA WP547 TT	~55-60	IG, 50-200 nm	Semi-continuous Spacing ~200 nm

3.3 Characterization of Permanent Damage in Cold Worked Alloy 690 Materials

As employed for the microstructural characterizations of the as-received materials, SEM secondary electron (SE) and BSE, transmission electron microscopy (TEM), and TEM/SEM energy dispersive spectroscopy (EDS) elemental composition maps were utilized to examine the various types of CW-induced damage. SEM was used to obtain a global perspective of the damage throughout the sample, whereas TEM and EDS mapping provided a more detailed, localized examination. It should be noted that identification of a void versus a crack through SEM imaging was often challenging in the TT samples due to their high IG carbide distribution. A void between two overlapping carbides may easily appear as a crack. In addition, TiN particles have a very low backscatter yield as compared to the remainder of the alloy and their contrast can be difficult to separate from that for a void. SEM secondary and backscatter image pairs were collected in many cases to help discriminate between TiN particles and voids.

3.3.1 Cold Work Damage in Alloy 690 CRDM RE243

All of the CRDM materials that were used for cold work studies have been examined for permanent grain boundary damage. Using the counting methodology adopted in the prior NUREG [7], the number of cracks and voids were counted from at least 10 grain boundaries across the sample. A summary of the degree of damage for the CRDM materials is provided in Table 3.4. Examples of damage microstructures for the alloy 690 CRDM RE243 heat are provided in the following paragraphs.

Table 3.4 Summary of carbide microstructures and damage morphologies in cold worked alloy 690 TT CRDM materials

Material	Carbide Location	Carbide Density	Crack Density	Void Density
Valinox RE243 11.6%CF	IG, 50-200 nm	Semi-continuous, spacing ~100 nm	Low	Low
Valinox RE243 17%CR	IG, 50-200 nm	Semi-continuous, spacing ~100 nm	Low	Low-Moderate
Valinox RE243 21%CF	IG, 50-200 nm	Semi-continuous, spacing ~100 nm	Low-Moderate	Moderate-High
Valinox RE243 30%CR	IG, 50-200 nm	Semi-continuous, spacing ~100 nm	Low-Moderate	High
Valinox RE243 31%CR	IG, 50-200 nm	Semi-continuous, spacing ~100 nm	Low-Moderate	High
Doosan 133454 21%CF	IG, 50-200 nm	Semi-continuous, spacing ~100 nm	Low-Moderate	High
Sumitomo E67074C 12.7%CF	IG, 50-300 nm	Semi-continuous, spacing ~100 nm	Low	Low-Moderate
Ciemat WP787 20%TS	IG, 50-200 nm	Semi-continuous, spacing ~100 nm	Low-Moderate	High

The 17%CR CRDM alloy 690TT and SA materials showed significant strain contrast in SEM images and limited TEM exams documented the expected high dislocation densities. There is evidence that deformation is localized at grain boundaries particularly for the TT materials with a semi-continuous distribution of small carbides. Isolated voids and cracked carbides were observed in the 17%CR alloy 690TT material as illustrated in Figure 3.5 and Figure 3.6. SEM exams indicated that the most common permanent damage in this material was small, well-spaced voids. Only a few cracked carbides were found, however a TEM sample prepared via focused ion beam (FIB) milling (Figure 3.6) revealed two cracks as well as a void along a carbided grain boundary in less than a 2 µm region. It can be difficult to discriminate between the formation of a crack or void in the scanning TEM image, but examination of the Cr-K elemental map shows that the cracks disrupt two continuous carbides. A secondary point of note in the Cr elemental map in Figure 3.6 is the overlap of two carbides in this section. Because TEM samples have a finite thickness, overlap of carbides on the grain boundaries is expected. Unfortunately, this brings into question as to whether observations on overlapping, faceted carbides signify a crack or a void. Often in SEM and TEM images, there are high contrast objects between carbides that appear angled, and thus complicate the identification. The easiest determination of void formation is seen by its shape and relationship to adjacent carbides in both **Figure 3.5** and **Figure 3.6**.

Since 17%CR alloy 690SA material was free of any grain boundary carbides, no cracking or voids associated with this second phase were observed. While there were isolated TiN particles dispersed in the matrix and a few on grain boundaries, none of these were found to be cracked or have voids associated with them.

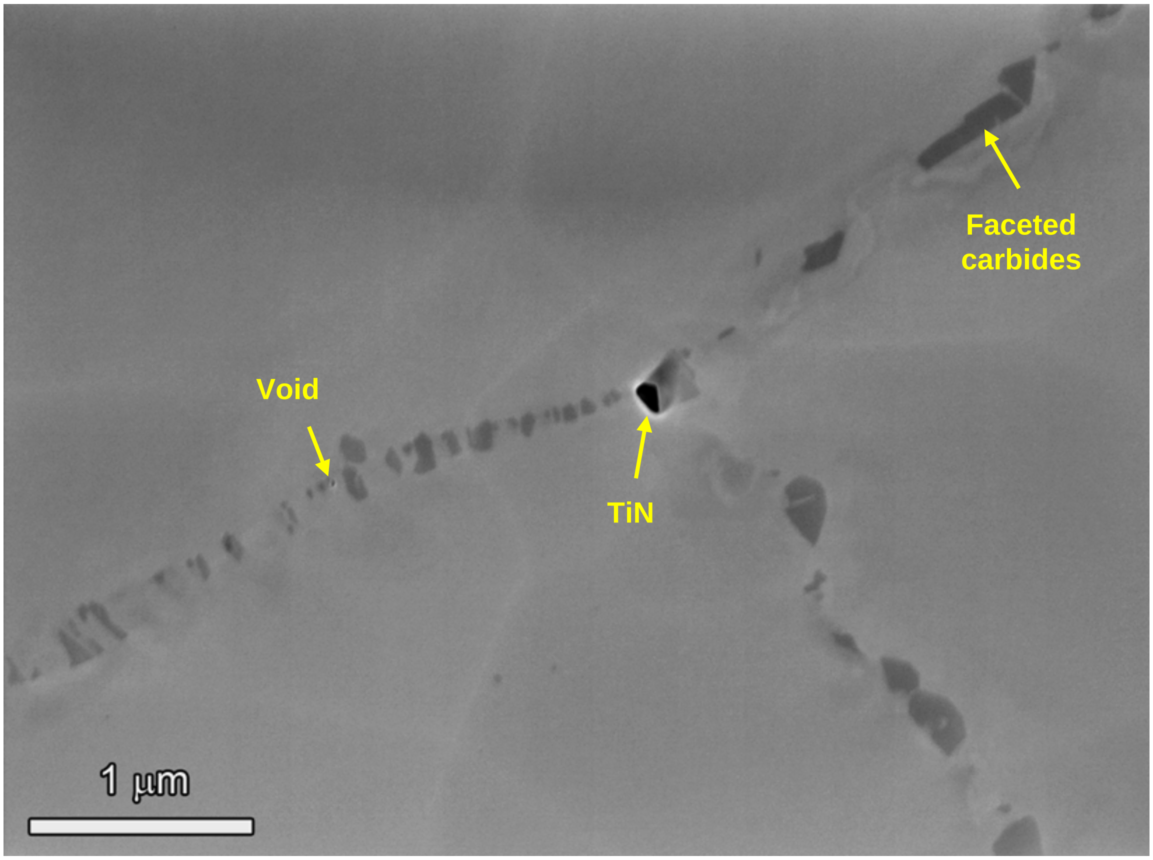

Figure 3.5 SEM backscatter micrograph illustrating representative image of $M_{23}C_6$ damage microstructure in 17%CR CRDM alloy 690TT (heat RE243)

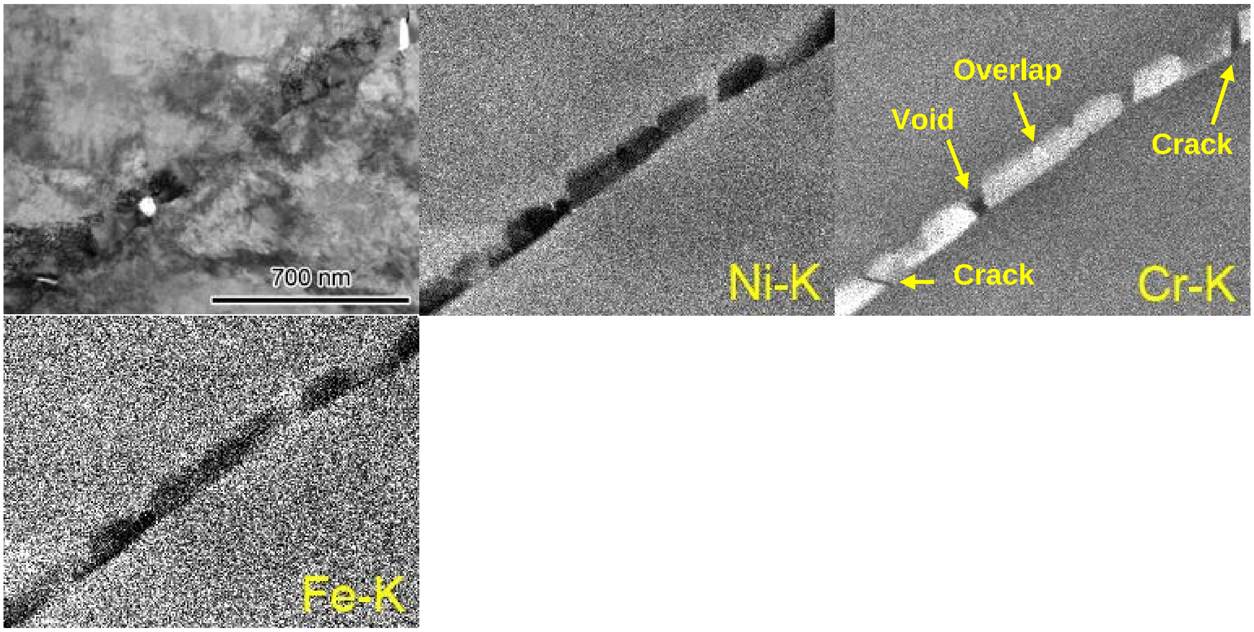

Figure 3.6 TEM elemental maps illustrating damage in 17%CR CRDM alloy 690TT (heat RE243)

The 31%CR CRDM alloy 690TT again showed an extremely high dislocation density and a much larger amount of localized permanent damage at grain boundaries as compared to the 17%CR alloy 690TT material. SEM analyses identified a large number of voids in both cellular carbide (Figure 3.7) and discrete carbide (Figure 3.8 and Figure 3.9) regions. Cellular carbide regions typically exhibited an array of various sized voids adjacent to $M_{23}C_6$ interfaces within the boundary migrated area. A much lower density of cracked carbides than voids were present in these structures. More importantly, there also appeared to be more voids than cracked carbides along boundaries with discrete $M_{23}C_6$ particles. As previously discussed, differentiating between the sporadic TiN particles, cracked carbides, and voids can be difficult. Examples of highly damaged grain boundary regions are presented in Figure 3.8 and a high density of local “dark” features can be seen resulting from low backscatter electron yield. After careful examination (often comparing backscatter and SE images), it was determined that most of the small (<75 nm) equiaxed and the elongated features (formed at the interfaces of faceted carbides) were voids. These elongated cavities appear to abruptly change in shape as the void grows between faceted carbides as seen in Figure 3.7, Figure 3.8(b) and Figure 3.8(c).

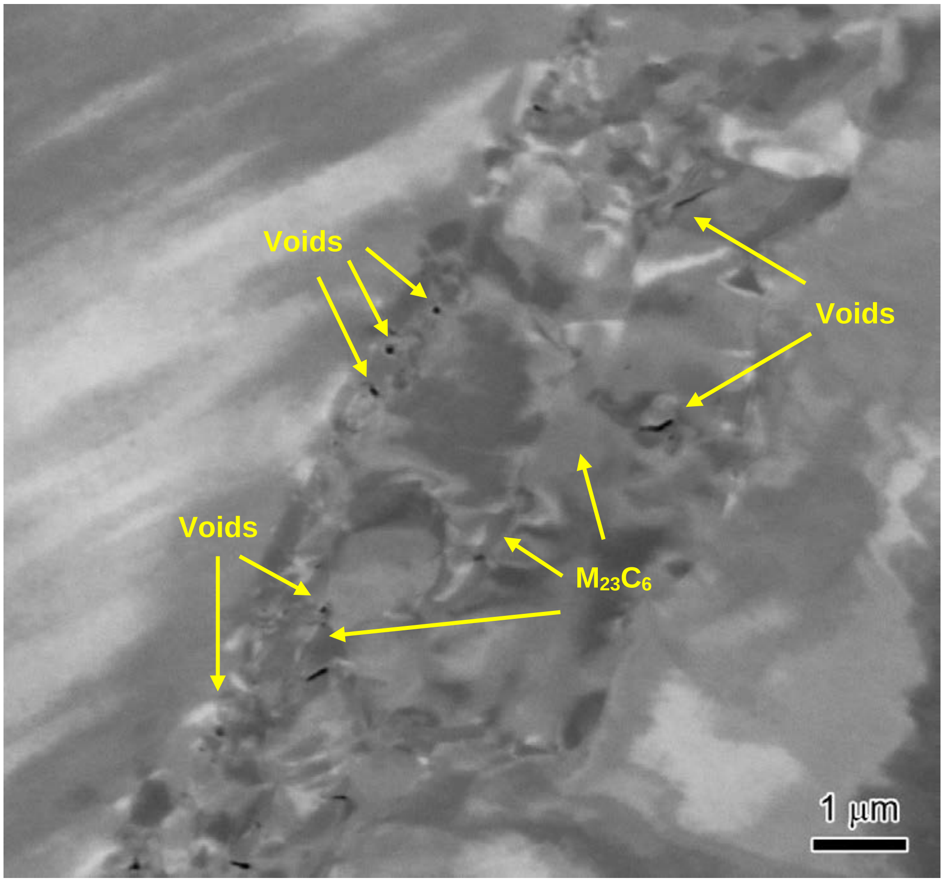

Figure 3.7 Low magnification SEM backscatter image showing CR-induced void formation within a cellular carbide microstructure region in the 30%CR CRDM alloy 690TT material (heat RE243). The strain contrast in this backscatter image masks the appearance of the $M_{23}C_6$ carbides, but the voids between carbides are readily apparent.

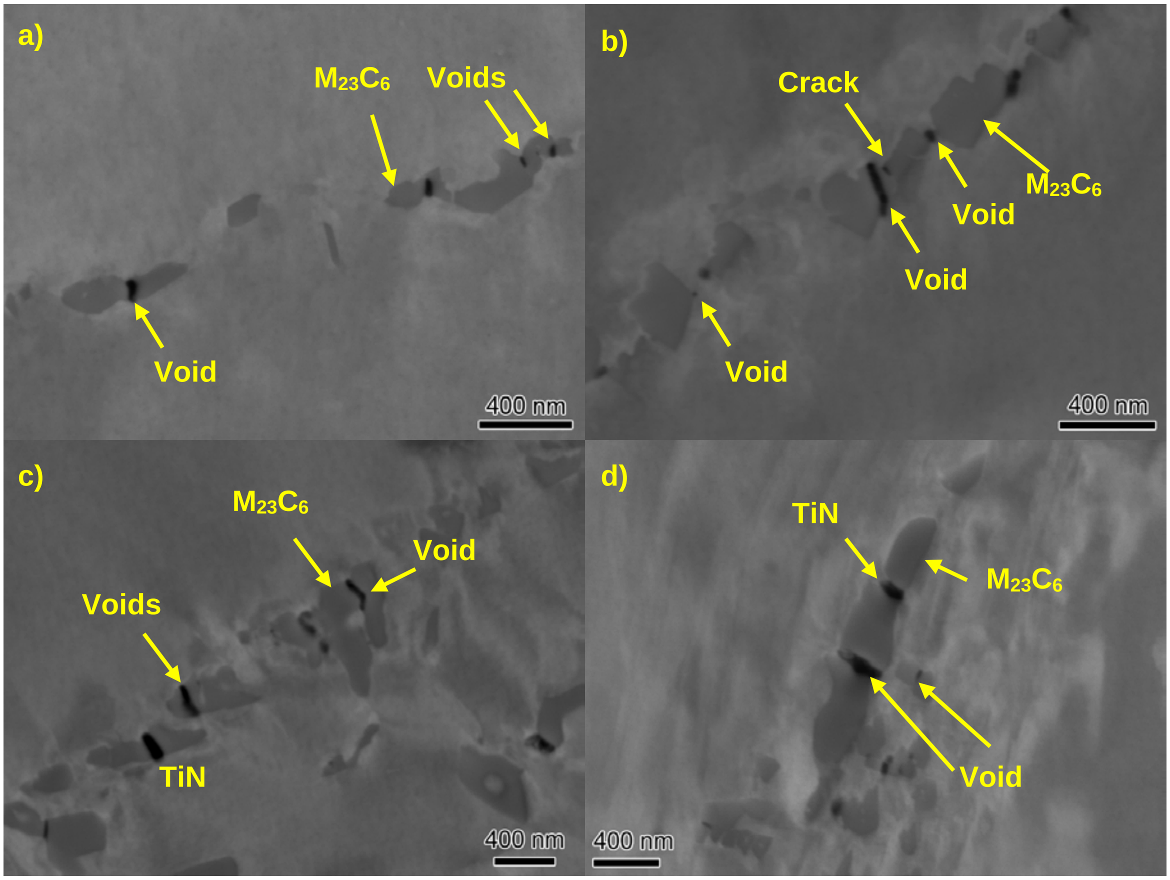

Figure 3.8 **High magnification SEM backscatter micrographs illustrating IG carbide damage microstructures in 31%CR CRDM alloy 690TT (heat RE243)**

SEM pair images are taken because of the different information gathered from each. Secondary electron (SE) contrast in Figure 3.9(a), (c) and (e) very easily distinguishes between voids/cracks and TiN particles. The increased surface area around a void or crack provides a higher secondary yield, whereas the TiN particles do not have this contrast. Figure 3.9(a) highlights this perfectly, as a void and a TiN particle appear close together in the middle of the micrograph. At a certain point though, SE contrast is not as useful for imaging cracks versus voids as backscatter contrast illustrated in Figure 3.9(b). In the upper left hand corner, the $M_{23}C_6$ carbide appears to be continuous but in the SE image the slight crack is tight enough that the additional surface area does not provide extra contrast. The complimentary backscatter contrast in Figure 3.9(b) identifies that this is indeed a crack. Similar comparisons can be seen in the remaining image pairs in Figure 3.9(c-d) and (e-f).

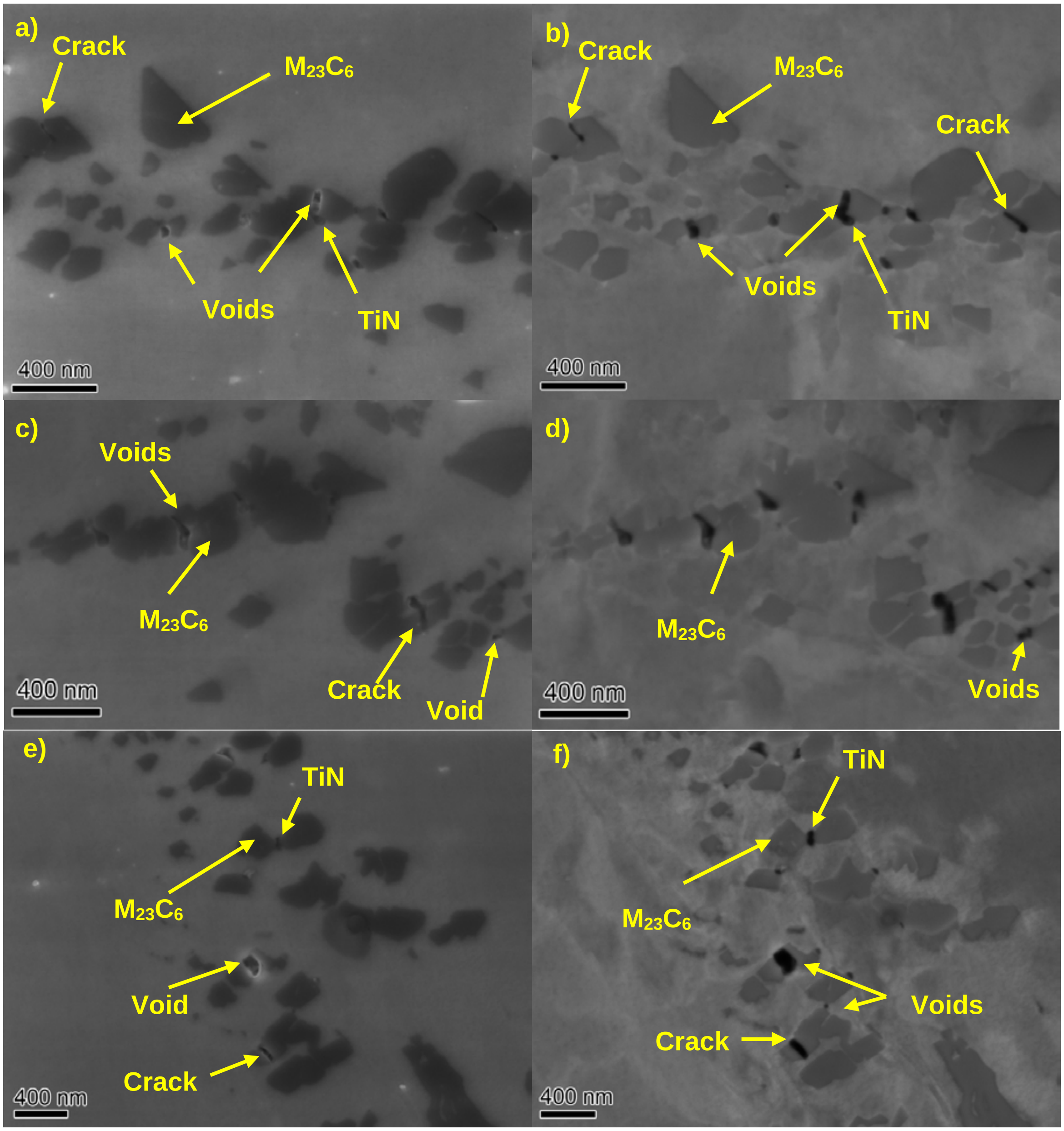

Figure 3.9 High magnification SEM backscatter/SE pair micrographs showing carbide damage microstructures in 31%CR CRDM alloy 690TT (heat RE243)

As a result of SEM and limited TEM examinations on the 31%CR alloy 690TT material, general conclusions can be made about the CR-induced damage microstructure. A significant difference in the permanent damage distributions is seen between the cellular and discrete carbide regions although both show a moderate density of small voids and a limited number of cracked carbides. It is important to note that most grain boundaries in the TT material have a semi-continuous distribution of discrete carbides. As a result, the primary CW-induced damage is the presence of small voids at IG carbide interfaces with a typical void spacing along the boundary length of ~1-2 µm apart. Along with this permanent damage, cold rolling also produces extremely high dislocation densities and localized strains at the boundaries.

The 31%CR alloy 690SA material exhibited quite different permanent damage characteristics apparently due the lack of $M_{23}C_6$ carbides at grain boundaries (as described in an earlier section). This material did not exhibit cracked carbides, since the only IG precipitates were well-spaced TiN particles. Some of these Ti-rich particles were cracked in the 31%CR material both along grain boundaries and in the matrix as illustrated in Figure 3.10. Voids were not found in the cross-sections examined except for an isolated example at a grain boundary triple point. Therefore, the degree of damage was significantly less for the SA versus the TT materials after cold rolling. Limited TEM examinations have documented extremely high dislocation densities in the 31%CR alloy 690CM material similar to that observed in the 31%CR alloy 690TT material and evidence for localized deformation associated with the TiN particles.

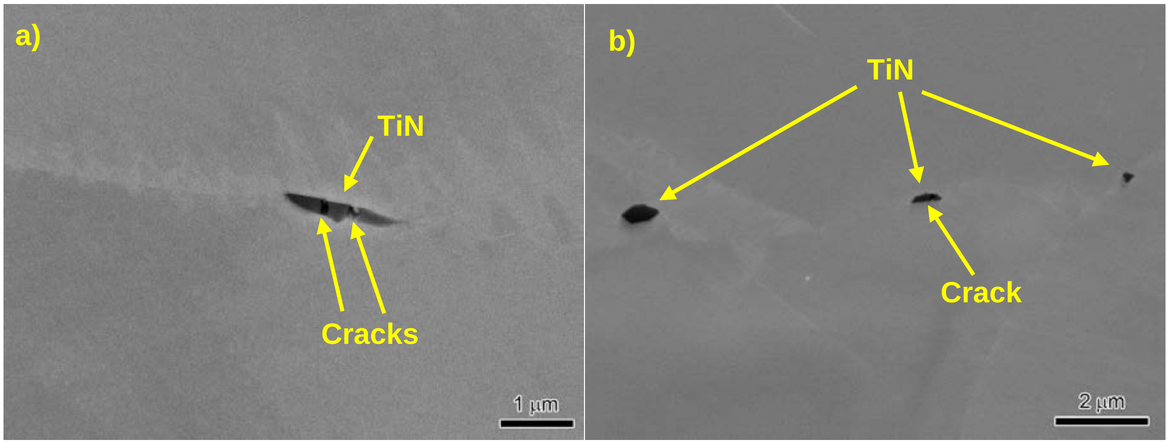

Figure 3.10 **SEM backscatter images illustrating general TiN damage microstructure in 31%CR CRDM alloy 690SA (heat RE243)**

Figure 3.11 illustrates the effect of increasing cold work damage on the same alloy 690 heat, ranging from 11.6% to 31%. At lower cold work levels (11.6% and 17%), there are no cracks and only a few sporadic voids observed on carbides along the grain boundary. At 21% cold work there is a low density of cracks observed, but the increase in void density as compared to the 17% is apparent. Finally, at levels of 30 and 31% cold work, the void density becomes high, although the crack density does not increase compared to the lower cold worked materials. Finally, examples of damage microstructures for the newly examined CRDM materials for this report are provided in Figure 3.12. These structures are typical of that observed in CRDM materials.

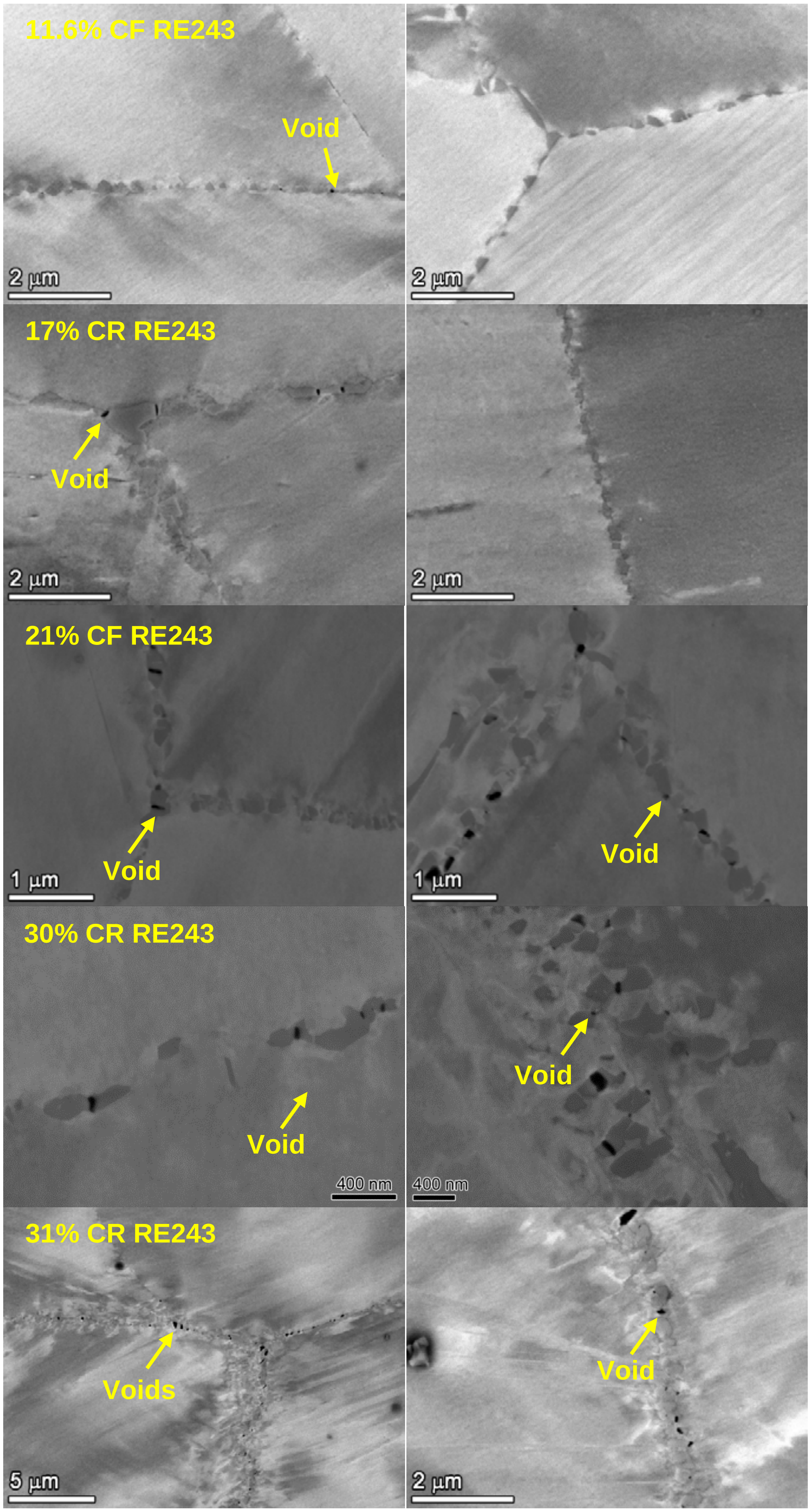

Figure 3.11 **High magnification SEM backscatter images showing the evolution in grain boundary damage with increasing cold work in alloy 690TT RE243**

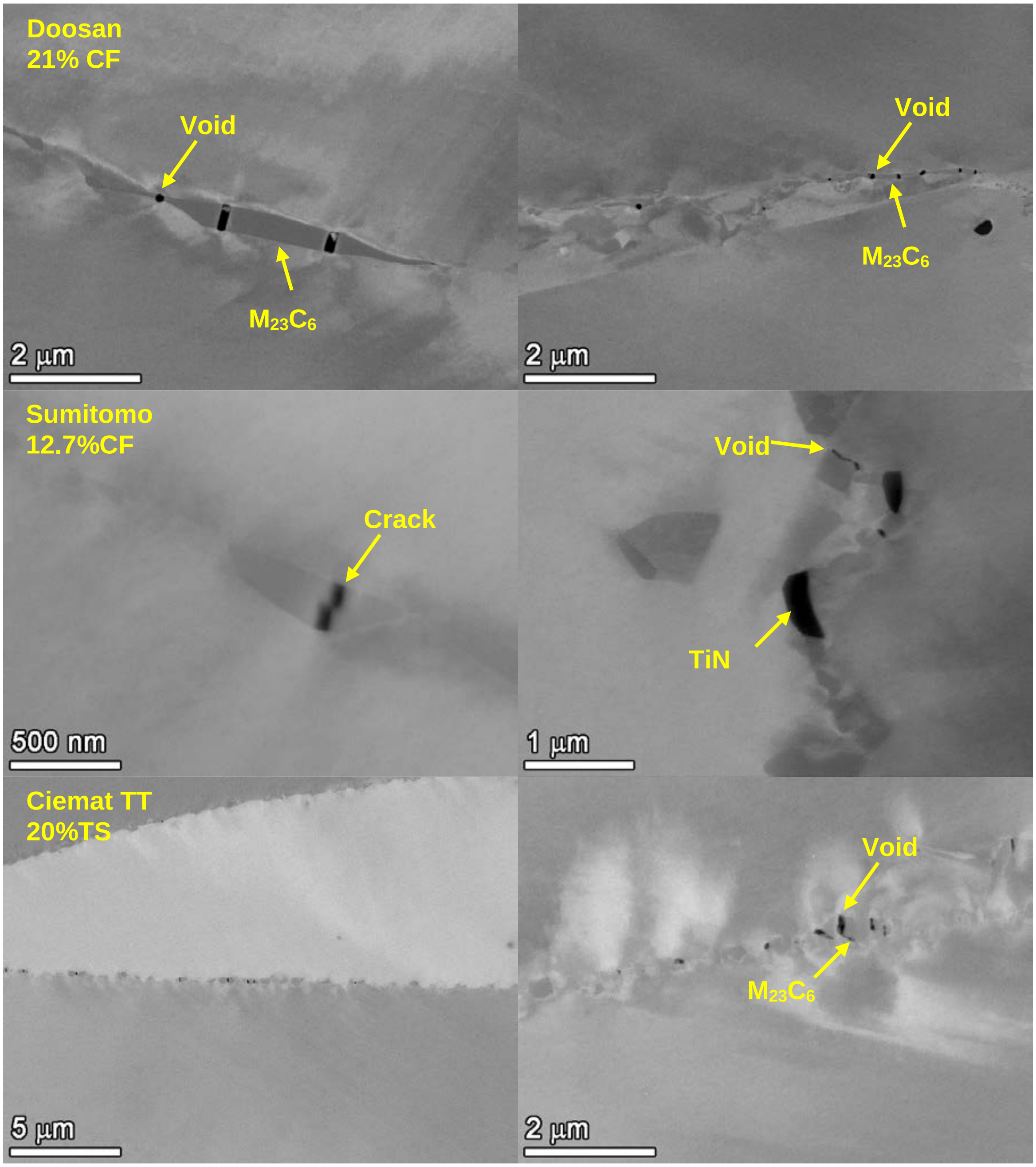

Figure 3.12 High magnification SEM backscatter images showing carbide damage microstructures for the new alloy 690 CRDM materials for this report

3.3.2 Cold Work Damage in Alloy 690 Plate Materials

A summary of the carbide and grain boundary damage structures for the plate and bar materials examined for this report is provided in Table 3.5. The ANL and GEG alloy 690MA materials were extensively characterized in the prior NUREG [7] and example images are not provided here, however SEM backscatter images of the new materials are provided in Figure 3.13.

Table 3.5 Summary of carbide microstructures and damage morphologies in cold worked alloy 690 plate and bar materials

Material	Carbide Location	Carbide Density	Cracks Density	Void Density
ANL MA 36%CR	IG, 0.3-0.5 µm	Semi-continuous Spacing ~100 nm	Low-Moderate	Moderate-High
ANL HTA 30%CF	IG, 0.01-1 µm	Low, sporadic distribution	None-low	None-low
GEG MA 20%CR	TG, 0.5-1 µm	Low, unevenly distributed on GBs	None-low	None-low
GEG HTA 20%CR	IG, 20-30 nm	Unevenly distributed on GBs	None-low	None-low
ENSA WP547 22%CR	IG, 50-200 nm	Semi-continuous Spacing ~200 nm	Low	Low-Moderate
ENSA WP547 32%CF	IG, 50-200 nm	Semi-continuous Spacing ~200 nm	Low	Moderate-High
TK-VDM 114092 22%CF	IG, 50-200 nm	Semi-continuous Spacing ~200 nm	Low-Moderate	Moderate
Allvac X87N-1 21%CF	IG, 50-200 nm	Semi-continuous Spacing ~200 nm	Low-Moderate	Moderate

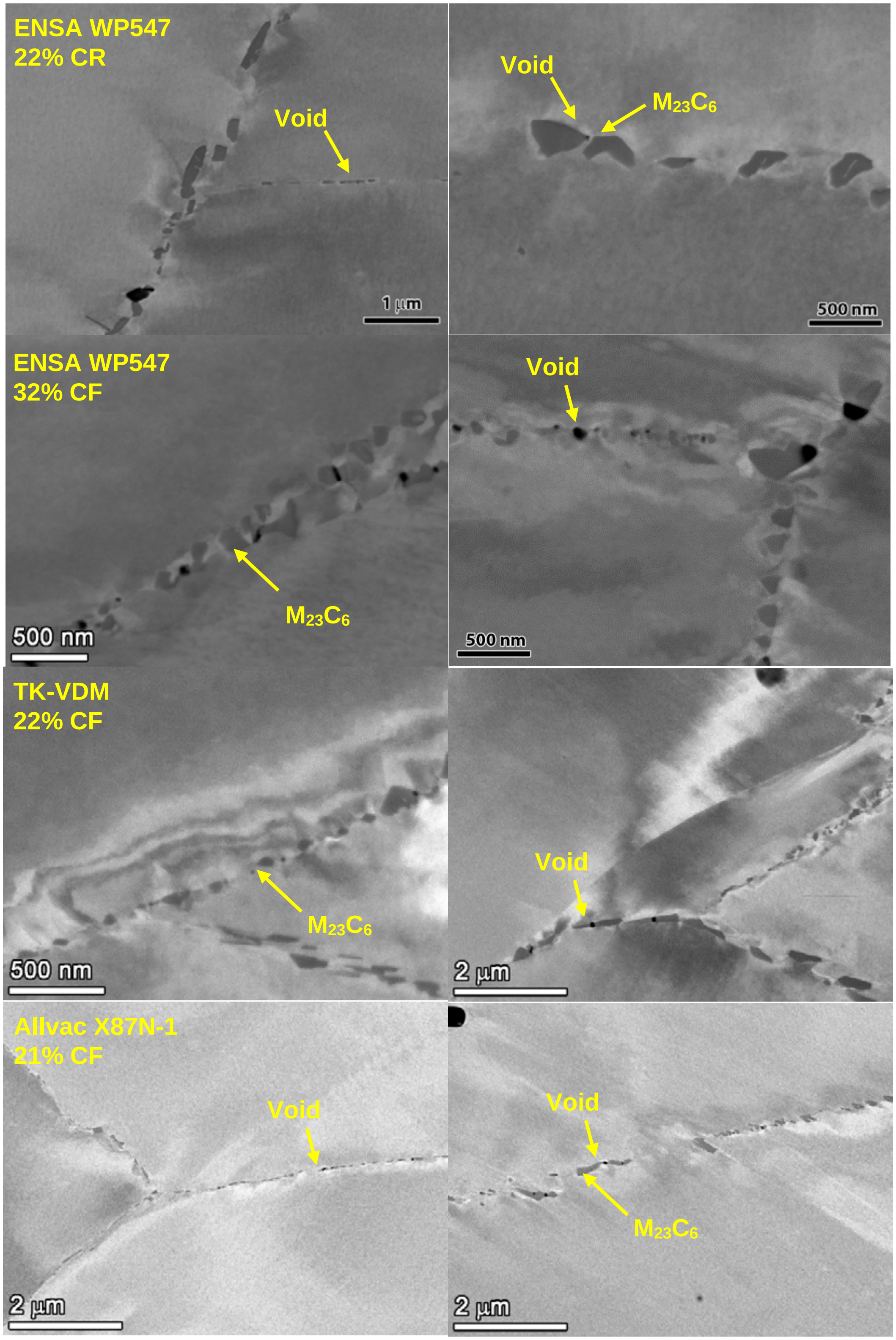

Figure 3.13 High magnification SEM backscatter micrographs showing carbide damage microstructures in alloy 690TT plate materials

3.4 Hardness Measurement Approach

Hardness testing was conducted after SEM and EBSD microstructural exams where a 0.05 µm colloidal silica final polish was required. This surface condition provided an ideal platform for hardness testing. Hardness experiments were carried out using a CM-700AT Clark Microhardness Tester equipped with a FutureTech FM-ARS9000 fully automated hardness testing system. The automated Vickers hardness system was chosen for its ability to rapidly perform and measure large indentation arrays that can then be converted to hardness contour plots. Contour plots are especially useful for evaluating materials that have the potential to exhibit hardness gradients due to microstructural or compositional variability. They have been extremely informative for evaluating weld metals, dissimilar metal welds and heat affected zone regions. For this work on alloy 690 materials, the contour plots were generated to ensure uniformity of the base metal and particularly in cold rolled materials where through-thickness differences in deformation can be produced. These effects were minimized in the current study since measurements were made along the CT specimen crack-growth plane and thus from a constant thickness location within the cold worked plate, bar or tube material.

In a Vickers hardness test, a pyramidal diamond indenter tip is pressed into the sample surface at a specified load. The residual impression left in the surface from the indenter tip is then measured allowing for the hardness to be calculated. Hardness is a measure of a material's resistance to localized plastic deformation and measured as:

$$H = \frac{P}{A} \tag{3.1}$$

where H is the hardness, P is the applied load and A is the surface area over which the load is applied. Loads applied during a Vickers test typically range from 100 to 1000 gram-force (gf) and are held for 10 to 15 seconds before removal. The geometry of the Vickers indenter tip must be precise for hardness measurements to be accurate. A diagram of a Vickers indenter tip is shown in Figure 3.14 below.

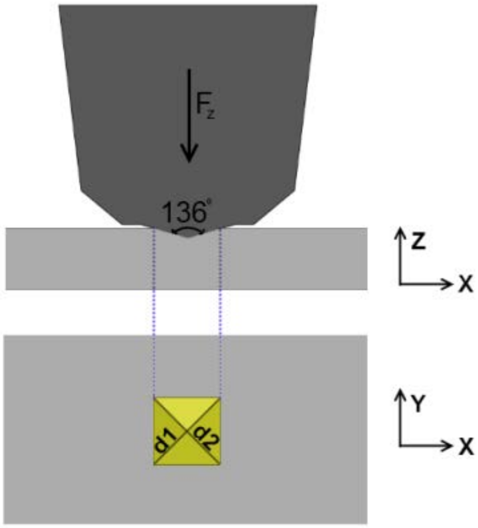

Figure 3.14 Schematic illustration of the residual impression left after a Vickers hardness indentation measurement. The hardness is calculated as a function of the main diagonals, d_1 and d_2 as shown.

The area of the impression left by the indenter tip is calculated by:

$$A = \frac{d^2}{2\sin\left(136^\circ/2\right)} \tag{3.2}$$

Where *d* is the diagonal of the residual impression and 136° is a geometric parameter of the indenter tip. A Vickers hardness (HV) can then be calculated in units of kilogram-force per square millimeter (kgf/mm^2) as:

$$HV = \frac{F}{A} \cong \frac{1.8544F}{d^2} \tag{3.3}$$

Beyond simply calculating hardness values, there are several aspects of hardness testing that should be considered when acquiring this information. The distance between individual indentations has to be accounted for and maintained at a distance of greater than 2.5*d* as recommended by ASTM E-384 [11] so that the plastic zone of surrounding an indent does not influence the hardness measured on subsequent neighboring indents. ISO 6507-1 [12] recommends a slightly higher spacing of greater than 3*d* for steel and copper alloys.

For this work, Vickers microindentation testing was performed using a 300 g load, 0.225 mm indent spacing and 12 s dwell time. Parameters were chosen based on the response for the as-received, lowest strength materials. The 0.225 mm indent spacing was chosen to maintain >2.5*d* spacing while maximizing the number of hardness data points acquired. Basing the pattern spacing on the as-received (lowest strength material) ensured that the indentation load and spacing for subsequent measurements could be held constant.

Depending upon the resultant hardness and indent size, the automated system utilizes either a 20x or 50x objective magnification to measure the residual indent and calculate the Vickers hardness. The current measurement configuration calculates this value by identifying the apex of each indent and extracting the d_1 and d_2 values for hardness determination. When testing alloy 690 materials, hardness measurements were recorded along the crack growth plane and, in most cases, ≥1 mm ahead of the crack tip. For a few samples, the distance between the crack tip and indentation pattern had to be modified to accommodate the specimen geometry or surface condition but the distance remained well beyond the tip plastic zone. Hardness contour plots presented in the following discussions were generated using OriginPro 8.6 and overlaid on optical images of the indented sample. No smoothing was applied to the contour plots and all data points are shown to provide an accurate assessment of the variability within the test region. Typical indentation arrays consisted of ~300 individual indentation measurements.

A tabulated summary of hardness data from the tested alloy 690 materials is given in Table 3.6 and plotted in Figure 3.15. Hardness results for all of these materials/specimens will be discussed individually in a following section. As expected, the average hardness of ~160 kgf/mm^2 for the as-received materials is significantly lower than the cold worked materials. Application of ~15%CW resulted in an average hardness of ~235 kgf/mm^2. ~20%CW resulted in an average hardness ranging from 250 to 300 kgf/mm^2. Additional deformation to ~30%CW further increased the hardness value to greater than 300 kgf/mm^2. Despite the differences in microstructure and carbide density indicated in the previous discussion, the hardness values were generally consistent with the extent of CW.

Table 3.6 Measured hardness values for the alloy 690 samples

Cold Work	ID	Sample Information	Average HV (kgf/mm^2)	Standard Deviation (kgf/mm^2)
0% CW	**B25K-2C**	B25K MA	173.0	4.1
	ANL	ANL MA	173.2	6.8
	CT014	RE 243 TT	157.4	5.9
	CT015	RE243 SA	154.7	6.0
	CT026	WP142 TT	162.6	16.6
	CT027	WP140 TT	163.4	5.5
	CT058	AREVA TT	187.0	10.5
	CT107	Doosan TT	164.8	6.0
	CT108	TK-VDM TT	155.6	6.0
12-17% CW	**CT104**	RE243 TT + 12%CF	222.3	12.6
	CT103	Sumitomo TT + 13%CF	242.2	11.8
	CT068	RE243 SA + 17%CR	251.3	16.2
	CT054	RE243 TT + 17%CR	249.1	15.6
20%-22% C W	**CT093**	WP787 TT + 20%TS	248.0	14.0
	CT069	GEG TT + 20%CR	286.5	14.9
	CT070	GEG HTA + 20%CR	290.5	15.6
	HU23	AMEC - 20%CR (4 passes)	275.8	16.2
	HU4	AMEC - 20%CR (10 passes)	264.9	12.4
	3 PU	AMEC TT + 20%TS	261.8	13.6
	34 HU	AMEC TT + 20%CR	263.2	12.4
	CT037	GEG MA + 20%CR	321.3	12.6
	CT100	RE243 TT + 21%CF	275.2	17.5
	CT101	Allvac (X87N-1) TT + 21%CF	296.6	13.9
	CT102	Doosan TT + 21%CF	285.2	16.7
	CT060	ENSA TT + 22%CR	288.8	15.4
26-32% CW	**CT036**	ANL MA + 26%CR	310.1	10.8
	CT073	ANL MA + 30%CF	316.0	17.1
	CT074	ANL SA + 30%CF	316.9	15.1
	CT038	RE243 TT + 31%CR	314.7	19.0
	CT039	RE243 SA + 31%CR	316.4	17.8
	CT053	RE243 TT + 31%CR + Recovery	273.5	15.7
	CT098	Sumitomo TT + 31%CF	317.8	14.6
	CT099	RE243 TT +31%CF	302.0	20.3
	CT059	ENSA TT + 32%CF	305.4	17.8
	CT094	TK-VDM TT + 32%CF	328.5	14.2

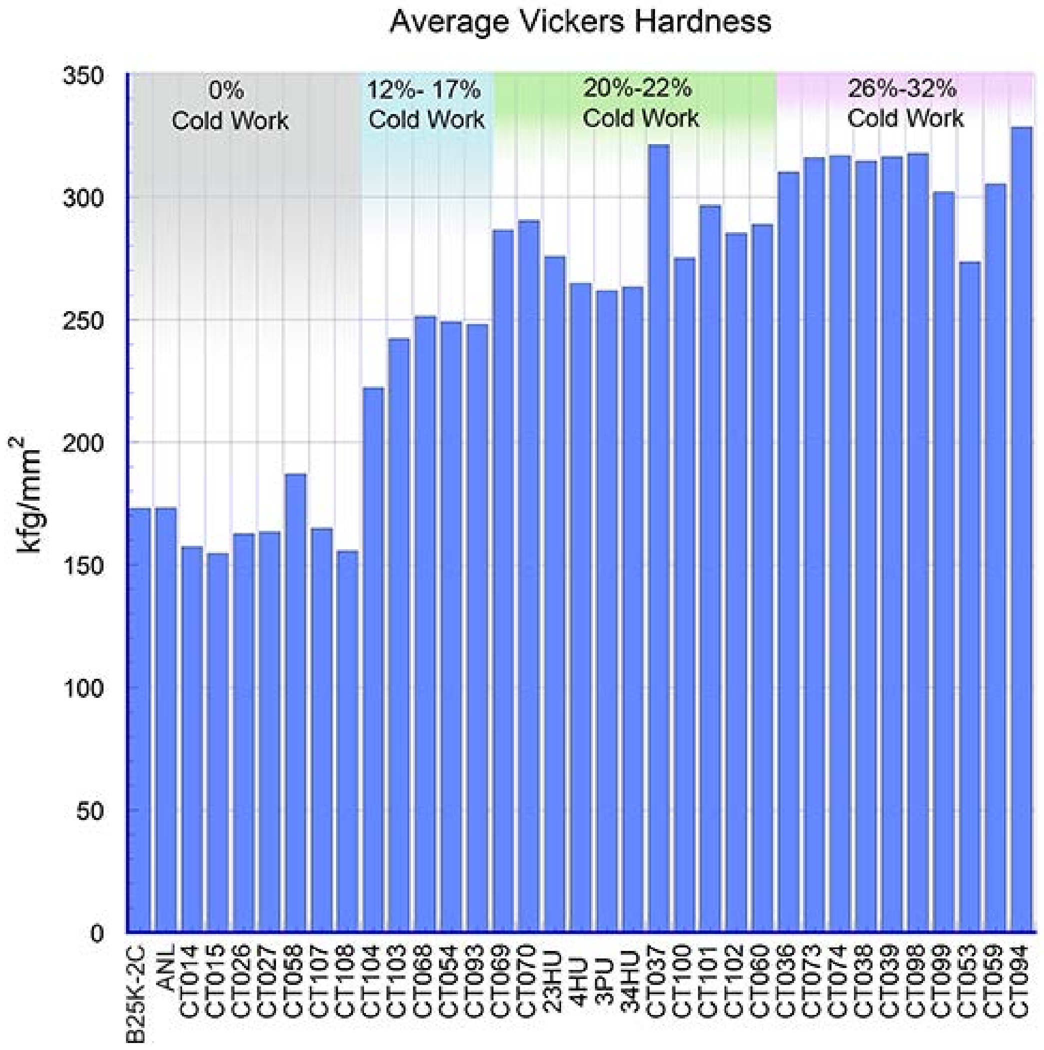

Figure 3.15 Average hardness is plotted for the tested samples that are grouped according to increasing percent cold work

In the following discussions, it should be noted that the color scales on the hardness contour maps were split into three hardness regimes that are denoted as Hardness Scale A through C in Table 3.7. These groupings were necessary to evaluate local differences in hardness within each material that would otherwise have been unapparent on a universal color/hardness scale for all materials.

3.5 Electron Backscatter Diffraction Measurement Approach

Samples were prepared for EBSD by mechanically polishing through a series of successively finer grits of diamond paste followed by a final polish on colloidal silica (0.05 µm). In cases where conductive epoxy was not utilized, samples were completely removed from epoxy to ensure that no electrical charging occurred during imaging. For high-resolution EBSD maps, charging minimization was a critical issue as even small amounts of epoxy led to sporadic sample charging, image drift and subsequent discontinuities in the EBSD maps. The EBSD analyses were conducted using a JEOL 7600F FEG-SEM equipped with a Nordlys camera interfaced with the Oxford/HKL Channel 5 software package. Stage stability in the JEOL 7600F is excellent, in part because the instrument is equipped with an active vibration cancellation stage, in many cases yielding sample drift as low as 0.5 µm for up to 30 hours. The samples were not coated with carbon and were only plasma cleaned to remove surface hydrocarbons prior to analysis. Unless otherwise noted, all samples were mounted such that the vertical axis in the figures corresponds to the notch direction in the CT test specimen.

Table 3.7 **Hardness scale range for the alloy 690 contour plots**

Cold Work	ID	Sample Information	Hardness Scale	Scale Range (kgf/mm^2)
0% CW	**B25K-2C**	B25K MA	A	105-185
	ANL	ANL MA	A	105-185
	CT014	RE 243 TT	A	105-185
	CT015	RE243 SA	A	105-185
	CT026	WP142 TT	A*	105-225*
	CT027	WP140 TT	A	105-185
	CT058	AREVA TT	A*	105-215*
	CT107	Doosan TT	A	105-185
	CT108	TK-VDM TT	A	105-185
12-17% CW	**CT104**	RE243 TT + 12%CF	A*	205-305*
	CT103	Sumitomo TT + 13%CF	B	225-305
	CT068	RE243 SA + 17%CR	B	225-305
	CT054	RE243 TT + 17%CR	B	225-305
20%-22% C W	**CT093**	WP787 TT + 20%TS	B	225-305
	CT069	GEG HTA+TT + 20%CR	B	225-305
	CT070	GEG HTA + 20%CR	B	225-305
	HU23	AMEC - 20%CR (4 passes)	B	225-305
	HU4	AMEC - 20%CR (10 passes)	B	225-305
	3 PU	AMEC TT + 20%TS	B	225-305
	34 HU	AMEC TT + 20%CR	B	225-305
	CT037	GEG MA + 20%CR	B*	225-350*
	CT100	RE243 TT + 21%CF	C	240-350
	CT101	Allvac (X87N-1) TT + 21%CF	C	240-350
	CT102	Doosan TT + 21%CF	C	240-350
	CT060	ENSA TT + 22%CR	C	240-350
26-32% CW	**CT036**	ANL MA + 26%CR	C	240-350
	CT073	ANL MA + 30%CF	C	240-350
	CT074	ANL HTA + 30%CF	C	240-350
	CT038	RE243 TT + 31%CR	C	240-350
	CT039	RE243 SA + 31%CR	C	240-350
	CT053	RE243 TT + 31%CR + Recovery	C	240-350
	CT098	Sumitomo TT + 31%CF	C	240-350
	CT099	RE243 TT + 31%CF	C	240-350
	CT059	ENSA TT + 32%CF	C	240-350
	CT094	TK-VDM TT + 32%CF	C	240-350

*Indicates an extended range for the hardness test

Generation of an EBSD map occurs as the electron beam is scanned across the region of interest at a pre-determined step spacing and individual diffraction patterns are acquired at each step position (called pixels from this point forward). Indexing each diffraction pattern provides both the crystal phase and crystal orientation at each pixel position, effectively mapping the orientation and phase relationships for the region of interest. Processing the data with the Channel 5 software reveals the grain size, types of boundaries, degree of crystal misorientation between individual pixels, and changes in any phases if present. In this study, the phase was limited to austenitic stainless steel, which provides an analogue for alloy 690 since both materials possess the same crystal structure and have nearly identical lattice parameters. While small carbides and TiN particles were apparent in the SEM images, they were typically too small to index reliably. Results focus on the overall crystal orientation and strain of the alloy 690 austenite phase and do not discuss orientation relationships of the small precipitates.

Two methods are used to effectively demonstrate the strain distribution within the various alloy 690 conditions. The first is visual mapping that can be generated within the Channel 5 software module, Tango. These include pattern quality maps, inverse pole figure maps, misorientation maps and local misorientation maps, all of which make use of the crystallographic orientation data at each pixel position. These maps provide visual clues as to the local accumulation of strain as represented by misorientation within the maps. The second analysis method is based on the density of low angle misorientation boundaries that the Channel 5 program can assign based on the difference in orientation between individual pixels in the map. This approach provides a global estimate of the accumulated strain within the region of interest that was introduced by CW in these samples. This method has an upper limit beyond which increasing plastic strain produces such a high misorientation density that the density of low angle boundaries may be too high to resolve, or the pattern quality degrades to the point that Kikuchi patterns cannot be resolved. This limit is material dependent and is affected by how the dislocation structure evolves in each material. Among the current set of materials with maximum CW level of 32%, this limiting density of misorientation boundaries was *not* reached, and the pattern quality was sufficient to allow effective analysis of the patterns. Together, these two approaches provided microstructural information on how the different levels of CW and various heat treatments relate to the final strain distributions.

To make use of the misorientation boundary distribution, a correlation was developed to relate the density of low angle misorientation boundaries with the known level of plastic strain, in this case simply represented by the degree of CW. There are a variety of parameters that have the potential to lead to erroneous conclusions. For this reason, it is important to derive this correlation from samples of the same composition that have been deformed in a similar fashion. In additional, the effect of grain size (discussed below) is not clearly defined and has the potential to be a significant source of deviation from the proposed correlation between percent strain and EBSB results.

The approach used follows the method proposed by LeHockey in the EBSD methods compilation edited by Schwartz, et al. [13], wherein the density of misorientation boundaries for range of misorientation angles, weighted by the magnitude of the misorientation, is summed together and normalized by the total number of pixels in the map. The IMD is the product of this summation and is given by the following relationship:

$$IMD_{\Phi} = \frac{\sum_{\Phi_{\min}}^{\Phi_{\max}} \Phi \bullet MD(\Phi)}{N} \tag{3.4}$$

where

Φ_{min} = Minimum resolvable angle of misorientation, in this case chosen as 0.3°
Φ_{max} = Maximum angular deviation assigned to plastic strain, chosen as 5°
N = Number of pixels in the map
$MD(\Phi)$ = Number of misorientation boundaries for a given angular misorientation
Φ = Corresponding magnitude of the angular misorientation, in radians

LeHockey found that the IMD scales linearly with increasing plastic strain, however samples that were tested in biaxial tension produced a correlation slope twice that of data from uniaxial tension tests. Thus, the method of imparting the strain can have an effect on the correlation between IMD and strain. For the specimens examined in this report, the majority of the strains were applied by either cold rolling or cold forging. Since these are similar deformation modes, they are expected to produce a similar relationship between strain and IMD.

Because varying the step spacing alters the correlation curve, the choice of step spacing was found to be a key parameter that must be kept constant to enable comparisons between different sample conditions. Maps were collected at 8x8 binning and indexing percentages were >90% for all conditions. The Nordlys camera was inserted to 190 mm, magnifying the diffraction pattern to improve the angular precision. This decreased the intensity of the scattered beam, but a slight increase in the beam current more than compensated for this with no detectable tradeoff in spatial resolution for the standard mapping conditions. The parameters chosen for the IMD analysis were a step spacing of 0.5 µm with a magnification of 250x for all conditions. Such a map required ~5.5 hours to image and contained on average ~750,000 data points. The map size and detail were necessary to accurately describe the spatial distribution of boundary misorientations within the sample. Maps were also run at 100x for the same step spacing, which produced data sets up to 4.5 million points. It was concluded that there was no difference in the misorientation boundary density measured at 100x or 250x, so 250x maps were chosen as the norm since it took ~1/6 of the time to acquire the smaller map.

EBSD maps were taken in low magnification (LM) mode to maximize the depth of field over the width of the tilted sample at magnifications from 35 to 10,000x and optimize pattern indexing during EBSD analysis. Note that LM mode has limited spatial resolution at higher magnifications in comparison to SEM mode, which would be preferred if maximum image resolution was a higher priority. The main drawback to the SEM mode on the JEOL 7600F is that the top of the Nordlys camera sits within the flux field of the objective lens, which leads to pattern distortion that can degrade the ability to index the diffraction patterns under certain conditions. This effect is mitigated by mapping in LM mode, because the objective lens is switched off, thus eliminating the flux field at the camera and associated pattern distortions.

One final parameter that needs to be discussed is the angular precision obtained in the maps and line scans. As discussed above, the Nordlys camera was positioned to magnify the diffraction pattern to help improve the angular accuracy, and pattern images were binned at 8x8 (4x4 for more heavily strained samples) for measuring orientations. A survey of the literature suggested that it is not unreasonable to expect a minimum misorientation limit of 0.2 to 0.3° that can be reliably detected under the conditions chosen for the series of analyses performed. To ensure that the measured misorientations are not the result of random noise, a Kuwahara noise filter available in the Tango module of the Channel 5 software program was used on each map. This filter is essentially an orientation-averaging algorithm that preserves real edges/boundaries. Each 250x map was processed in the following manner: wild spikes were removed and the map was smoothed to 6 nearest neighbors, then given a single pass through the modified Kuwahara filter using a 3x3 size grid and a 2° smoothing angle. The smoothing and filtering approach was found to yield contours of misorientation boundaries ≥ 0.3° that closely matched the observed grayscale changes in the pattern quality and inverse pole figure maps that are sensitive to minute changes in orientation. The histograms were binned at 0.2°, but no misorientation boundaries lower than 0.3° were included in the histograms nor included in the calculations. The binning of 0.2° was chosen to help reveal the variations within the misorientation boundary distributions. Histograms were collected through 15°, but rarely did the highest misorientation exceed 10°, which is nominally the level chosen for high angle grain boundaries. EBSD mapping was then performed on the set of alloy 690 samples and IMD values calculated, the results of which are shown in Figure 3.16 and Table 3.8. EBSD results for all of these materials/specimens will be discussed individually in a following section combined with the hardness measurements.

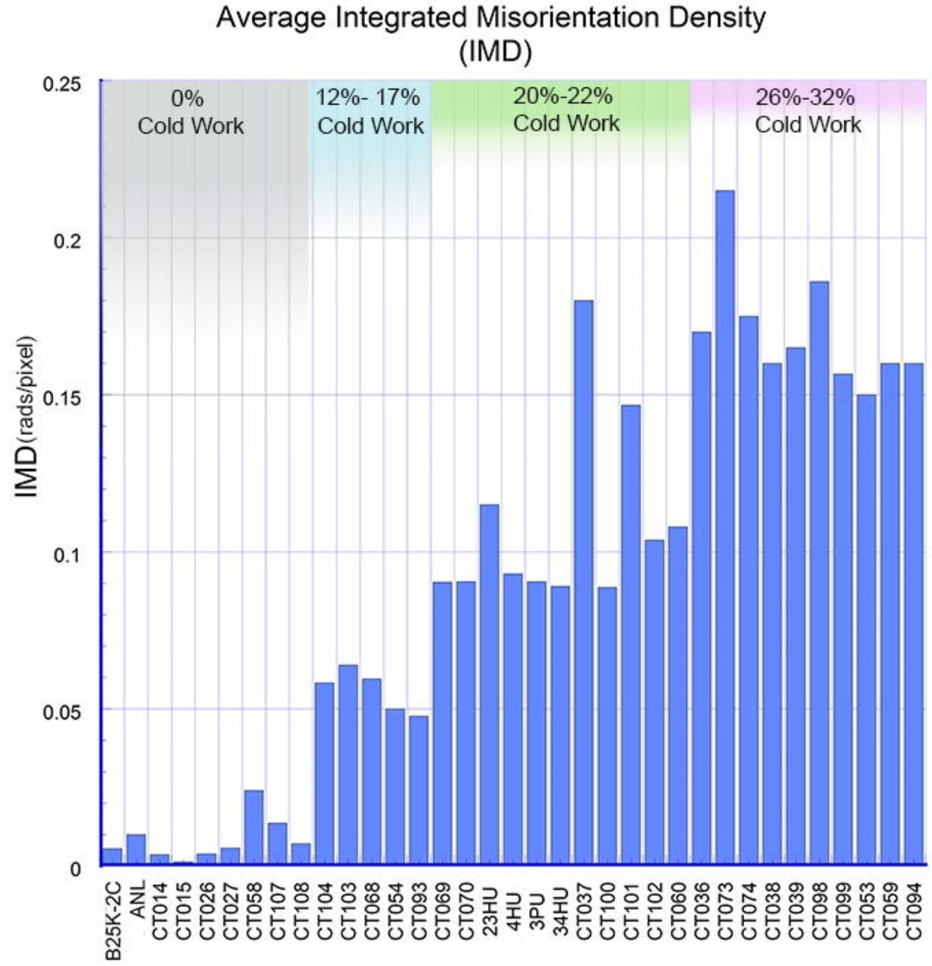

Figure 3.16 **Average IMD is plotted for the tested alloy 690 samples that are grouped according to increasing %CW**

Table 3.8 Calculated IMD values for the alloy 690 materials.

ID	Sample Information	Average IMD	Standard Deviation
B25K-2C	GEG MA	0.0056	0.000*
ANL	ANL MA	0.0100	0.000*
CT014	RE 243 TT	0.0036	0.001
CT015	RE243 SA	0.0013	0.001
CT026	WP142 TT	0.0039	0.0004
CT027	WP140 TT	0.0057	0.002
CT058	WP787 TT	0.024	0.013
CT107	Doosan TT	0.013	0.002
CT108	TK-VDM TT	0.007	0.0002
CT104	RE243 TT + 12%CF	0.0583	0.0021
CT103	Sumitomo TT + 13%CF	0.064	0.0014
CT068	RE243 SA + 17%CR	0.0595	0.002
CT054	RE243 TT + 17%CR	0.050	0.001
CT093	WP787 TT + 20%TS	0.047	0.005
CT069	GEG TT + 20%CR	0.1010	0.008
CT070	GEG HTA + 20%CR	0.0903	0.009
HU23	AMEC - 20%CF (4 passes)	0.1150	0.007
HU4	AMEC - 20%CF (10 passes)	0.0930	0.007
3 PU	AMEC TT 20%TS	0.0905	0.009
34 HU	AMEC TT 20%CR	0.0890	0.004
CT037	GEG MA + 20%CR	0.1800	0.000*
CT100	RE243 TT + 21%CF	0.0887	0.006
CT101	Allvac (X87N-1) TT + 21%CF	0.1467	0.012
CT102	Doosan TT + 21%CF	0.1037	0.011
CT060	ENSA TT + 22%CR	0.1080	0.017
CT036	ANL MA + 26%CR	0.1700	0.000*
CT073	ANL MA + 30%CF	0.2150	0.007
CT074	ANL SA 30%CF	0.1750	0.007
CT038	RE243 TT + 31%CR	0.1600	0.000*
CT039	RE243 SA + 31%CR	0.1650	0.007
CT053	RE243 TT + 31%CR + Recovery	0.1500	0.010
CT098	Sumitomo TT + 31%CF	0.1860	0.017
CT099	RE243 TT + 31%CF	0.1566	0.021
CT059	ENSA TT + 32%CF	0.1600	0.010
CT094	TK-VDM TT + 32%CF	0.1600	0.000*

*Indicates a case were the standard deviation is not applicable because the IMD value was only measured from one region of the sample. For all other cases averages were calculated based on IMD measurements from three or more areas of the sample.

3.6 Hardness and EBSD Results Arranged by Increasing Cold Work

3.6.1 As Received GEG B25K & ANL NX3297HK12 Bar/Plate Materials

These two materials in their as-received condition were the only ones that were measured from coupons instead of tested CT specimen. The GEG B25K as-received MA material was cut and sectioned to allow for mechanical properties assessment across three different orthogonal orientations. Sampling orientations are shown in Figure 3.17. Only one orientation of the as-received ANL MA material was tested.

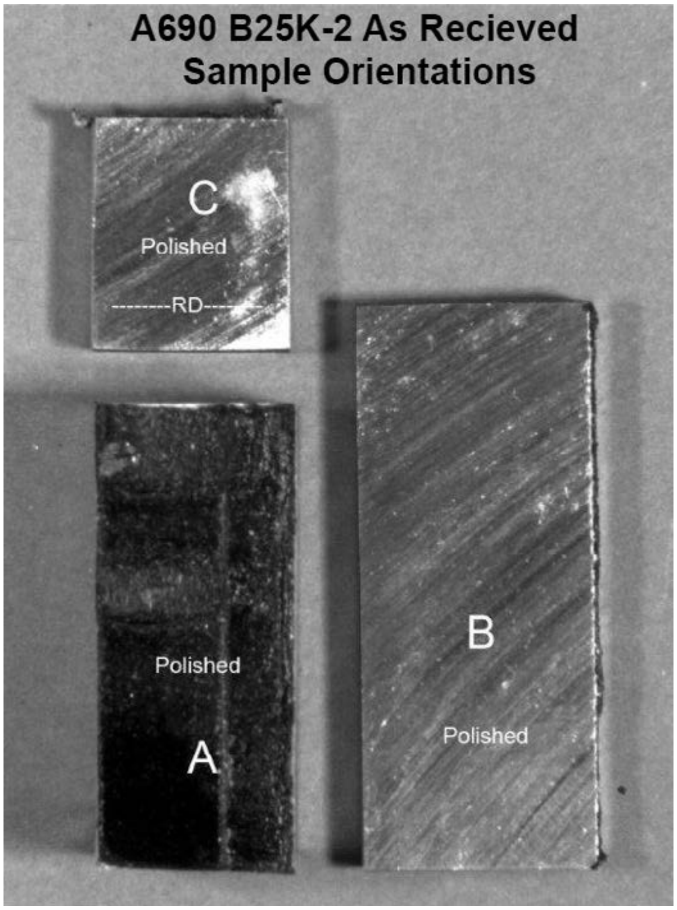

Figure 3.17 As received GEG MA sample showing sections which were cut and removed for hardness and EBSD examination. The rolling direction as indicated in the upper left is horizontally aligned.

Overall the hardness and EBSD analysis performed on these samples yielded very similar results and are shown in Figure 3.18 and Figure 3.19, respectively. The hardness contour plot from the B25K-2A orientation exhibited a reduction on the order of 8% when compared with the other two B25K-2 orientations and the ANL-MA material. Inspection of the EBSD maps in Figure 3.19 showed that this decreased hardness was correlated with a slightly elevated grain size. In general, the ANL MA material was indistinguishable in hardness, orientation and IMD maps from the GEG B25K-2 MA specimens.

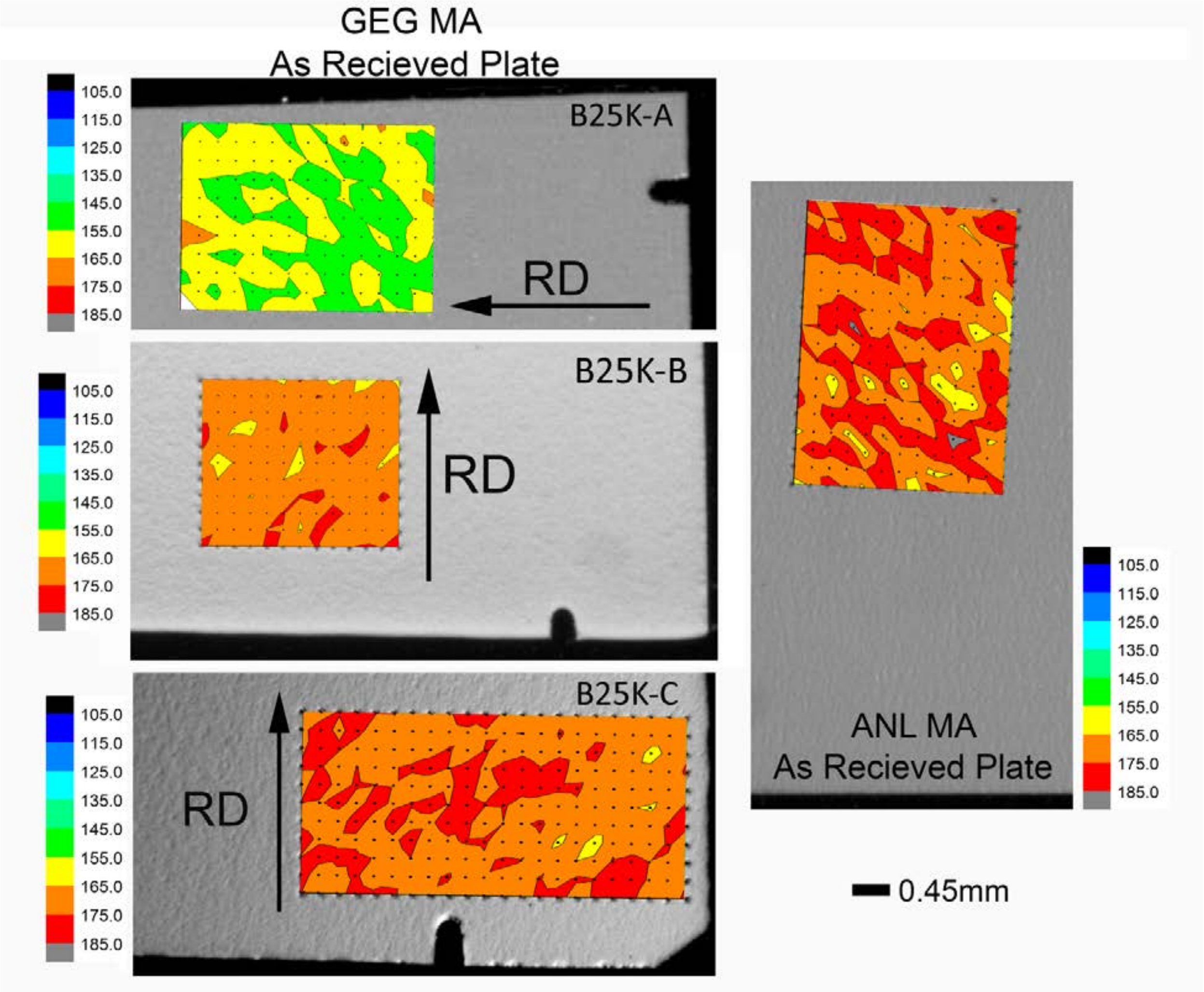

Figure 3.18 Three orientations cut from GEG MA B25K-2 as received material (left) show uniform hardness distributions which align closely with the measurements from the ANL as-received MA plate material. The B25K-2A sample orientation exhibited a slight overall reduction in hardness. All maps are plotted on the same hardness color scale (Scale A).

The EBSD maps in Figure 3.19 show three sets of images for each material. The first row of images contains pattern quality maps. The grayscale images are produced as a result of the diffraction pattern quality with darker regions indicating a poorer quality, in this case as a result of local strain or orientation contrast. The second row of images contain local misorientation maps plotted on a 0-5° misorientation scale. As expected for the as-received unstrained materials, there is minimal if any local misorientation. The bottom set of images depict inverse pole figure maps that define the out of plane crystallographic orientation. In general, these images depict a high twin density and overall random crystallographic texture for these samples.

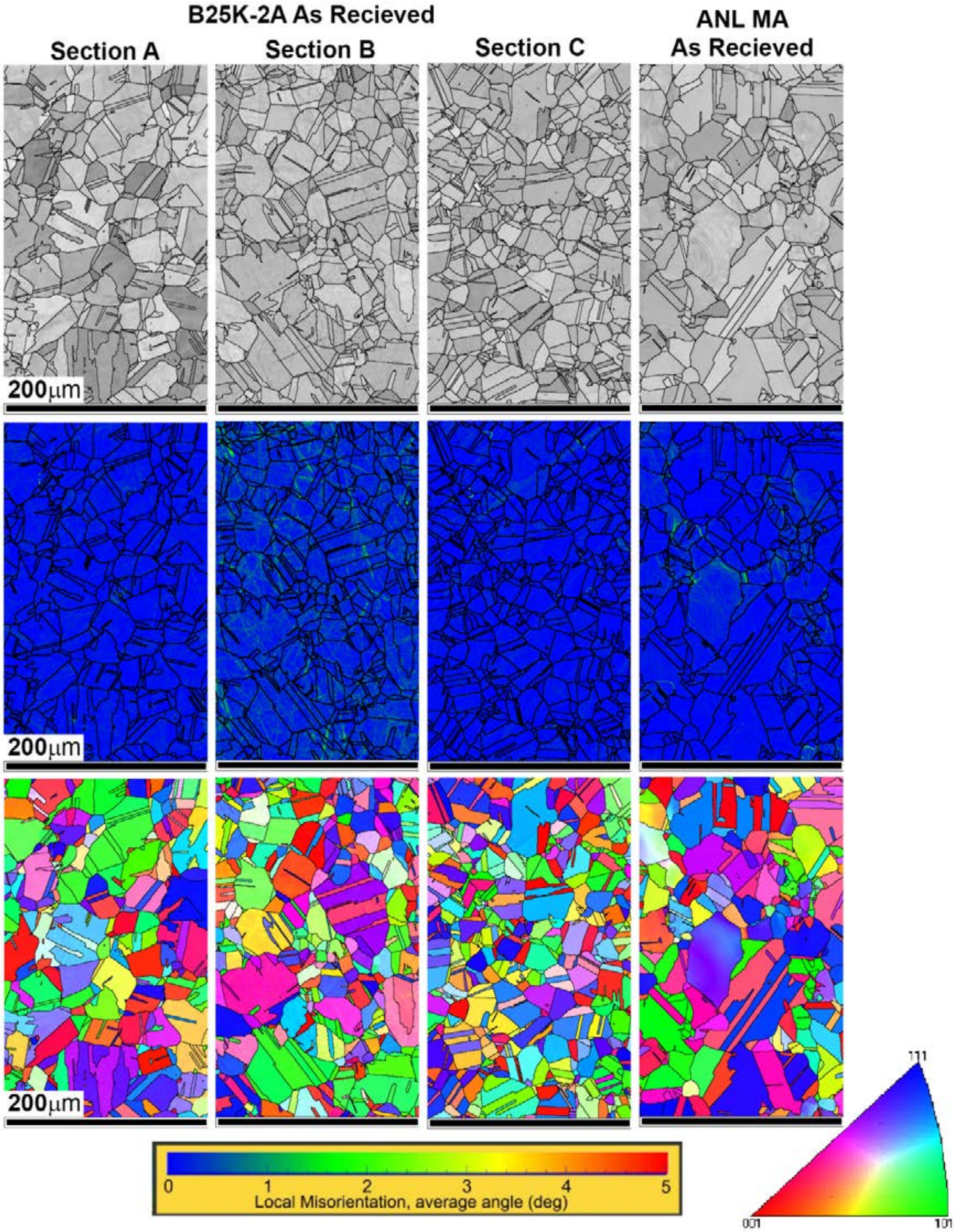

Figure 3.19 Comparison of EBSD results from the as-received alloy 690 materials. The top panels depict image quality maps, the middle panels the local misorientation, and the bottom panels the inverse pole figures. In general all four materials exhibit very similar microstructures with minimal strain.

3.6.2 As-received RE243 SA, RE243 TT, WP140 TT, WP142 TT, AREVA TT, Doosan TT, and TK-VDM TT

These TT CRDM and plate materials had larger grain size than the B25K MA and ANL MA materials as shown in Figure 3.20. This is likely due to the lower temperature associated with a mill anneal treatment. Note that twinning is a common occurrence in alloy 690.

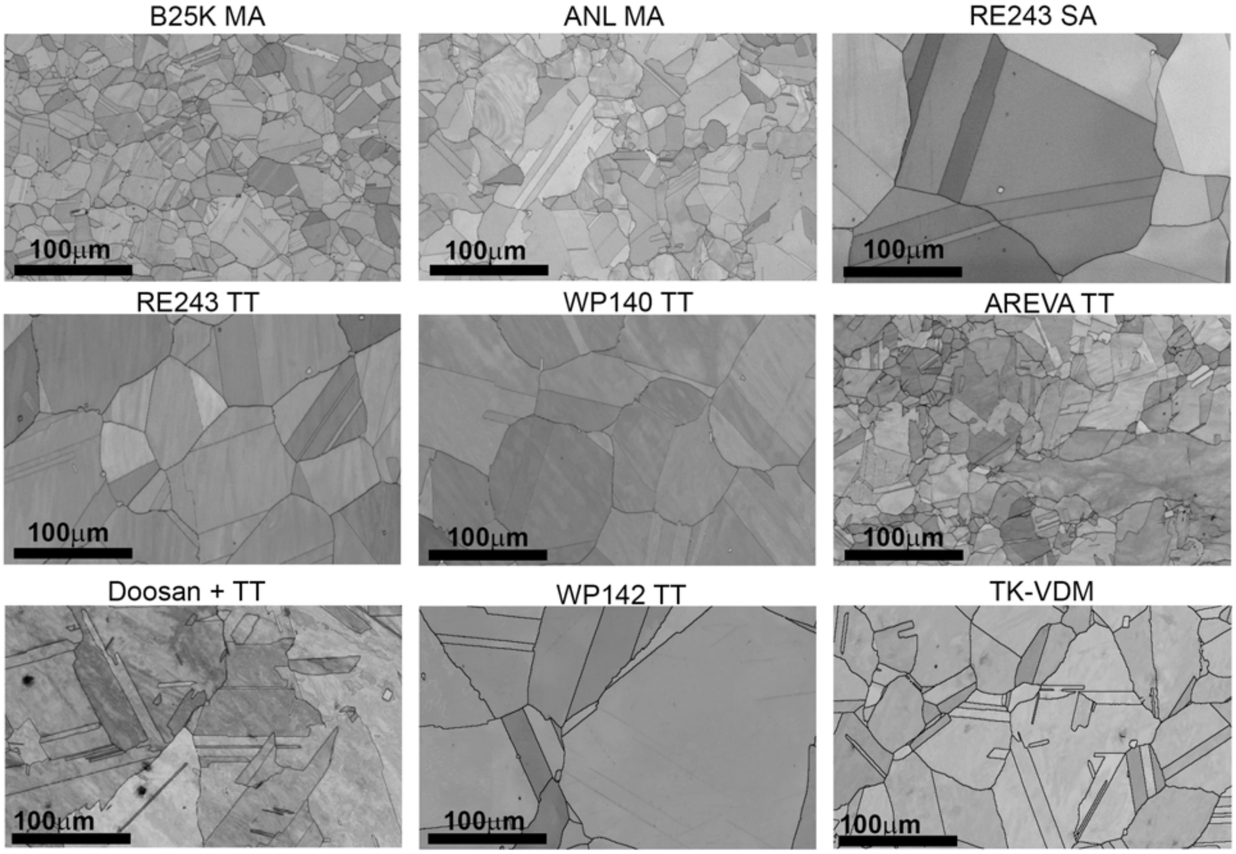

Figure 3.20 EBSD pattern quality images showing microstructural variation present in the non-cold worked condition.

EBSD local misorientation (LM) mapping in Figure 3.21 revealed that minimal amounts of strain are present in these materials regardless of the grain size variation. A more subtle aspect is that the SA condition has the lowest density of local misorientation overall indicating that this material is essentially free of any residual strain unlike the MA conditions.

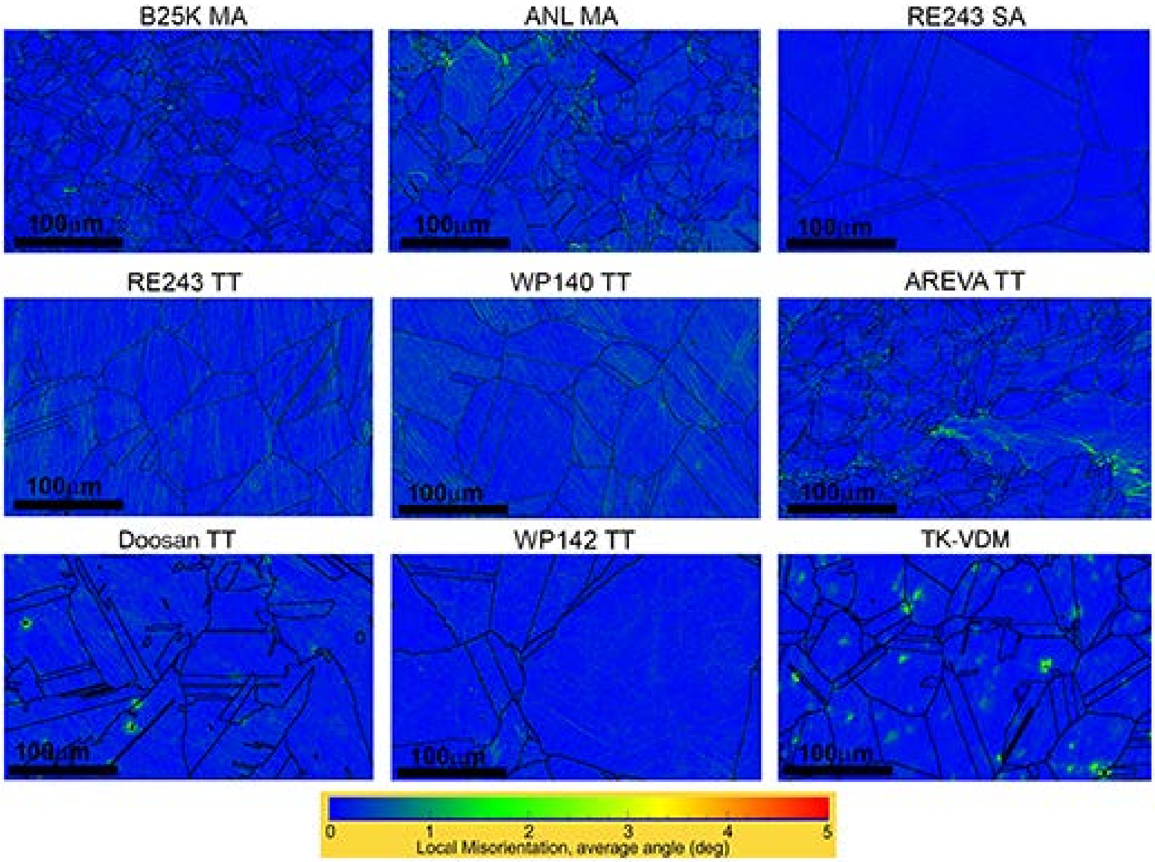

Figure 3.21 EBSD local misorientation maps showing an overall low degree of misorientation present in the non-cold worked samples.

Hardness contour plots of these as-received materials were generated and are shown in Figure 3.22. The two mill annealed samples (GEG and ANL) have a similar average hardness of ~173 kgf/mm^2. The RE243 material in both the TT and SA conditions shows an overall lower hardness that is relatively uniform at ~156 kgf/mm^2. Results of the RE243 TT material are very close to the WP140 TT specimen of 163 kgf/mm^2. The unique responses for these materials were for the WP142 TT and AREVA TT specimens that exhibited strong hardness gradients. The AREVA TT sample showed an increase in hardness in the crack growth direction and elevated average hardness of 187 kgf/mm^2. The WP142 specimen is more easily explained as the hardness gradient shown here is likely due to additional damage introduced as the specimen was aggressively fractured open, likely producing a small amount of strain in the vicinity of where the hardness measurements were performed. Hardness and EBSD values recorded for this specimen were taken further from the fractured surface in a region thought to be representative of the bulk response of the material.

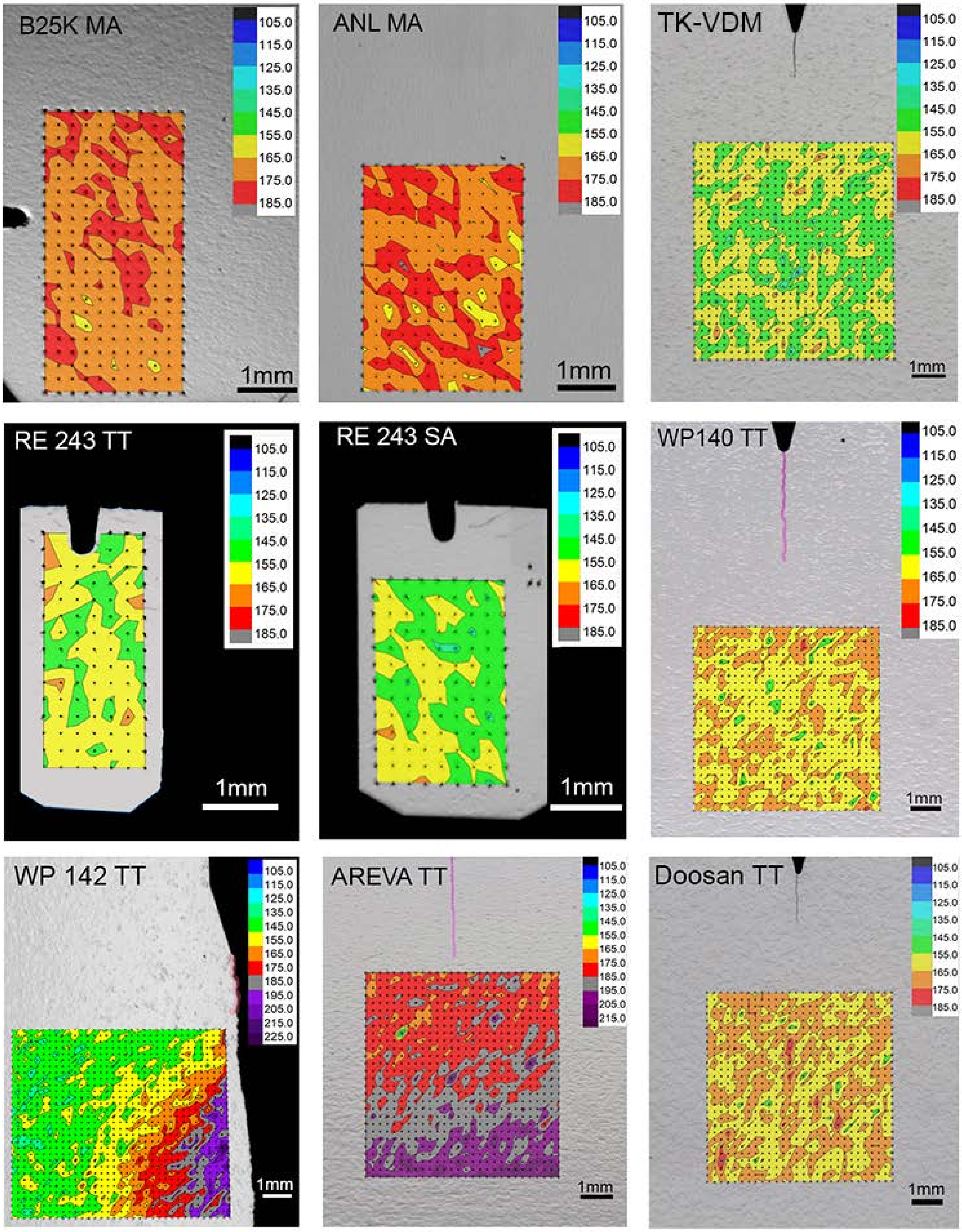

Figure 3.22 Hardness contour plots from the non-cold worked samples. MA conditions show similar hardness values. The thermally treated materials show more sample-to-sample variability.

3.6.3 Low Cold Work: Valinox RE243 TT + 12%CF and Sumitomo E67074C TT + 13%CF

EBSD pattern quality and local misorientation maps for the two most lightly cold worked samples are shown in Figure 3.23. The RE243 specimen showed a considerably lower hardness (~10%) than the similarly cold worked Sumitomo sample. Local misorientation distributions for the two were different; the RE243 material showed the typical near-boundary misorientation accumulation while the Sumitomo material showed pockets of intragranular high local misorientation.

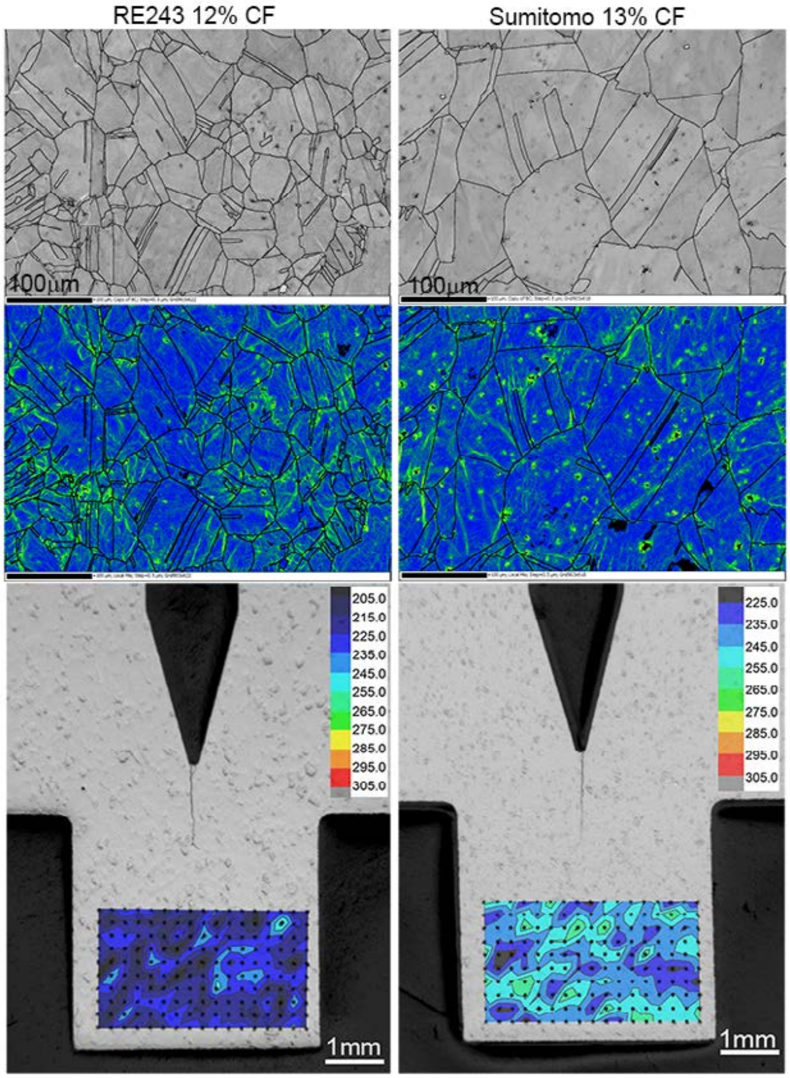

Figure 3.23 **EBSD pattern quality images (top) local misorientation maps (center) and Hardness contour overlays (bottom) for the most lightly cold worked samples CT103 and CT104. The 13%CF sample is slightly harder also exhibiting a unique local misorientation distribution.**

3.6.4 Low-to-Moderate Cold Work: RE243 TT + 17%CR and RE243 SA + 17%CR

For both of these samples, the extent of the crack is highlighted pink on the CT specimen, and the corresponding hardness contour plot is overlaid in Figure 3.24 and Figure 3.25 for the two materials along with microstructure and local misorientation maps from the region of interest. It should be noted that the color scale of the hardness contour map (Scale B) has an increased range compared to that used for the as received materials (Scale A). Because of the limited area of analysis available from the tested the 17%CR SA CT specimen, the hardness contour plot is from a smaller-than-normal sampling area.

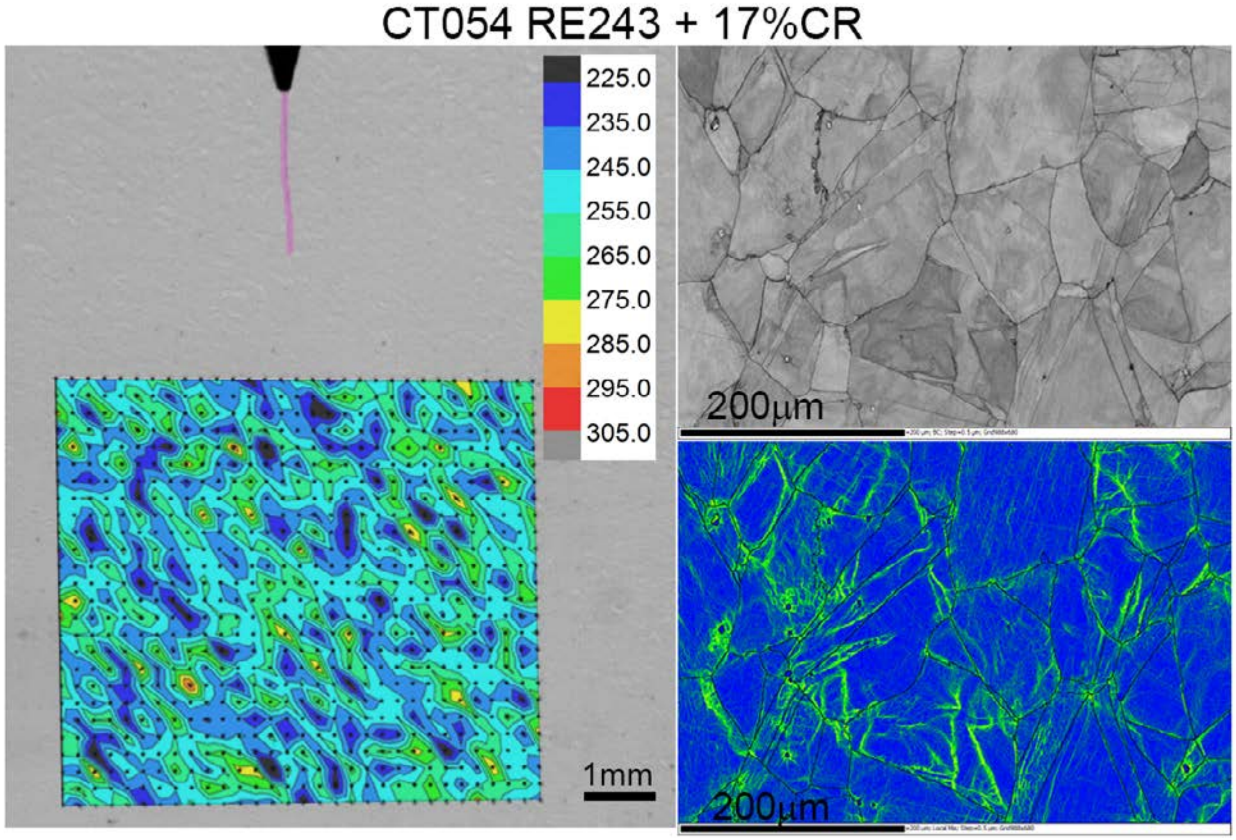

Figure 3.24 **Summary of the results gathered on the 17%CR RE243 SA (CT054) specimen. The hardness contour plot (left) shows a local hardness variation of ~30 kgf/mm^2. The EBSD maps (right) show local misorientation to be isolated near grain boundaries. Pink line is the crack path.**

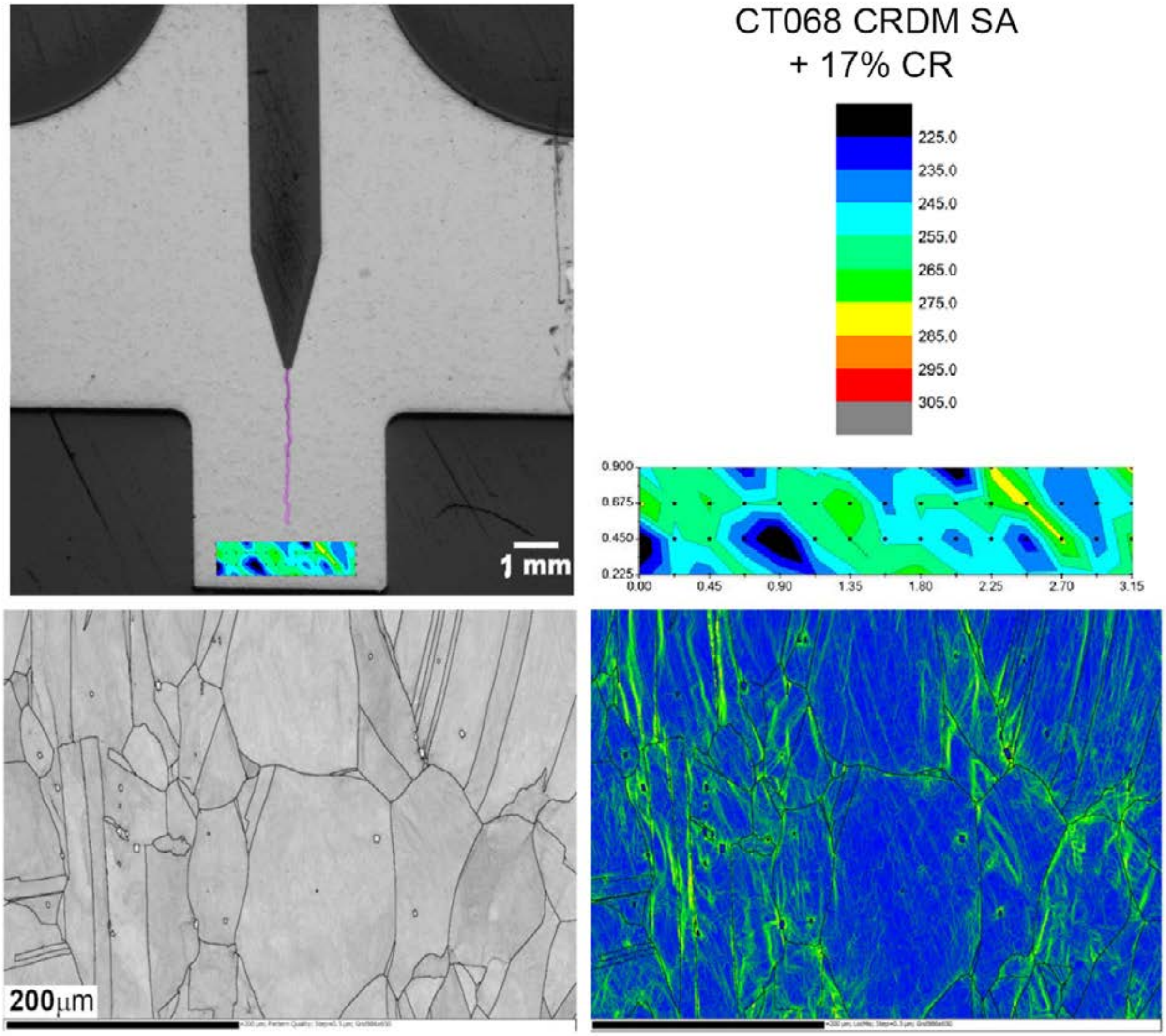

Figure 3.25 **Summary of the 17%CR RE243 SA sample hardness (top) and EBSD results (bottom). Plots show very similar response to the CT054 sample.**

Hardness maps from the two samples indicate nearly identical material response. Localized regions of variable hardness were observed, and IMD maps show similar misorientation distributions that are confined to the near-boundary regions, likely due to dislocation pileups. The local misorientation maps presented in Figure 3.24 and Figure 3.25 demonstrate that regions of high deformation are concentrated along boundaries.

3.6.5 Moderate Cold Work: GEG B25K (MA, HTA, HTA+TT) + 20%CR

The as-received GEG B25K material was examined at 20%CR in three different initial conditions, MA, high temperature annealed (HTA) and HTA+TT. High temperature annealing was performed at 1100°C for 1 hour followed by a water quench, while the thermal treatment was at 720°C for 10 hours. Hardness contour plots, EBSD pattern quality, and local misorientation maps of these 20%CR materials are compared in Figure 3.26.

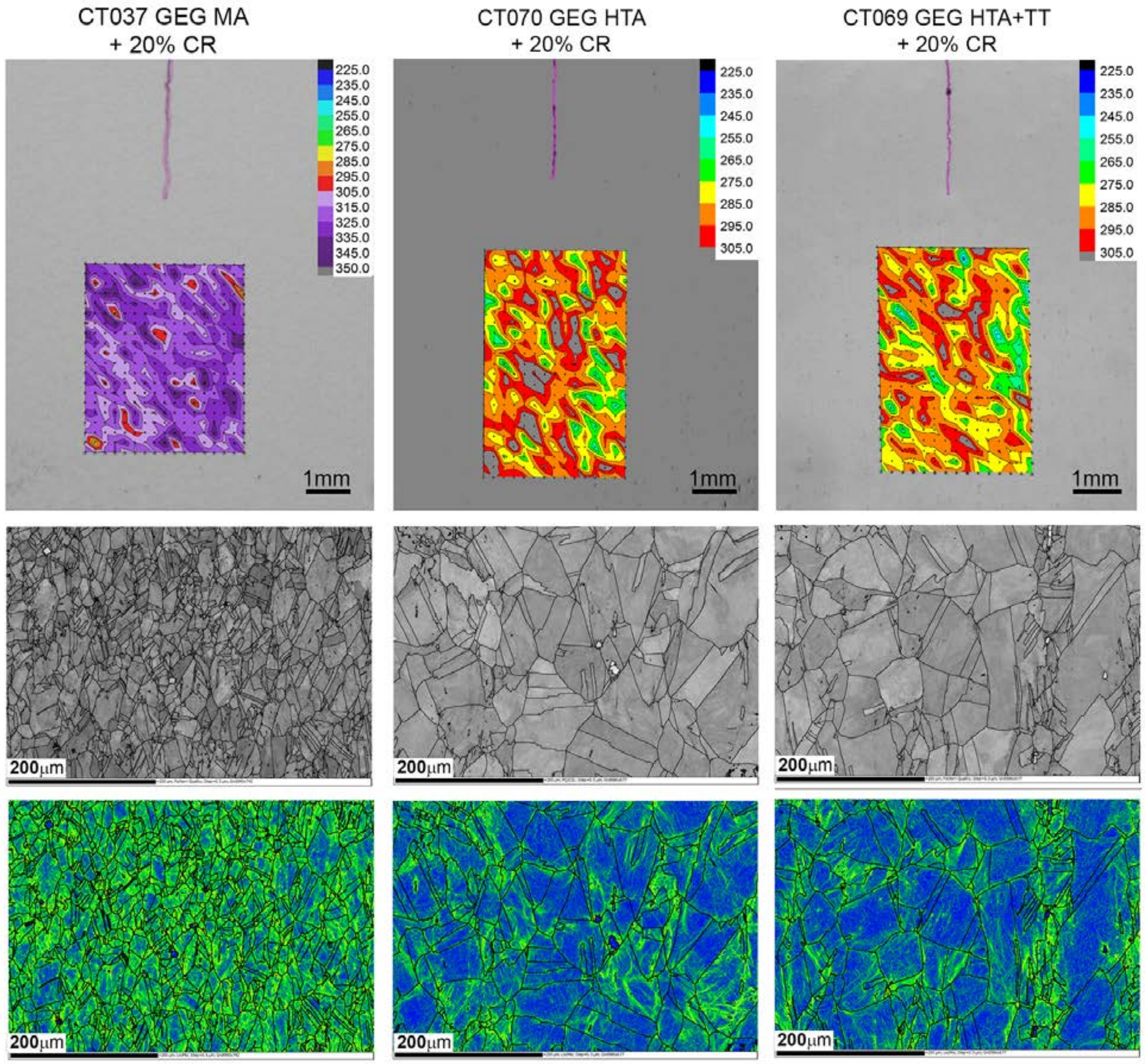

Figure 3.26 Summary of the hardness and EBSD maps for the 20%CR GEG materials having a variety of different heat treatments prior to cold rolling. The scale of the MA sample had to be increased to illustrate the peak hardness.

Comparing these three conditions illustrates a dramatic difference in hardness and local misorientation before and after the HTA heat treatment. The MA material cold rolled to 20% showed the highest hardness (321 kgf/mm^2) of all the moderately cold worked specimens that were evaluated. The contour plots show the material to be uniform, exhibiting no gradients ahead of the crack tip. The EBSD maps in the bottom panels of Figure 3.26 indicate that the 20%CR MA material has much higher levels of strain than the cold worked HTA or HTA+TT materials.

In comparison to the GEG B25K sample in the as-received MA condition (Figure 3.19), the 20%CR GEG MA exhibits a much smaller grain size. This is difficult to explain and suggests a different starting material microstructure perhaps due to variations in the original bar. Cold rolling to a 20% reduction can produce significant mechanical twinning and slightly elongate grains, but it will not alter the overall grain size. The combination of small grain size and high local strain in the 20%CR MA materials as compared with the other 20%CR GEG materials is likely the cause of its correspondingly high hardness and local misorientation values.

Lastly, the cold rolled HTA+TT and HTA samples showed nearly identical behavior in both their hardness and EBSD results suggesting that the thermal treatment may not have been successfully applied to the HTA+TT material. The observation of identical carbide microstructures in Figure 3.27 supports this conclusion. The two materials were also found to behave identically during SCC growth testing in PWR primary water.

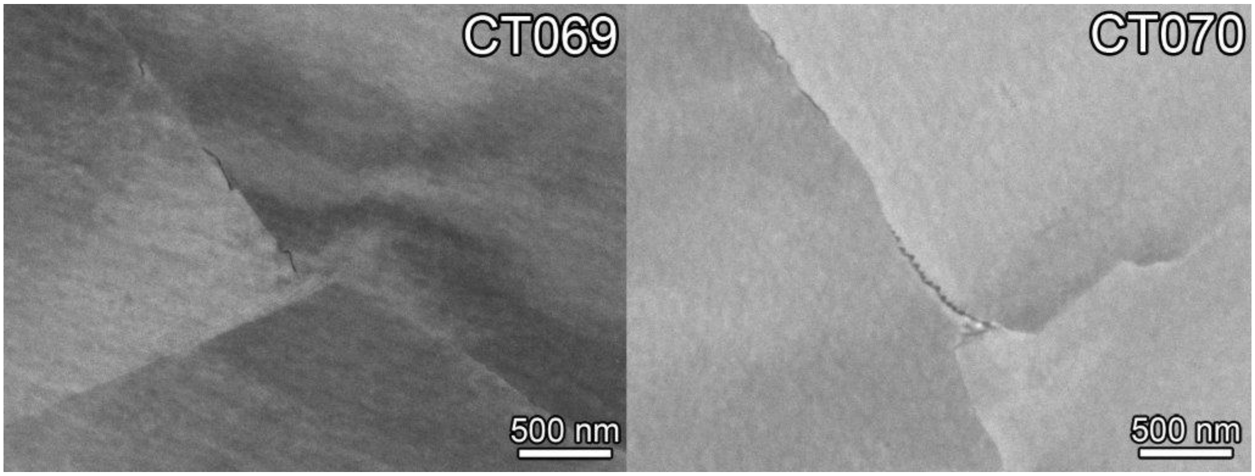

Figure 3.27 Carbide microsctructures for the GEG HTA+TT (CT069) and GEG HTA (CT070) materials showing essentially identical grain boundary carbide distributions

3.6.6 Moderate Cold Work by Tensile Strain: CIEMAT Valinox WP787 TT + 20%TS

Results for the 20%TS material from CIEMAT are shown in Figure 3.28. This sample exhibited hardness and local misorientation distributions nearly identical to the 17% cold worked RE243 and CRDM+SA samples (CT054 & CT068). Grain size was also very similar. Damage accumulation in this material as shown by the local misorientation distribution suggests that at these intermediate levels of cold work, the misorientation distribution between tensile strained and cold rolled materials appears very similar. Deformation is concentrated along boundaries and consistent with the previously examined materials.

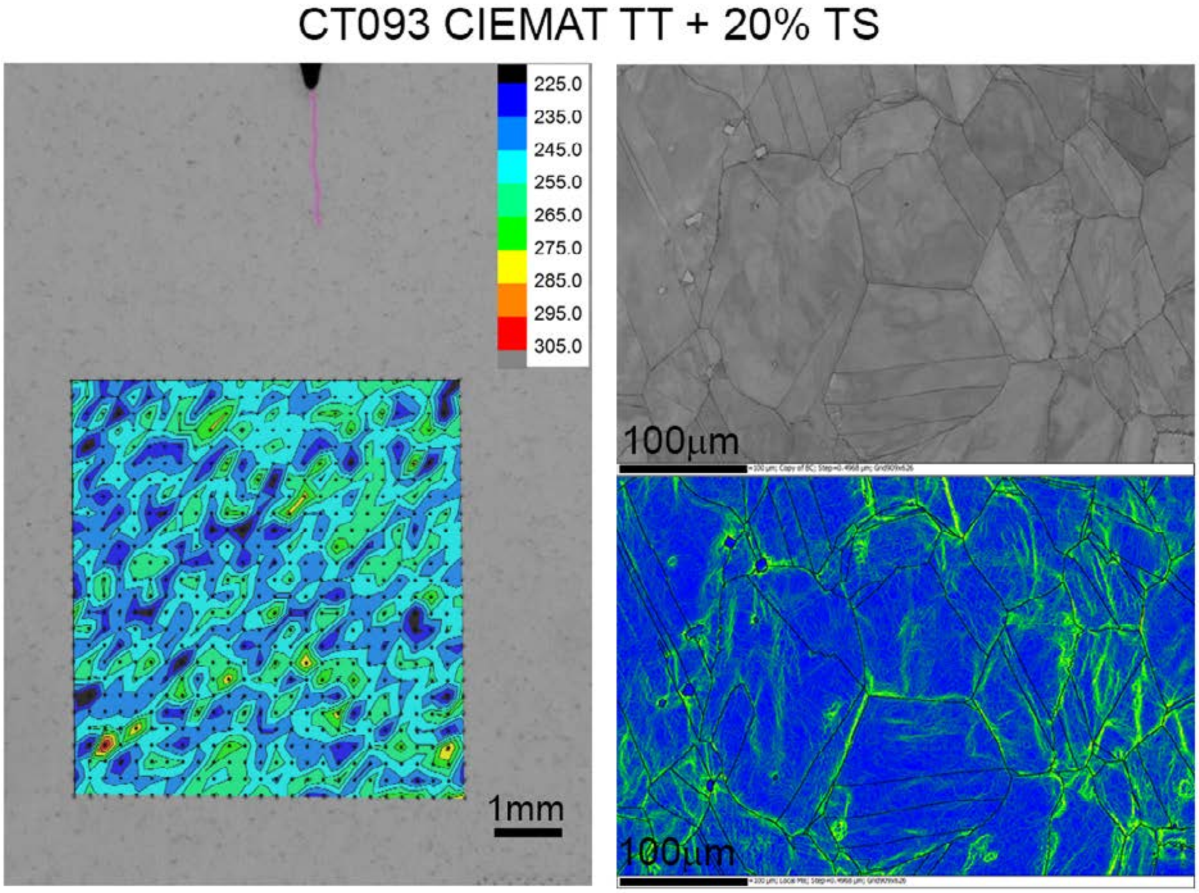

Figure 3.28 Hardness (left) and EBSD pattern quality (upper right) and local misorientation maps (lower right) for the CIEMAT WP787 material. This sample showed cold work response consistent with the CT054 and CT068.

3.6.7 Moderate Cold Work: AMEC 20%CW - 4 CR Passes Versus 10 CR Passes

These specimens were SCC tested by AMEC and provided to PNNL for analysis. Hardness contour plots for the AMEC 4HU and the 23HU materials are shown in Figure 3.29. These materials were extracted from CT specimens with the location of the final crack tip indicated by a pink outline near the top of each image. While the final level of cold rolling for both samples is identical (20%CR), the 23HU material underwent substantially more deformation per pass as compared to 4HU. Lower hardness values of 225-244 kgf/mm^2 are present in the 4HU (10 pass) sample, while 23HU (4 pass) has consistently higher hardness values (270-290 kgf/mm^2) indicating a difference in the final microstructural damage.

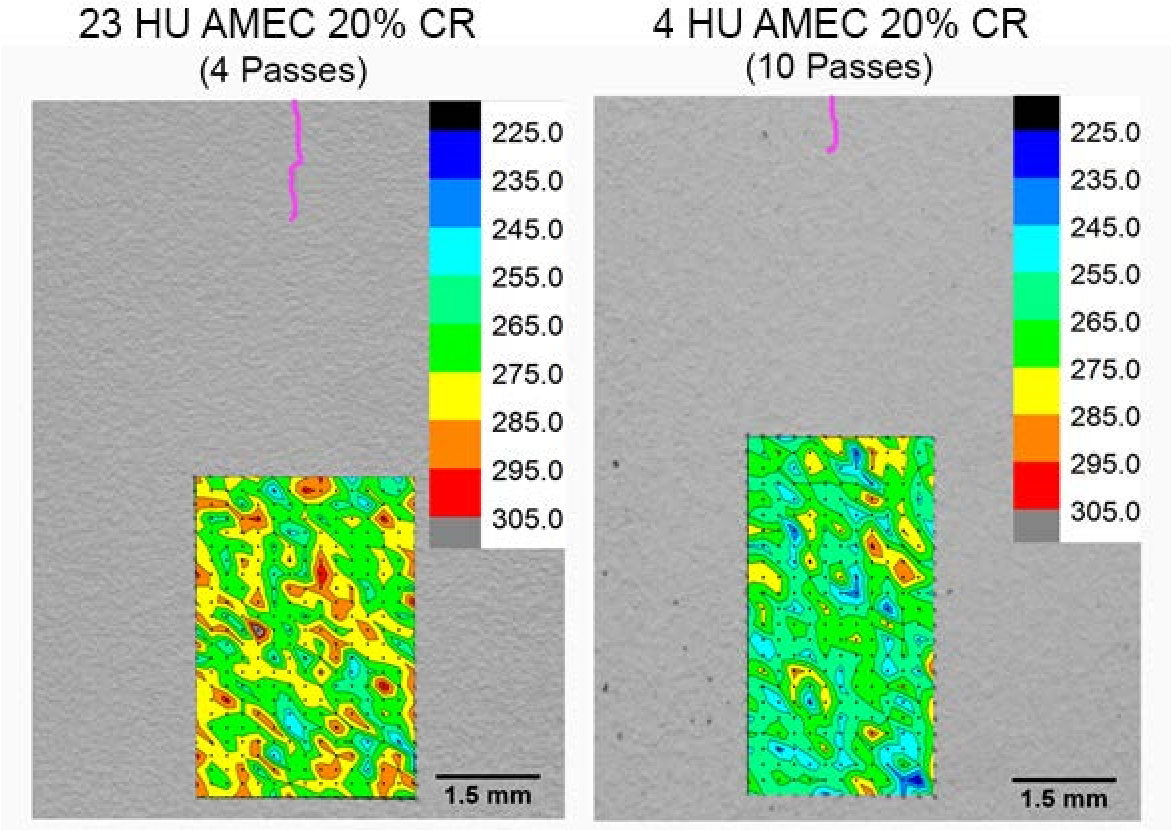

Figure 3.29 **Hardness contour plots of 23HU and 4HU AMEC materials showing a higher accumulation of microstructural damage is present at the same %CR due to the increased reduction per pass involved in the fabrication of the 23HU sample**

The 23HU (4 pass) and 4HU (10 pass) samples were also evaluated using EBSD and are shown as pattern quality and local misorientation maps in Figure 3.30. Consistent with the hardness results, EBSD maps of these samples show the presence of a more refined grain structure in the 23HU (4 pass) material. Additionally, decreased strain contrast is seen in the pattern quality map of the 4HU (10 pass) sample, coinciding with the generally lower hardness values of the same material. Local misorientation plots of these samples reveal a significantly greater intragranular strain than the 17%CR CT068 sample in Figure 3.25.

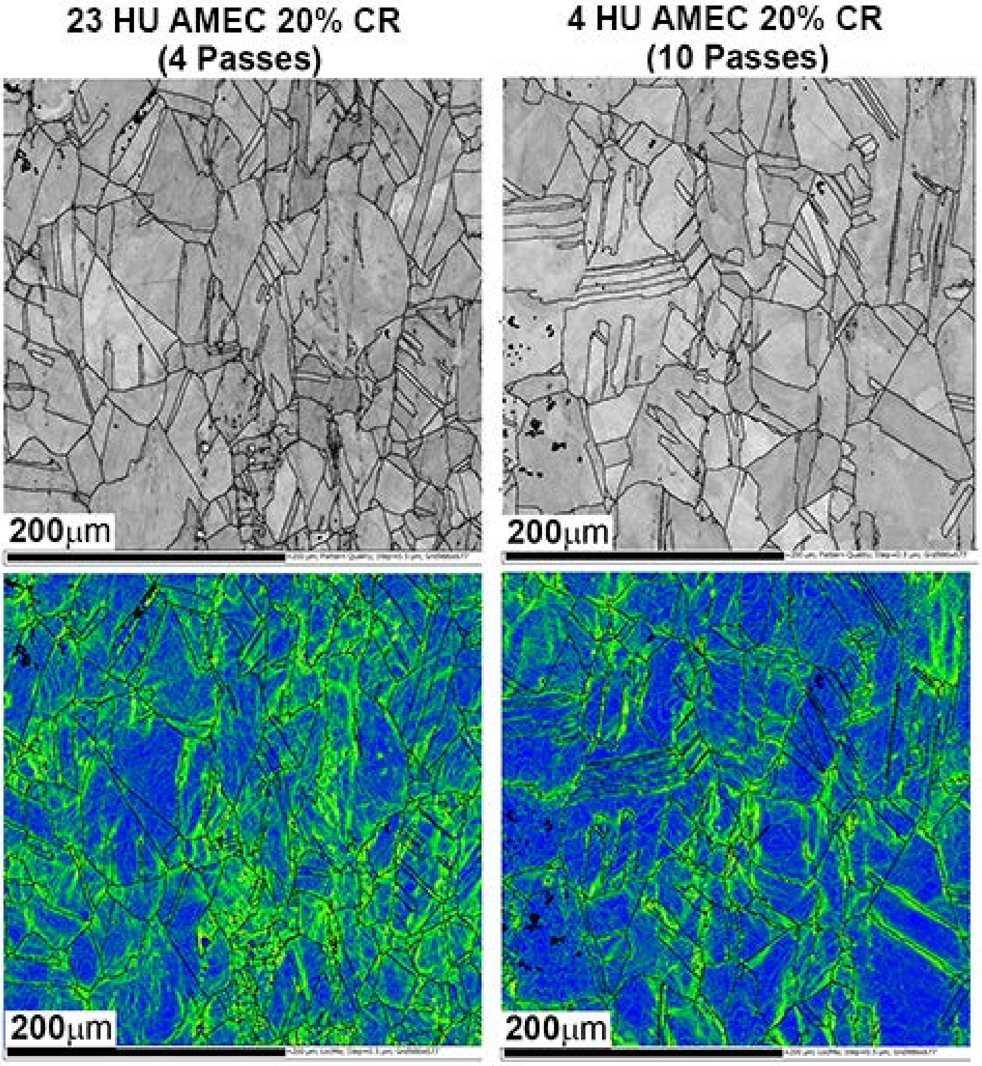

Figure 3.30 EBSD pattern quality maps (top row) and local misorientation plots (bottom row) for the 23HU and 4HU 20%CR AMEC materials

In summary, inspection of the pattern quality and local misorientation maps from the AMEC 23HU (4 passes) compared to the 4HU (10 passes) 20%CR sample indicates that varying the level of deformation per pass changes the strain distribution. While the differences between the two are subtle, a higher density of intragranular local misorientation can be seen for the 23HU versus the 4HU sample. Additionally, decreased strain contrast can also be seen in the pattern quality map of the 4HU sample. EBSD results are consistent with the hardness maps in Figure 3.29, which also show significant variation between these samples at the same final %CW.

3.6.8 Moderate Cold Work: AMEC 3PU (20%TS alloy 690MA) Versus 34PU (20%CR alloy 690MA)

Another interesting pair of specimens obtained from AMEC are 3PU and 34HU. Both are from the same heat of alloy 690MA, but 3PU was 20% tensile strained while 34 HU was 20% cold rolled. This provides an excellent opportunity to compare the difference in response between tensile straining and cold rolling (or cold forging). Hardness contour plots and EBSD mapping of the 20%CR 3PU and 34HU MA+TT alloy 690 materials are shown in Figure 3.31. No observable differences are apparent in either the microstructure or local misorientation distributions, indicating that the two methods of deformation produced very similar levels of strain and hardness increase.

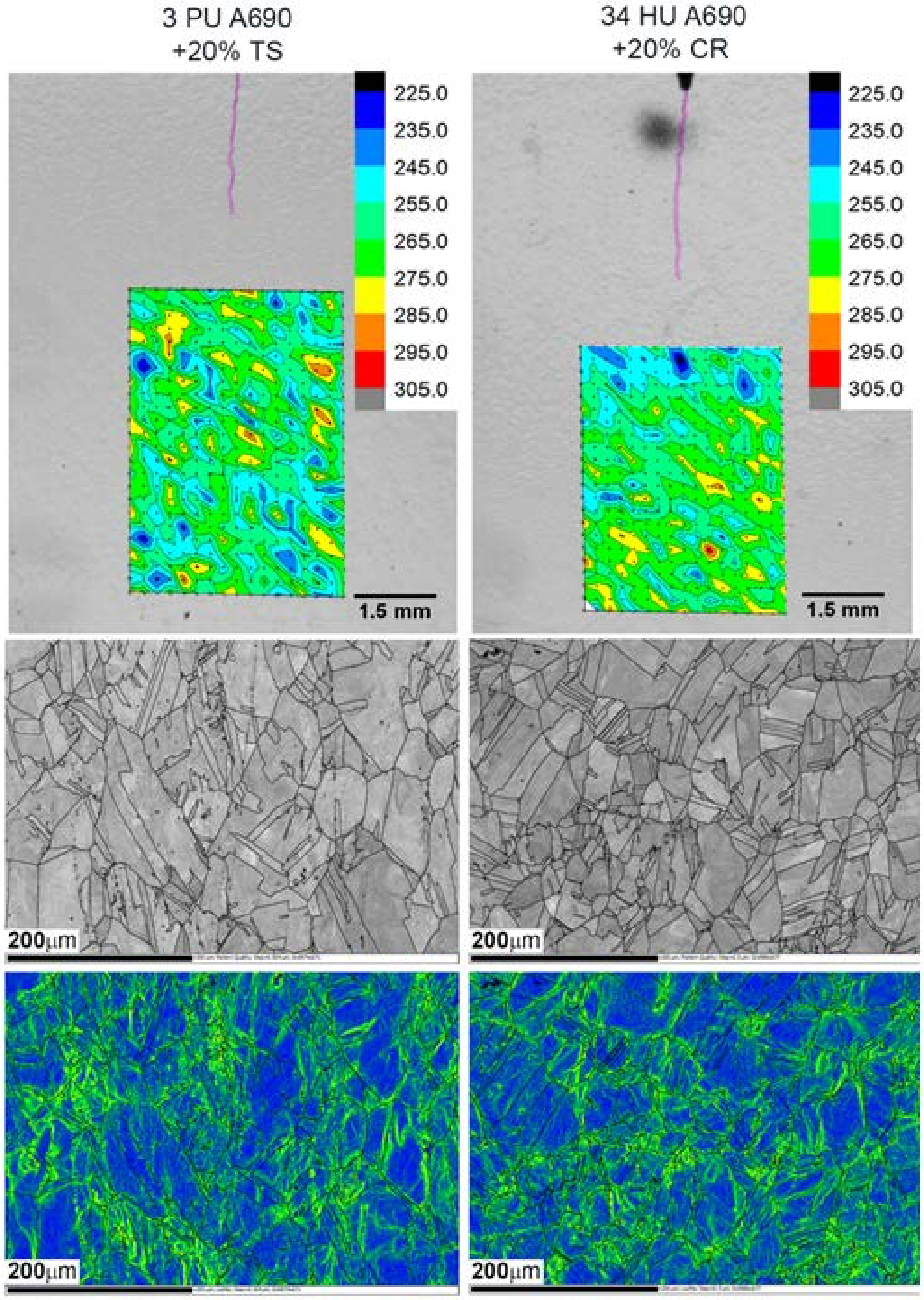

Figure 3.31 **Hardness contour plots (top), EBSD pattern quality maps (middle) and local misorientation plots (bottom) for 20%TS 3PU and 20%CR 34 HU alloy 690 materials. No significant distinctions are apparent distinguishing the materials from one another in the measured hardness, IMD parameter or observed grain size.**

3.6.9 Other Moderately Cold Worked Samples in TT Condition: 21%CF RE243 TT (CT100), 21%CF Doosan TT (CT102), 21%CF Allvac TT (CT101) and 22%CR ENSA TT (CT060)

Of the four TT specimens tested, the Allvac (CT101) material showed a considerably refined grain size. As expected, the grain size reduction also resulted in an increase in hardness for the given amount of cold work as shown in Figure 3.32. Local misorientation mapping indicated that the Allvac material had the highest local misorientation density of the moderately cold worked samples in the TT condition.

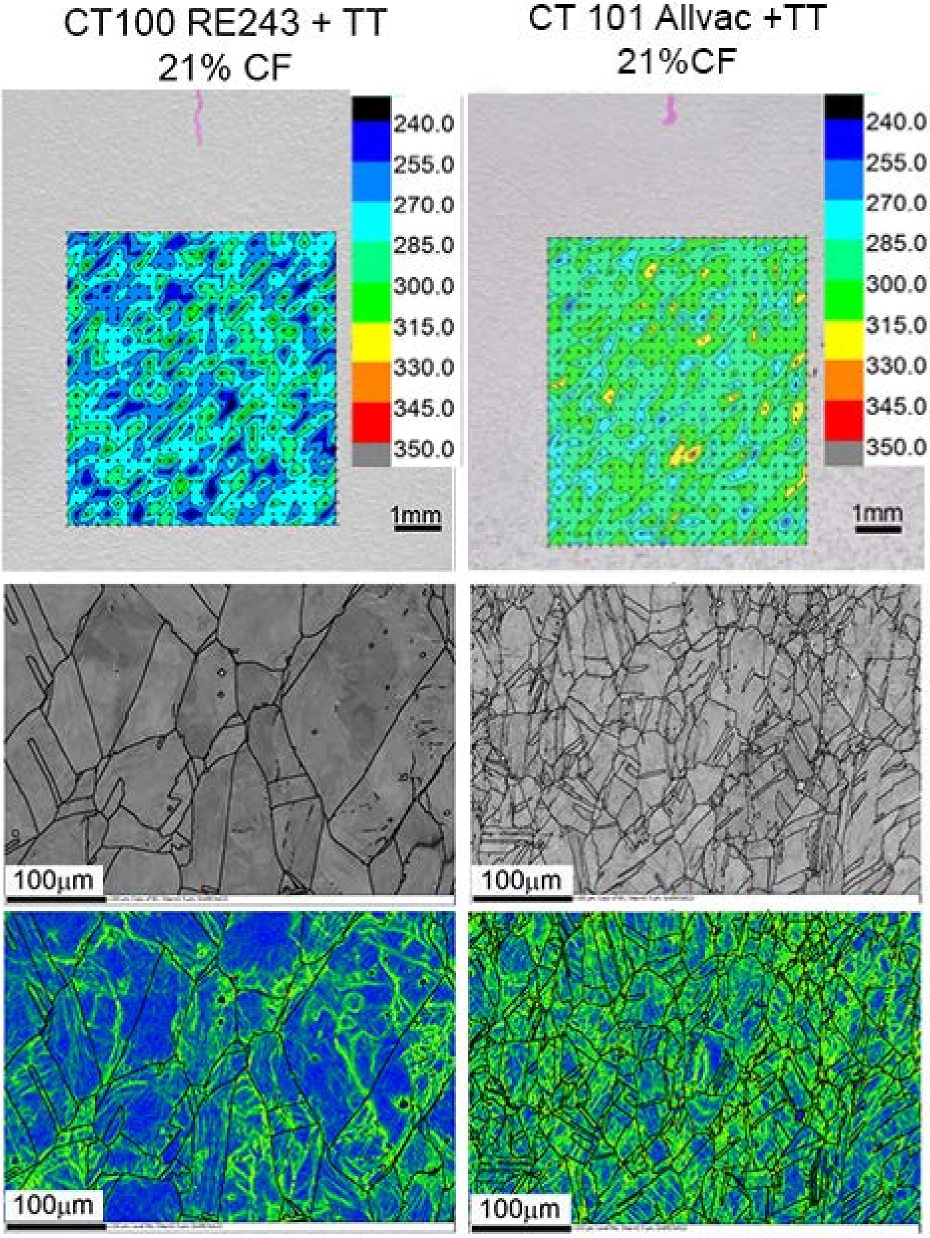

Figure 3.32 Hardness contour plots (top), EBSD pattern quality maps (middle) and local misorientation plots (bottom) for different heats in the TT condition at 21%CF. A substantial reduction in grain size, along with elevated hardness and LM density was seen in the Allvac material.

Results for CT102 and CT060 are shown in Figure 3.33. These specimens had nearly identical hardness contour plots, grain size and local misorientation distributions despite the heat-to-heat variation and the difference in cold working method (cold forged vs. cold rolled).

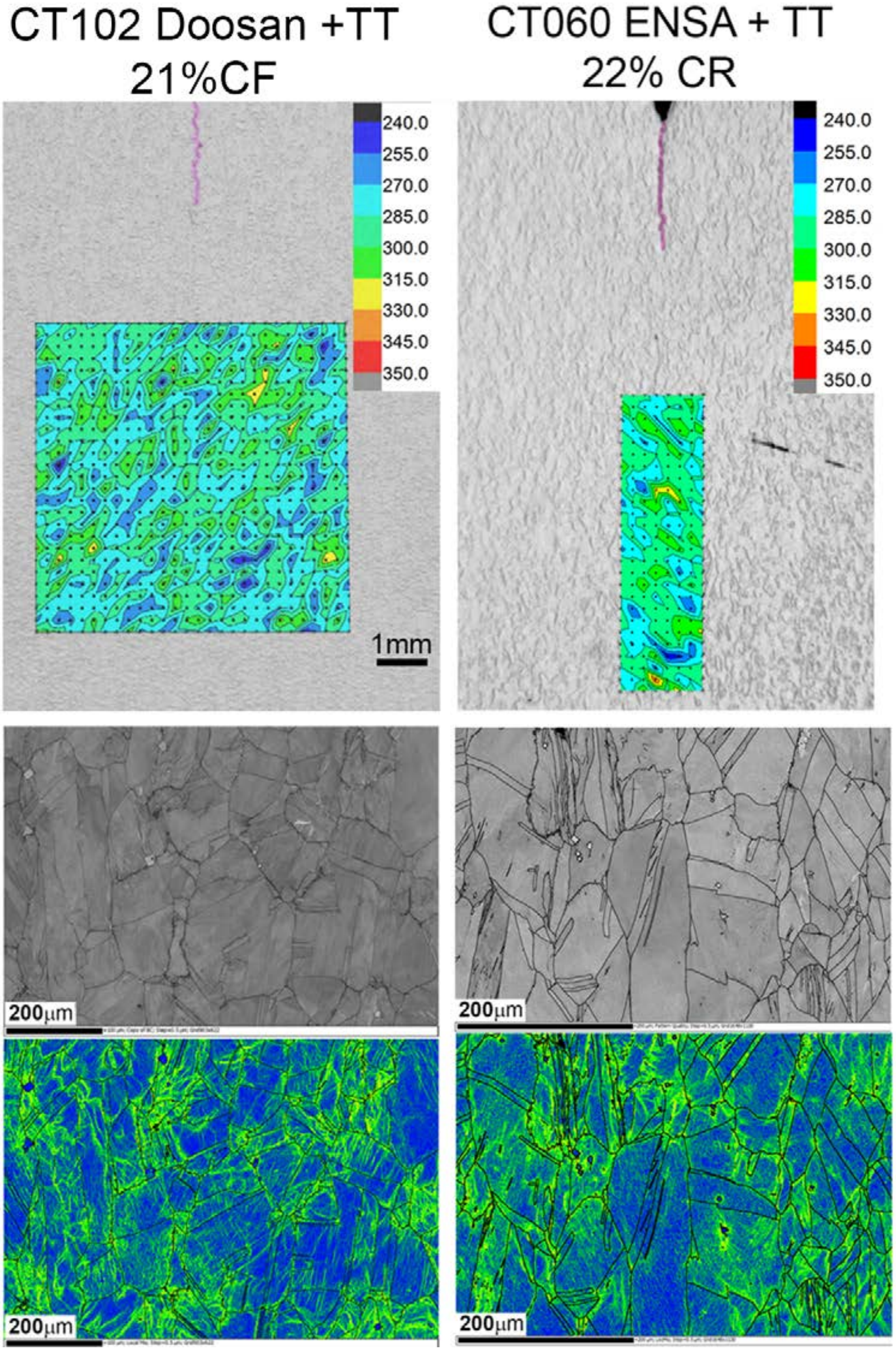

Figure 3.33 Hardness contour plots (top), EBSD pattern quality maps (middle) and local misorientation plots (bottom) for the Doosan and ENSA heats in the TT condition at 21%CF and 22%CR, respectively

3.6.10 Heavily Cold Worked Materials Overview

The heavily cold worked samples (≥26% CW) discussed in this section are arranged and compared according to the heat treatment conditions that were applied to the specimens. Table 3.9 below summarizes the applied conditions. The sections below will describe hardness and EBSD results for subsets of these specimens.

Table 3.9 Heavily cold worked alloy 690 CT specimens

Sample ID	Heat & Condition	Cold Work
CT036	ANL MA	26%CR
CT073	ANL MA	30%CF
CT074	ANL HTA	30%CF
CT039	RE243 SA	31%CR
CT053	RE243 TT + Rec	31%CR
CT038	RE243 TT	31%CR
CT098	Sumitomo TT	31%CF
CT099	RE243 TT	31%CF
CT059	ENSA TT	32%CF
CT094	TK-VDM TT	32% CF

3.6.10.1 Heavily Cold Worked Plate Samples in the MA Condition: 26%CR ANL MA (CT036) and 30%CF ANL MA (CT073)

Results from samples CT036 (26%CR ANL MA) and CT073 (30%CF ANL MA) were very similar and are shown in Figure 3.34. The CT036 specimen had an average hardness of 310 kgf/mm^2, and CT073 had an average hardness value of 316 kgf/mm^2. EBSD pattern quality images show the samples have similar grain size, and local misorientation mapping indicates the effective strain distributions are dense with regions of lower strain. One interesting aspect indicated by the hardness results of the CT073 specimen was the presence of an area of low hardness identified in the center of the sample. It does not obviously correlate to any change in the IMD representation of the local strains.

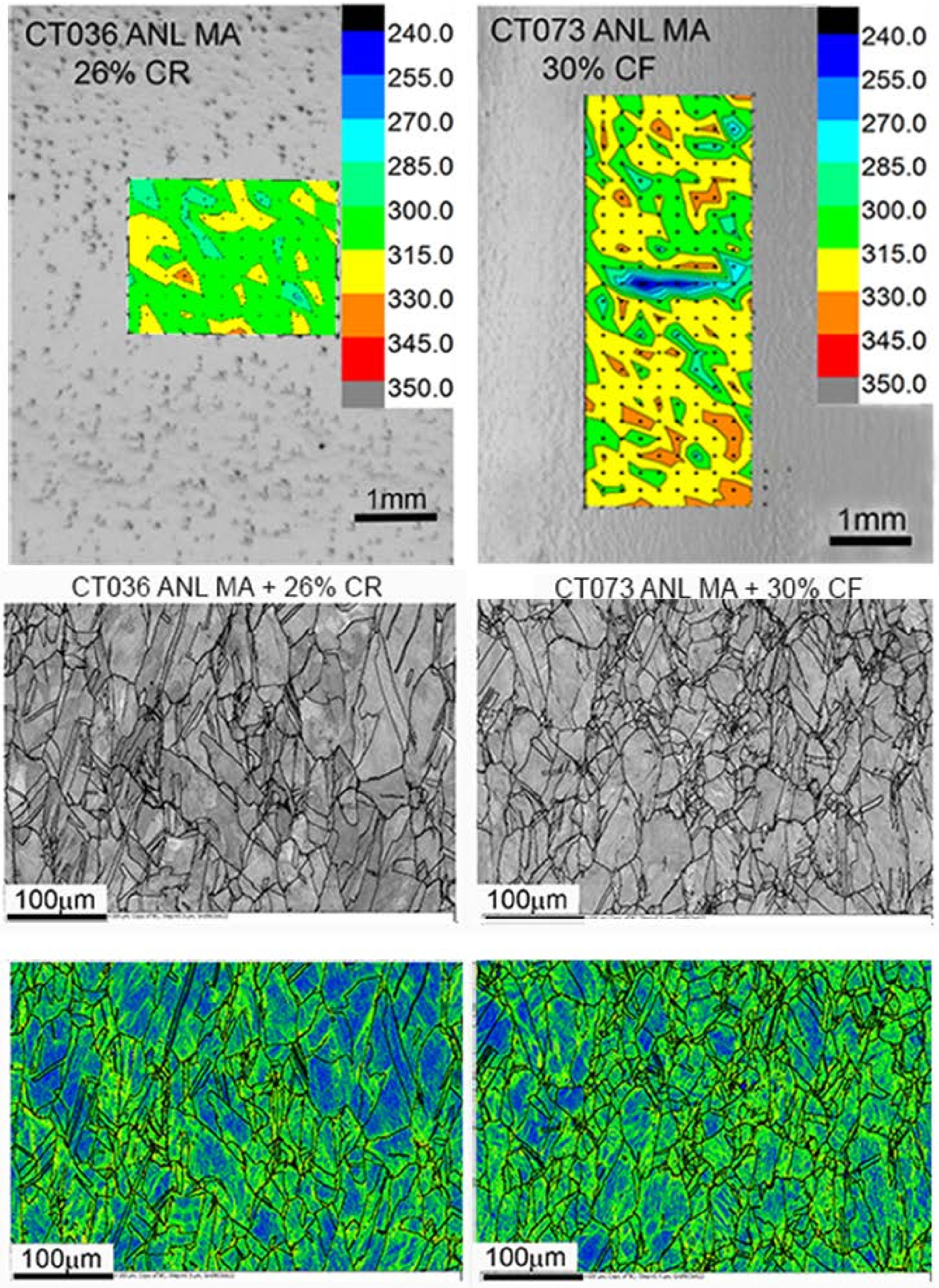

Figure 3.34 Hardness contour plots (top), EBSD pattern quality maps (middle) and local misorientation plots (bottom) of the ANL material in the MA condition at different levels and modes of cold work (26%CR and 30%CF).

3.6.10.2 *Heavily Cold Worked Samples in HTA, SA and RT Condition: 30%CF ANL HTA (CT074), 31%CR RE243 SA (CT039) and 31%CR RE243 TT with Recovery Treatment (CT053)*

The two annealed materials presented in Figure 3.35 are 30%CF ANL HTA (CT074) and 31%CR RE243 (CT039). Before cold working, both samples were given a high-temperature heat treatment at 1100°C followed by a water quench. The higher carbon content in the ANL material prevented full carbide dissolution during the anneal and left a very low density of carbides as was previously described. Hardness results indicate there was no measureable difference between these two specimens with averages of ~316 kgf/mm^2. The two specimens exhibit hardness contour plots that are very consistent with each other, along with similar local misorientation distributions. The 31%CR RE243 TT that was given a recovery treatment (CT053) has a significant reduction in hardness and local misorientation when compared to materials at a similar level of cold work, likely due to the 700°C 1 hr recovery heat treatment.

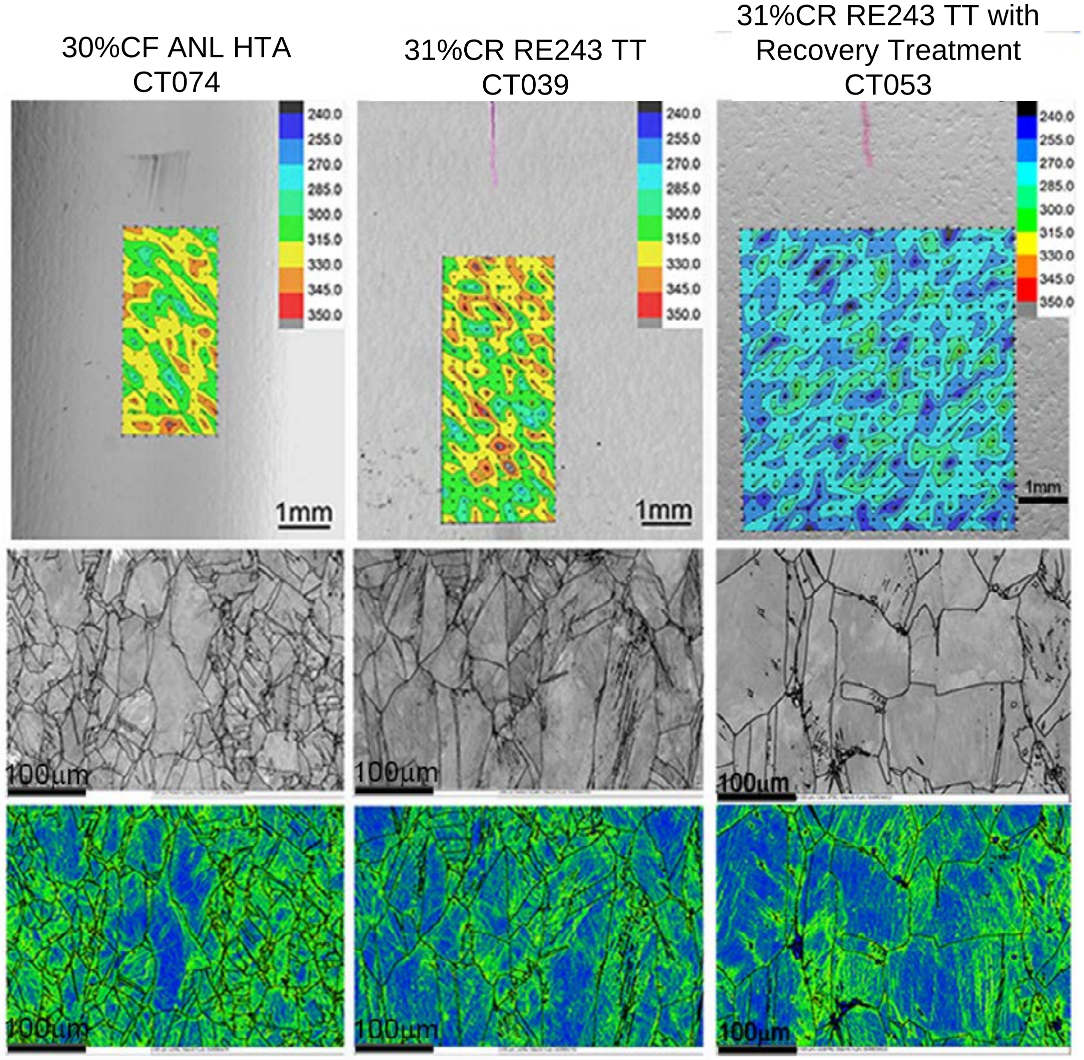

Figure 3.35 Hardness contour plots (top), EBSD pattern quality maps (middle) and local misorientation plots (bottom) of heavily cold worked samples. The recovery heat treatment given to CT053 after cold working lowered the hardness.

3.6.10.3 Heavily Cold Worked CRDM Specimens: 31%CF Sumitomo TT (CT098) and 31%CF RE243 TT (CT099)

The 31%CF Sumitomo TT (CT098) and 31%CF RE243 TT (CT099) results are shown in Figure 3.36. The Sumitomo material had a substantially reduced grain size when compared to the RE243 specimen of the same condition. This may be a factor in the lower average hardness and IMD results for the 31%CF RE243 versus the 31%CF Sumitomo materials.

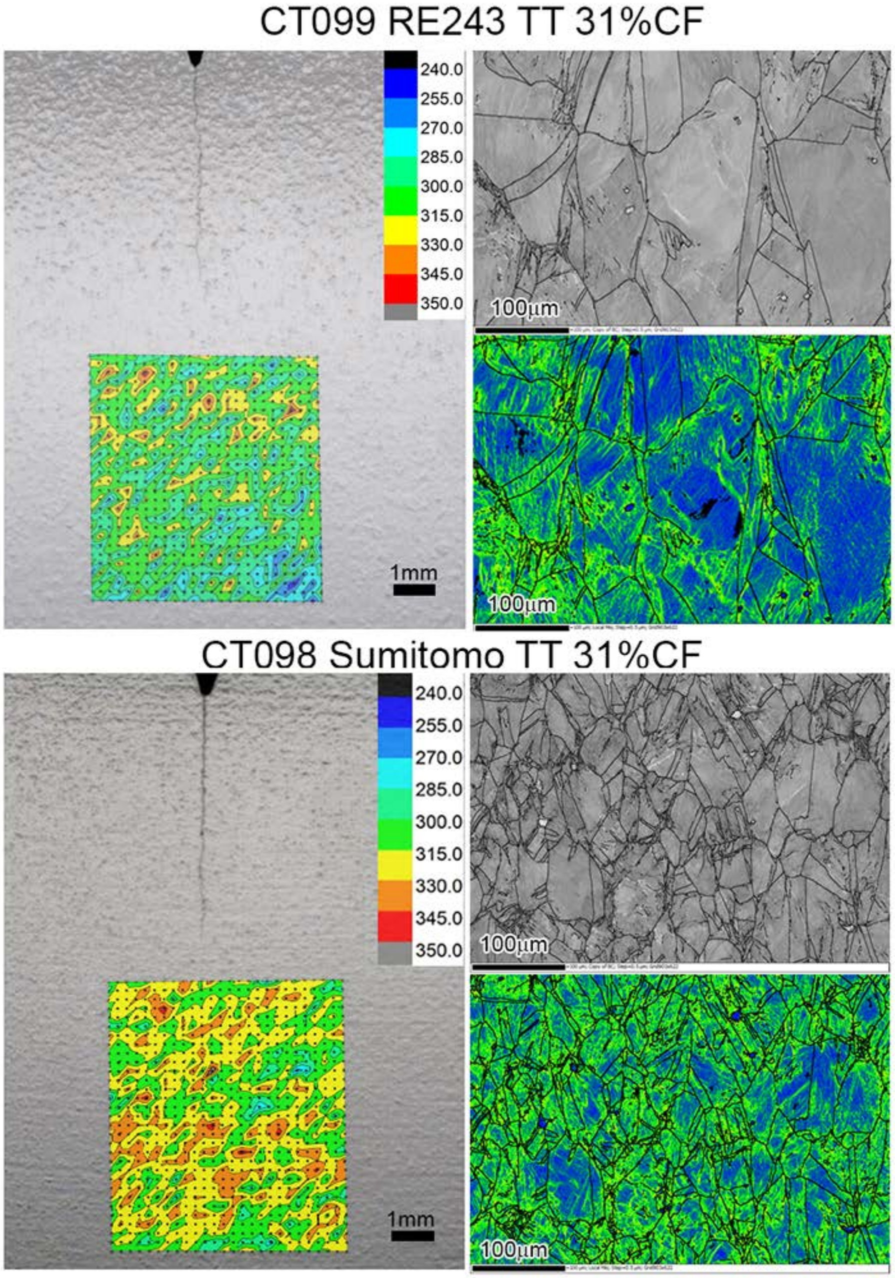
CT099 RE243 TT 31%CF

CT098 Sumitomo TT 31%CF

Figure 3.36 Hardness and EBSD results for the 31% RE243 TT specimen (CT099) compared to the 31%CF Sumitomo TT specimen (CT098). Grain size differences were readily apparent, likely causing the visible hardness and local misorientation distribution differences.

3.6.10.4 Heavily Cold Worked TT Plate Specimens: 32%CF ENSA TT (CT059) and 32%CF TK-VDM TT (CT094)

The ENSA CT059 and TK-VDM CT094 specimens were the most heavily cold worked samples at 32%CF. The grain size of these specimens remained fairly large (Figure 3.37), and cold working resulting in an average hardness of 305 kgf/mm^2 (CT059) and 328.5 kgf/mm^2 (CT094). The CT094 specimen exhibited the highest hardness of all the samples that were tested, showing more frequent regions of locally elevated hardness than the ENSA material or other materials. Both samples showed very dense misorientation distributions.

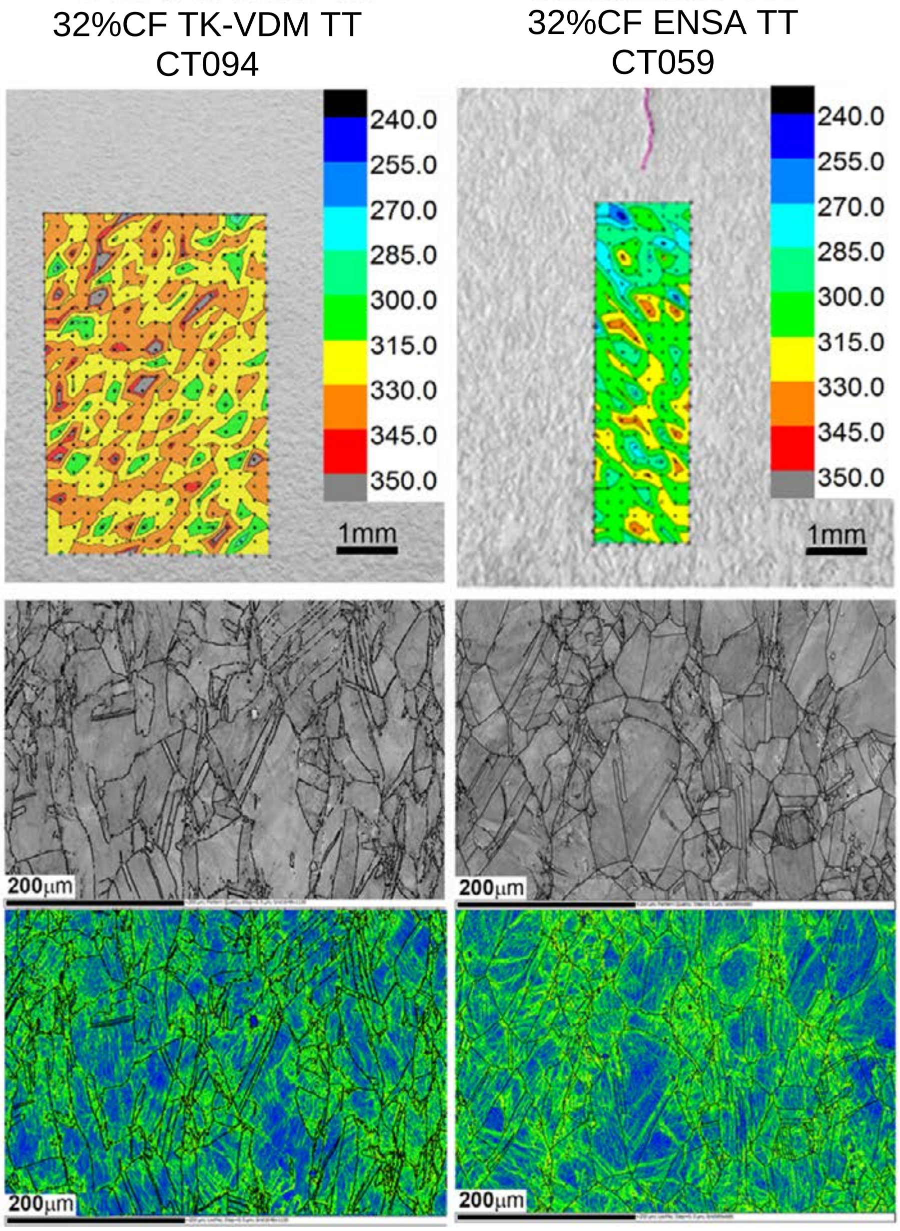

Figure 3.37 Hardness contour plots (top), EBSD pattern quality maps (middle) and local misorientation plots (bottom) of the most heavily cold worked samples tested TK-VDM (CT094) and ENSA (CT059) at 32% cold forged

3.7 Cold Work Effects on Microstructure and Strain Distributions Summary

In order to better compare the EBSD results among the many alloy 690 materials examined, pattern quality and local misorientation maps for all materials are presented in Figure 3.38 and Figure 3.39, respectively. The degree of cold work among samples increases from the top to bottom. This allows a direct assessment of microstructures and strain distributions among these different heats, material conditions, and levels of CW.

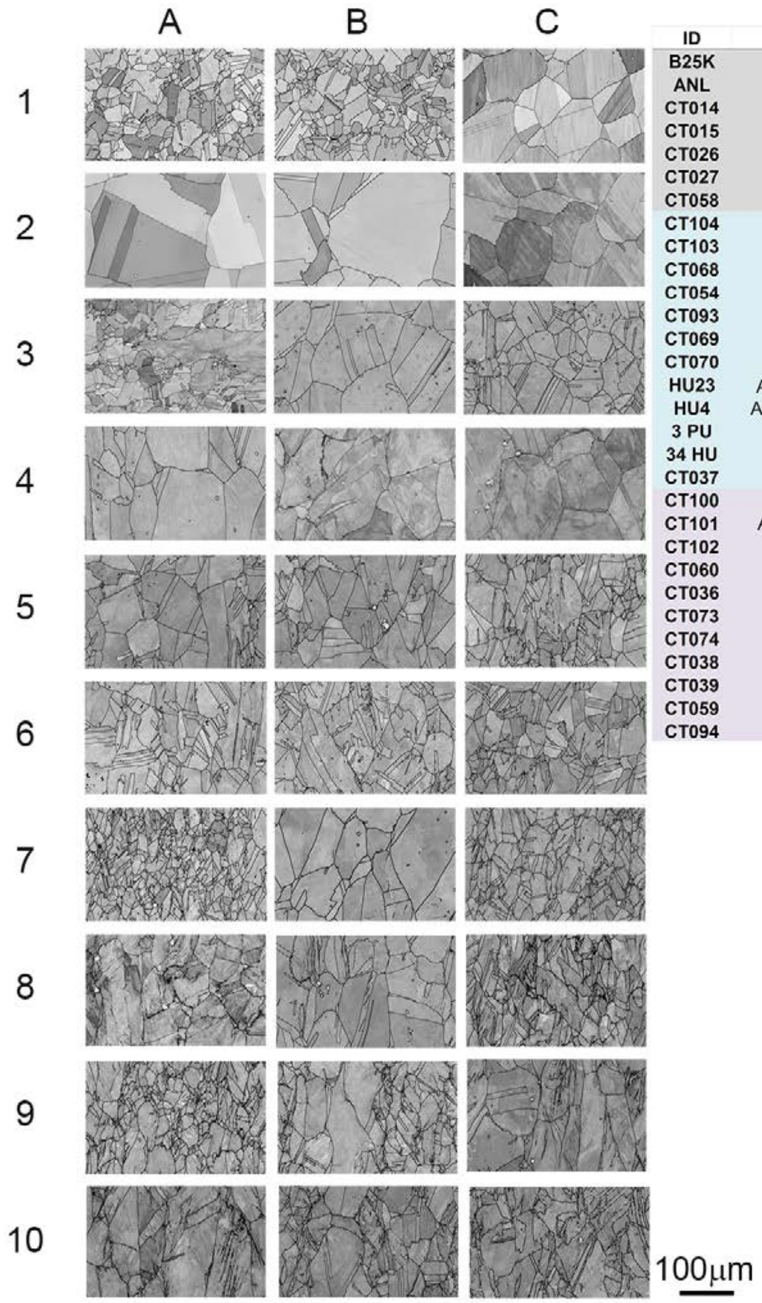

ID	Sample Information	Row	Column
B25K	As Received MA	1	A
ANL	As Received MA	1	B
CT014	RE 243 + TT	1	C
CT015	RE243 + SA	2	A
CT026	WP142 + TT	2	B
CT027	WP140 + TT	2	C
CT058	AREVA + TT	3	A
CT104	RE243 12% CF	3	B
CT103	Sumitomo 13% CF	3	C
CT068	RE243 SA 17% CR	4	A
CT054	RE243 + 17% CR	4	B
CT093	CIEMAT + TT 20% TS	4	C
CT069	GEG HTA+TT 20%CR	5	A
CT070	GEG HTA 20%CR	5	B
HU23	AMEC 20%CR (4 passes)	5	C
HU4	AMEC 20%CR (10 passes)	6	A
3 PU	AMEC MA+TT 20%TS	6	B
34 HU	AMEC MA+TT 20%CR	6	C
CT037	GEG MA 20%CR	7	A
CT100	RE243 + TT 21% CF	7	B
CT101	Allvac (X87N-1) 21% CF	7	C
CT102	Doosan TT 21% CF	8	A
CT060	ENSA TT 22%CR	8	B
CT036	ANL MA 26%CR	8	C
CT073	ANL MA 30%CF	9	A
CT074	ANL HTA+SA 30%CF	9	B
CT038	RE243 TT + 31%CR	9	C
CT039	RE243 SA + 31%CR	10	A
CT059	ENSA TT 32%CF	10	B
CT094	TK-VDM 32% CF	10	C

Figure 3.38 EBSD Pattern quality images showing the microstructures of all the alloy 690 materials through a variety of heat treatment conditions and levels of cold work. All images are at the same scale.

The results presented in Figure 3.39 focus on visually identifying strain on a local scale. As seen in Figure 3.38, significant microstructural variations were tested, but the general trend of increasing LM density with %CW is clearly visible.

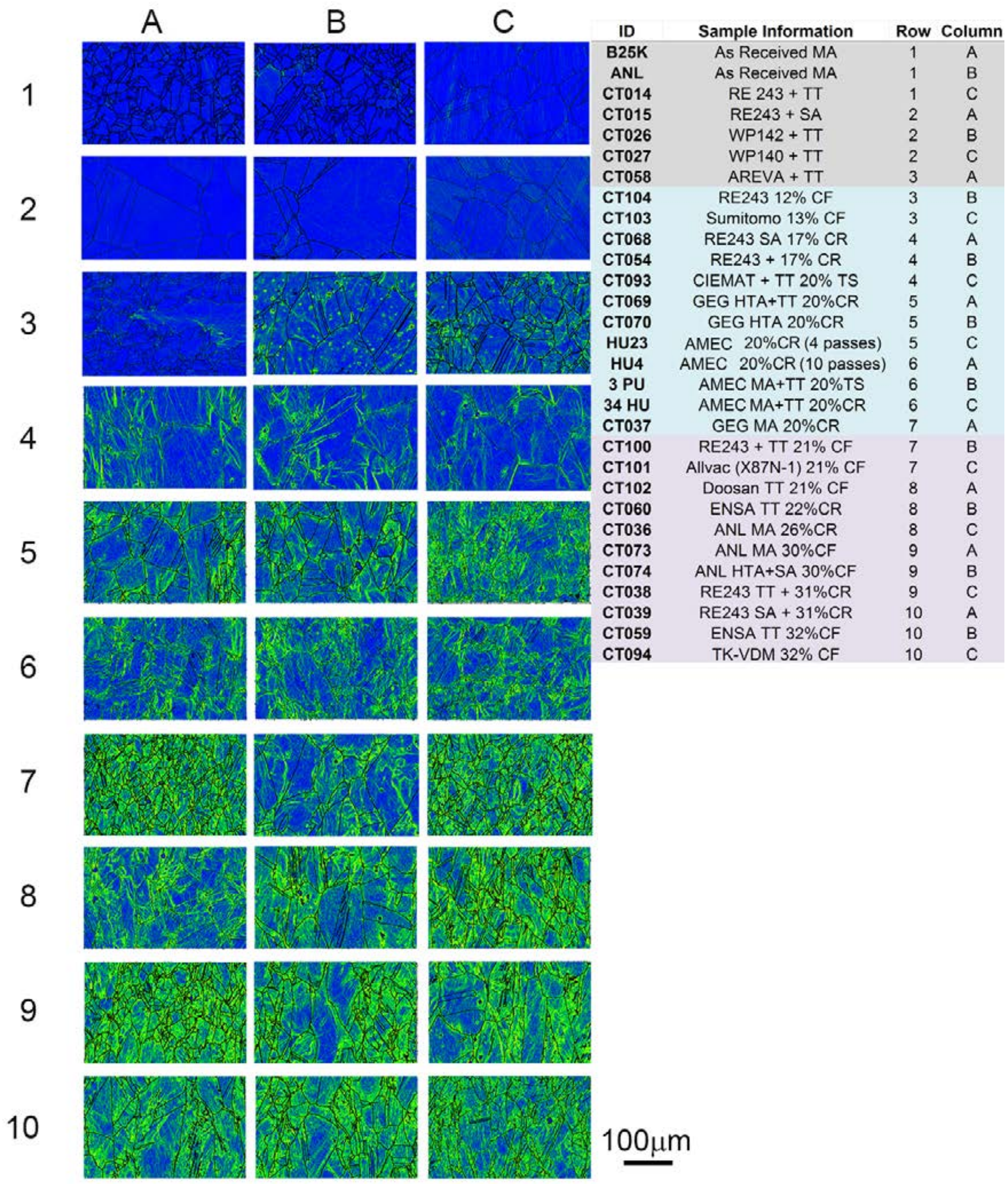

ID	Sample Information	Row	Column
B25K	As Received MA	1	A
ANL	As Received MA	1	B
CT014	RE 243 + TT	1	C
CT015	RE243 + SA	2	A
CT026	WP142 + TT	2	B
CT027	WP140 + TT	2	C
CT058	AREVA + TT	3	A
CT104	RE243 12% CF	3	B
CT103	Sumitomo 13% CF	3	C
CT068	RE243 SA 17% CR	4	A
CT054	RE243 + 17% CR	4	B
CT093	CIEMAT + TT 20% TS	4	C
CT069	GEG HTA+TT 20%CR	5	A
CT070	GEG HTA 20%CR	5	B
HU23	AMEC 20%CR (4 passes)	5	C
HU4	AMEC 20%CR (10 passes)	6	A
3 PU	AMEC MA+TT 20%TS	6	B
34 HU	AMEC MA+TT 20%CR	6	C
CT037	GEG MA 20%CR	7	A
CT100	RE243 + TT 21% CF	7	B
CT101	Allvac (X87N-1) 21% CF	7	C
CT102	Doosan TT 21% CF	8	A
CT060	ENSA TT 22%CR	8	B
CT036	ANL MA 26%CR	8	C
CT073	ANL MA 30%CF	9	A
CT074	ANL HTA+SA 30%CF	9	B
CT038	RE243 TT + 31%CR	9	C
CT039	RE243 SA + 31%CR	10	A
CT059	ENSA TT 32%CF	10	B
CT094	TK-VDM 32% CF	10	C

Figure 3.39 **EBSD Pattern quality images showing the local misorientation distributions of alloy 690 materials through a variety of heat treatment conditions and levels of cold work. The degree of cold work among samples increases from the top row with as-received materials down to the bottom rows where the highest cold worked materials are shown. The as-received materials showed little to no low angle misorientation.**

The as-received materials exhibit little or no strain, while materials cold worked to ~30% reduction show high levels of strain throughout the mapped region. An interesting comparison can be seen for various specimens with ~20%CW. Most show strain distributions are isolated to near boundary regions, except for the CT037 GEG B25K specimen that has strain distributions migrating toward grain interiors, similar to 30%CW materials. This could be a result of the smaller grain size and high twin density in the GEG B25K MA 20%CR specimen or due to differences in the MA starting materials.

The hardness mapping performed is a very useful tool for providing information about local variations that can often be related to specific microstructural features in a material. Hardness contour maps were generated to better investigate the distribution of hardening within the materials and enable comparisons for cases with identical levels of cold work. For example, the hardness contour maps for the 20%CR specimens 23HU and 4HU in Figure 3.29 provide more detailed insights into the rolling-induced hardening as a function of the number of passes. Maps reveal local regions of higher hardness in 23HU (4 rolling passes) than in 4HU (10 passes) even though both have similar average hardness values in Table 3.6. Beyond local variation, the hardness mapping when used to extract global area averaged values also provides the ability to investigate a variety of correlations to local misorientation, strain and crack growth rates.

3.8 Correlations Between Strain and Hardness Results for Alloy 690 Materials

Several relations have been developed between basic mechanical properties and microstructural observations showing that strain distributions within a material are a function of several parameters including grain size, second phase density and distribution, applied stress, strain rate sensitivity and the strain hardening exponent. The availability of both hardness and IMD data allows the linear relationship between strain and IMD reported by LeHockey [13] to be tested. The basis for this test is the power law strain hardening equation for plastic strain given in Equation 3.5 where σ is the uniaxial stress, σ_y is the uniaxial yield stress, ε is the plastic strain, k is a constant, and n is the strain-hardening exponent.

$$\sigma - \sigma_y = k\varepsilon^n \tag{3.5}$$

Using the Tabor relation for Vickers hardness, the yield stress can be considered as linearly proportional to the hardness (H). If the IMD is linearly proportional to macroscopic plastic strain, then Equation 3.5 can be rewritten as:

$$\Delta H = k_{IMD} IMD^n \tag{3.6}$$

This equation indicates that increases in hardness (ΔH) over the non-cold worked condition will increase with IMD in the same way that hardness increase would be affected by plastic strain. If k and n are allowed to be fitting parameters, then the resulting value for n should match closely with that for non-CW Alloy 690. As shown in Figure 3.40, the data are consistent with Equation 3.6, and the value of 0.412 calculated for n is in agreement with the expected value for non-CW alloy 690 (~40-50% uniform elongation).

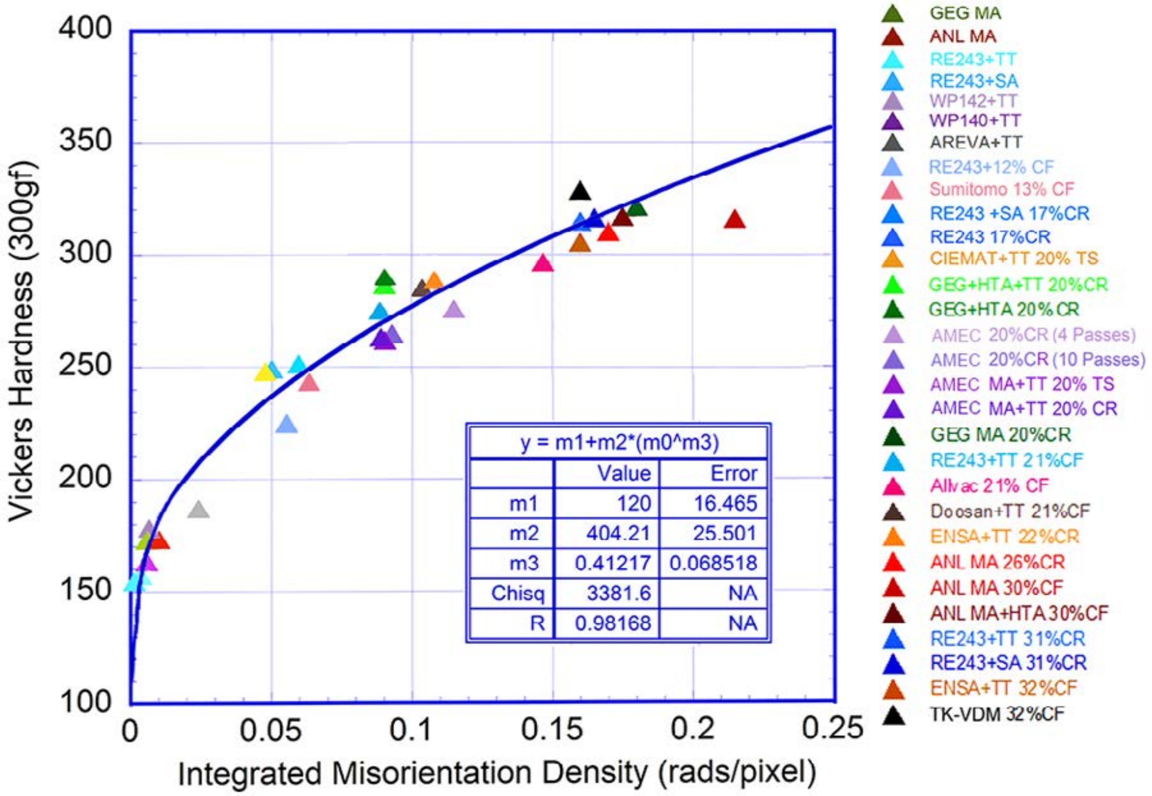

y = m1+m2*(m0^m3)

	Value	Error
m1	120	16.465
m2	404.21	25.501
m3	0.41217	0.068518
Chisq	3381.6	NA
R	0.98168	NA

Figure 3.40 Vickers hardness plotted against the integrated misorientation density (IMD) showing the expected square root dependence and calculation of the strain hardening exponent (m3 curve fit parameter listed in the plot)

Because the relationship in Equation 3.6 was shown to fit the IMD data very well, this implies that the measured IMD of the specimen should be linearly related to the total strain within the sample. Using this relation, IMD was plotted versus percent cold work as shown in Figure 3.41 with a straight-line fit to the data. Non-uniform spatial development of strain during cold working is very likely a strong contributor to the scatter around the trend line. However, differences in starting microstructure such as preexisting strain or a different microstructure that promotes more rapid development of strain for a given cold work level may also be contributing.

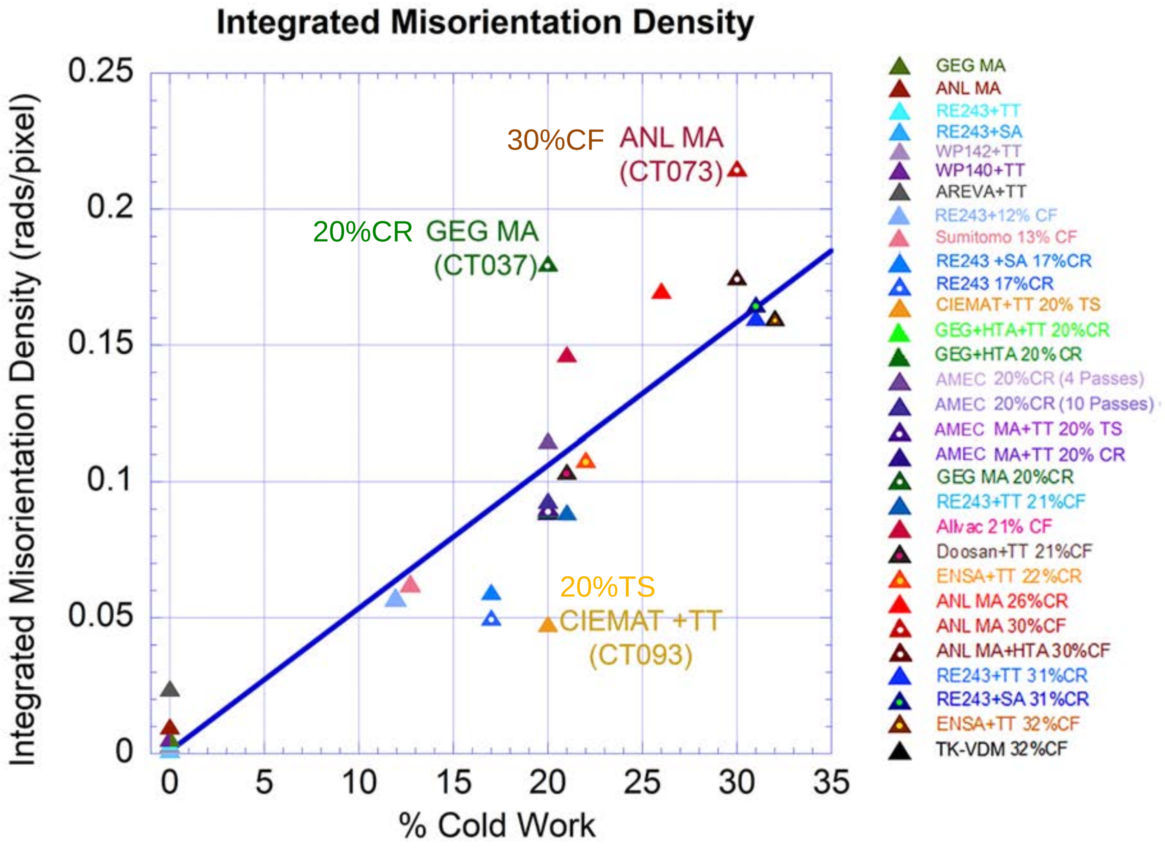

Figure 3.41 IMD is plotted against the %CW showing the expected linear dependence. Three specimens CT073, CT037 and CT093 were shown to deviate from the expected trend.

Three specimens were quite far from the trend line in Figure 3.41: CT037 (GEG MA + 20%CR), CT073 (ANL HTA + 30%CF) and CT093 (CIEMAT TT + 20%TS). The microstructures of these materials at the grain size level are compared in Figure 3.42 to specimens more closely matching the IMD vs CW trend line. An obvious difference for these three outlier materials is the grain size, specifically, the 30%CF ANL MA and the 20%CR GEG MA had much smaller grain size and were well above the trend line (higher IMD for a given level of CW) while the 20%TS Ciemat TT had a larger grain size and was well below the trend line. The implication is that grain size affects the rate of development of strain within the material as determined by IMD.

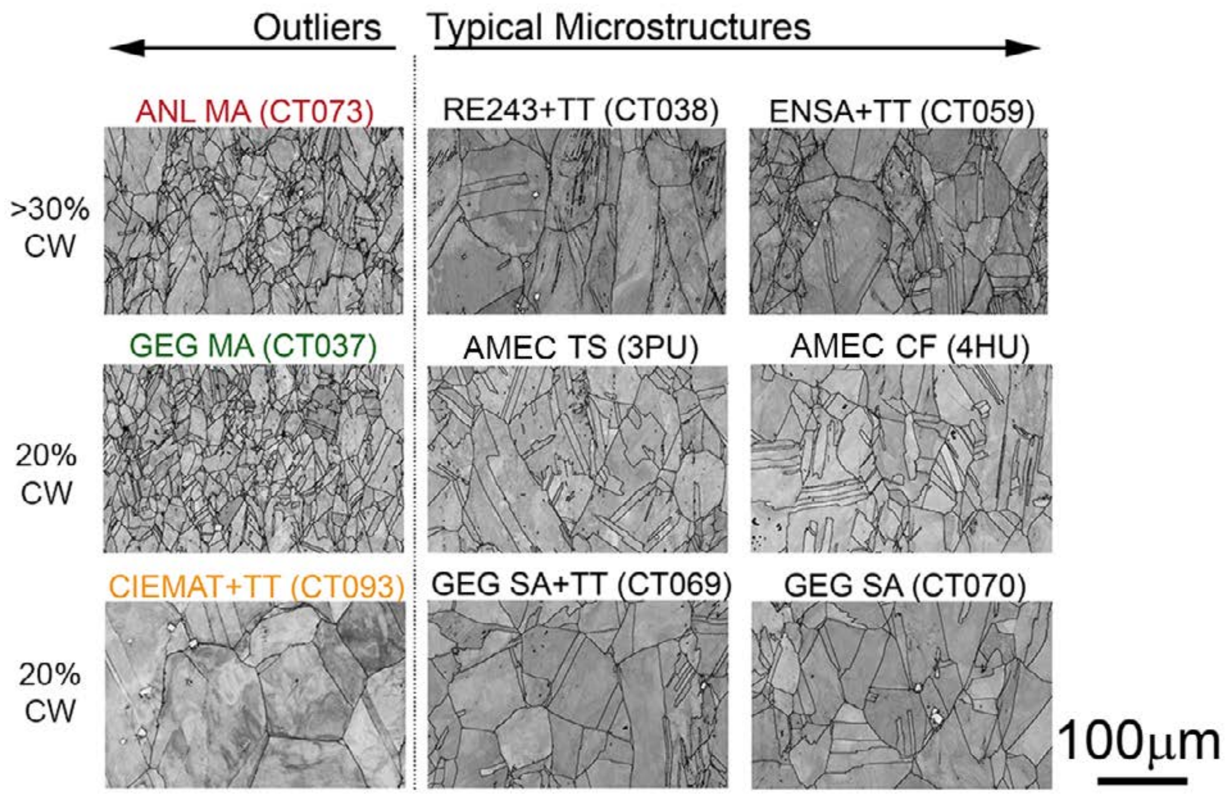

Figure 3.42 Outlier materials (left column) compared against typical microstructures/ grain sizes at the same level of cold work (center and right columns). The ANL and GEG specimens show smaller than average grain size while the CIEMAT material has a larger than typical grain size.

This concept that grain size is influencing the strain development is further supported by plotting the hardness as a function of the %CW as depicted in Figure 3.43. The trend line shown in this plot was produced by multiplying the trend line developed for hardness versus IMD (Figure 3.40) by the linear trend line developed for IMD versus cold work in Figure 3.41. The high degree of scatter is removed when the cold work x-axis, is replaced with the integrated misorientation density (Figure 3.40). The increased scatter seen when plotting hardness versus %CW illustrates how the CW can be a poor predictor of local material strain and damage. Specimens showing the strongest deviation in Figure 3.43 coincide with the specimens exhibiting grain sizes different from the average value.

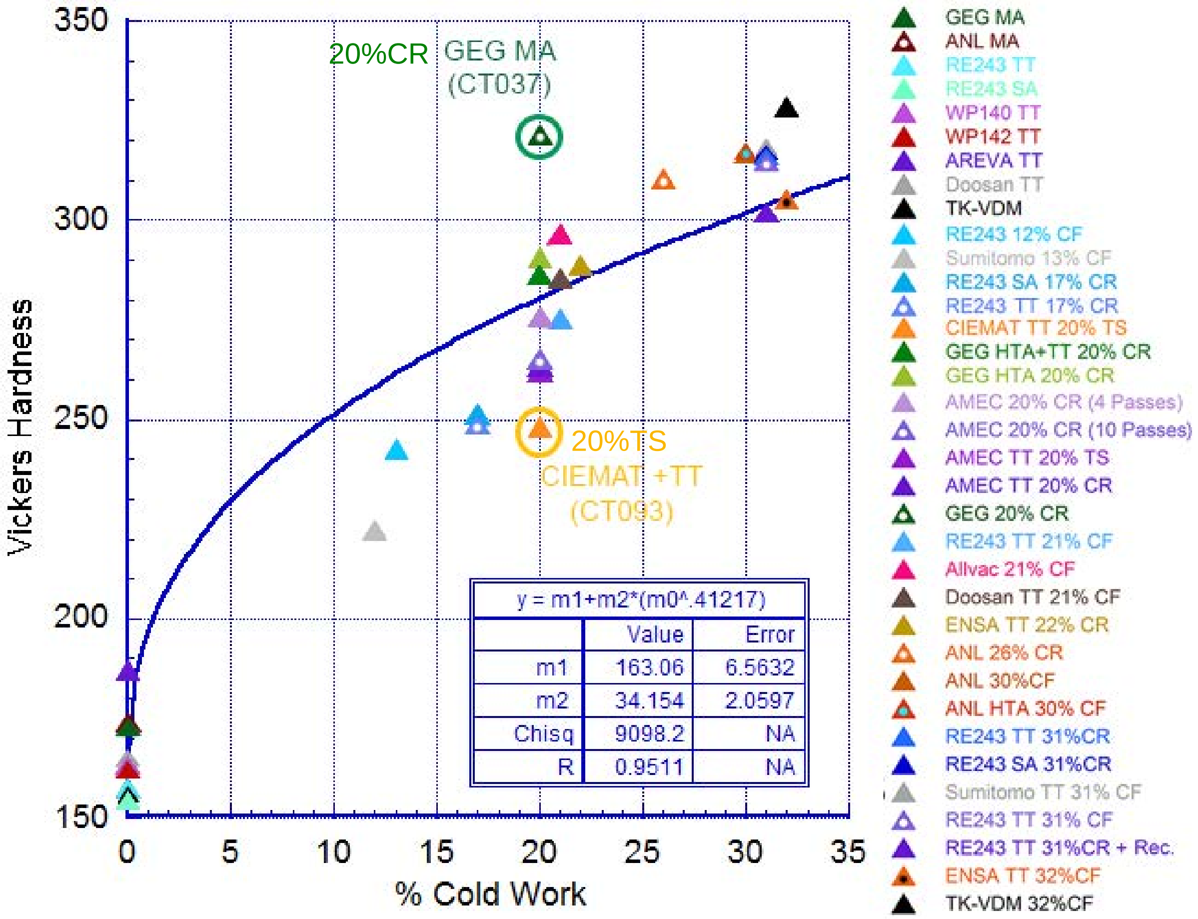

y = m1+m2*(m0^.41217)

	Value	Error
m1	163.06	6.5632
m2	34.154	2.0597
Chisq	9098.2	NA
R	0.9511	NA

Figure 3.43 **Hardness versus %CW shows poor agreement with the trend line. This illustrates a need for a parameter other than %CW when making correlations to strain and damage in a material.**

The results shown to this point are representative of data that was compiled from several different material heats, conditions, and microstructures. This analysis has resulted in the generation of a curve that indicates that IMD is an accurate measure of cold work induced strain. This is further reinforced by comparing IMD to cold work for a single material and single starting condition. The RE 243 TT materials are plotted in Figure 3.44 and show very little scatter around their predicted trend lines.

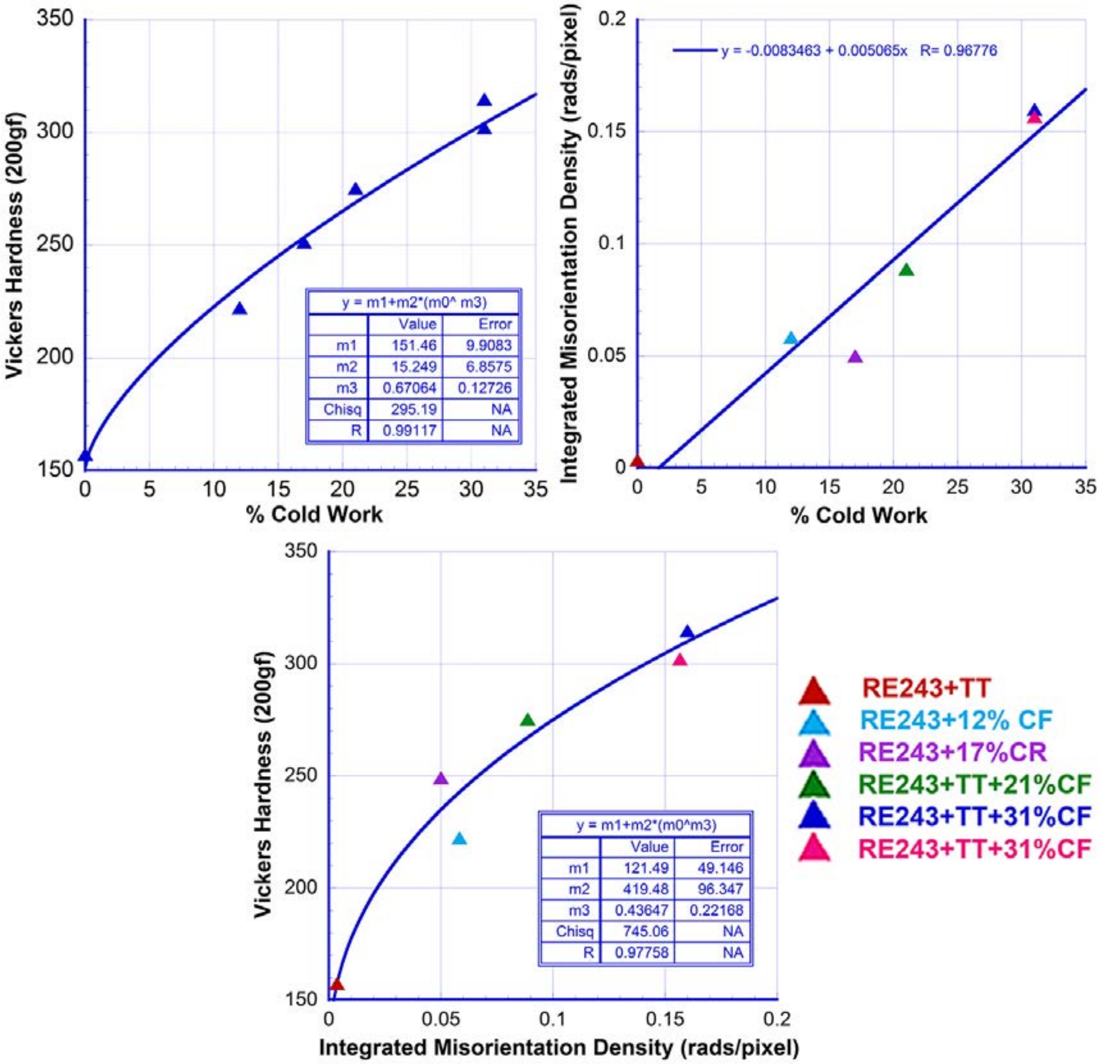

Figure 3.44 Hardness, %CW, and IMD plots for the subset of RE243 materials. Eliminating heat to heat and microstructural variance results in excellent agreement with the expected trends and illustrates a way to accurately assess damage in the 690 material.

In summary, EBSD and hardness results among Alloy 690 materials show that these methods provide important information for understanding how cold work and microstructure affect development of strain. Hardness mapping provides a measure of the average material strength while individual measurements can provide information about local variations within the microstructure. IMD obtained from EBSD misorientation data has been shown by others to be linearly proportional to strain on the grain size level, and the comparison of IMD to hardness in the present work reinforces the correlation to plastic strain assessment.

3.9 Analysis of Heat Affected Zone (HAZ) in Weld Specimens

EBSD mapping was performed across the heat affected zone on three alloy 690 specimens; CT067 (CIEMAT WP547 to alloy 52), CT086 (ANL NX3297HK12 to alloy 152) and CT087 (KAPL alloy 690 to alloy 52M). Samples were analyzed as a function of distance across the weld fusion line in an attempt to assess the level of strain in the vicinity of the HAZ. EBSD mapping conditions were altered slightly to allow for mapping of larger sample areas than was performed on the cold worked materials. The step size was maintained a constant 500 nm however SEM magnification was lowered from 250x to 150x for measurement of local misorientation. EBSD results from these three specimens are included in Figure 3.45-Figure 3.47. The measured local misorientation densities across the fusion line were on average very low, and consistent with the non-cold worked materials that were evaluated at the beginning of this chapter and are summarized in Table 3.8.

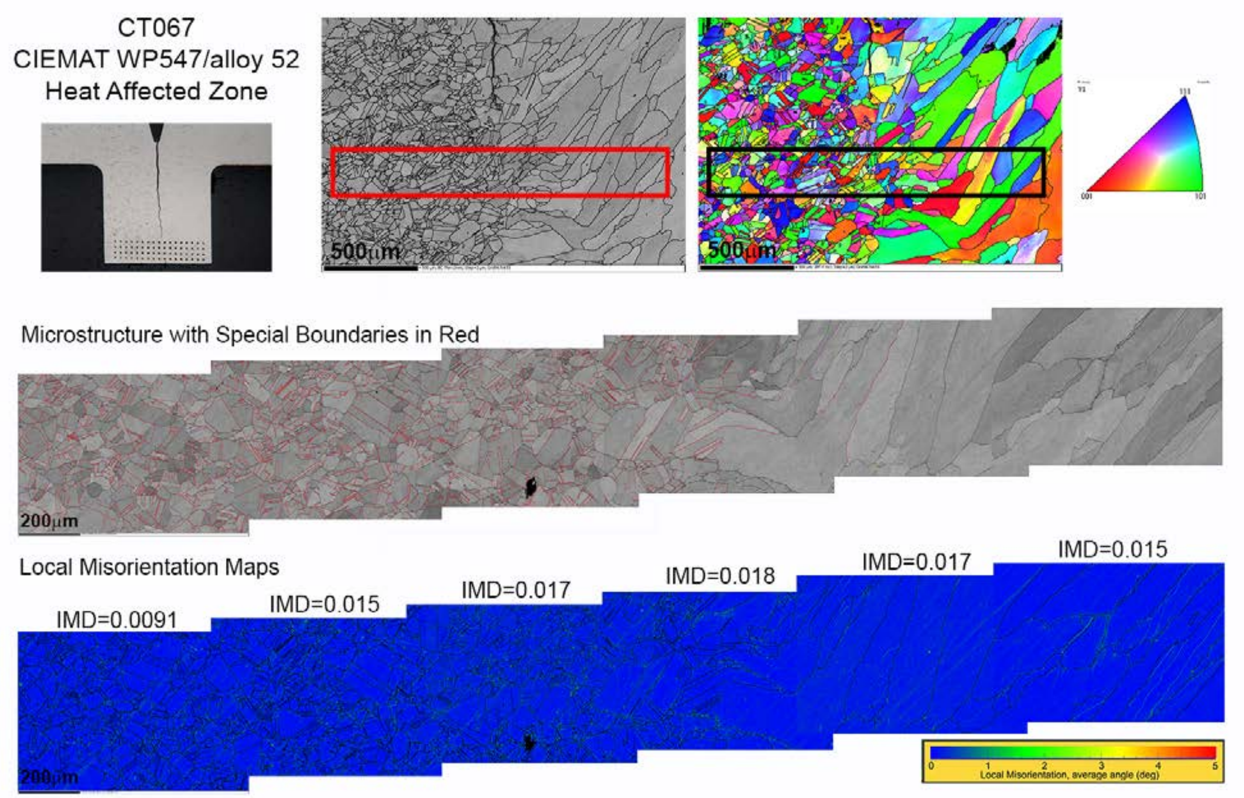

Figure 3.45 **EBSD results of the CT067 (WP547 to alloy 52) specimen weld indicate a very low local misorientation density across the weld fusion line. IMD values in rads/pixel are displayed above each of the maps shown and indicate the highest misorientation density is near the weld fusion line. Special boundaries (twinning) highlighted in red were shown to be present in the base metal and not the weld metal.**

Analysis of the CT087 specimen had to be performed across the crack tip due to geometric constraints and the absence of a significant amount of base metal material in other areas near the fusion line. For these reasons, mapping was performed using the parameters stated at the beginning of this section, but the resultant maps were divided in half for calculation of the IMD value in an effort to better elucidate the presence of strain gradients in the sample. The results shown in **Figure 3.46** indicate that strain in the weld metal increases very slightly moving away from the fusion line. The boundary region between weld metal and base metal shows a significant and steady increase in the local misorientation density, however due to the proximity of the crack tip it is difficult to attribute this increase to the presence of the weld interface or distortions caused from crack propagation. The degree of twinning in the base metal was observed to decrease in the vicinity of the fusion line.

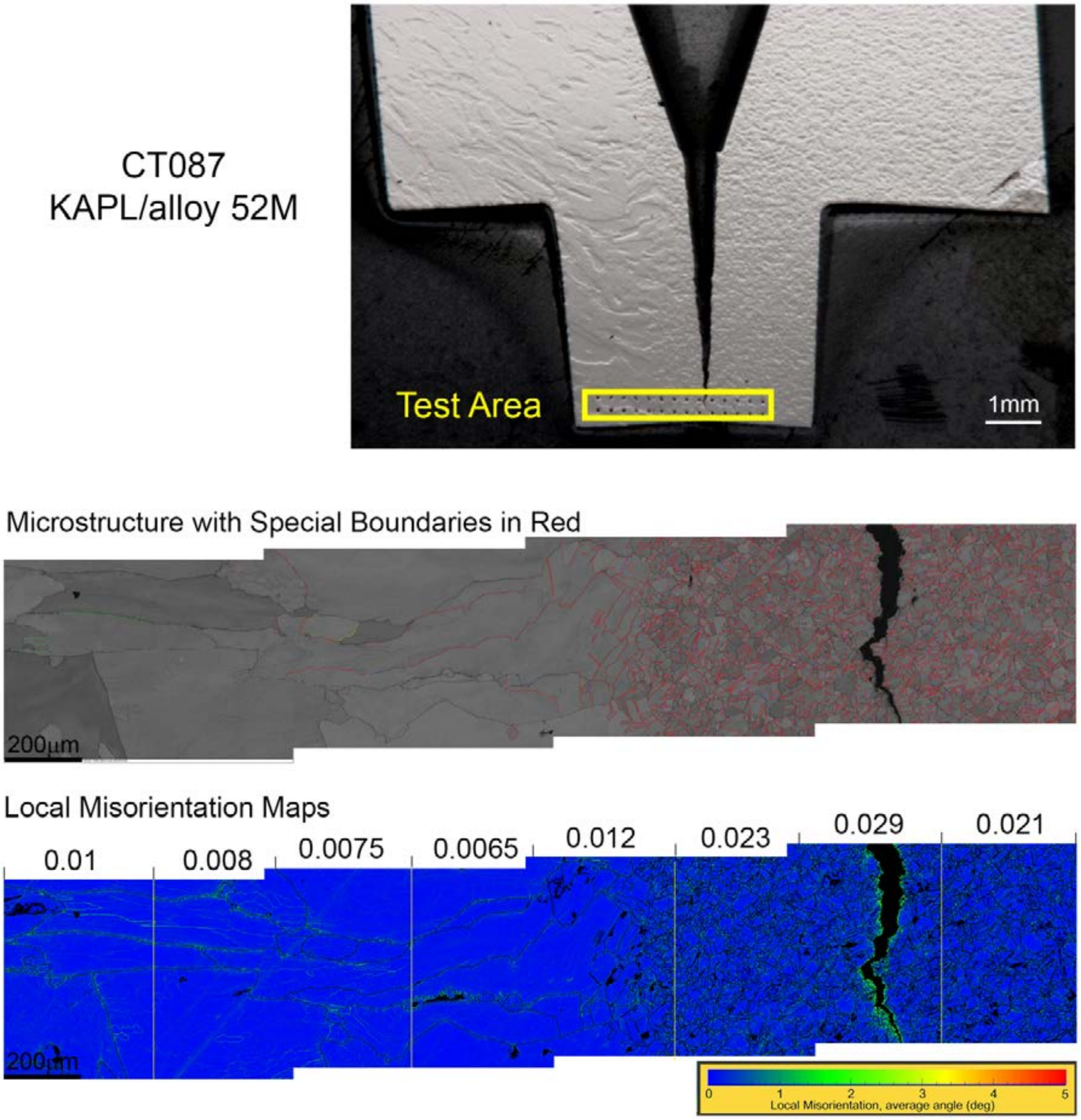

Figure 3.46 Results of the CT087 specimen (KAPL/alloy 52M) weld shows similar results to that of the CT067 specimen. Local misorientation values were well below 1 degree. Changes in misorientation are indicated above the local misorientation map.

The final weld sample analyzed was CT086 (ANL alloy 152). The IMD values for this specimen also coincided with that of non-cold worked material. Maximum strains in the base metal were seen in a mapped region centered approximately 0.6 mm from the fusion line. Damage in the weld metal was also shown to increase moving away from the fusion line. It should be noted that the gradients measured on all of these materials are very minor and are on the order of the standard deviations measured from the non-cold worked alloy 690, which was approximately 0.001 rads/pixel.

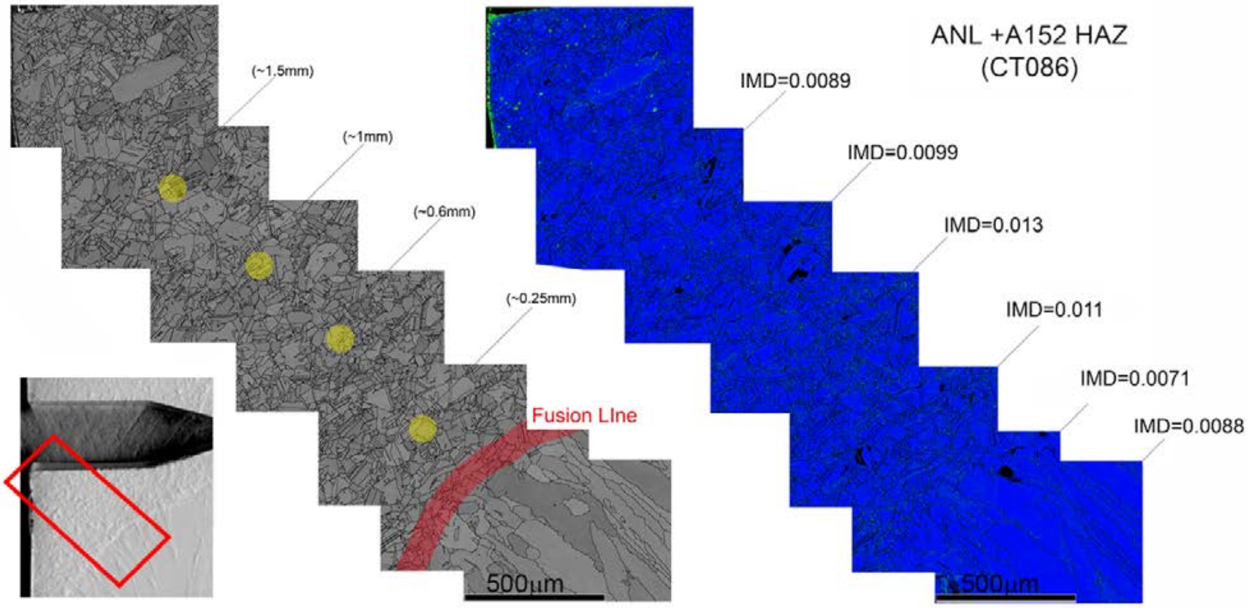

Figure 3.47 **EBSD results of the ANL alloy 152 specimen showing very low integrated misorientation density comparable to that of the non-cold worked alloy 690 condition. IMD values are indicated next to the image used for their calculation and are measured in rads/pixel. Gradients over the area shown are very minor.**

In addition to EBSD measurements, Vickers hardness testing was also performed across the fusion line for these three specimens. Results from hardness testing are compared in Figure 3.48-Figure 3.50. Similar to the EBSD results, hardness gradients were minimal. Decreases in hardness were seen in the weld metal which was likely a result of the significant grain size difference between the weld and base metal. The base metal showed less variability in hardness across all the welds that were measured.

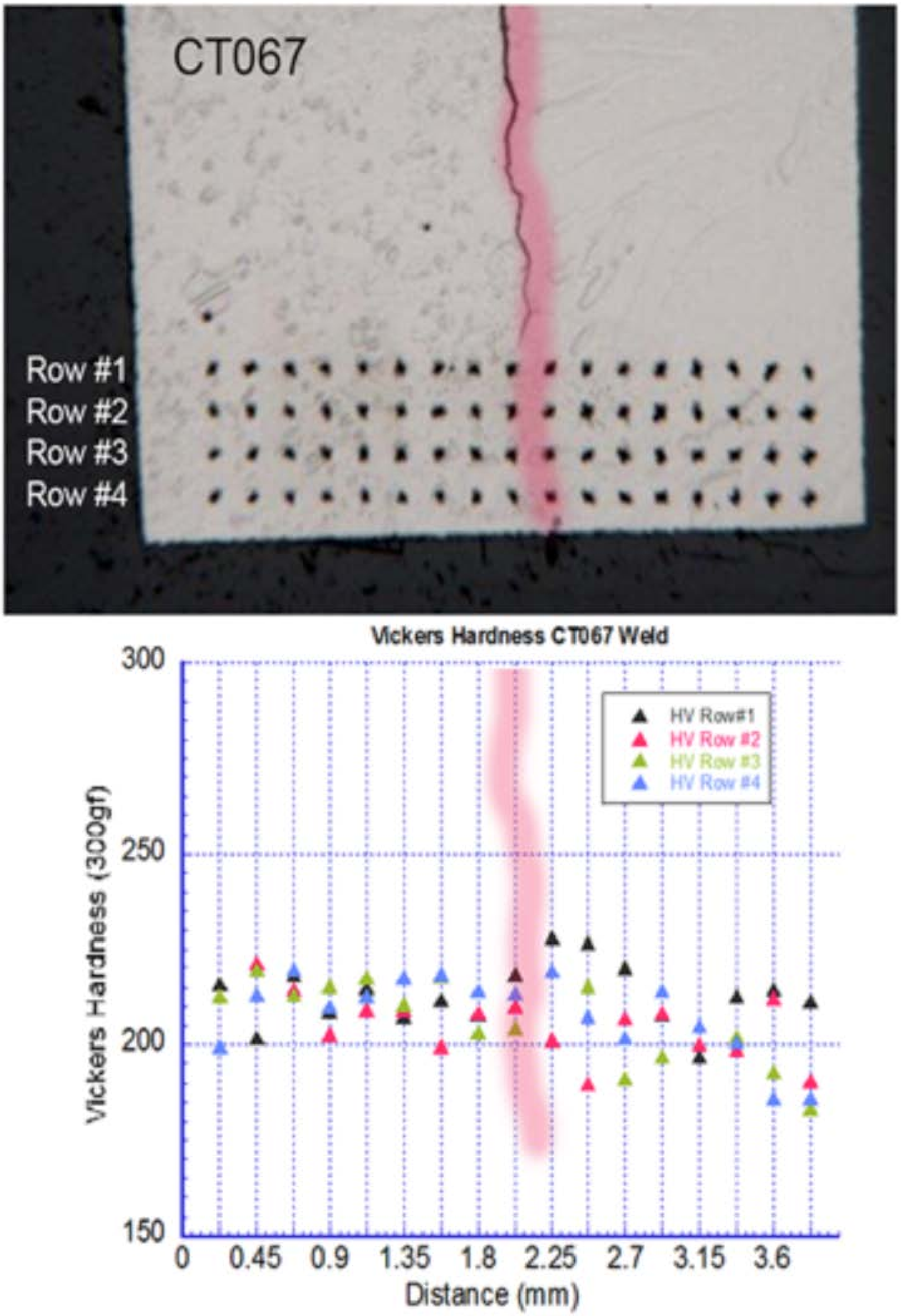

Figure 3.48 Hardness plots as a function of distance across the fusion line for CT067. The pink line denotes the location of the fusion line. Hardness results show that variation is higher in the weld metal (right side of fusion line).

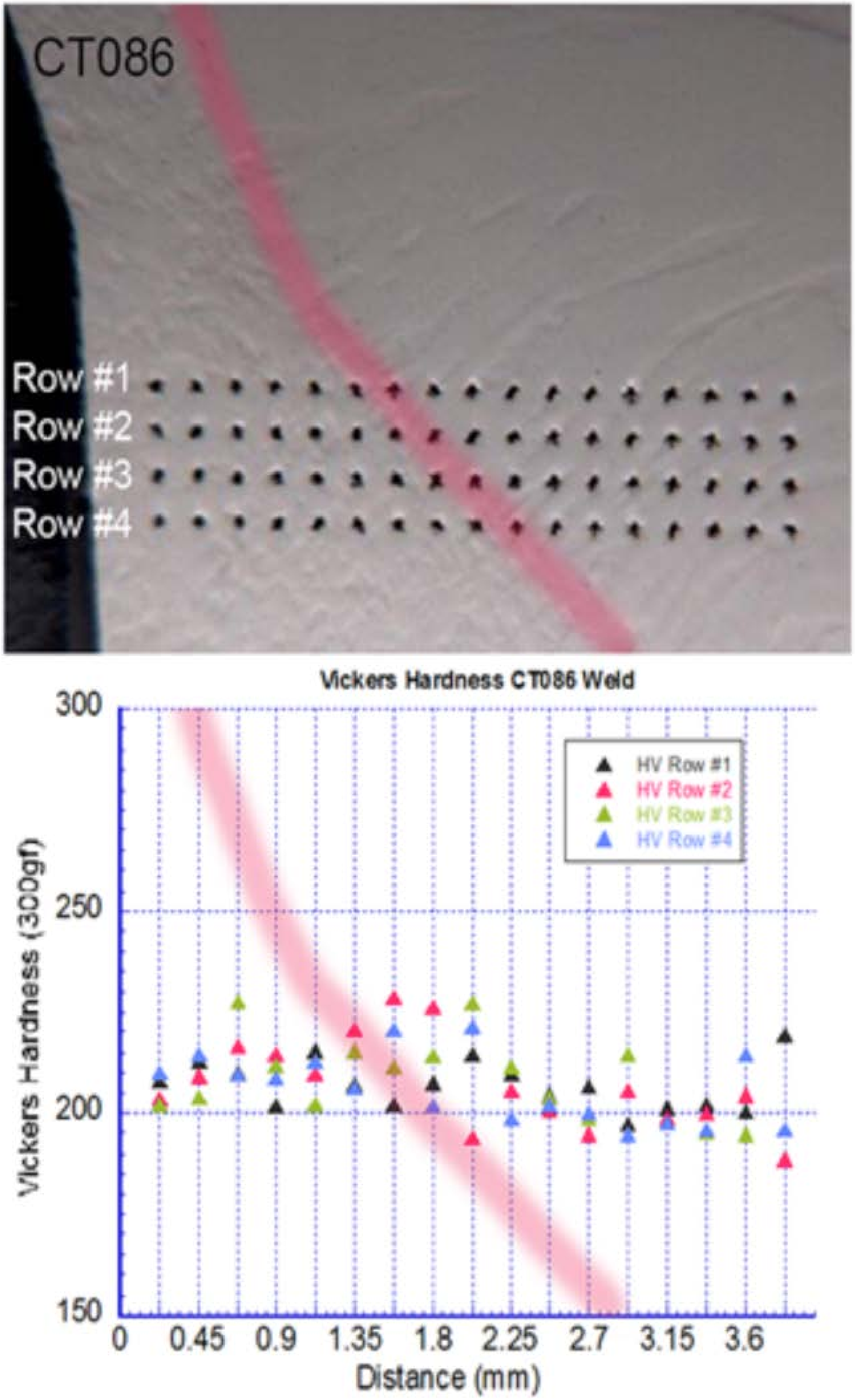

Figure 3.49 Hardness plots as a function of distance across the fusion line for CT086. The pink line denotes the location of the fusion line. Hardness results show that variation is higher in the weld metal (right side of fusion line).

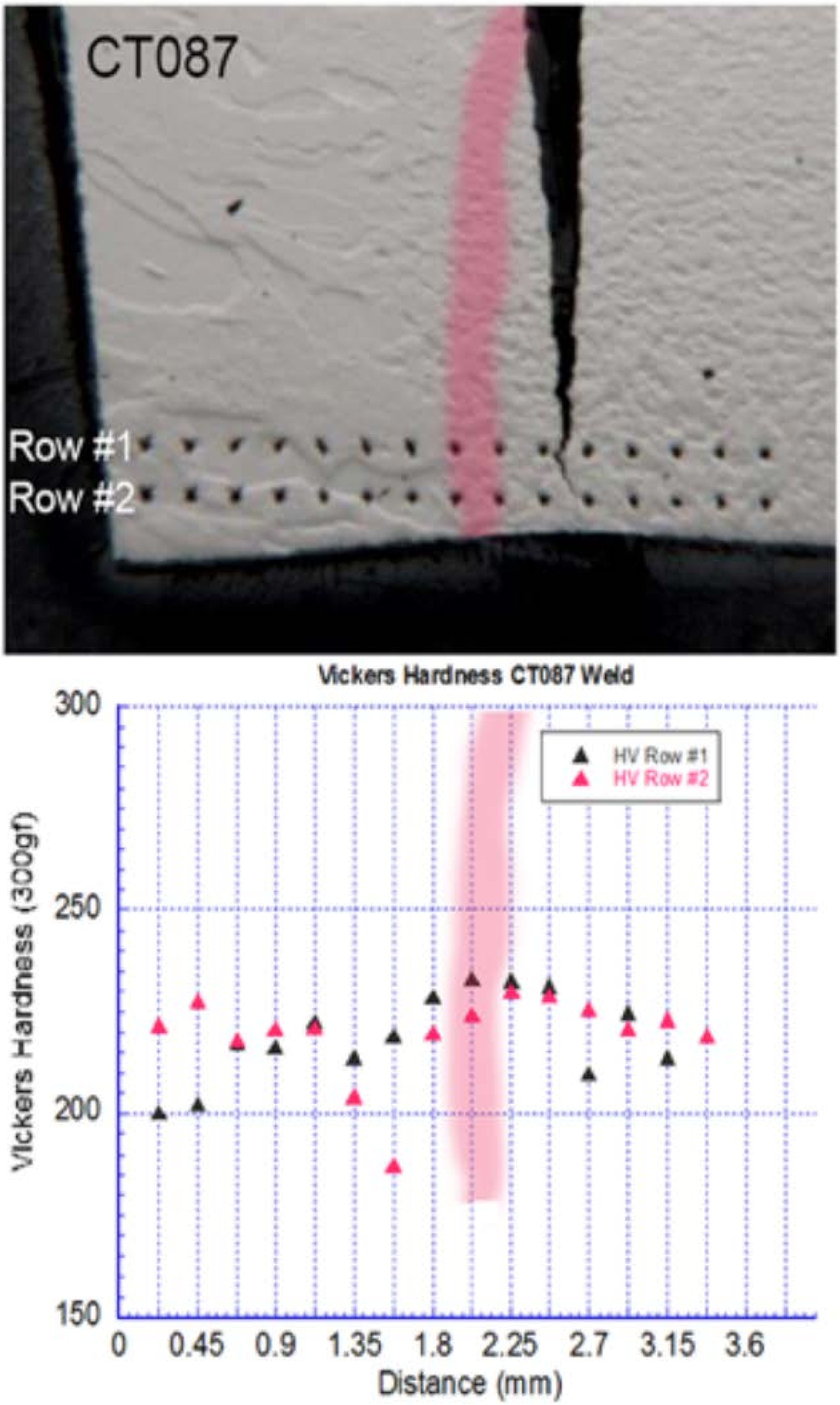

Figure 3.50 Hardness plots as a function of distance across the fusion line for CT087. The pink line denotes the location of the fusion line. Hardness results show that variation is higher in the weld metal (left side of fusion line).

In summary, IMD values in the HAZ regions of the three specimens were found to be ~0.01-0.02 rads/pixel while hardness values were ~200-230 kgf/mm^2. For comparison, Table 3.10 contains data presented previously in this chapter on hardness and IMD of as-received and low cold worked alloy 690. As can be seen, the HAZ IMD values fall within the high range of that for as-received material, and the HAZ hardness is somewhat higher than non-CW material. The HAZ hardness is estimated to correlate to ~10% CW alloy 690.

Table 3.10 Hardness and IMD of low cold worked alloy 690 specimens

Cold Work	ID	Sample Information	Average HV (kgf/mm^2)	Average IMD (rads/pixel)
0% CW	**B25K-2C**	B25K MA	173.0	0.0056
	ANL	ANL MA	173.2	0.0100
	CT014	RE 243 TT	157.4	0.0036
	CT015	RE243 SA	154.7	0.0013
	CT026	WP142 TT	162.6	0.0039
	CT027	WP140 TT	163.4	0.0057
	CT058	AREVA TT	187.0	0.024
	CT107	Doosan TT	164.8	0.013
	CT108	TK-VDM TT	155.6	0.007
12-17% CW	**CT104**	RE243 TT + 12%CF	222.3	0.0583
	CT103	Sumitomo TT + 13%CF	242.2	0.064
	CT068	RE243 SA + 17%CR	251.3	0.0595
	CT054	RE243 TT + 17%CR	249.1	0.050

4 SCC CRACK-GROWTH TESTING ON ALLOY 690 CRDM MATERIALS

4.1 Chapter Overview

This chapter covers SCC testing on the CRDM materials with test specimen information summarized in Table 4.1. The Doosan TK-VDM heat was in a solid bar geometry, while the other heats were in tube geometry. Results on the specimens listed in gray were reported in a previous NUREG in this series [6,7], so only summary results on these materials will be presented here. For the new tests, the Valinox heat RE243 continued to be a key material. Retests were conducted on the 17%CR material, this time at 360°C. Additional tests were conducted on 11.6%, 21%, 31%CF material, and a test was also conducted on 31%CR material that was given a “recovery” heat treatment at 700°C. Several other CRDM materials were also tested including another Valinox heat that had been 20% tensile strained (TS), the Sumitomo heat in the 12.7% and 31%CF conditions, and the Doosan TK-VDM heat in the as-received and 21%CF conditions. Results will first be presented on the Valinox RE243 TT heat in order of increasing cold work.

Table 4.1 Alloy 690 CRDM SCC test specimens covered in this chapter. Specimens listed in gray were previously reported in the prior NUREG [6,7].

ID	Source/Producer	Heat #	Form	Treatment	HV (kgf/mm^2)
CT026	Valinox/Valinox	WP142	Tube	TT*	163
CT027	Valinox/Valinox	WP140	Tube	TT*	163
CT015	Valinox/Valinox	RE243	Tube	TT*	155
CT104	Valinox/Valinox	RE243	Tube	TT*+11.6%CF S-L/S-T	222
CT020	Valinox/Valinox	RE243	Tube	TT*+17%CR S-L	256
CT054	Valinox/Valinox	RE243	Tube	TT*+17%CR S-L	249
CT100	Valinox/Valinox	RE243	Tube	TT*+21%CF S-L/S-T	275
CT022	Valinox/Valinox	RE243	Tube	TT*+30%CR T-L	305
CT038	Valinox/Valinox	RE243	Tube	TT*+31%CR S-L	315
CT099	Valinox/Valinox	RE243	Tube	TT*+31%CF S-L/S-T	302
CT053	Valinox/Valinox	RE243	Tube	TT*+31%CR S-L+RT‡	274
CT014	Valinox/Valinox	RE243	Tube	TT*+SA†	157
CT019	Valinox/Valinox	RE243	Tube	TT*+SA+17%CR S-L	245
CT068	Valinox/Valinox	RE243	Tube	TT*+SA+17%CR S-L	251
CT023	Valinox/Valinox	RE243	Tube	TT*+SA+30%CR T-L	291
CT039	Valinox/Valinox	RE243	Tube	TT*+SA+31%CR S-L	316
CT093	CIEMAT/Valinox	WP787	Tube	TT*+20%TS	248
CT103	EPRI/Sumitomo	E67074C	Tube	TT*+12.7%CF S-L/S-T	242
CT098	EPRI/Sumitomo	E67074C	Tube	TT*+31%CF S-L/S-T	318
CT108	EPRI-Doosan/TK-VDM	133454	Bar	TT*	156
CT102	EPRI-Doosan/TK-VDM	133454	Bar	TT*+21%CF S-L/S-T	285

* As-received, thermally treated condition of the material
† 1100°C/1h + Water Quench
‡ Recovery Treatment (RT) - 700°C/1 h + Air Cool

4.2 SCC Tests on Valinox RE243 CRDM Alloy 690TT Materials

4.2.1 Crack Growth Testing of 11.6%CF Valinox RE243 Material - CT104

For all Valinox CRDM specimens in the CF condition, blocks of material were cut from tubing and were forged in the direction of the tubing z-axis. The specimens were oriented so that the crack plane normal was parallel to the forging direction. Relative to the tubing, the specimens were in the L-R orientation as indicated in Figure 4.1. For comparison, the CR S-L specimens were prepared so that the roller-to-roller direction was the tubing theta plane, and the specimen test orientation relative to the tubing was the C-L orientation.

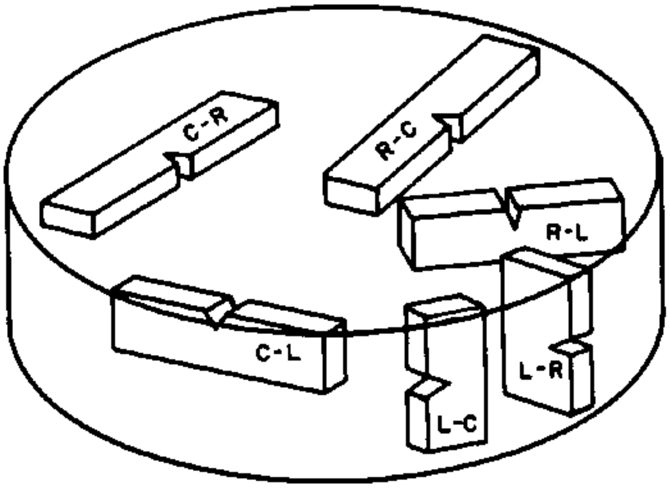

Figure 4.1 Possible CT specimen orientations in the tube/rod C-L-R notation system

As with all the tests covered in this report, the 11.6%CF Valinox RE243 specimen was tested in series with a second specimen, in this case a 12.7%CF Sumitomo CRDM specimen. Data on the Sumitomo specimen are reported in Section 4.3. A summary of test conditions and specimen response for the Valinox specimen are given in Table 4.2, while an overview plot of the entire test is provided in Figure 4.2. The test was started with a standard transitioning sequence that runs through 0.1 Hz, 0.01 Hz, 980s/20s (rise/fall), 980s/20s + 2.5-hour hold (at K_{max}), and finally reaching constant K. All the cyclic loading steps had a load ratio, R, of 0.5 unless otherwise noted. For the first constant K observation (shown in Figure 4.3), the specimen exhibited a CGR of ~$1.7x10^{-9}$ mm/s over a period of ~600 hours, falling between what has been observed for this heat in the as-received and 17%CR S-L conditions.

Table 4.2 Test conditions and specimen response for the 11.6%CF Valinox RE243 alloy 690TT specimen, CT104

								CT104 A690 VX CRDM 11..6% CF Heat RE243		
Test Step	Start (h)	Duration (h)	R	Freq (Hz)	Hold (h)	Dissolved Hydrogen (cc/kg H_2)	Temp (°C)	Kmax (MPa√m)	CGR (mm/s)	Approx. Crack Extension (mm)
1	0	8	0.5	0.1	0	25	360	30	4.2E-06	0.100
2	8	35	0.5	0.01	0	25	360	30	7.4E-07	0.101
3	43	227	0.5	980s/20s	0	25	360	30	1.4E-07	0.114
4	270	241	0.5	980s/20s	2.5	25	360	30	1.9E-08	0.014
5	511	167	0.5	980s/20s	2.5	25	360	30	1.9E-08	0.013
6	678	553	---	const K	---	25	360	30	1.7E-09	0.004
7	1231	237	0.5	980s/20s	2.5	25	360	30	1.6E-08	0.012
8	1468	672	0.5	9980s/20s	0	25	360	30	1.9E-08	0.041
9	2140	311	0.5	9980s/20s	2.5	25	360	30	1.3E-08	0.016
10	2451	1054	---	const K	---	25	360	30	4.2E-09	0.014
11	3505	289	0.5	9980s/20s	2.5	25	360	30	1.9E-08	0.024
12	3794	130	0.5	9980s/20s	0	25	360	30->37	NM	0.036
13	3924	104	0.5	9980s/20s	0	25	360	37	5.9E-08	0.026
14	4028	185	0.5	9980s/20s	2.5	25	360	37	3.1E-08	0.025
15	4213	608	---	const K	---	25	360	37	5.9E-09	0.012
16	4821	172	0.5	9980s/20s	2.5	25	360	37	3.9E-08	0.020
17	4993	102	0.5	9980s/20s	2.5	25	360	37->42	NM	0.030
18	5095	232	0.5	9980s/20s	2.5	25	360	42	4.3E-08	0.041
20	5327	1026	---	const K	---	25	360	42	8.6E-09	0.031

NM = Not measured

After the first constant K observation, the same cycle+hold loading condition that was used just prior to constant K was reapplied to check for the presence of any untracked crack extension that can be hidden by ligament or contact formation behind the crack front. (This issue and approach to resolve was discussed in Section 2.3.) After confirmation of no untracked crack extension, it was decided to apply alternate transitioning conditions. A pure cyclic loading step of 9980s/20s was used in place of the 980s/20s + 2.5-h hold step (Figure 4.4). Both have the same overall cycle time, but the crack-tip dynamic strain rate is reduced by a factor of 10. This is thought to be advantageous for resistant materials where too fast of a cyclic loading rate may inhibit transitioning to IGSCC. If an improvement in transitioning occurs, the CGR would be expected to increase. The two cyclic loading conditions produced essentially identical CGRs suggesting no improvement in SCC transitioning. However, this alternate cyclic loading frequency was maintained to determine if there was any impact on constant K response.

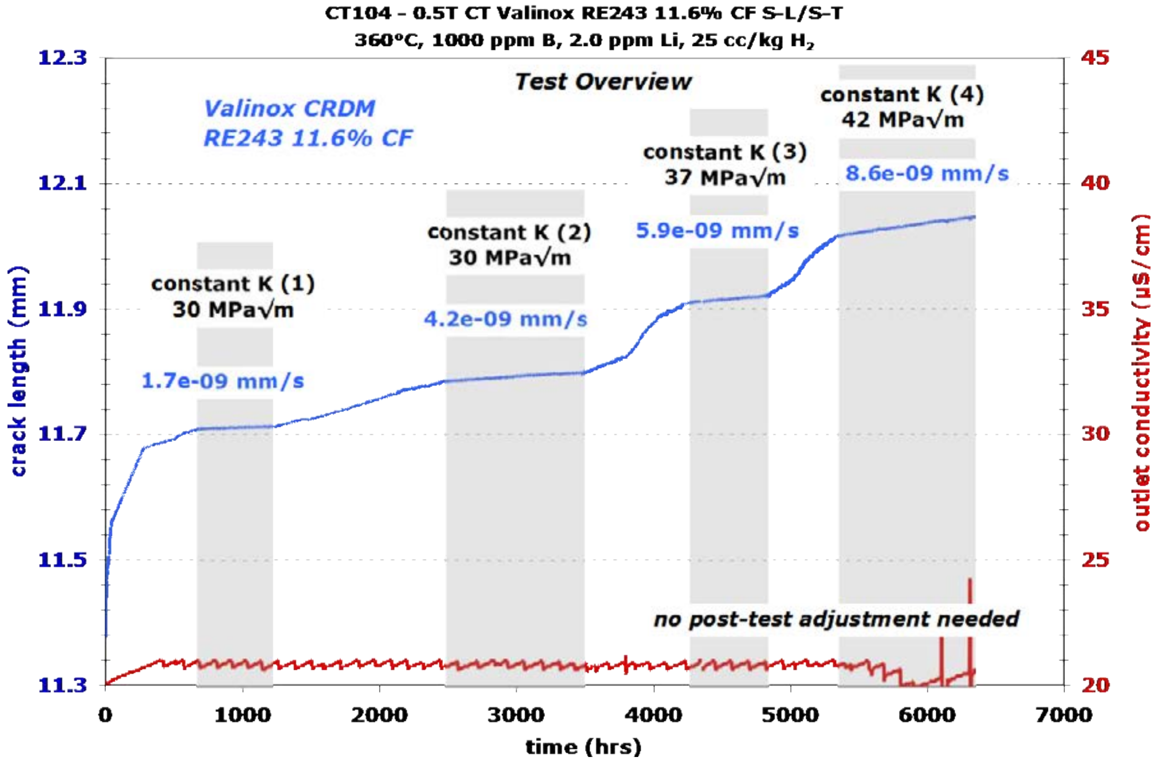

Figure 4.2 Overview of the entire SCC test on the 11.6%CF Valinox RE243 alloy 690TT specimen CT104

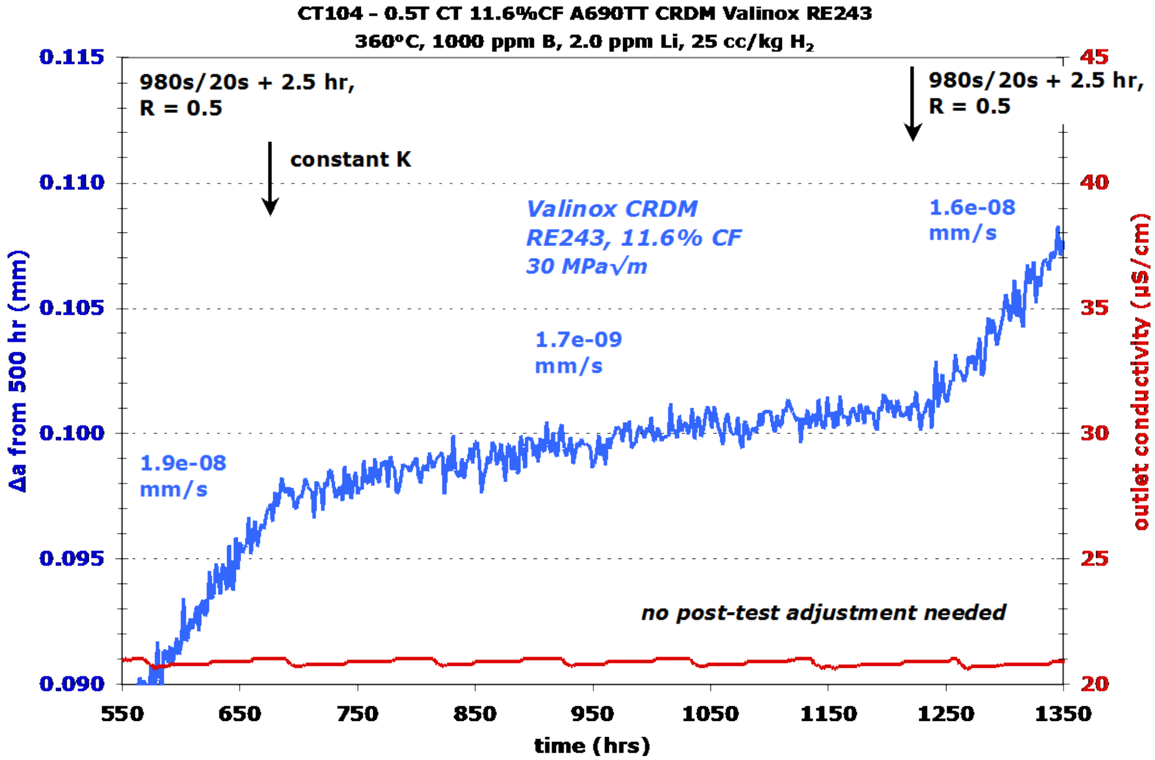

Figure 4.3 Crack growth response for the 11.6%CF Valinox RE243 specimen CT104 during the first constant K observation

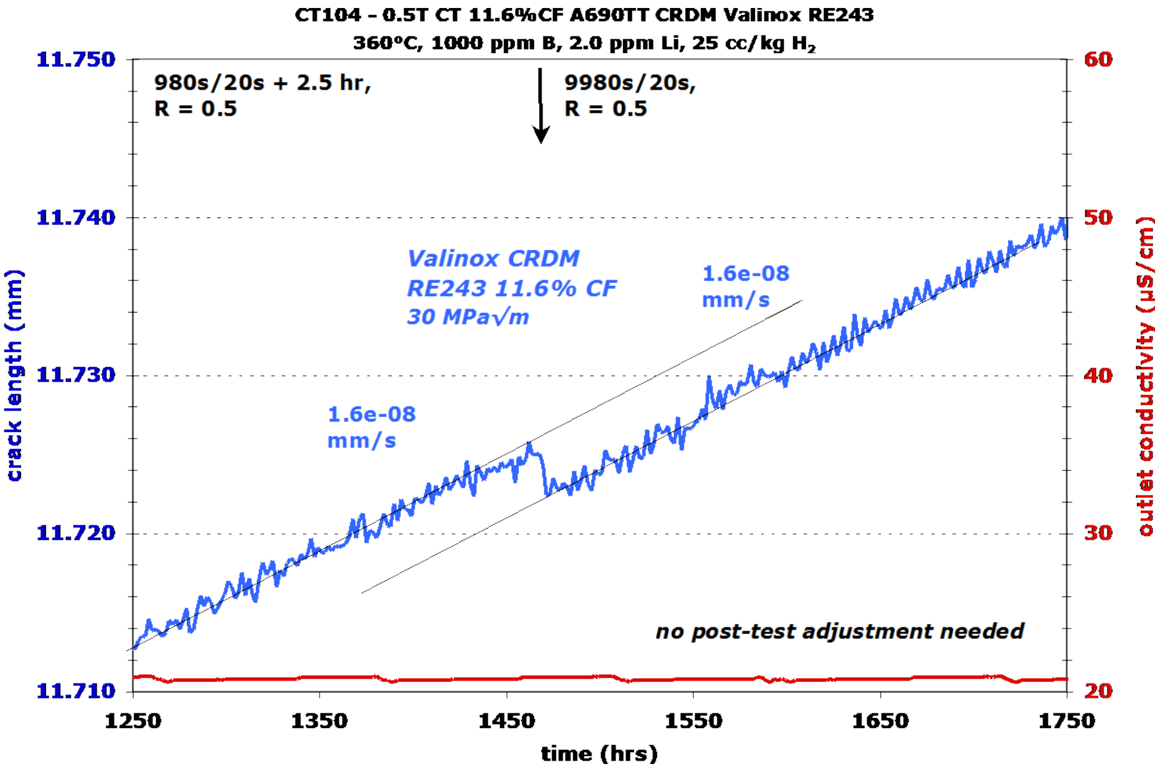

Figure 4.4 Similar transitioning CGRs obtained for cycle+hold and pure cyclic loading with both conditions having the same overall cycle time of 10,000 seconds

A 2.5-h hold was added to the 9980s/20s cyclic load for about 300 hours, and then the test was converted to constant K for the second time with the response shown in Figure 4.5. Somewhat surprisingly, a steady propagation rate of ~4x10^{-9} mm/s was obtained and persisted for the entire ~1000 hour observation period, producing ~15 µm of crack extension. This CGR is as high as that obtained in this material when it was tested in a 17%CR S-L condition. At the end of the observation period, cycle+hold loading was reapplied producing a similar CGR to that before the constant K observation, indicating little or no ligament/contact formation and no untracked crack extension. The higher CGR suggests that the lower crack-tip strain rate in the 9980s/20s cycle was more effective at improving IG engagement, but it could also simply be that more transitioning was needed and that if the same steps were performed with a 980s/20s load cycle, the higher constant K CGR would have been obtained. Nevertheless, the 9980s/20s load cycle for the final transitioning steps was retained for the remainder of the test and has been applied to several other tests to help clarify its effectiveness.

As part of the planned studies on cold worked materials, the next phase of the test was to examine the effect of stress intensity on SCC CGRs. Stress intensity was increased to 35 MPa√m by dK/da over ~40 µm of crack extension during continuous cyclic loading at 9980s/20s. After steady response was established at 35 MPa√m for this cyclic loading condition, a 2.5-h hold was added for ~20 µm of crack extension, and then the test was converted to constant K. A steady propagation rate of 5.9x10^{-9} mm/s, approximately 1.5x higher than at 30 MPa√m, was observed over 600 hours with no indication of untracked crack growth. Stress intensity was increased a second time to 42 MPa√m following this same methodology. The propagation rate settled at ~9x10^{-9} mm/s (2x higher than at 30 MPa√m) during the subsequent constant K observation as shown in Figure 4.6. These higher rates appear to be due to the higher K, but it is also possible that the additional transitioning produced a higher degree of IG engagement influencing the SCC CGR. After a ~1000 hour constant K observation, the test was ended and the specimen was sectioned up for post-test examination.

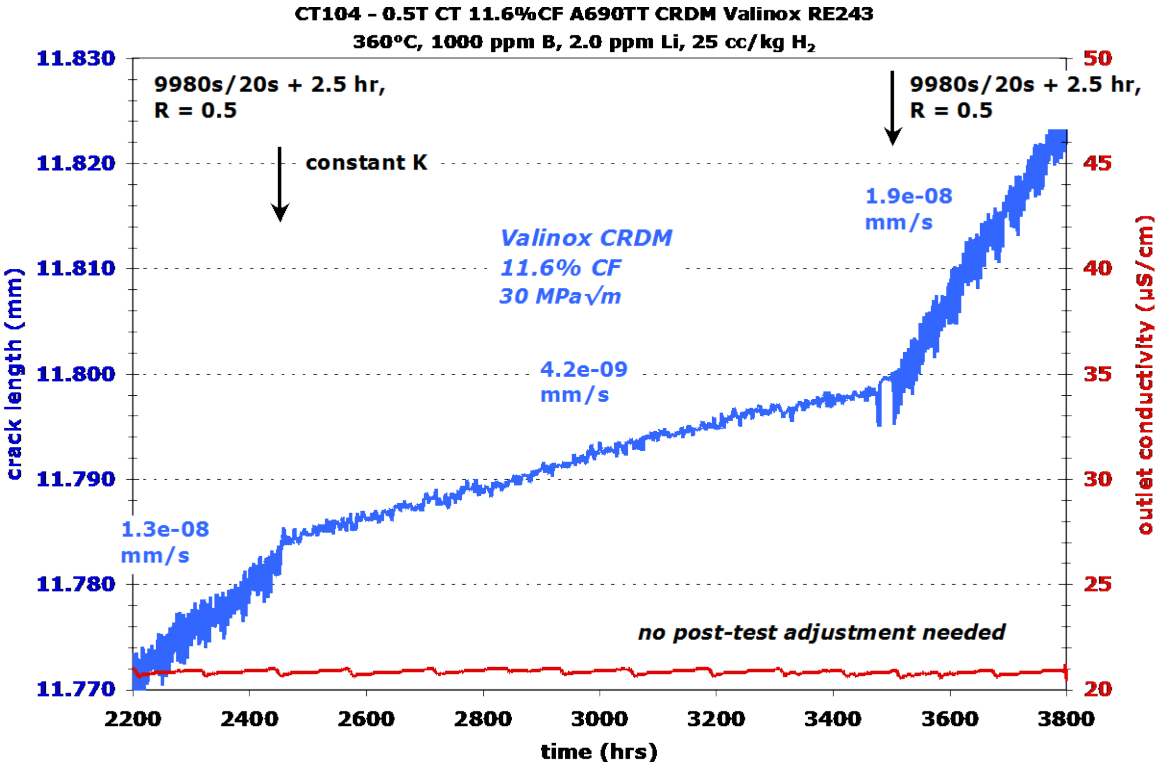

Figure 4.5 **Crack growth response for the 11.6%CF Valinox RE243 specimen CT104 during the second constant K observation**

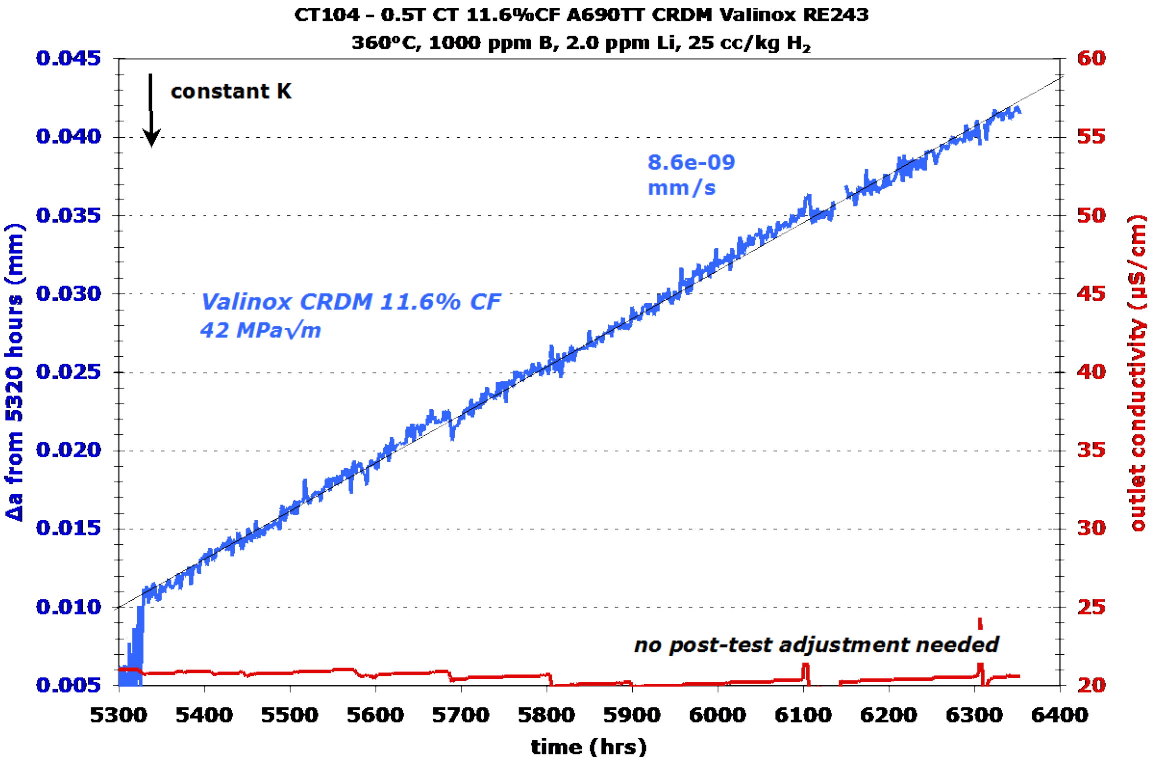

Figure 4.6 Crack growth response for the 11.6%CF Valinox RE243 specimen CT104 during the fourth and final constant K observation that was at 42 MPa√m

Following the prescription outlined in Chapter 2, the specimens were cut into 1/3-2/3 pieces, and the 2/3 piece was fatigued open for crack surface observation. Comparison of the DCPD crack length to the observed crack length in the optical image in Figure 4.7 shows that DCPD over predicted the actual <u>average</u> crack extension by 15% (although the <u>maximum</u> in-situ crack extension slightly exceeded the DCPD crack extension). This small over prediction in the average crack length means that the actual CGRs were ~15% lower.

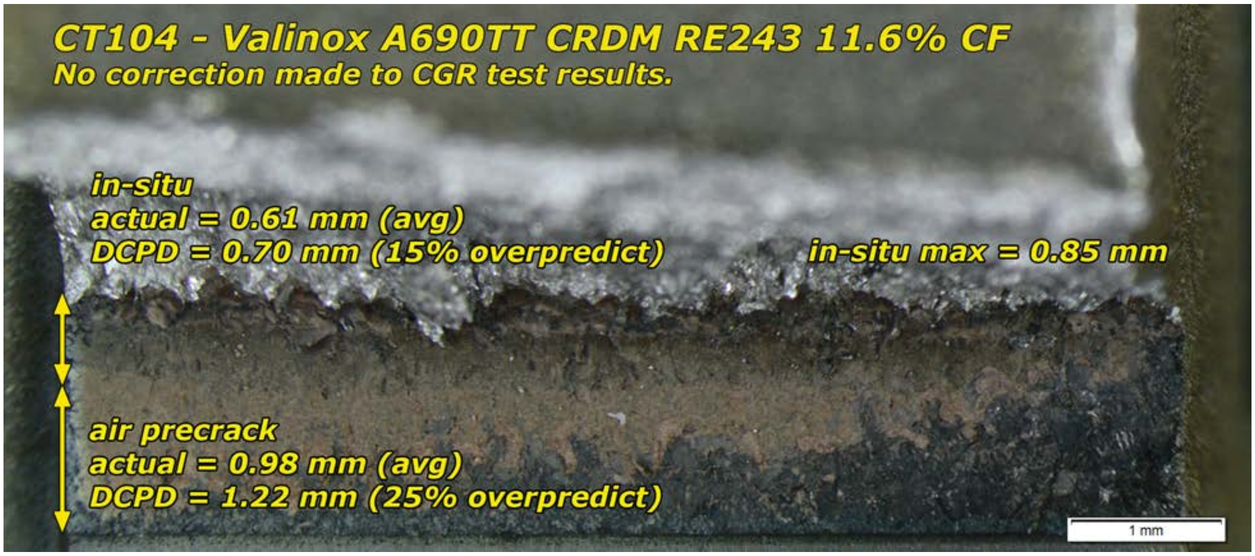

Figure 4.7 Optical image of the as-tested crack growth surface of the 11.6%CF Valinox RE243 specimen

SEM examinations are presented in Figure 4.8 and Figure 4.9. The SEM-BSE image clearly shows the final crack front location, while the SE image better defines the IG regions. The crack front is predominantly IG (found to be ~80%) with only a few pockets of TG morphology. Several measurements along the crack front suggest an average IG crack extension of ~250 µm. On the overall crack growth plot in Figure 4.2, this roughly correlates back to the start of the 9980s/20s load cycling at ~1200 hours when accounting for the ~15% over prediction of crack extension in the plot. Attempts to measure IG engagement behind the final crack front can be challenging because the shape of the crack front as it passed this location is not precisely known. However when a straight line is drawn at the estimated location of the second SCC observation (~200 µm behind the final crack front), IG engagement was estimated at ~37%. These observations of higher IG engagement at higher K levels agree well with the higher SCC CGRs measured.

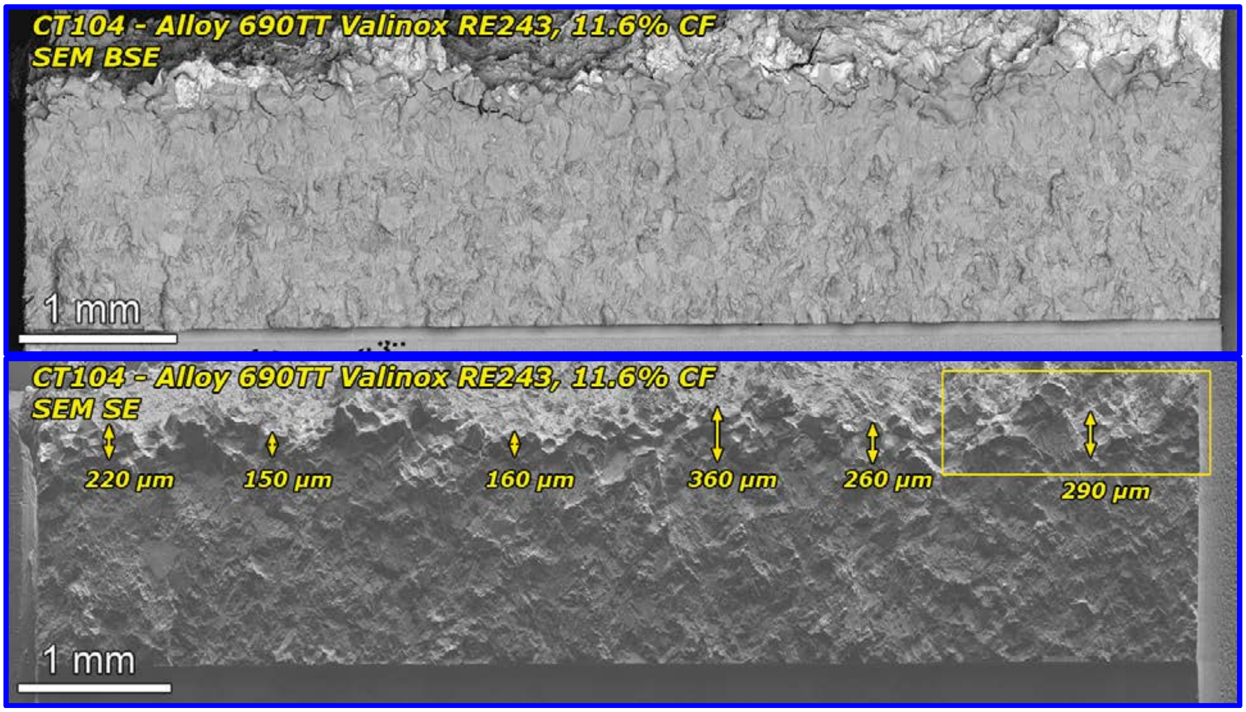

Figure 4.8 **Overview SEM images of the cleaned (sonicated) crack growth surface of the 11.6%CF Valinox RE243 specimen (CT104) in SEM SE and SEM BSE imaging modes. The boxed region is shown at greater magnification in Figure 4.9.**

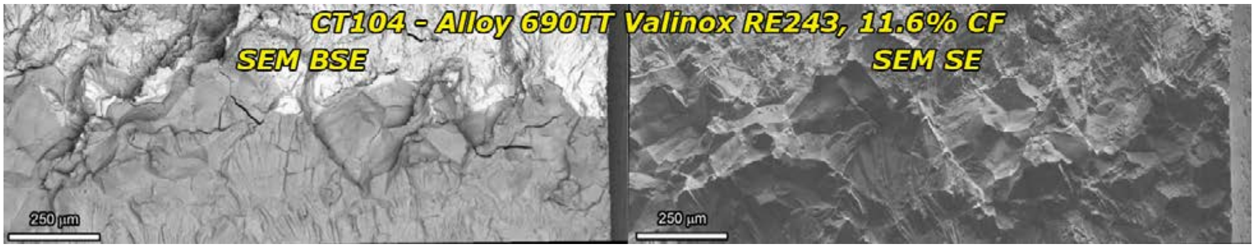

Figure 4.9 **Higher magnification images of CT104 showing the IG nature near the crack front**

4.2.2 Crack Growth Testing of 17%CR S-L Valinox RE243 Material - CT054

This specimen was tested in series with a TT+31%CR S-L specimen (CT053) that was given a dislocation recovery heat treatment (RT). Test results on the RT specimen are presented later in this section. A summary of test conditions and specimen response for the 17%CR S-L specimen are given in Table 4.3, while an overview plot of the entire test is provided in Figure 4.10. As indicated in the table and plot, only a single transitioning sequence followed by a single constant K observation was performed. Transitioning consisted of running through 0.1 Hz, 0.01 Hz, 0.001 Hz, 980s/20s and 980s/20s + 2.5-hour hold (at K_{max}). The cycle+hold step was maintained for ~30 µm which represents roughly 1/3 of a grain diameter for this material. Steady crack advance was observed during this final transitioning step and during the subsequent constant K observation as shown in Figure 4.11. Constant K was maintained for ~900 hours accumulating ~7 µm of DCPD-indicated crack advance. The propagation rate decreased slightly during constant K from $3.3x10^{-9}$ mm/s to $2.2x10^{-9}$ mm/s. This response was reasonably consistent with a previous test (CT020) on this 17%CR S-L material at 325°C that produced CGRs of $<1x10^{-9}$ mm/s in multiple constant K observations, so the test was ended and the specimen was sectioned for examination.

Table 4.3 Test conditions and specimen response for the 17%CR S-L Valinox alloy 690TT CRDM RE243 specimen CT054

								CT054 A690 TT+17% CR S-L		
Test Phase	Start (h)	Duration (h)	R	Freq (Hz)	Hold (h)	Dissolved Hydrogen (cc/kg H_2)	Temp (°C)	Kmax ($MPa\sqrt{m}$)	CGR (mm/s)	Approx. Crack Extension (mm)
1	0	18	0.5	0.1	0	25	360	30	3.8E-06	0.270
2	18	102	0.5	0.01	0	25	360	30	6.9E-07	0.250
3	120	215	0.5	0.01	0	25	360	30	1.0E-07	0.080
4	335	124	0.5	980s/20s	0	25	360	30	1.0E-07	0.060
5	459	479	0.5	0.001	2.5	25	360	30	1.3E-08	0.024
6	938	877	---	const K	---	25	360	30	2.2E-09	0.007

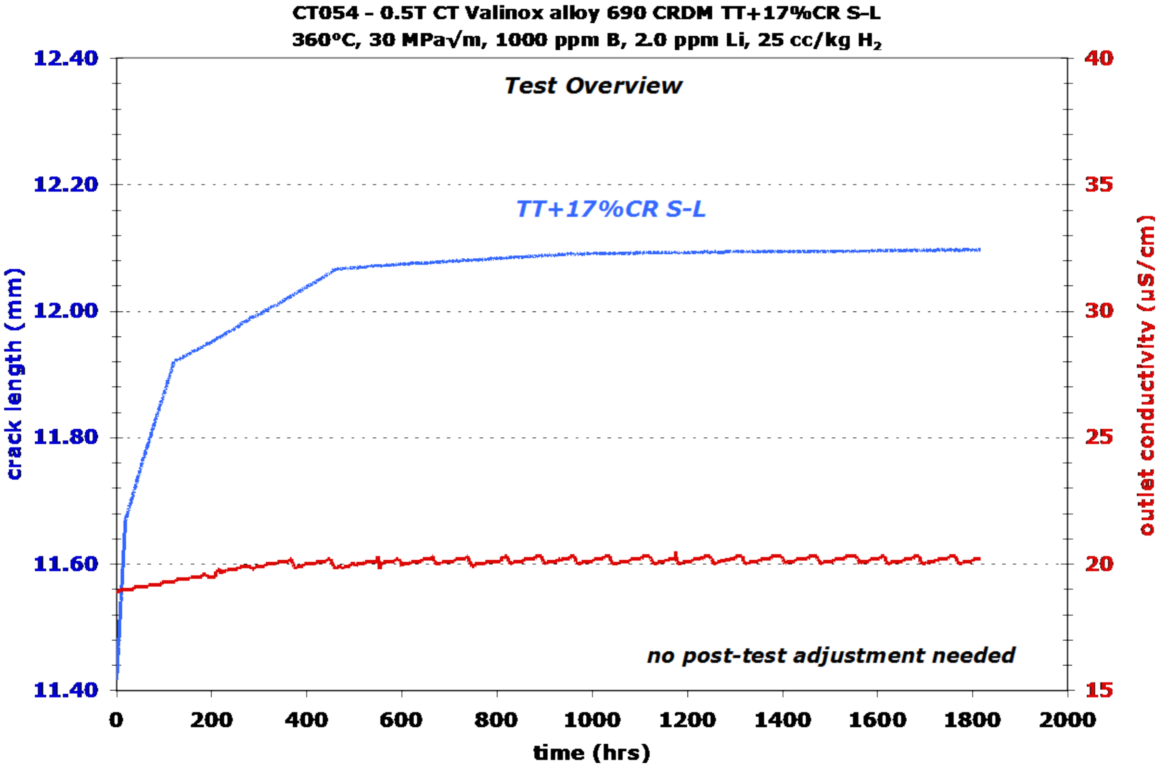

Figure 4.10 Overview of the entire SCC test on the 17%CR S-L Valinox RE243 specimen CT054

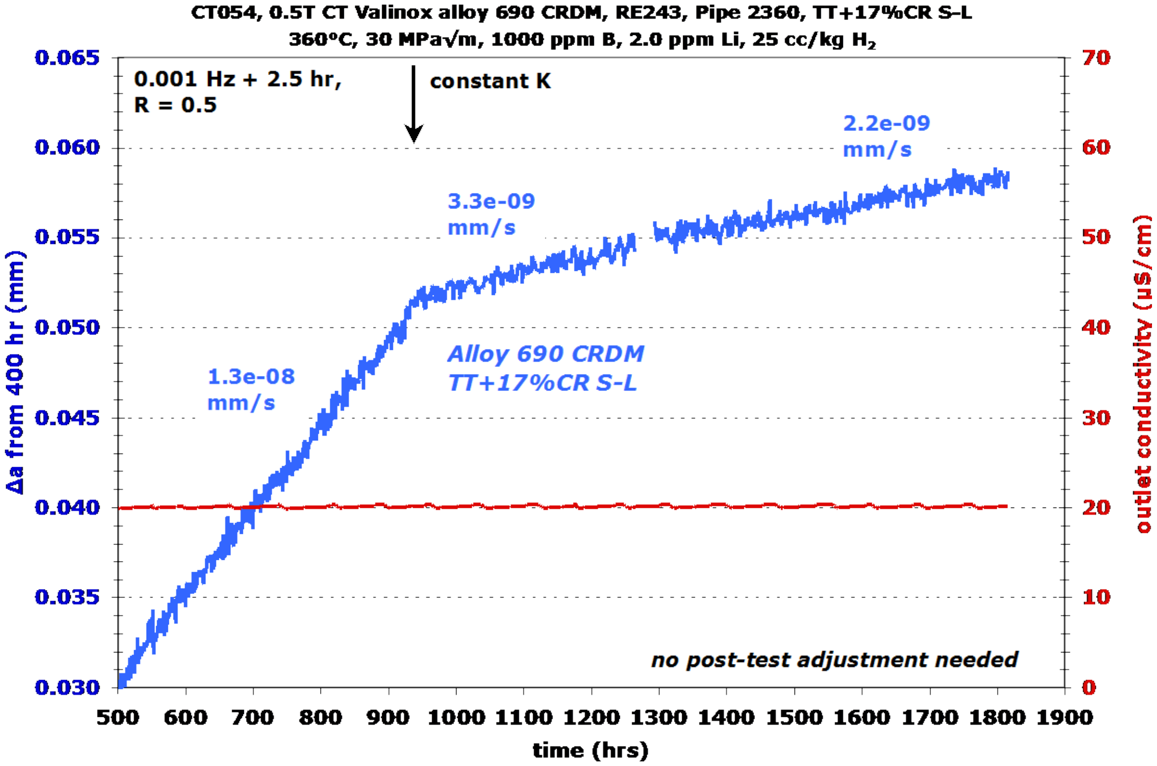

Figure 4.11 Constant K response of the 17%CR S-L Valinox RE243 specimen

An optical image of the entire unsonicated crack-growth surface is shown in Figure 4.12. Precracking was readily distinguished from the testing in water, but there were no obvious defining features to allow further subjugation of the crack growth behavior. An unusual aspect of this crack growth surface is that a few IG protrusions were apparent along the final crack front. These protrusions are highlighted in the SEM-BSE image in Figure 4.13. The crack front was found to be ~18% IG engaged, much less than the 11.6%CF specimen CT104 which was >90% engaged. There are a number of possible reasons for this difference. The hardness (Table 3.6) of the 11.6%CF specimen was slightly lower than the 17%CR specimen, but the EBSD data (Table 3.8) suggest slightly higher strains in the 11.6%CF, so in aggregate these data suggest the two materials were similar in strength and strain. However, there are several differences in how the tests were run. The 11.6%CF specimen was subjected to multiple transitioning sequences over a large amount of crack extension, more gentle crack-tip loading rates were used for most of the test and K was progressively increased throughout the test. If the 17%CR S-L had been subjected to the same sequences, it is not unreasonable to assume that similar levels of engagement would have been achieved.

A challenging aspect of this crack front is determining during what phases of the testing these protrusions formed and extended. Prior testing experience indicates that susceptible alloy 690 will develop significant IG engagement during 0.001 Hz (or 980s/20s) + 2.5-h hold loading step. It is thought that these IG protrusions advanced faster than the TG portions of the crack front during this loading step, and then continued to advance during constant K testing.

Crack surface measurements and comparison to the DCPD-based crack length data revealed that DCPD under predicted actual crack extension during pure cyclic loading by just 6-7% for both air precracking and in-situ transitioning. No unambiguous correction could be determined for the cycle+hold and constant K phases. The primary issue is that the amount of actual crack extension during cycle+hold could not be identified. However for the purpose of discussion, the average total IG advance was calculated and compared to the constant K extension. The average total IG advance was determined by calculating the area of all the IG regions along the crack front and dividing by the width of the observed crack front. By this measurement, there was 12 µm of IG advance. If this occurred entirely during constant K, the DCPD correction would be 1.7x. Since some fraction of the IG extension was thought to occur during cycle+hold, the correction factor is certain to be much less and is likely to be very close to 1x. With the available information, it has been assumed that DCPD accurately tracked the constant K crack extension for this test.

The SCC propagation rates between the 11.6%CF (CT104) and 17%CR (CT020 and CT054) specimens can also be compared. While the highest CGR that was obtained for the 11.6%CF specimen was 8.6x10^{-9} mm/s, this was later in the test at 39 MPa√m after substantial transitioning. The first constant K observation at 30 MPa√m was preceded by nearly identical transitioning steps as for the 17%CR specimen CT104 and produced a 1.7x10^{-9} mm/s CGR that is comparable to what was observed for the 17%CR specimen CT054. It is reasonable to presume that similar CGRs to the 11.6%CF later in the test may have been obtained if the same transitioning steps and K increases had been followed. Similar CGRs may have also been obtained in the 17%CR specimens if multiple transitioning attempts had been performed at 30 MPa√m.

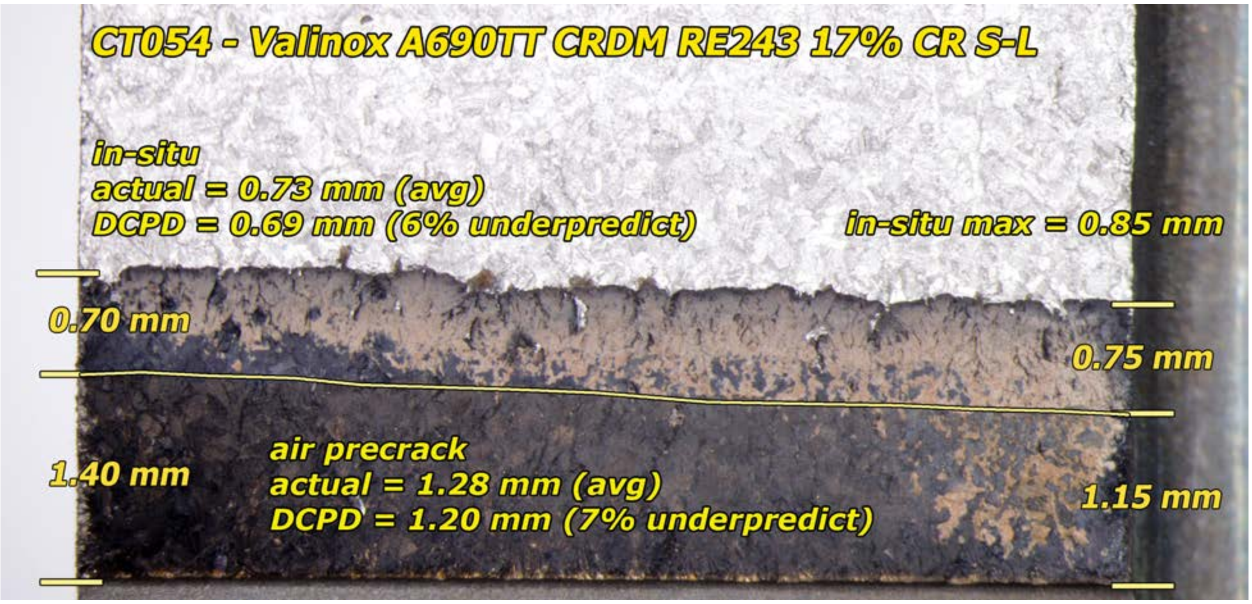

Figure 4.12 Optical image of the as-tested crack growth surface of the 17%CR S-L Valinox RE243 specimen, CT054.

Figure 4.13 SEM-BSE image of the crack front for the 17%CR S-L Valinox RE243 specimen, CT054. (A) and (B) show the crack front with and without boxes that denote the location of IG protrusions along the crack front. Crack front was 18% engaged.

4.2.3 Crack Growth Testing of 21%CF S-L/S-T Valinox RE243 Material - CT100

A summary of test conditions and specimen response for the 21%CF specimen are given in Table 4.4, while an overview plot of the entire test is provided in Figure 4.14. This specimen was tested in series with a TT+20%TS specimen with test results presented later in Section 4.4.

Five constant K observations were performed for this test that covered K values of 30-31, 38, and 45-46 MPa√m. Stress intensity was increased by a dK/da method covering at least 30 µm of crack extension. The final transitioning step before switching to constant K was 980s/20s (R=0.5) + 2.5-h hold. Crack extension during each constant K assessment was at least 50 µm except for the first observation that was only 17 µm. Application of cycle+hold loading after constant K, such as presented in Figure 4.15, reveal a temporarily accelerated CGR indicating contact or ligament formation during constant K. Adjusted SCC propagation rates based on this jump in crack length were 1.5-2x higher than DCPD-indicated CGRs. As indicated in the table and overview plot, the unadjusted SCC propagation rates show a monotonic increase with K while the adjusted values suggest little or no effect of K. The magnitude of the DCPD CGRs are on the high end for a material in a ~20%CW condition, but are consistent with the response for this material in the 11.6%CF and 31%CF/CR conditions.

Table 4.4 Test conditions and specimen response for the 21%CF S-L/S-T Valinox alloy 690 CRDM RE243 specimen CT100

								Valinox A690TT RE243 21% CF S-L/S-T		
Test Step	Start (h)	Duration (h)	R	Freq (Hz)	Hold (h)	Dissolved Hydrogen (cc/kg H_2)	Temp (°C)	Kmax (MPa√m)	CGR (mm/s)	Approx. Crack Extension (mm)
1	0	8	0.5	0.1	0	25	360	30	4.2E-06	0.130
2	8	32	0.5	0.01	0	25	360	30	8.3E-07	0.106
3	40	224	0.5	980s/20s	0	25	360	30	1.5E-07	0.125
4	264	666	0.5	980s/20s	2.5	25	360	30	2.5E-08	0.053
5	930	620	---	const K	---	25	360	30	1.6E-08	0.017
5*	930	620	---	const K	---	25	360	30	2.6E-08	---
6	1550	299	0.5	980s/20s	2.5	25	360	30	4.6E-08	0.065
7	1849	332	0.5	980s/20s	10	25	360	30	2.3E-08	0.031
8	2181	321	0.5	980s/20s	24	25	360	30	2.1E-08	0.029
9	2502	168	0.5	980s/20s	10	25	360	30	2.8E-08	0.018
10	2670	375	0.5	980s/20s	2.5	25	360	31	4.4E-08	0.086
11	3045	279	0.5	12s/12s	2.77	25	360	31	3.3E-08	0.041
12	3324	312	0.5	980s/20s	2.5	25	360	31	4.9E-08	0.046
13	3636	666	---	const K	---	25	360	31	2.1E-08	0.049
13*	3636	666	---	const K	---	25	360	31	3.8E-08	---
14	4302	242	0.5	980s/20s	2.5	25	360	31	1.5E-07	0.031
15	4544	81	0.5	980s/20s	2.5	25	360	31->38	NM	0.043
16	4625	92	0.5	980s/20s	2.5	25	360	38	1.4E-07	0.044
17	4717	708	---	const K	---	25	360	38	2.5E-08	0.063
17*	4717	708	---	const K	---	25	360	38	4.7E-08	---
18	5425	207	0.5	980s/20s	2.5	25	360	39	1.1E-07	0.109
19	5632	30	0.5	980s/20s	2.5	25	360	39->45	NM	0.023
20	5662	172	0.5	980s/20s	2.5	25	360	45	1.3E-07	0.086
21	5834	816	---	const K	---	25	360	45	2.6E-08	0.073
21*	5834	816	---	const K	---	25	360	45	3.9E-08	---
22	6650	169	0.5	980s/20s	2.5	25	360	46	1.5E-07	0.137
23	6819	858	---	const K	---	25	360	46	3.5E-08	0.089

* Ligament/contact adjusted CGR
NM - Not measured.

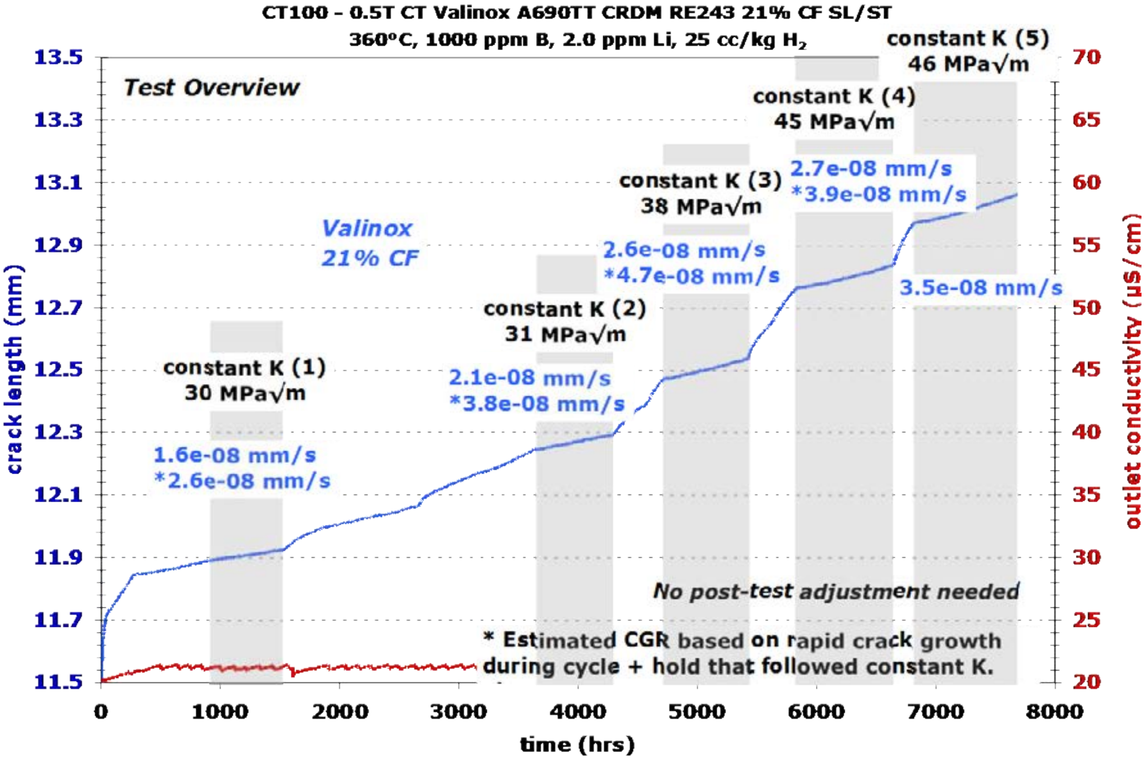

Figure 4.14 Overview of the entire SCC test on the 21%CF S-L/S-T Valinox RE243 specimen, CT100

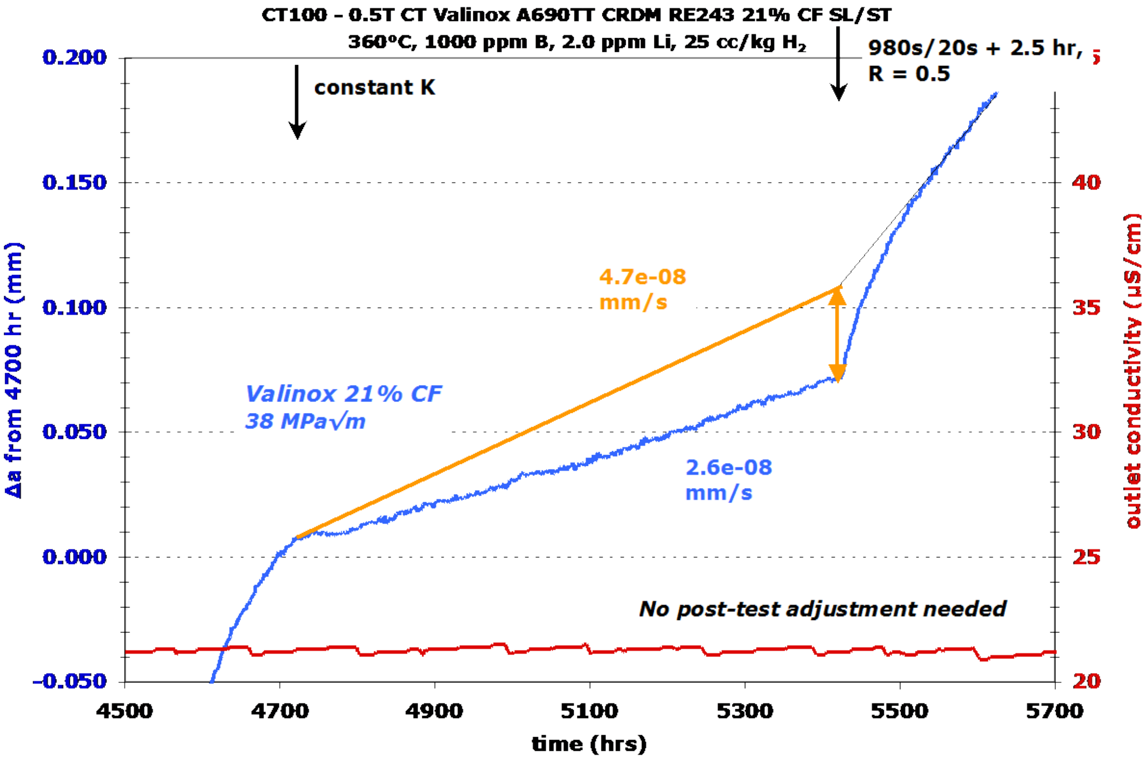

Figure 4.15 Constant K response of the 21%CF S-L/S-T Valinox RE243 specimen CT100 at 38 MPa√m

Post-test observations of the crack growth surface are shown in Figure 4.16 (optical) and Figure 4.17 (SEM). The variation in the in-situ extension ranged from ~1.4 to ~2 mm with an average across the crack front of ~1.6 mm. DCPD estimated in-situ extension was also ~1.6 mm, so no post-test corrections to the results was applied. As indicated in the SEM image, the crack front was measured to be 87% IG with IG cracking extending ~1.4 mm back from the final crack front. Even at the onset of IG cracking, the crack morphology is predominately IG, again with ~85% engagement. This indicates that the 980s/20s + 2.5-h hold loading that was used throughout the majority of the test was effective at maintaining IG engagement in this material. However as is evident in the optical and combined SEM BSE images, there were several unbroken ligaments, and some were more than 1 mm behind the final crack front. This indicates that a 980s/20s+2.5-h hold cyclic loading condition was insufficient to break these ligaments. It will be shown later that much more aggressive cycling (such as 0.1 Hz at R=0.5) has also proven to be ineffective in tests for other CW alloy 690 (CT099). There is substantial variability in the crack front shape, again suggesting that while cycle+hold is effective at maintaining the IG growth, it does allow some variability in crack length, both in the overall shape and the degree of jaggedness. Straightening of the jagged crack front in combination with breaking or reducing the size of some ligaments is thought to be the cause of the accelerated crack growth during cycle+hold after constant K exposures.

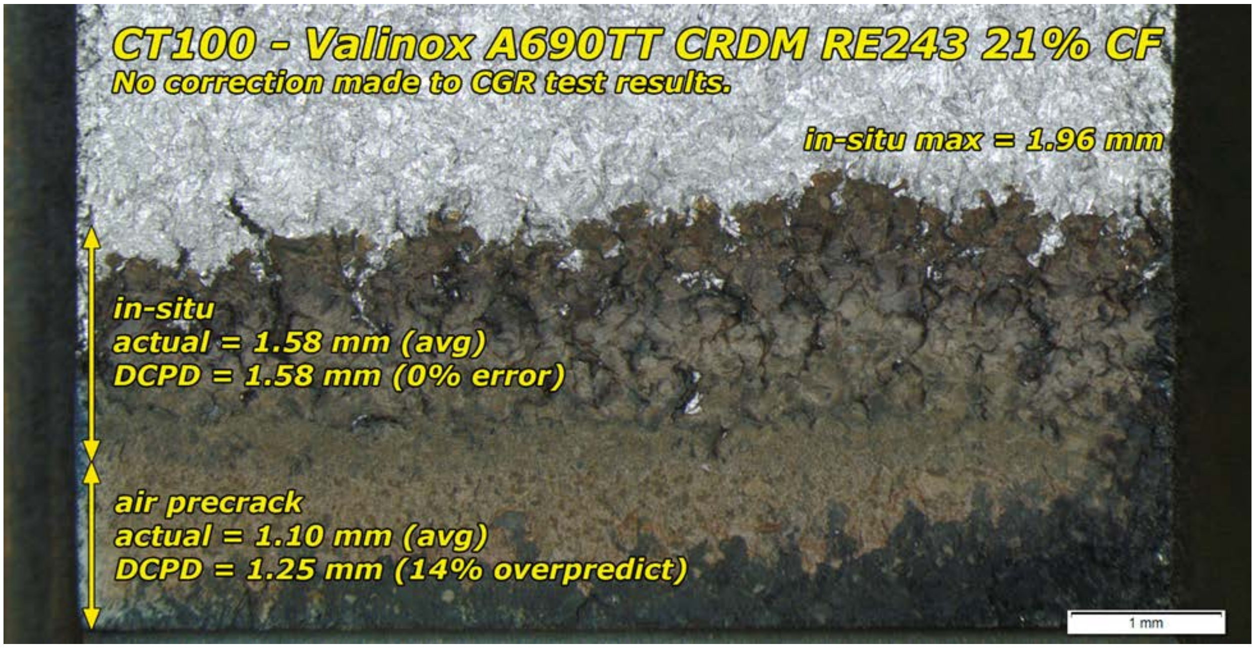

Figure 4.16 **Optical image of the as-tested crack growth surface of the 21%CF S-L/S-T Valinox RE243 specimen CT100.**

Figure 4.17 **SEM-BSE image of the crack front for the 21%CF S-L/S-T Valinox RE243 specimen CT100. The final crack front was 87% engaged.**

4.2.4 Crack Growth Testing of 31%CF S-L/S-T Valinox RE243 Material - CT099

This specimen was tested in series with a TT+31%CF Sumitomo CRDM specimen. Test results on the Sumitomo specimen are presented in the next section. A summary of test conditions and specimen response for the 31%CF specimen are given in Table 4.5, while an overview plot of the entire test is provided in Figure 4.18.

A primary interest in this test was the examination of the effect of K on SCC CGR and was jointly funding by our Light Water Reactor Sustainability project on SCC initiation for the Office of Nuclear Energy, U.S. Department of Energy. Testing began at 30 MPa√m to provide a baseline response and produce a fully engaged IGSCC crack front. Cycle+hold loading applied after constant K resulted in accelerated CGRs that point to ligament/contact formation during constant K (Figure 4.19). Adjusted constant K CGRs were found to be ~1x10^{-7} mm/s, consistent with the response of this heat when it was tested in a 31%CR S-L condition. After assessing the SCC response twice at 30 MPa√m, K was decreased to ~20 MPa√m by -dK/da over ~100 µm. This was followed by another ~150 µm of transitioning before evaluating SCC CGR behavior.

The constant K CGR at the corrected K of ~18 MPa√m was found to be ~4x10^{-9} mm/s as shown in Figure 4.20. The regular variations in crack length correlated with automated water chemistry adjustments to maintain B and Li levels and is likely due to the effect of the water conductivity change for a very tight crack. After obtaining ~12 µm of crack extension over ~900 hours, the application of cycle+hold loading showed no indication of contact or ligament formation. Over the next ~5000 hours, constant K SCC CGR observations were performed at progressively higher K levels, eventually returning to a DCPD-indicated K value of ~28 MPa√m, close to the value of 30 MPa√m at the start of the test. The adjusted CGR was found to be ~7x10^{-8} mm/s, slightly lower than what was observed at the start of the test. Increasing K to ~31.5 MPa√m did not cause any further increase in CGR as shown in **Figure 4.21**. It was thought that the slightly reduced SCC CGR upon returning to ~30 MPa√m was due to ligament or contact formation over

Table 4.5 Test conditions and specimen response for the 31%CF S-L/S-T Valinox alloy 690TT CRDM RE243 specimen CT099

								CT099 Valinox 31.0% CF A690TT Heat RE243		
Test Phase	Start (h)	Duration (h)	R	Freq (Hz)	Hold (h)	Dissolved Hydrogen (cc/kg H_2)	Temp (°C)	Kmax (MPa√m)	CGR (mm/s)	Approx. Crack Ext. (mm)
1	0	7	0.5	0.1	0	25	360	30	7.2E-06	0.142
2	7	15	0.5	0.01	0	25	360	30	1.5E-06	0.078
3	22	78	0.5	980s/20s	0	25	360	30	3.6E-07	0.095
4	100	200	0.5	980s/20s	2.5	25	360	30	1.2E-07	0.095
5	300	320	---	const K	---	25	360	29	6.4E-08	0.071
5*	300	---	---	const K	---	25	360	29	1.0E-07	---
6	620	155	0.5	980s/20s	2.5	25	360	29	3.5E-07	0.216
7	775	424	---	const K	---	25	360	29	6.1E-08	0.086
7*	775	---	---	const K	---	25	360	29	1.0E-07	---
8	1199	151	0.5	980s/20s	2.5	25	360	28	3.4E-07	0.268
9	1350	225	0.5	980s/20s	10	25	360	28	1.3E-07	0.098
10	1575	284	0.5	980s/20s	24	25	360	28	6.9E-08	0.076
11	1859	61	0.5	980s/20s	2.5	25	360	27	4.6E-07	0.141
12	1920	210	0.67	980s/20s	2.5	25	360	27->21	Decr.	0.037
13	2130	165	0.55	980s/20s	1	25	360	21->19	Decr.	0.017
14	2295	170	0.55	980s/20s	1	25	360	19	1.5E-08	0.008
15	2465	81	0.55	480s/20s	0	25	360	19	3.0E-08	0.004
16	2546	191	0.5	480s/20s	0	25	360	19	3.0E-08	0.018
17	2737	293	0.5	480s/20s	0	25	360	19	3.4E-08	0.086
18	3030	328	0.5	980s/20s	0	25	360	19	1.2E-08	0.015
19	3358	339	0.5	980s/20s	2.5	25	360	19	1.2E-08	0.021
20	3697	939	---	const K	---	25	360	19	4.3E-09	0.013
21	4636	546	0.5	980s/20s	2.5	25	360	18	4.2E-08	0.040
22	5182	94	0.5	980s/20s	2.5	25	360	18->20	Incr.	0.032
23	5276	188	0.5	980s/20s	2.5	25	360	20	1.0E-07	0.057
24	5464	580	---	const K	---	25	360	20	1.2E-08	0.032
25	6044	172	0.5	980s/20s	2.5	25	360	20	1.2E-07	0.079
26	6216	75	0.5	980s/20s	2.5	25	360	20->24	Incr.	0.065
27	6291	151	0.5	980s/20s	2.5	25	360	24	2.6E-07	0.156
28	6442	464	---	const K	---	25	360	24	2.6E-08	0.039
28*	6442	---	---	const K	---	25	360	24	3.6E-08	---
29	6906	103	0.5	980s/20s	2.5	25	360	24	2.5E-07	0.100
30	7009	59	0.5	980s/20s	2.5	25	360	24->29	Incr.	0.112
31	7068	152	0.5	980s/20s	2.5	25	360	29	5.2E-07	0.250
32	7220	598	---	const K	---	25	360	29	2.6E-08	0.070
32*	7220	---	---	const K	---	25	360	29	6.8E-08	---
33	7818	214	0.5	980s/20s	2.5	25	360	28	2.4E-07	0.264
34	8032	30	0.5	980s/20s	2.5	25	360	28->32	Incr.	0.045
35	8062	91	0.5	980s/20s	2.5	25	360	32	3.1E-07	0.141
36	8153	437	---	const K	---	25	360	32	3.8E-08	0.058
36*	8153	---	---	const K	---	25	360	32	6.7E-08	---
37	8590	174	0.5	980s/20s	2.5	25	360	31	3.0E-07	0.223
38	8764	3	0.5	0.1	2.5	25	360	31	1.8E-05	0.433
39	8767	133	0.5	980s/20s	0	25	360	31	3.0E-07	0.130
40	8900	480	0.5	980s/20s	2.5	25	360	30	4.2E-08	0.081
41	9380	189	---	const K	---	25	360	30	2.4E-08	0.015

Incr. = Increasing CGR observed
Decr. = Decreasing CGR observed

the course of the test, so aggressive 0.1 Hz (R=0.5) cycling was applied for ~0.5 mm of crack extension and was followed by retransitioning. The subsequent constant K response was unchanged and since the DCPD-indicated crack length was at the limit of available crack extension for a 0.5T CT specimen, the decision was made to end the test and conduct post-test examinations on the specimen.

Testing revealed a strong effect of K on SCC CGRs measured at constant K. Propagation rates were found to decrease by a factor of 20-25x between 30 and ~18 MPa√m. While it is possible that the low K CGRs were influenced by starting the test at 30 MPa√m, significant crack extension during transitioning at 18 MPa√m was performed to move the crack beyond the estimated size of the prior plastic zone before observing constant K response.

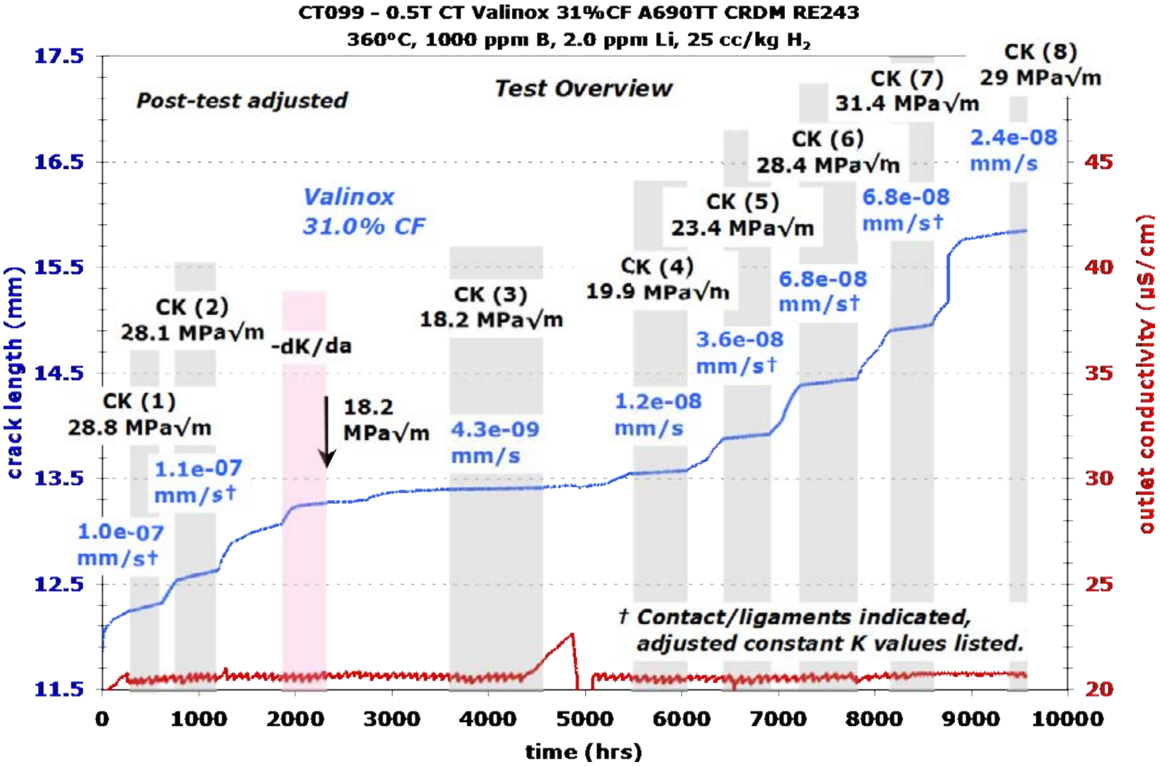

Figure 4.18 Overview of the entire SCC test on the 31%CF S-L/S-T Valinox CRDM RE243 specimen CT099

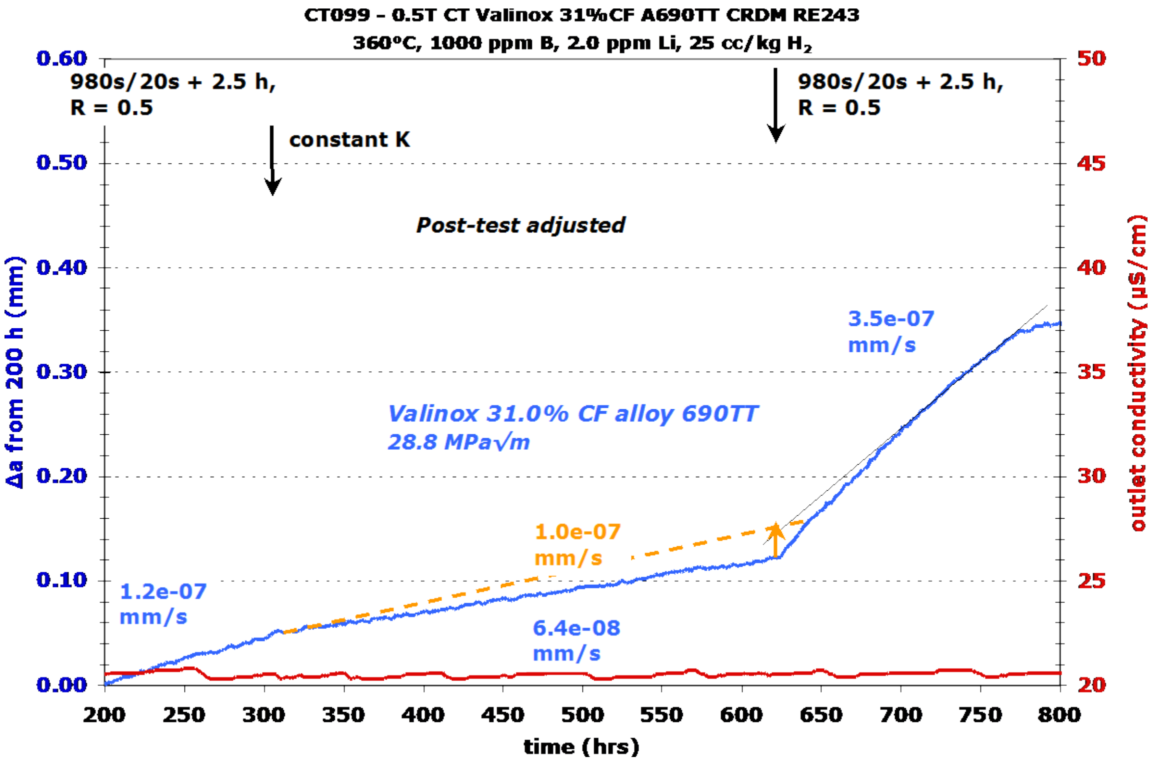

Figure 4.19 Constant K response of the 31%CF S-L/S-T Valinox RE243 specimen CT099 at ~29 MPa√m early in the test

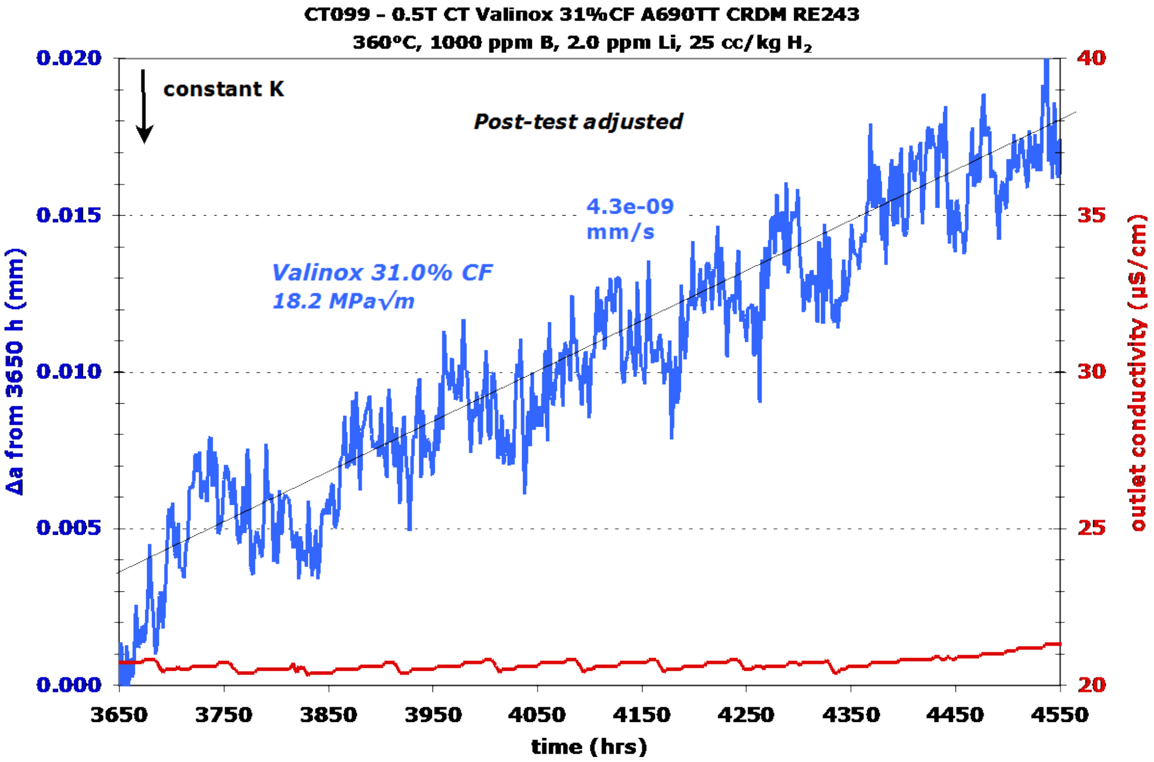

Figure 4.20 Constant K response of the 31%CF S-L/S-T Valinox RE243 specimen CT099 at ~18 MPa√m

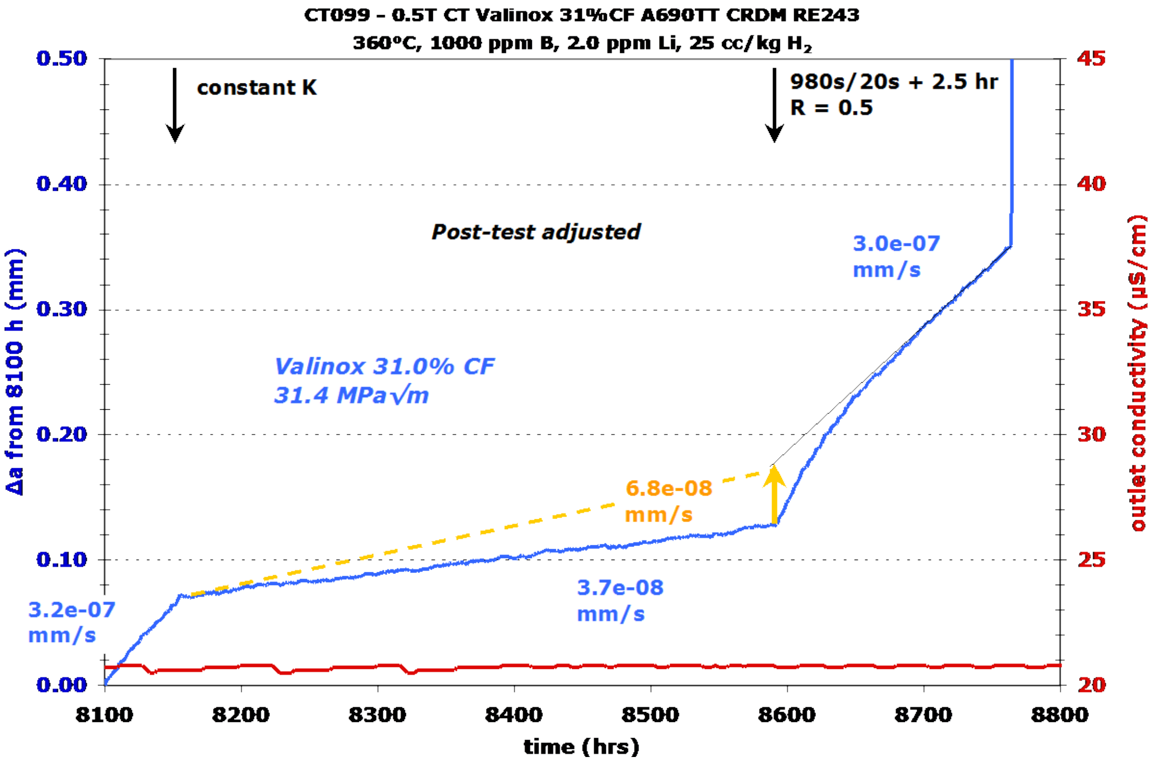

Figure 4.21 **Constant K response of the 31%CF S-L/S-T Valinox RE243 specimen CT099 at ~31.4 MPa√m near the end of the test**

An optical image of the crack surface of the 31%CF Valinox CRDM specimen is presented in Figure 4.22. There is some variability in crack length at the grain size level and there is one substantial uncracked ligament associated with the crack front, but overall, the crack front is relatively straight. The in-situ DCPD crack length was found to match very well with the observed crack length, so no post-test adjustments to crack length were needed. As can be seen, several substantial size ligaments formed during the test, one of which formed at the very start of the in-situ testing. Some of these may have formed as a result of the low K testing, but there is nothing on the crack surface that could support this possibility. It is clear that the aggressive load cycling applied shortly before ending the test was not effective at removing the ligaments. If ligaments had been broken or decreased in size, the oxide appearance would be different in those regions (such as it is along the final crack front) due to the relatively short exposure time.

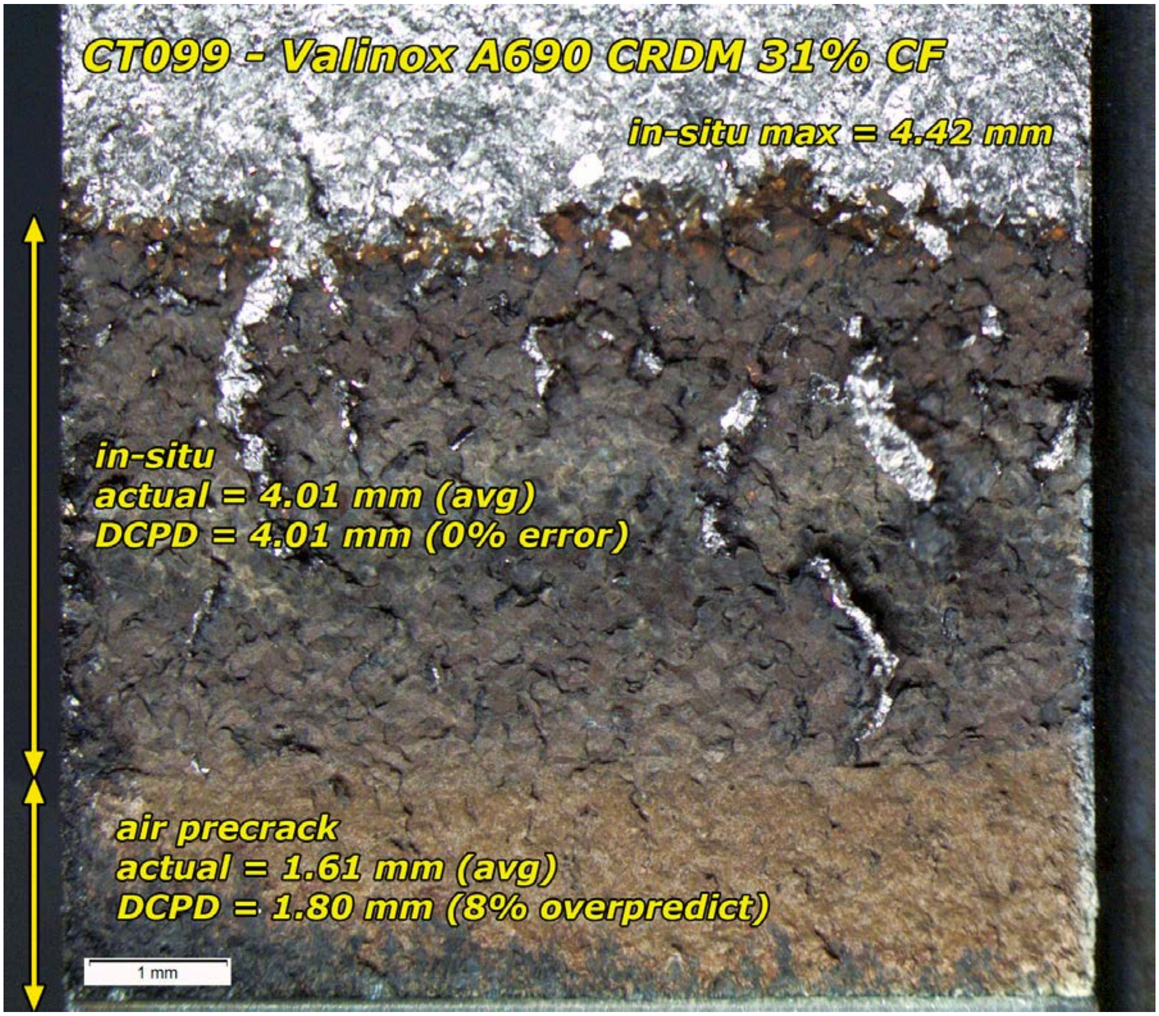

Figure 4.22 **Optical image of the as-tested crack growth surface of the 31%CF S-L/S-T Valinox RE243 specimen CT099**

The SEM image in Figure 4.23 reveals that the crack transitioned to IG growth essentially at the onset of in-situ testing which started with relatively aggressive load cycling of 0.1 Hz at R=0.5. This ability to go IG at such an aggressive load cycling condition is substantiated by the fact that IG cracking was maintained near the end of the test where 0.1 Hz load cycling at R=0.5 was again applied at approximately the same K. This susceptibility can be compared to the 21%CF (CT100) and 11.6%CF (CT104) Valinox specimens where it appears that IG cracking did not begin until reaching 980s/20s load cycling or 9980s/20s load cycling, respectively. In-situ cracking was found to be ≥95% IG for any line drawn across the surface.

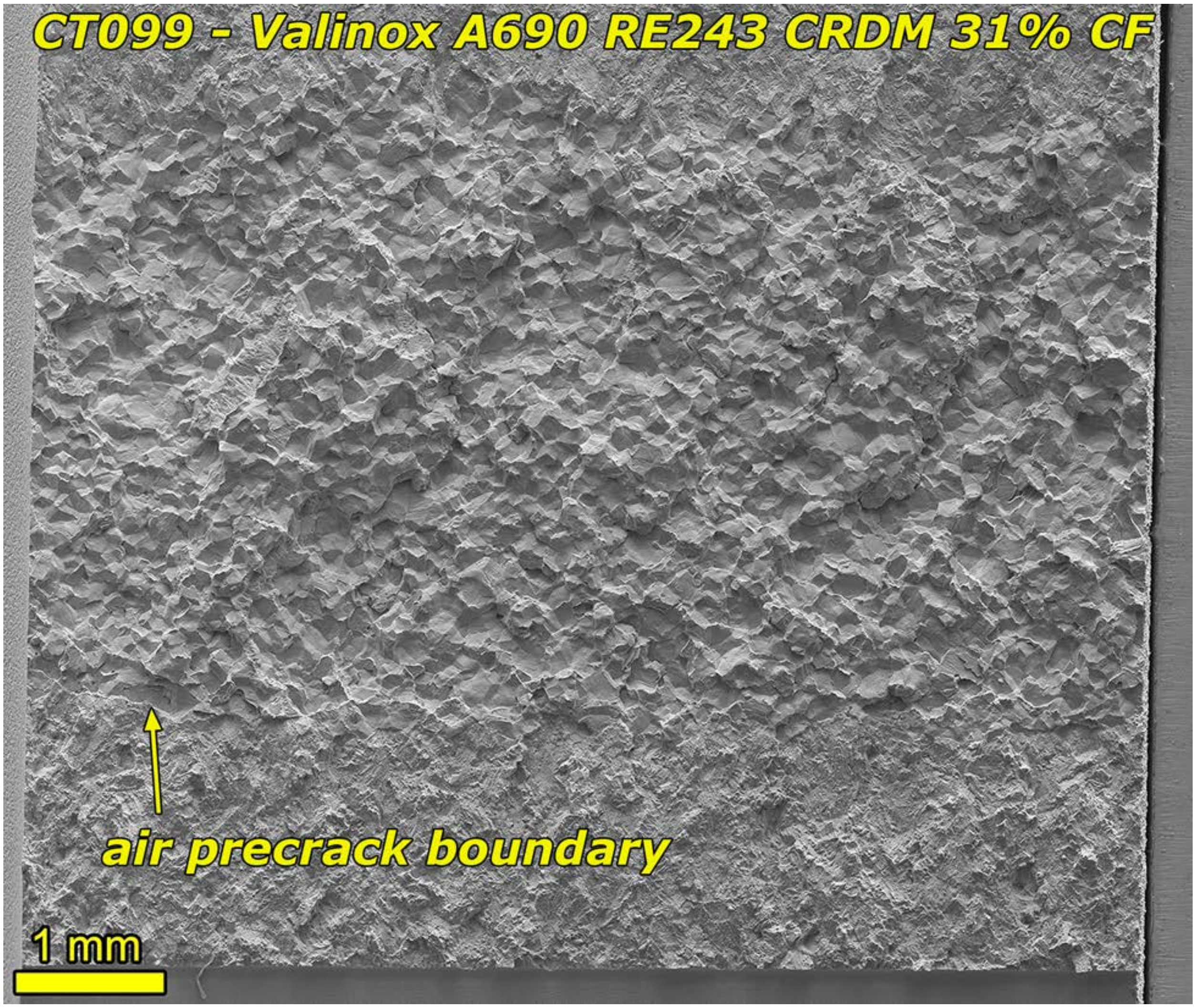

Figure 4.23 **SEM-BSE image of the crack front for the 31%CF S-L/S-T Valinox RE243 specimen CT099. The final crack front was ≥95% engaged.**

4.2.5 Crack Growth Testing of Valinox RE243 31%CR S-L + Recovery Specimen - CT053

This specimen was tested in series with a TT+17%CR S-L Valinox CRDM specimen CT104 and results were presented earlier. A summary of test conditions and specimen response for the recovery heat treatment (RT) specimen CT053 is given in Table 4.6, while an overview plot of the entire test is provided in Figure 4.24.

As indicated in the table and plot, only a single transitioning sequence followed by a single constant K observation was performed. Transitioning consisted of running through 0.1 Hz, 0.01 Hz, 0.001 Hz, 980s/20s, and 980s/20s + 2.5-hour hold. The cycle+hold step was maintained for ~30 µm which represents roughly 1/3 of a grain diameter for this material. Steady crack advance was observed during this final transitioning step and during the subsequent constant K observation as shown in Figure 4.25. Constant K was continued for ~900 hours accumulating ~10 µm of DCPD-indicated crack advance. The propagation rate during constant K was observed to be a steady value of ~4.3×10^{-9} mm/s, substantially lower than the ~1×10^{-7} mm/s constant K CGR that was observed for this same material without the recovery heat treatment.

As was shown in Chapter 3, the hardness and IMD values were reduced by the recovery heat treatment to values ~10-15% below that for the 31%CR material.

Table 4.6 Test conditions and specimen response for the 31%CR S-L + RT Valinox alloy 690TT CRDM RE243 specimen CT053

								CT053 A690 TT+31% CR S-L + HT		
Test Phase	Start (h)	Duration (h)	R	Freq (Hz)	Hold (h)	Dissolved Hydrogen (cc/kg H_2)	Temp (°C)	Kmax (MPa√m)	CGR (mm/s)	Approx. Crack Extension (mm)
1	0	18	0.5	0.1	0	25	360	30	4.1E-06	0.300
2	18	102	0.5	0.01	0	25	360	30	7.6E-07	0.300
3	120	215	0.5	0.01	0	25	360	30	1.6E-07	0.100
4	335	124	0.5	980s/20s	0	25	360	30	1.6E-07	0.065
5	459	479	0.5	0.001	2.5	25	360	30	1.5E-08	0.027
6	938	877	---	const K	---	25	360	30	4.3E-09	0.011

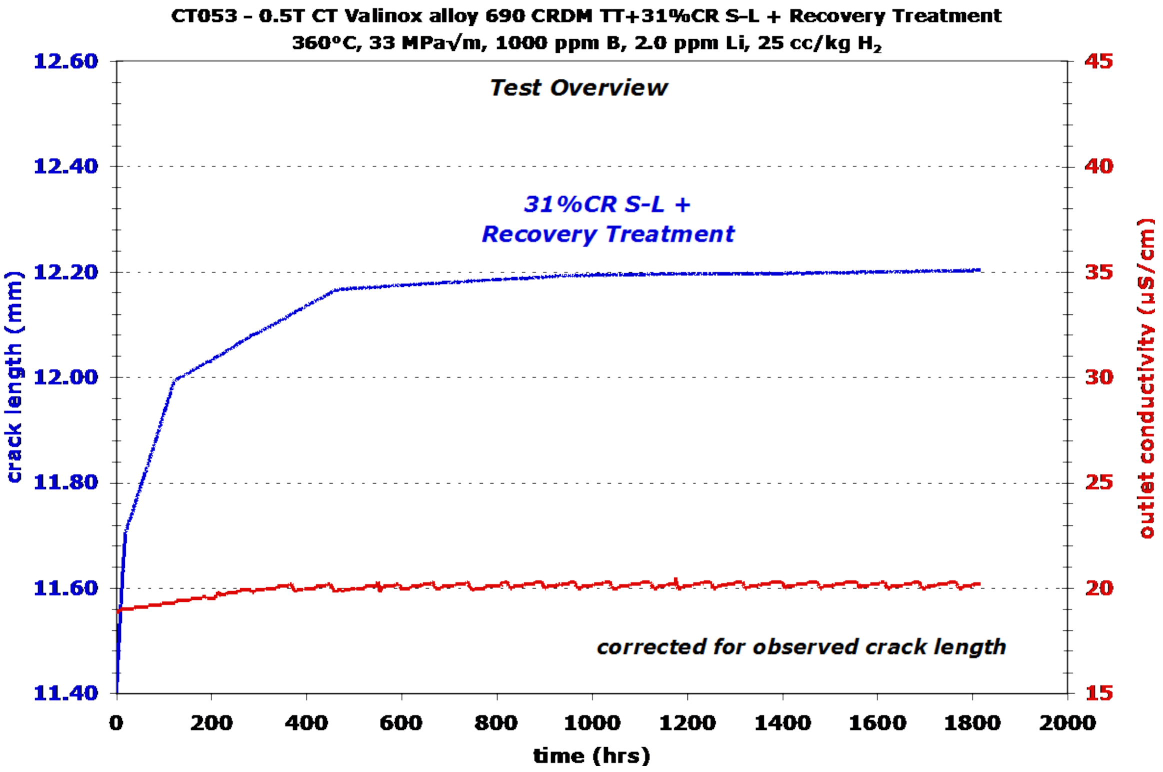

Figure 4.24 Overview of the entire SCC test on the 31%CR S-L + RT Valinox RE243 specimen CT053

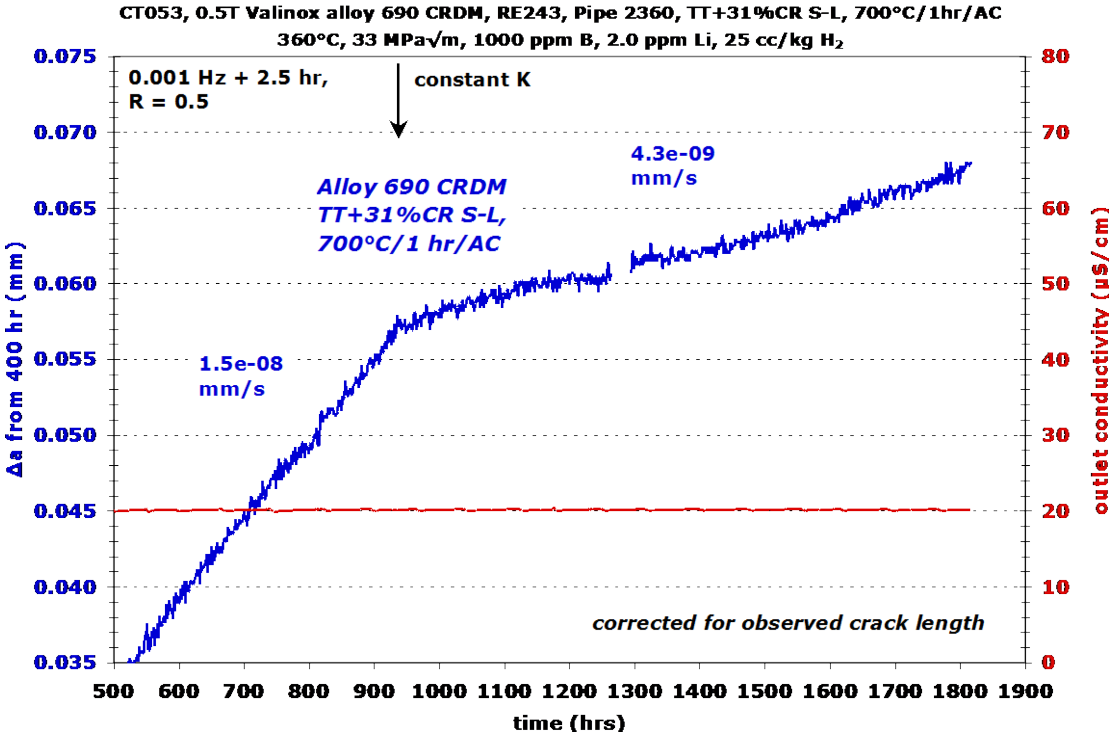

Figure 4.25 Constant K response of the 31%CR S-L + RT Valinox RE243 specimen CT053 at 30 MPa√m

After this single constant K observation, the test was ended to examine the specimen. Optical and SEM-BSE images of the crack surface are presented in Figure 4.26 and Figure 4.27, respectively. The air precrack length was found to vary strongly with the length being much shorter near the surface than in the specimen interior. This may be due to the interior of the specimen taking longer to reach full temperature during the recovery heat treatment which could produce a variation in strength across the specimen thickness with more rapid fatigue propagation in the higher strength interior. It is important to note that the in-situ transitioning portion of the test appears to have uniform crack extension from exterior to interior inconsistent with this explanation. The optical image shows protrusions along the final crack front that were verified by SEM to be IG cracking during final transitioning and constant K loading.

IG engagement was determined to be 45% based on the width of the IG protrusions (yellow boxes in Figure 4.27). Several crack length corrections were considered. A straightforward correction to the air precrack region was not possible due to the large variation in crack length. The main effect this has on the in-situ portion of the test is the starting K. The maximum starting stress intensity is calculated to be 34.5 MPa√m at the center of the specimen while the minimum was 28.5 MPa√m near the side surface. A value of 33 MPa√m is a reasonable representation of the average K, although the variation in K did not affect the in-situ cyclic loading response. The higher cycle fatigue transitioning makes up the majority of the in-situ crack extension, and because of this, it is straightforward to calculate that DCPD over predicted this portion of crack extension by ~18%. Determining the constant K extension is more challenging because the IG extension is likely due to both constant K and cycle+hold transitioning. If an area average is taken of the IG extension, the correction factor to the DCPD crack length is 0.89x due to both cycle+hold and constant K while it's 3.4x if its due to only constant K. Experience with tests on other specimens suggests that the IG extension is due to both, so no correction to the constant K CGR was made.

This material was tested in tandem with a TT+17%CR S-L material (CT054). This was done because it was thought that these two materials might behave similarly, and in fact, they did. Both showed partial IG engagement (below 50%), and constant K CGRs in the range of ~3-4x10^{-9} mm/s. This suggests that the recovery heat treatment substantially altered the 31%CR dislocation density and hardness to be more similar to the 17%CR S-L material. Hardness and EBSD strain measurements reported in (Table 3.6 and Table 3.8) revealed that values were higher than the 17%CR and 21%CF RE243 materials, but less than the 31%CR material.

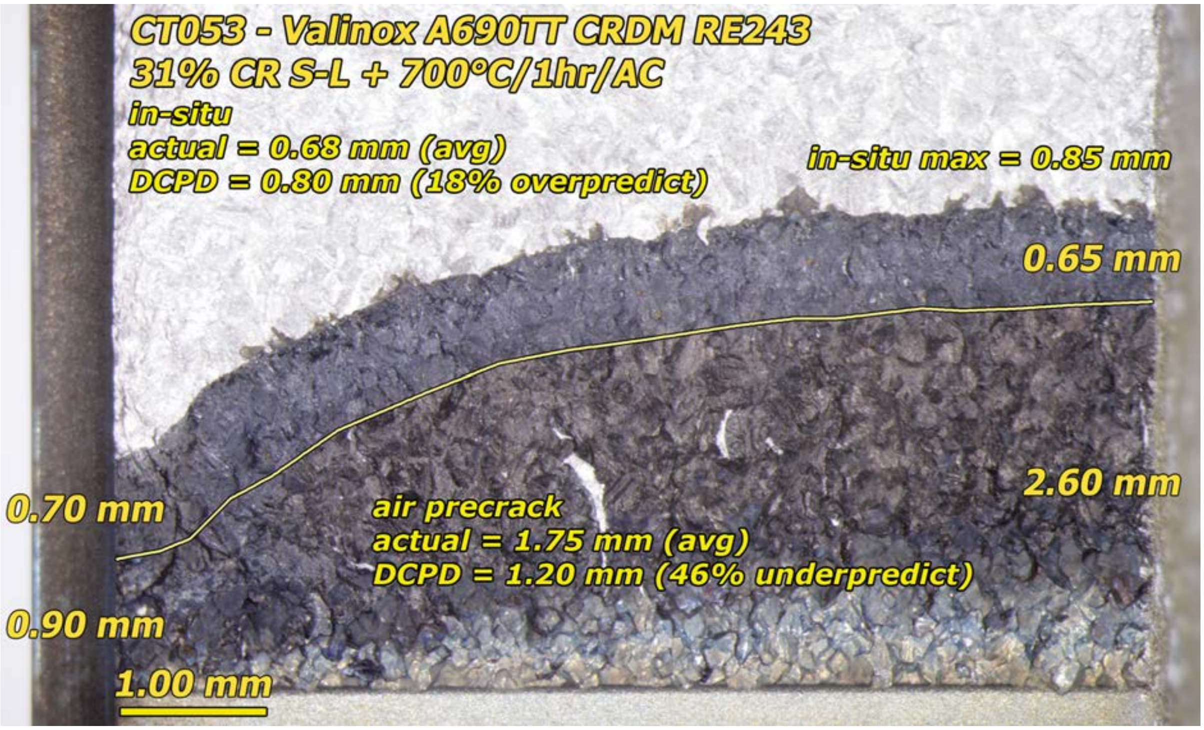

Figure 4.26 **Optical image of the cleaned crack growth surface of the 31%CR S-L + RT Valinox RE243 specimen CT053**

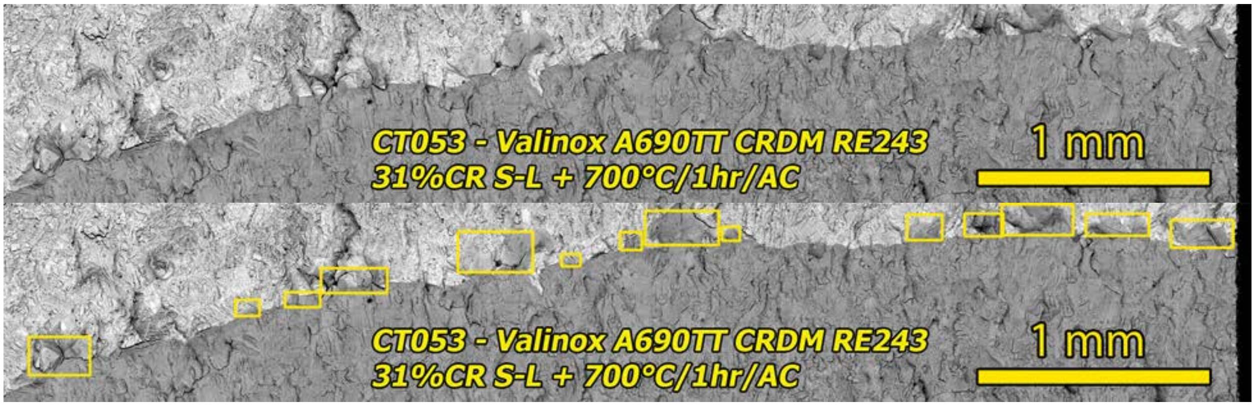

Figure 4.27 **SEM-BSE image of the crack front for the 31%CR S-L + RT Valinox RE243 specimen CT053. The final crack front was ~45% IG engaged.**

4.2.6 Crack Growth Testing of the SA+17%CR S-L Valinox RE243 Material - CT068

This specimen was tested in series with an HAZ plate specimen (CT067) that will be described later in the report. A summary of test conditions and specimen response for the SA+17%CR S-L specimen are given in Table 4.7 while an overview plot of the entire test is provided in Figure 4.28. This material was previously tested at 325°C (CT019) and as reported in the previous NUREG, no IG engagement and low SCC CGRs (<1x10^{-9} mm/s) were observed. Because the TT+17%CR S-L specimen had been retested at 360°C and exhibited some IG cracking, it was decided to retest this material as well and expand data for the comparison between SA and TT materials in several different CW conditions.

Table 4.7 Test conditions and specimen response for the SA+17%CR S-L Valinox alloy 690 CRDM RE243 specimen CT068

							CT068 Valinox 17%CR S-L A690SA		
Test Phase	Duration (h)	R	Freq (Hz)	Hold (h)	Dissolved Hydrogen (cc/kg H_2)	Temp (°C)	Kmax (MPa√m)	CGR (mm/s)	Approx. Crack Extension (mm)
1	12	0.5	0.1	0	25	360	31	5.1E-06	0.203
2	63	0.5	0.01	0	25	360	31	1.1E-06	0.241
3	185	0.5	0.001	0	25	360	31	1.7E-07	0.110
4	315	0.5	0.001	2.5	25	360	31	1.7E-08	0.022
5	170	0.5	980s/20s	2.5	25	360	31	1.7E-08	0.013
6	885	---	const K	---	25	360	31	2.2E-09	0.006
7	145	0.5	980s/20s	0	25	360	31	1.4E-07	0.075
8	365	0.5	980s/20s	1	25	360	31	3.4E-08	0.046
9	183	0.5	980s/20s	2.5	25	360	31	1.7E-08	0.011
10	318	---	const K	---	25	360	31	1.7E-09	0.002
11	117	0.5	980s/20s	2.5	25	360	30->35	4.5E-08	0.017
12	245	0.5	980s/20s	2.5	25	360	36	2.4E-08	0.022
13	593	---	const K	---	25	360	36	1.6E-09	0.004
14	92	0.5	0.01	0	25	360	36	1.1E-06	0.370
15	133	0.5	0.001	0	25	360	36	1.7E-07	0.083
16	259	0.5	0.001	2.5	25	360	36	2.1E-08	0.018
17	1236	---	const K	---	25	360	36	1.1E-09	0.004
18	30	0.5	0.1	0	25	360	35	6.1E-06	0.573
19	104	0.5	0.01	0	25	360	35	1.1E-06	0.388
20	169	0.5	980s/20s	0	25	360	35	1.8E-07	0.104
21	116	0.5	980s/20s	0	25	360	35->38	2.0E-07	0.076
22	229	0.5	980s/20s	2.5	25	360	38	2.2E-08	0.019
23	490	---	const K	---	25	360	38	6.7E-10	0.002
24	181	0.5	0.04	2.77	25	360	38	1.1E-08	0.007

As shown in the overview plot (Figure 4.28), the material was extensively studied at 360°C. The constant K response was observed at five different stress intensities ranging from 31 to 38 MPa√m with substantial transitioning in between. The highest constant K CGR was observed during the first constant K observation as shown in Figure 4.29. The propagation rate started at 2.7×10^{-9} mm/s and decreased slowly, reaching 2.2×10^{-9} mm/s after ~650 hours and 7 µm of crack extension. This value is nearly identical to that of the TT+17%CR S-L specimen tested at the same conditions. Subsequent transitioning attempts results in progressively lower constant K CGRs as K was increased. The test was ended after ~6700 hours and the specimen was sectioned for optical and SEM examination.

Post-test measurement of the crack surface by optical imaging (Figure 4.30) revealed that DCPD-measured crack length was within 8% of the actual crack length, so no correction was needed to the test data. The optical image also showed a complete lack of IG engagement along the final crack front, consistent with the low CGRs observed during the final constant K observation before ending the test. While large differences in CGR have been observed between the 31%CR SA and TT Valinox RE243, the lack of crack growth of either of the materials in the non-CW condition makes it not surprising that the gap between the SA and TT CGRs becomes progressively smaller as the degree of cold work is reduced.

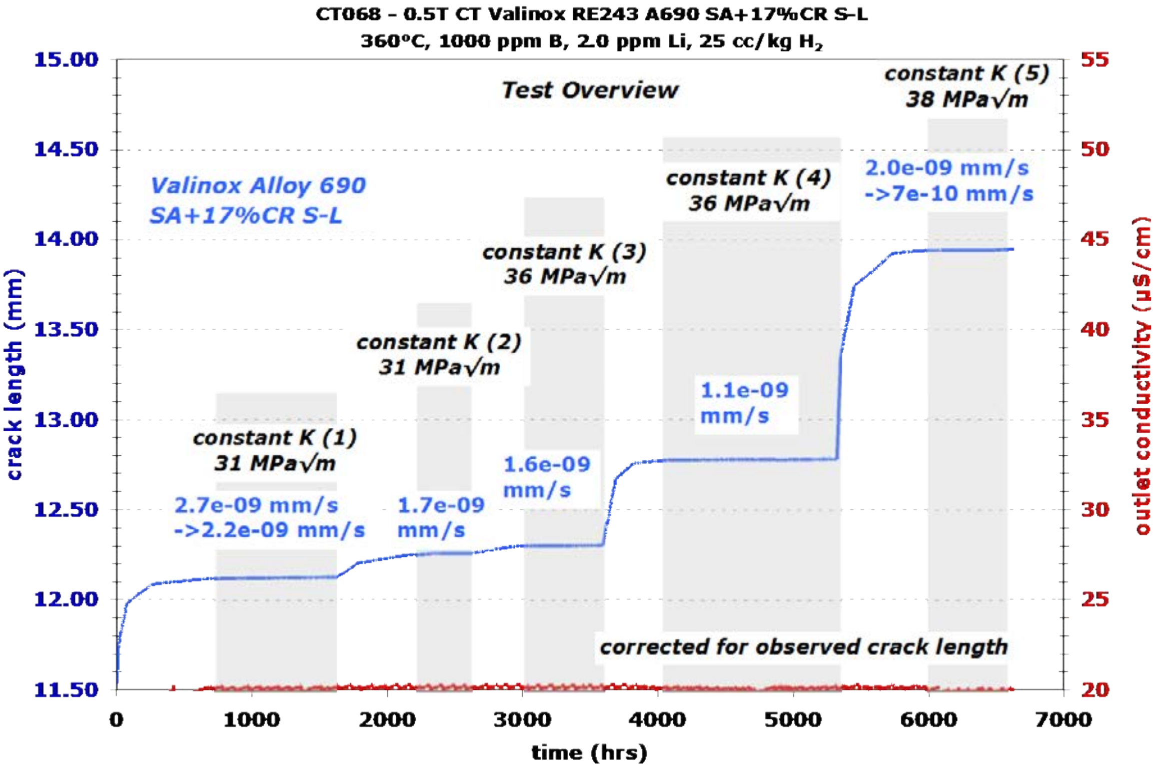

Figure 4.28 **Overview of the entire SCC test on the SA+17%CR S-L Valinox alloy 690 CRDM RE243 specimen CT068**

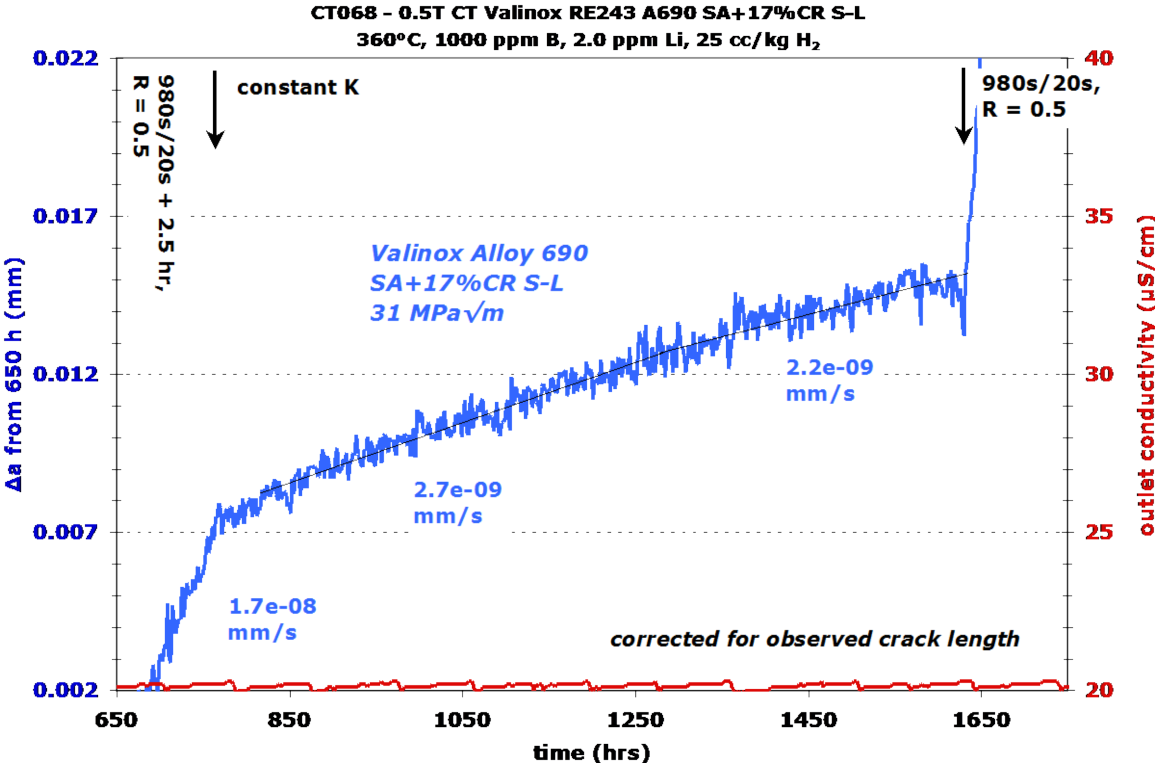

Figure 4.29 Constant K response of the SA+17%CR S-L Valinox RE243 specimen CT068 at 31 MPa√m

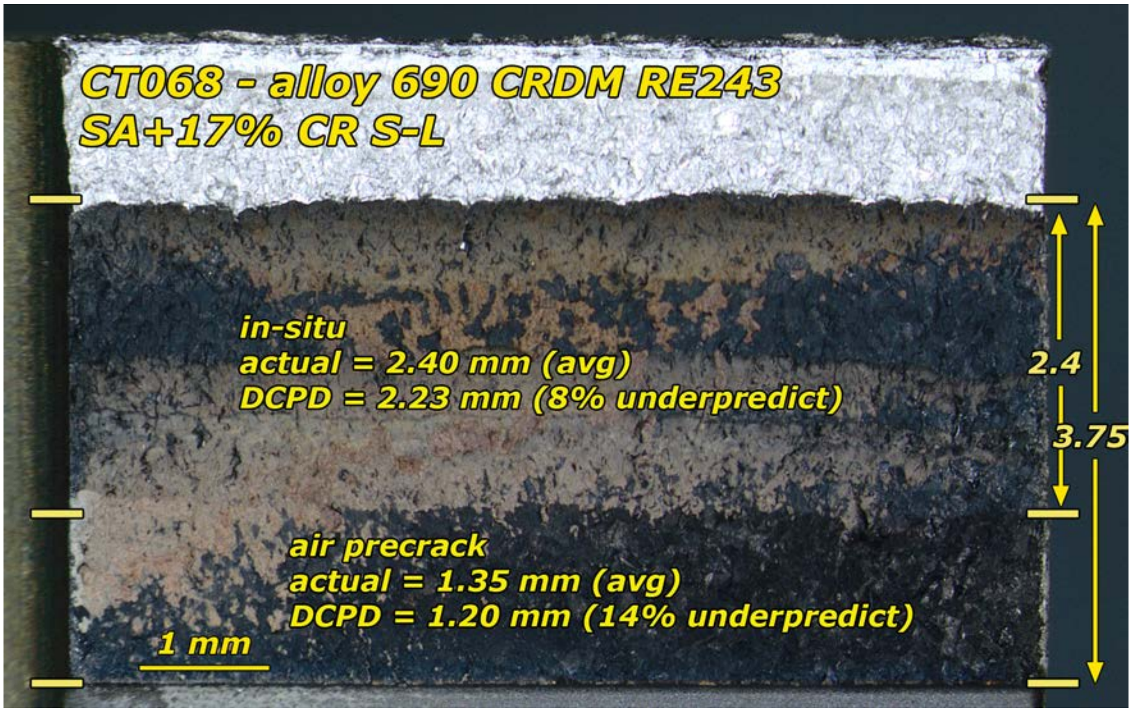

Figure 4.30 Optical image of the cleaned crack growth surface of the SA+17%CR S-L Valinox RE243 specimen CT068

4.3 SCC Tests on Other Heats of CRDM Alloy 690TT Materials

4.3.1 Crack Growth Testing of the CIEMAT 20%TS Valinox WP787 Specimen - CT093

This specimen was tested in series in two different tests. In the first test, it was paired with a 22%CF plate specimen (CT094 described later in the report). Very little crack extension took place in the CIEMAT specimen because the companion (controlling) specimen grew at a much faster rate, causing a reduction in K for the CIEMAT specimen, and a strong -dK/da effect. In the second test, it was paired with the 21%CF Valinox RE243 specimen that was described earlier in the report. Results on the Ciemat specimen are only reported for the second test. The CT was cut in T-L orientation from a large tensile specimen that was strained by CIEMAT (Figure 4.31). CIEMAT reports the material as 20%TS, but when accounting for elastic loading in their tensile trace, only 18% engineering strain was achieved. The test is reported as 20%TS to be consistent with CIEMAT's nomenclature. A summary of test conditions and specimen response for the 20%TS specimen are given in Table 4.8, while an overview plot of the entire second test is provided in Figure 4.32.

As shown in the overview plot, the material was extensively studied at 360°C. The constant K response was observed at five times for a total of three different K values ranging from 30 to 43 MPa√m with substantial transitioning in between. Evidence for ligament/contact formation during constant K testing was observed in each instance where cycle+hold was applied after constant K. Adjusted SCC propagation rates were found to increase from ~1.0×10^{-8} mm/s at 30 MPa to ~1.8×10^{-8} mm/s at higher K suggesting a very mild K dependence. The rate at 30 MPa√m is consistent with the range of values observed for alloy 690 materials discussed in this report that were cold rolled or cold forged to 17-21% reduction. The highest constant K CGR was observed at 37 MPa√m as shown in Figure 4.33. As part of planned efforts to understand the origin of the postulated ligament/contact formation, the test was ended at constant K in an attempt to identify features on the crack-growth surface.

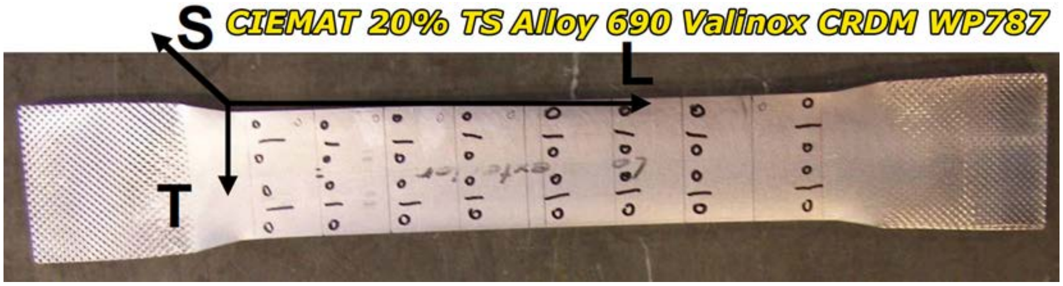

Figure 4.31 CIEMAT tensile strained alloy 690 CRDM WP787 used to produce CT093. Image courtesy of CIEMAT.

Table 4.8 Test conditions and specimen response for the 20%TS Valinox alloy 690TT CRDM WP787 specimen CT093

								Ciemat A690TT WP787 20% TS		
Test Step	Start (h)	Duration (h)	R	Freq (Hz)	Hold (h)	Dissolved Hydrogen (cc/kg H_2)	Temp (°C)	Kmax (MPa√m)	CGR (mm/s)	Approx. Crack Extension (mm)
1	0	8	0.5	0.1	0	25	360	30	4.2E-06	0.160
2	8	32	0.5	0.01	0	25	360	30	8.3E-07	0.099
3	40	224	0.5	980s/20s	0	25	360	30	1.5E-07	0.114
4	264	666	0.5	980s/20s	2.5	25	360	30	1.9E-08	0.046
5	930	620	---	const K	---	25	360	30	4.8E-09	0.007
5*	930	620	---	const K	---	25	360	30	1.0E-08	0.020
6	1550	299	0.5	980s/20s	2.5	25	360	30	2.1E-08	0.027
7	1849	332	0.5	980s/20s	10	25	360	30	1.1E-08	0.013
8	2181	321	0.5	980s/20s	24	25	360	30	9.0E-09	0.011
9	2502	168	0.5	980s/20s	10	25	360	30	1.5E-08	0.009
10	2670	375	0.5	980s/20s	2.5	25	360	30	2.2E-08	0.046
11	3045	279	0.5	12s/12s	2.77	25	360	30	1.8E-08	0.023
12	3324	312	0.5	980s/20s	2.5	25	360	30	2.2E-08	0.022
13	3636	666	---	const K	---	25	360	30	3.1E-09	0.015
13*	3636	666	---	const K	---	25	360	30	1.1E-08	0.000
14	4302	242	0.5	980s/20s	2.5	25	360	30	3.7E-08	0.030
15	4544	81	0.5	980s/20s	2.5	25	360	30->37	NM	0.030
16	4625	92	0.5	980s/20s	2.5	25	360	37	6.3E-08	0.025
17	4717	708	---	const K	---	25	360	37	1.1E-08	0.027
17*	4717	708	---	const K	---	25	360	37	1.8E-08	0.000
18	5425	207	0.5	980s/20s	2.5	25	360	37	6.3E-08	0.057
19	5632	30	0.5	980s/20s	2.5	25	360	37->43	NM	0.029
20	5662	172	0.5	980s/20s	2.5	25	360	43	7.0E-08	0.050
21	5834	816	---	const K	---	25	360	43	1.0E-08	0.027
21*	5834	816	---	const K	---	25	360	43	1.6E-08	0.000
22	6650	169	0.5	980s/20s	2.5	25	360	43	6.5E-08	0.056
23	6819	858	---	const K	---	25	360	43	1.1E-08	0.027

* Ligament/contact adjusted CGR

NM - Not measured.

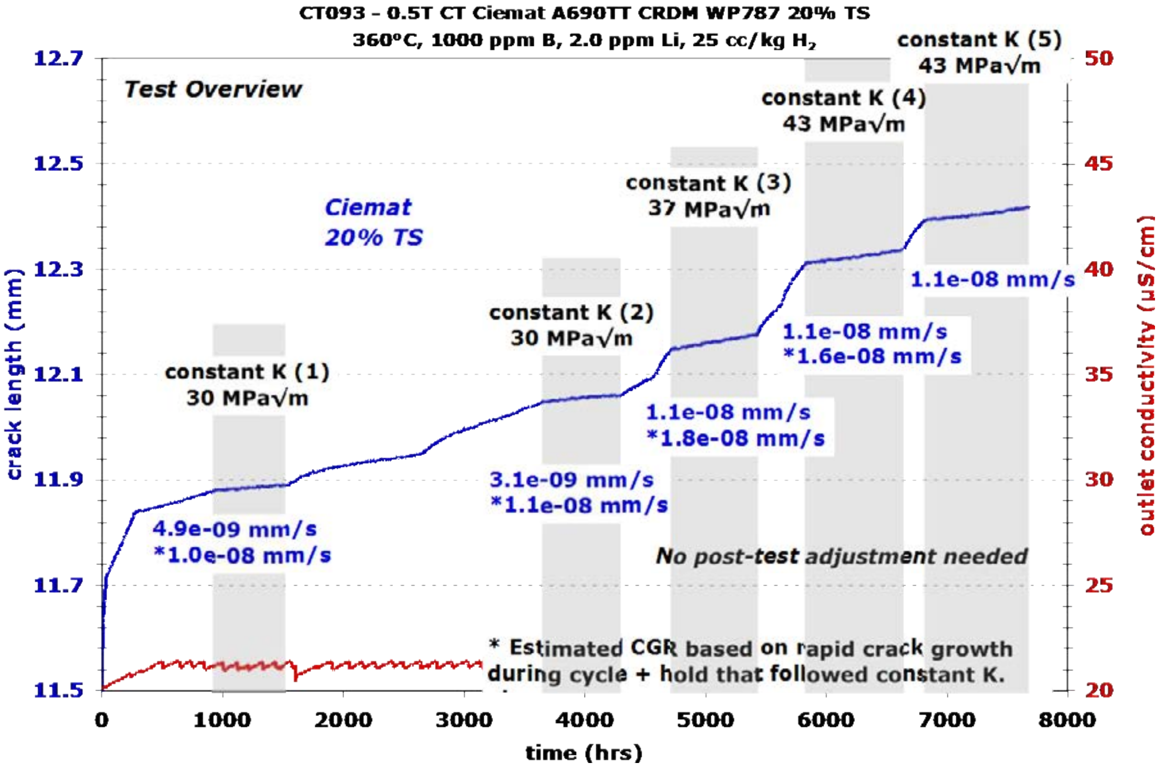

Figure 4.32 Overview of the second continuing test on the 20%TS WP787 specimen CT093

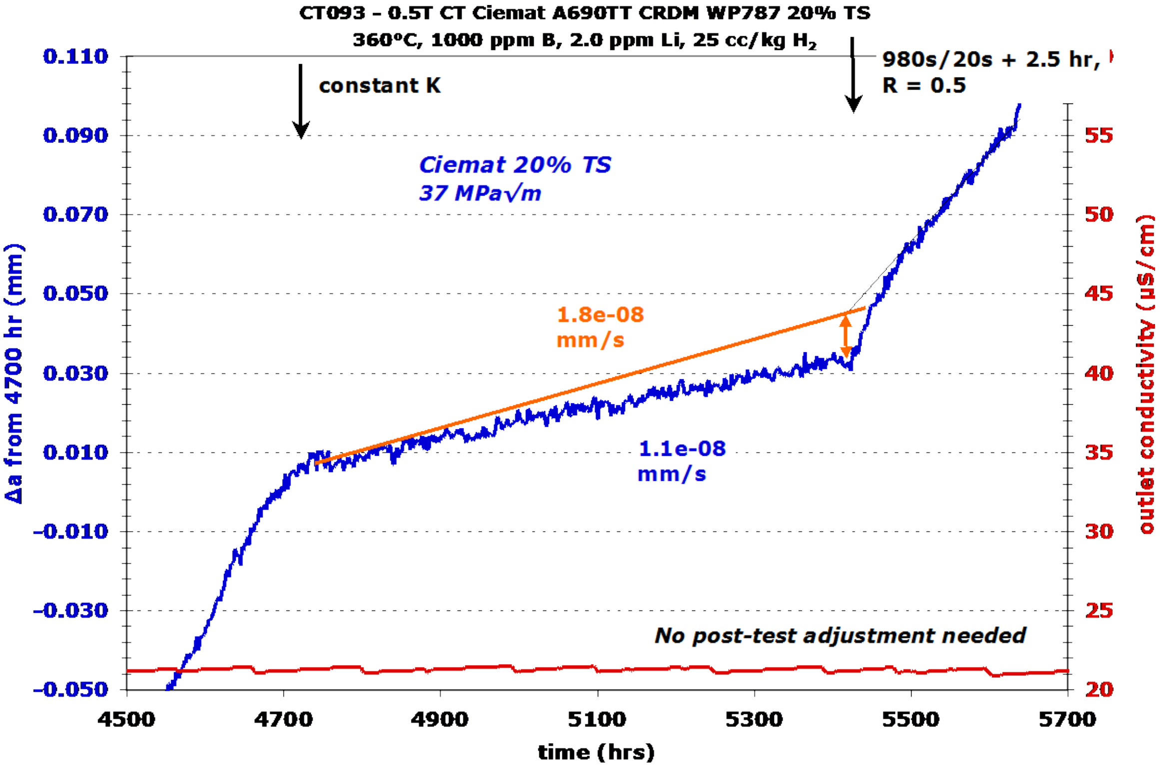

Figure 4.33 Constant K response of the 20%TS WP787 specimen CT093 at 37 MPa√m

Post-test measurement of the crack surface by optical imaging (Figure 4.34) revealed that DCPD-measured crack length was within 3% of the actual average crack length, so no correction was needed to the CGR test data. As with many of the other tests that have been described thus far, the crack front was not skewed in length from one side of the specimen to the other, but it had many fingers or ligaments. While even 0.1 Hz load cycling is not able to eliminate some ligaments, it is thought that accelerated crack growth during cycle+hold after a constant K observation is caused by reduction in size or elimination of ligaments.

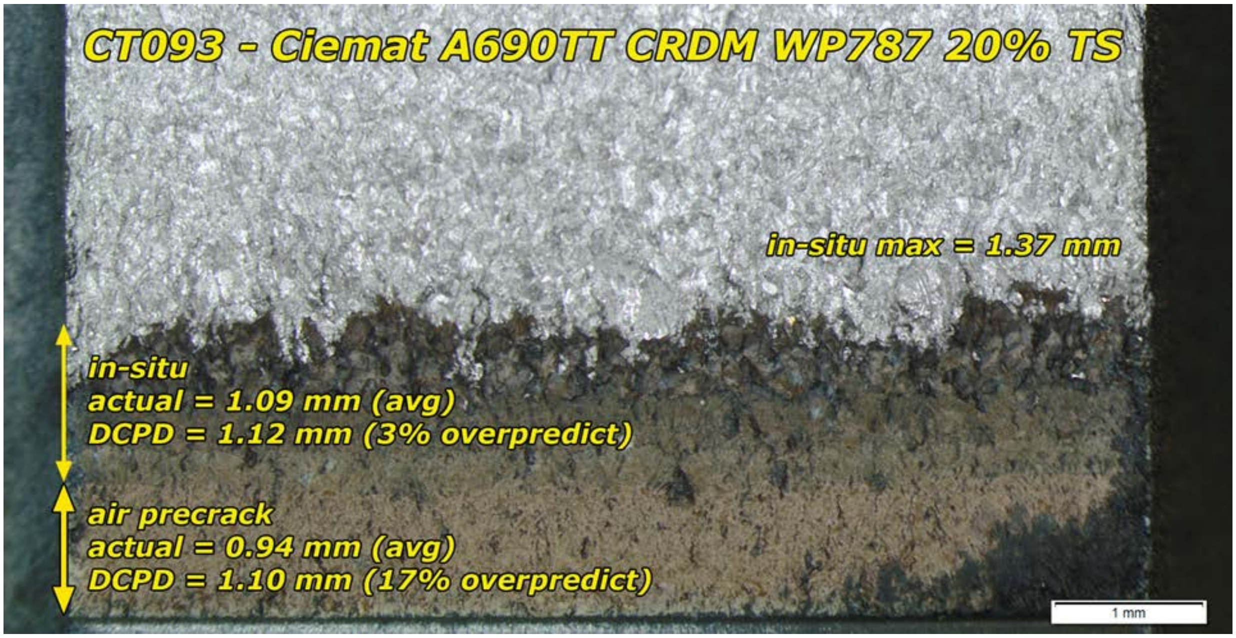

Figure 4.34 Optical image of the as-tested crack growth surface of the 20%TS WP787 specimen, CT093

Analysis of the SEM-BSE image of the opposite side of the specimen (Figure 4.35) revealed 0.35-0.75 mm of crack growth that was ≥90% IG, consistent with the amount of crack extension that took place during gentle cycling and constant K starting from ~200 hours into the second test. This degree of IG engagement and crack extension is consistent with the observed CGRs.

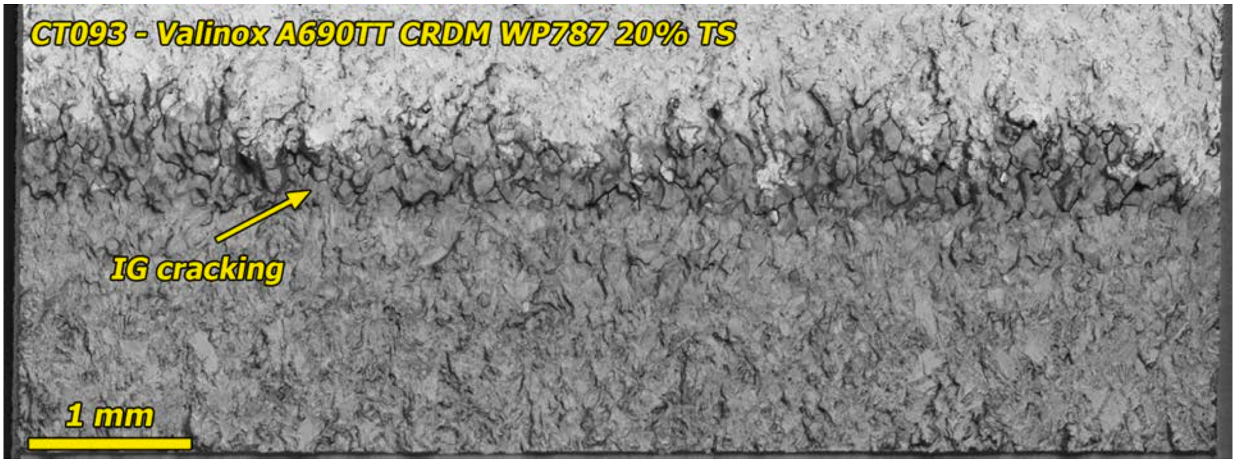

Figure 4.35 SEM BSE image of the cleaned crack growth surface of the 20%TS WP787 specimen CT093

4.3.2 Crack Growth Testing of the 12.7%CF Sumitomo E67074C Specimen - CT103

This specimen was tested in series with an 11.6%CF Valinox RE243 specimen (CT104 described earlier in the report). A summary of test conditions and specimen response for the 12.7%CF specimen is given in Table 4.9 while an overview plot of the entire test is provided in Figure 4.36. As shown in the overview plot, the constant K response was observed at four different K levels ranging from 29 to 40 MPa√m with substantial transitioning in between. Evidence for ligament/contact formation during constant K testing by observing cycle+hold response was not observed (Figure 4.37). This material was found to be very resistant to SCC at this level of CW with all four constant K observations resulting in <1x10^{-9} mm/s CGRs despite extensive transitioning efforts that included a slow 9980s/20s load cycle. The companion specimen (11.6%CF Valinox RE243) was much more susceptible with a maximum steady constant K propagation rate of ~9x10^{-9} mm/s.

Table 4.9 Test conditions and specimen response for the 12.7%CF Sumitomo alloy 690TT CRDM E67074C specimen CT103

								CT103 A690 STO CRDM 12.7% CF Heat E67074C		
Test Step	Start (h)	Duration (h)	R	Freq (Hz)	Hold (h)	Dissolved Hydrogen (cc/kg H_2)	Temp (°C)	Kmax (MPa√m)	CGR (mm/s)	Approx. Crack Extension (mm)
1	0	8	0.5	0.1	0	25	360	30	3.2E-06	0.100
2	8	35	0.5	0.01	0	25	360	30	5.9E-07	0.098
3	43	227	0.5	980s/20s	0	25	360	30	1.2E-07	0.119
4	270	241	0.5	980s/20s	2.5	25	360	30	1.3E-08	0.014
5	511	167	0.5	980s/20s	2.5	25	360	30	1.3E-08	0.011
6	678	553	---	const K	---	25	360	30	7.9E-10	0.002
7	1231	237	0.5	980s/20s	2.5	25	360	30	1.3E-08	0.012
8	1468	672	0.5	9980s/20s	0	25	360	30	1.6E-08	0.043
9	2140	311	0.5	9980s/20s	2.5	25	360	30	9.9E-09	0.016
10	2451	1054	---	const K	---	25	360	30	1.7E-10	0.001
11	3505	289	0.5	9980s/20s	2.5	25	360	30	1.4E-08	0.014
12	3794	130	0.5	9980s/20s	0	25	360	30->37	NM	0.027
13	3924	104	0.5	9980s/20s	0	25	360	37	4.1E-08	0.019
14	4028	185	0.5	9980s/20s	2.5	25	360	37	2.4E-08	0.019
15	4213	608	---	const K	---	25	360	37	4.9E-10	0.004
16	4821	172	0.5	9980s/20s	2.5	25	360	37	2.3E-08	0.014
17	4993	102	0.5	9980s/20s	2.5	25	360	37->42	NM	0.024
18	5095	232	0.5	9980s/20s	2.5	25	360	42	3.0E-08	0.033
20	5327	1026	---	const K	---	25	360	42	6.1E-10	0.003

NM = not measured

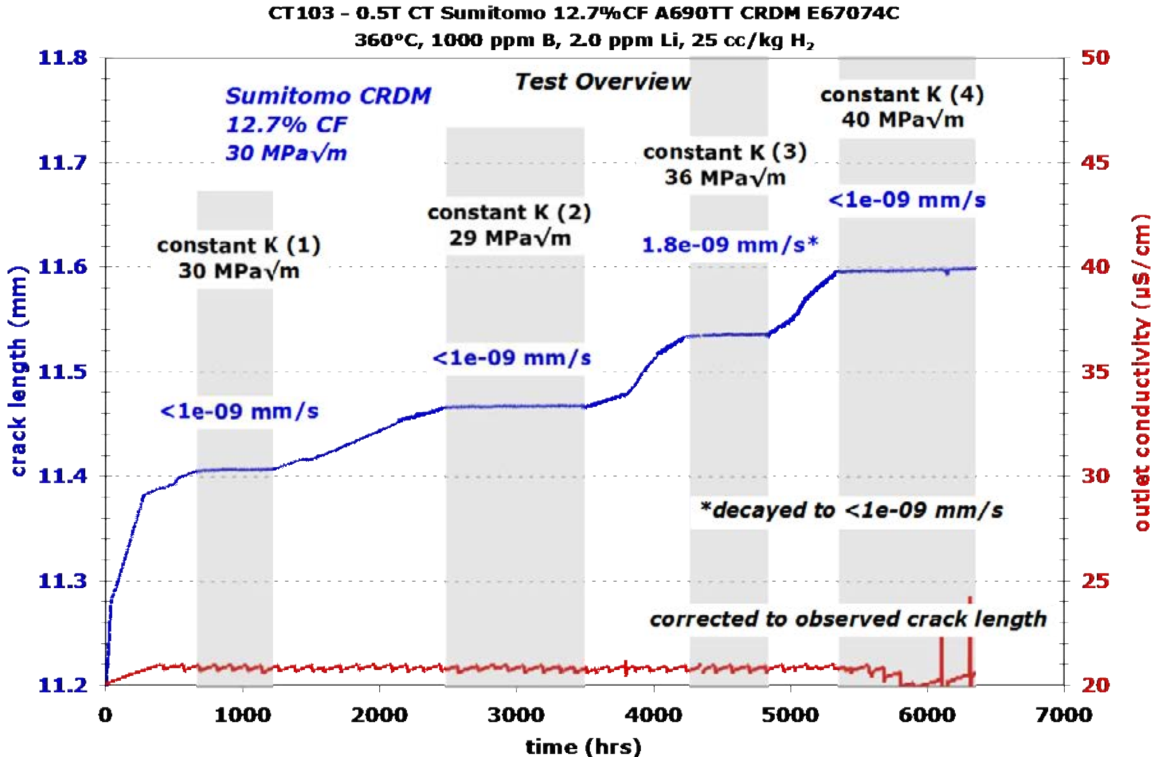

Figure 4.36 Overview of the entire SCC test on the 12.7%CF Sumitomo E67074C specimen CT103

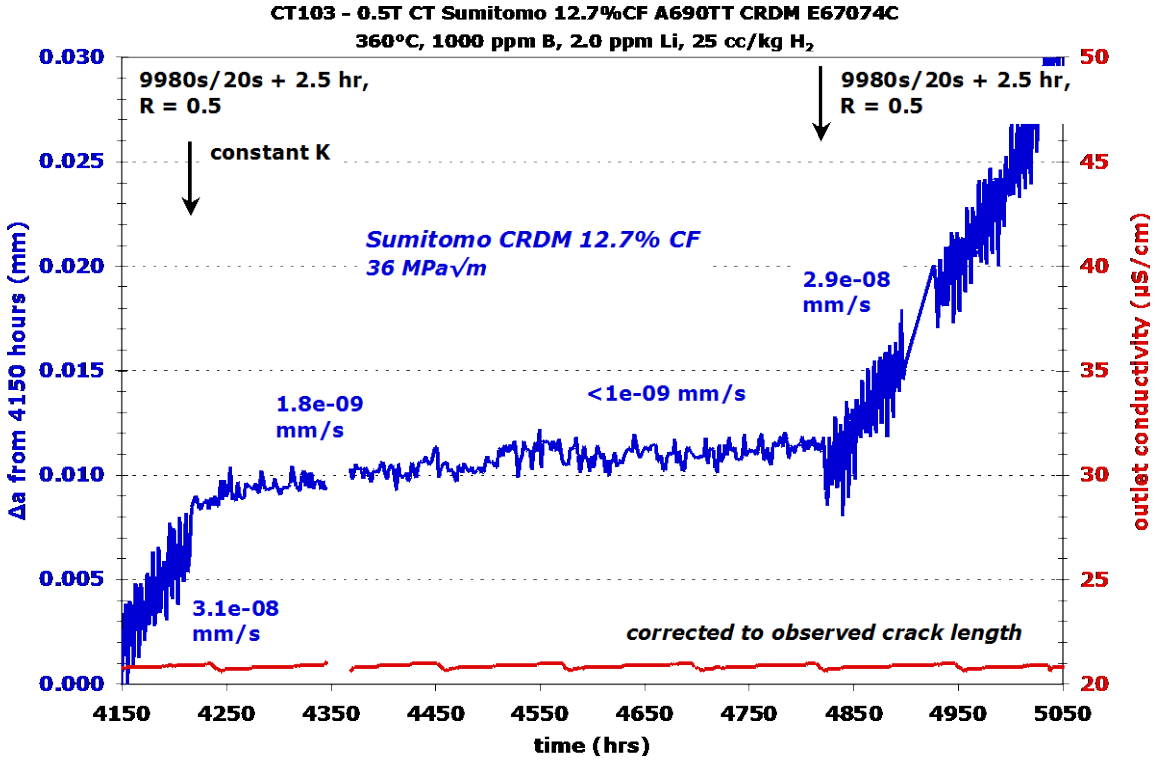

Figure 4.37 Constant K response of the 12.7%CF Sumitomo E67074C specimen CT103 at 36 MPa√m

Post-test measurement of the crack surface by optical imaging (Figure 4.38) revealed that DCPD-measured crack growth over predicted actual crack growth by ~23%. As a result, actual K values and CGRs were slightly lower than estimated during the test. Only a small amount of total crack growth occurred in this SCC resistant material. The optical image has many small protrusions suggesting IG engagement, however high magnification SEM images determined that the final crack front was only ~23% engaged. Further back from the final crack front at locations where the test was at a K of 30 MPa√m appeared to have a smaller fraction of IG features, A low magnification SEM image of the entire crack growth surface is shown in Figure 4.39, while a higher magnification image with examples of IG cracking is shown in Figure 4.40.

The other materials with this general range of cold work that have been tested include the 11.6%CF and 17% CR Valinox RE243. Interestingly, the hardness and the EBSD misorientation (IMD) measurements for the Sumitomo material are both higher than the 11.6%CF Valinox that exhibited 10x higher CGRs and was nearly fully engaged. The 17%CR Valinox specimen had slightly higher IMD, but somewhat lower hardness than the Sumitomo and was slightly less engaged. Grain boundary carbide microstructures were similar for the Valinox and Sumitomo CRDM TT materials. These comparative results suggest that even for similarities in key parameters, differences in SCC response can be observed for materials with low-to-moderate levels of cold work.

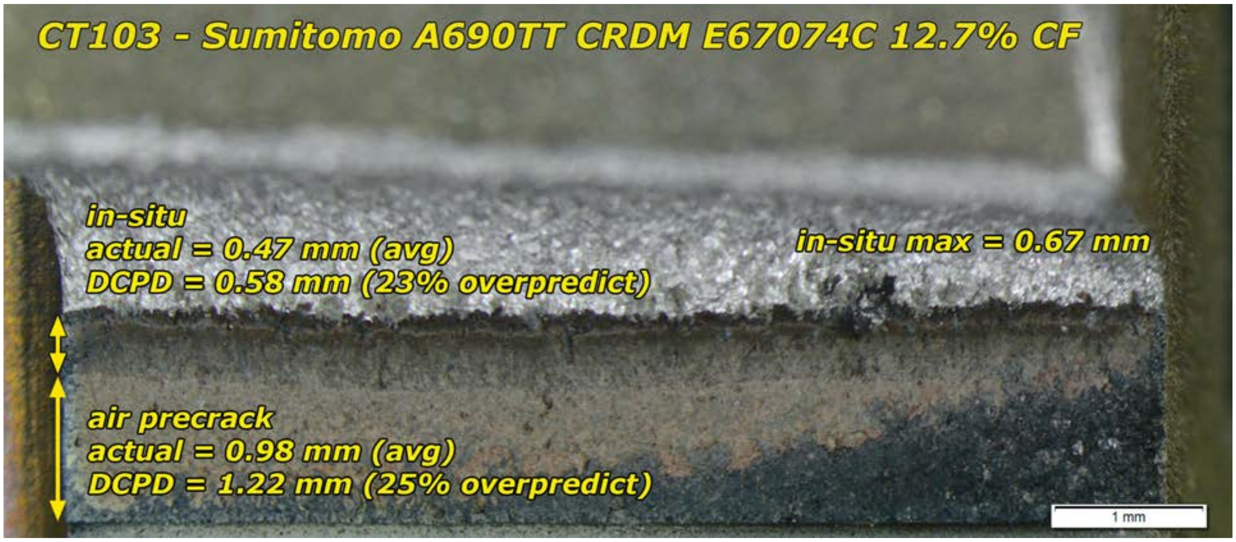

Figure 4.38 **Optical image of the as-tested crack growth surface of the 12.7%CF Sumitomo E67074C specimen CT103**

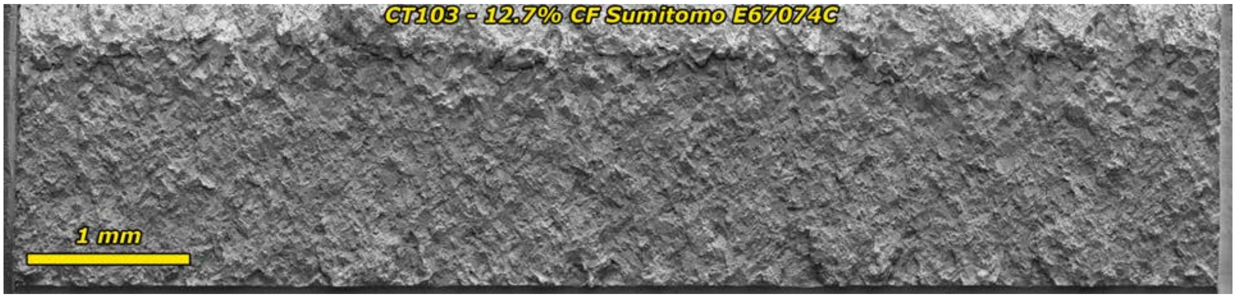

Figure 4.39 **SEM BSE image of the cleaned crack growth surface of the 12.7%CF Sumitomo E67074C specimen CT103**

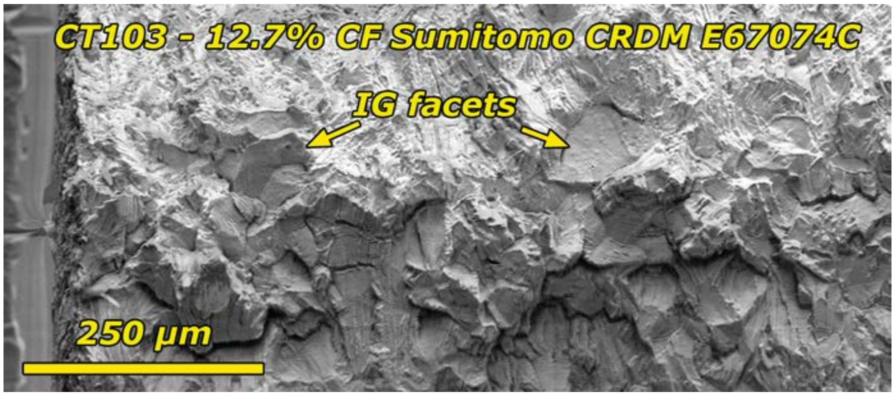

Figure 4.40 **Higher magnification SEM BSE image of the cleaned crack growth surface of the 12.7%CF Sumitomo E67074C specimen, CT103. The final crack front was found to be 23% IG.**

4.3.3 Crack Growth Testing of the 31%CF Sumitomo E67074C Specimen - CT098

This specimen was tested in series with a 31%CF Valinox RE243 specimen (CT099 described earlier in the report). A summary of test conditions and specimen response for the 31%CF Sumitomo specimen is given in **Table 4.10** while an overview plot of the entire test is provided in **Figure 4.41**. The methodology and goals for this test were described in detail previously for CT099. Briefly, the goal for this test was to assess the effect of K on crack growth particularly assessing behavior at lower K values. As with the 31%CF Valinox RE243, the Sumitomo material exhibited high SCC CGRs at the base stress intensity of 30 MPa√m (**Figure 4.42**) with propagation rates dropping by orders of magnitude as the K was decreased to ~20 MPa√m (**Figure 4.43**). Upon returning to ~30 MPa√m later in the test, SCC CGRs were found to be ~50% of their previous value earlier in the test for a similar K (**Figure 4.44**). Aggressive load cycling was applied in an attempt to break any tenacious ligaments, but as shown in the overview, SCC CGRs were unaffected. With all the available crack extension almost entirely consumed, the test was ended to destructively examine the specimen.

Table 4.10 Test conditions and specimen response for the 31%CF Sumitomo alloy 690TT CRDM E67074C specimen CT098

								CT098 Sumitomo 31.2% CF A690 TT Heat E67074C		
Test Phase	Start (h)	Duration (h)	R	Freq (Hz)	Hold (h)	Dissolved Hydrogen (cc/kg H_2)	Temp (°C)	Kmax (MPa√m)	CGR (mm/s)	Approx. Crack Ext. (mm)
1	0	7	0.5	0.1	0	25	360	30	5.8E-06	0.160
2	7	15	0.5	0.01	0	25	360	30	1.2E-06	0.089
3	22	78	0.5	980s/20s	0	25	360	30	3.3E-07	0.109
4	100	200	0.5	980s/20s	2.5	25	360	30	3.3E-07	0.239
5	300	320	---	const K	---	25	360	30	5.9E-08	0.083
5*	300	---	---	const K	---	25	360	30	2.0E-07	---
6	620	155	0.5	980s/20s	2.5	25	360	30	4.0E-07	0.431
7	775	424	---	const K	---	25	360	30	4.1E-08	0.070
7*	775	---	---	const K	---	25	360	30	1.4E-07	---
8	1199	151	0.5	980s/20s	2.5	25	360	30	4.1E-07	0.453
9	1350	225	0.5	980s/20s	10	25	360	30	1.5E-07	0.157
10	1575	284	0.5	980s/20s	24	25	360	30	7.3E-08	0.112
11	1859	61	0.5	980s/20s	2.5	25	360	30	5.8E-07	0.217
12	1920	210	0.67	980s/20s	2.5	25	360	30->23	Decr.	0.061
13	2130	165	0.55	980s/20s	1	25	360	23->20	Decr.	0.032
14	2295	170	0.55	980s/20s	1	25	360	20	1.2E-08	0.008
15	2465	81	0.55	480s/20s	0	25	360	20	2.0E-08	0.003
16	2546	191	0.5	480s/20s	0	25	360	20	2.0E-08	0.018
17	2737	293	0.5	480s/20s	0	25	360	20	2.1E-08	0.080
18	3030	328	0.5	980s/20s	0	25	360	20	6.7E-09	0.009
19	3358	339	0.5	980s/20s	2.5	25	360	20	6.7E-09	0.012
20	3697	939	---	const K	---	25	360	20	1.7E-09	0.007
21	4636	546	0.5	980s/20s	2.5	25	360	20	3.9E-08	0.061
22	5182	94	0.5	980s/20s	2.5	25	360	20->22	Incr.	0.030
23	5276	188	0.5	980s/20s	2.5	25	360	22	8.0E-08	0.057
24	5464	580	---	const K	---	25	360	22	7.1E-09	0.014
25	6044	172	0.5	980s/20s	2.5	25	360	22	8.7E-08	0.091
26	6216	75	0.5	980s/20s	2.5	25	360	22->26	Incr.	0.034
27	6291	151	0.5	980s/20s	2.5	25	360	26	1.6E-07	0.120
28	6442	464	---	const K	---	25	360	26	1.2E-08	0.029
28*	6442	---	---	const K	---	25	360	26	2.2E-08	---
29	6906	103	0.5	980s/20s	2.5	25	360	26	1.9E-07	0.107
30	7009	59	0.5	980s/20s	2.5	25	360	26->32	Incr.	0.103
31	7068	152	0.5	980s/20s	2.5	25	360	32	4.2E-07	0.292
32	7220	598	---	const K	---	25	360	32	2.4E-08	0.061
32*	7220	---	---	const K	---	25	360	32	7.7E-08	---
33	7818	214	0.5	980s/20s	2.5	25	360	32	2.9E-07	0.433
34	8032	30	0.5	980s/20s	2.5	25	360	32->37	Incr.	0.053
35	8062	91	0.5	980s/20s	2.5	25	360	37	4.1E-07	0.193
36	8153	437	---	const K	---	25	360	37	2.1E-08	0.038
36*	8153	---	---	const K	---	25	360	37	7.6E-08	---
37	8590	174	0.5	980s/20s	2.5	25	360	36	4.0E-07	0.385
38	8764	3	0.5	0.1	2.5	25	360	36	1.1E-05	0.482
39	8767	133	0.5	980s/20s	0	25	360	37	2.4E-07	0.119
40	8900	480	0.5	980s/20s	2.5	25	360	37	1.2E-07	0.191
41	9380	189	---	const K	---	25	360	37	1.8E-08	0.016

Incr. = Increasing CGR observed
Decr. = Decreasing CGR observed

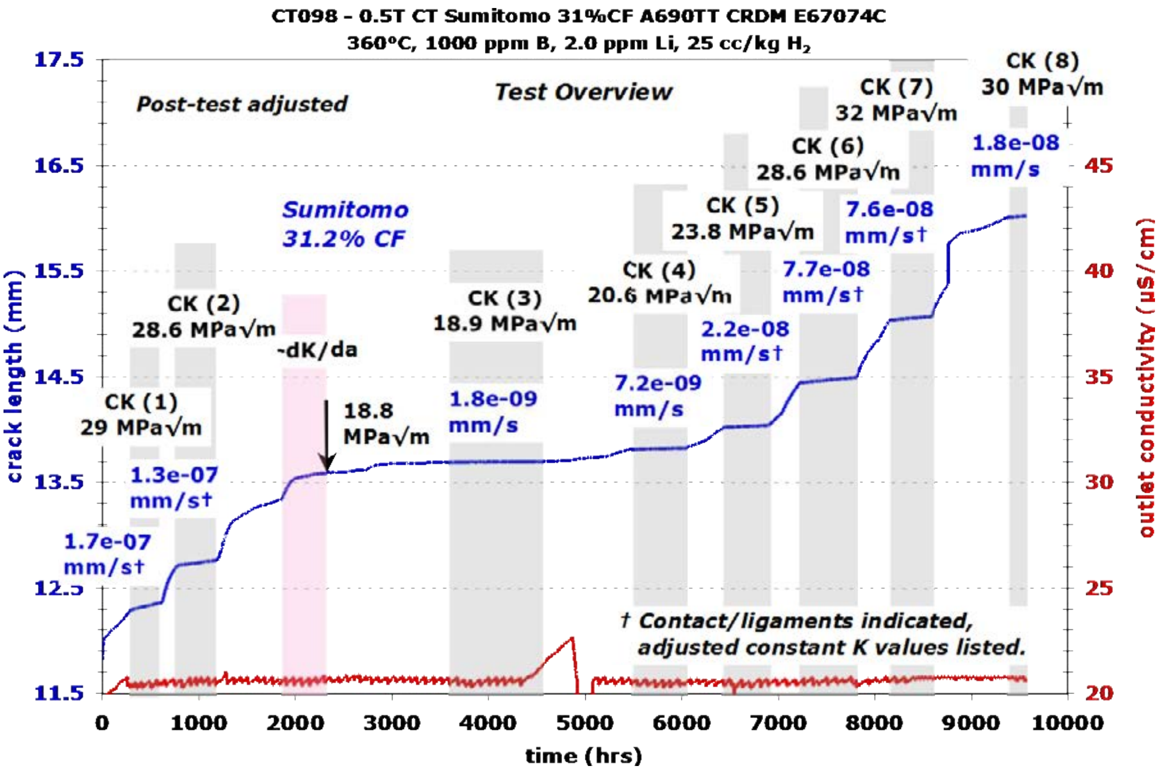

Figure 4.41 Overview of the entire SCC test on the 31%CF Sumitomo E67074C specimen CT098

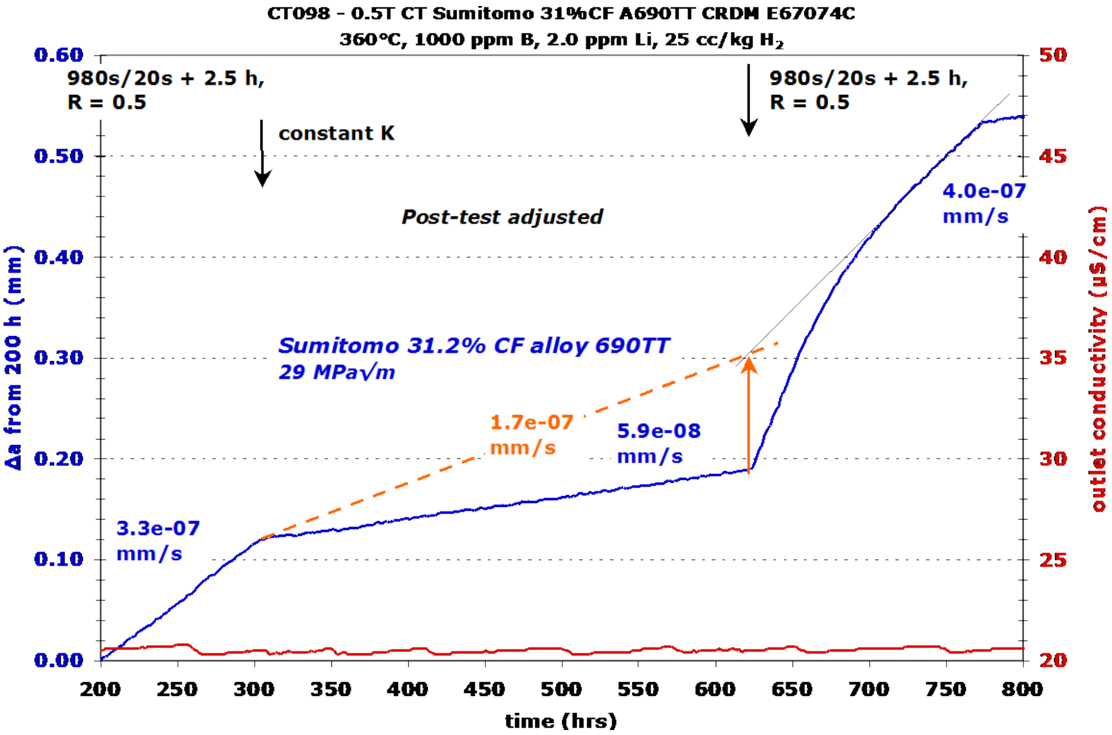

Figure 4.42 Constant K response of the 31%CF Sumitomo E67074C specimen CT098, at 29 MPa√m near the beginning of the test

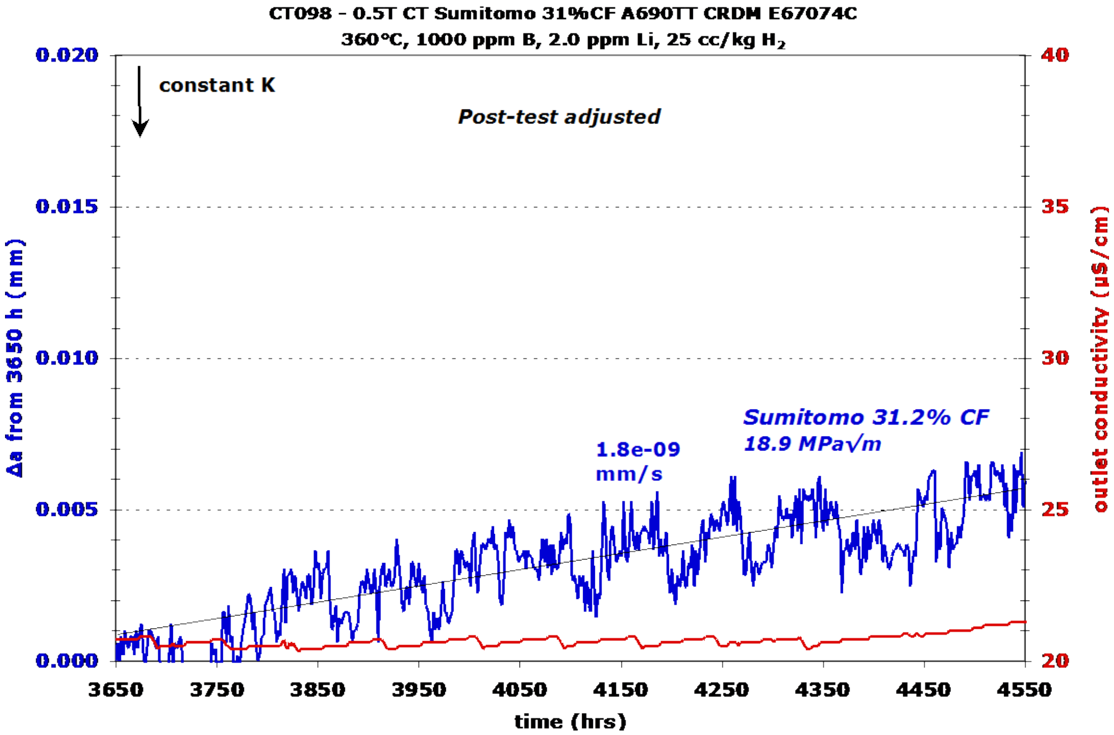

Figure 4.43 Constant K response of the 31%CF Sumitomo E67074C specimen CT098 at 19 MPa√m

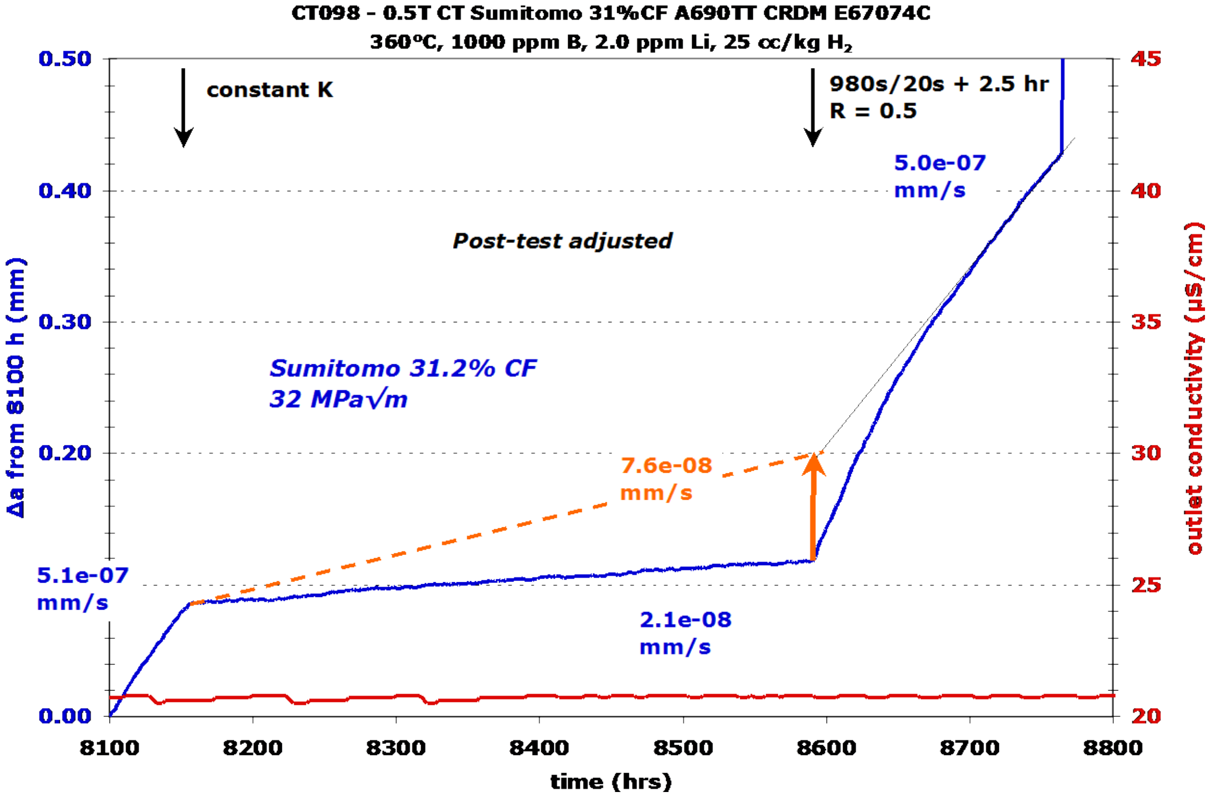

Figure 4.44 Constant K response of the 31%CF Sumitomo E67074C specimen CT098 at 32 MPa√m near the end of the test

An optical image of the crack surface of the 31%CF Sumitomo CRDM specimen is presented in Figure 4.45. There is some variability in crack length at the multiple grain size level, but the crack front is relatively straight. Many uncracked ligaments, some ~0.75 mm in size can be seen showing that even highly susceptible alloy 690 can have ligament formation. This specimen that was run in series with CT099, is another example showing that aggressive load cycling is not necessarily sufficient for removing ligaments. DCPD was found to over predict the actual in-situ crack extension by 25%, thus actual K values and crack growth rates are slightly lower than what was indicated by DCPD during the test.

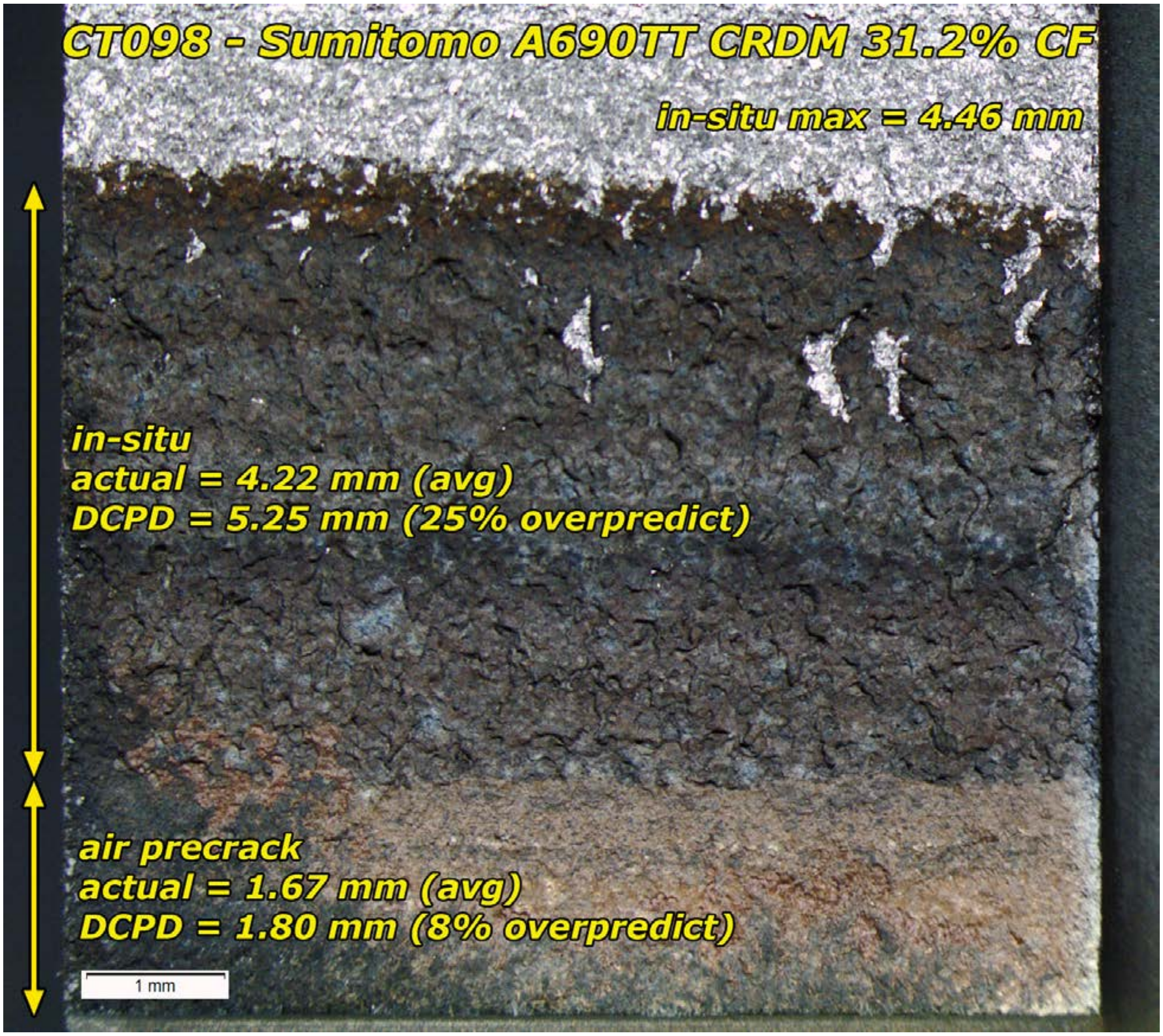

Figure 4.45 Optical image of the as-tested crack growth surface of the 31%CF Sumitomo E67074C specimen CT098

A complementary SEM-SE image for the entire crack surface is shown in Figure 4.46. SEM images were taken from the opposite face than used for optical imaging, so the appearance is flipped. As previously noted, IGSCC cracking appears to have started from the very onset of testing in high-temperature PWR water even at aggressive 0.1 Hz (R-0.5) load cycling. A line drawn across the crack surface whether near the onset of testing or near the final crack front was found to be ≥95% IG. Higher magnification imaging of the boxed region is shown in Figure 4.47. Arrows point to oxidized TG cracking that took place during testing. These were generally small in size compared to the post-test TG fracture. It is thought that this TG cracking took place as a result of in-situ load cycling, supporting the need to periodically load cycle the specimen to remove as many ligaments as possible even for SCC-susceptible, highly CW alloy 690.

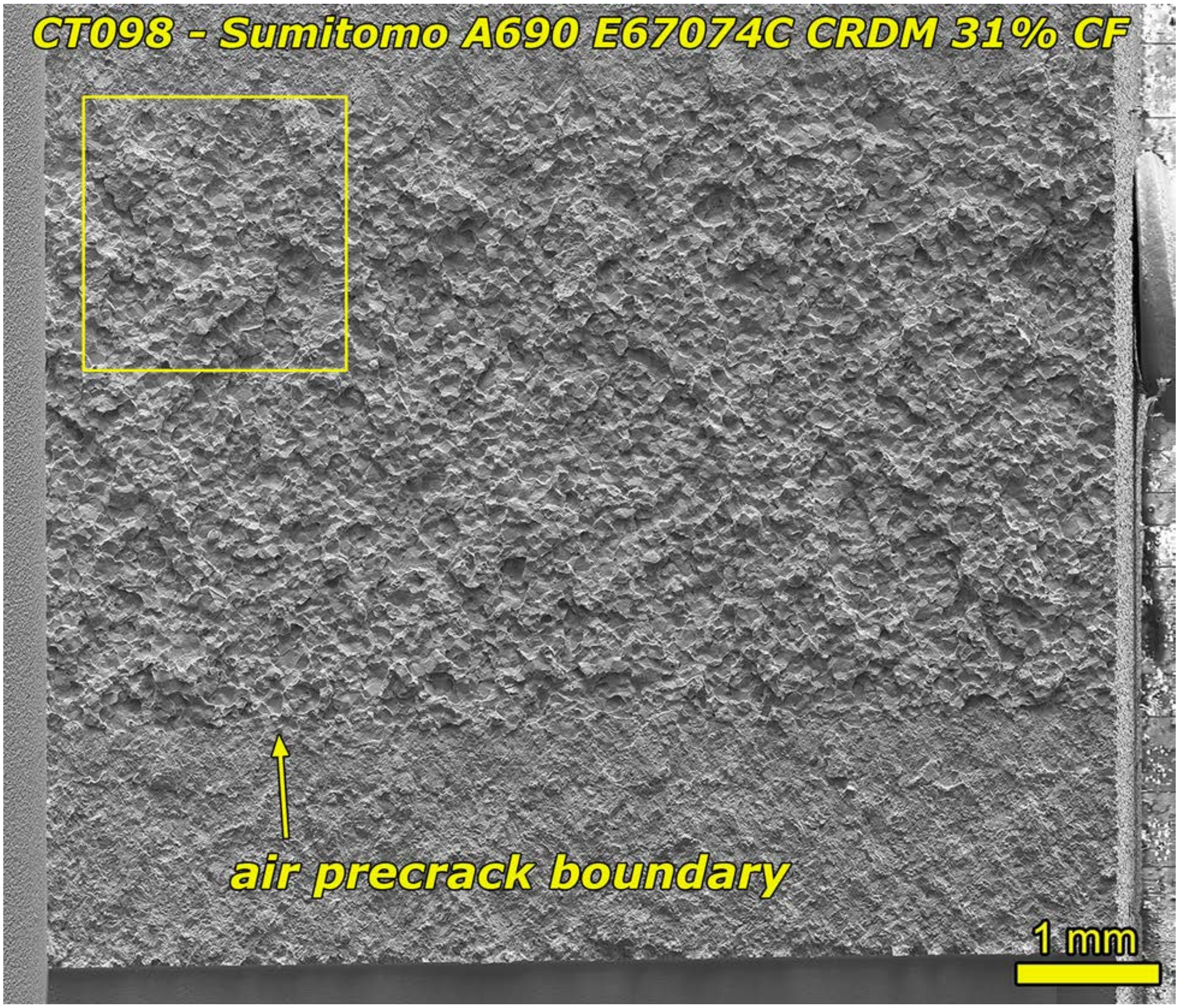

Figure 4.46 **SEM BSE image of the cleaned crack growth surface of the 31%CF Sumitomo E67074C specimen CT098. The final crack front was found to be ≥95% IG anywhere in the IG region. Yellow-boxed region is area of higher magnification imaging in Figure 4.47. Note that SEM images are from the opposite crack face than what was used for optical images.**

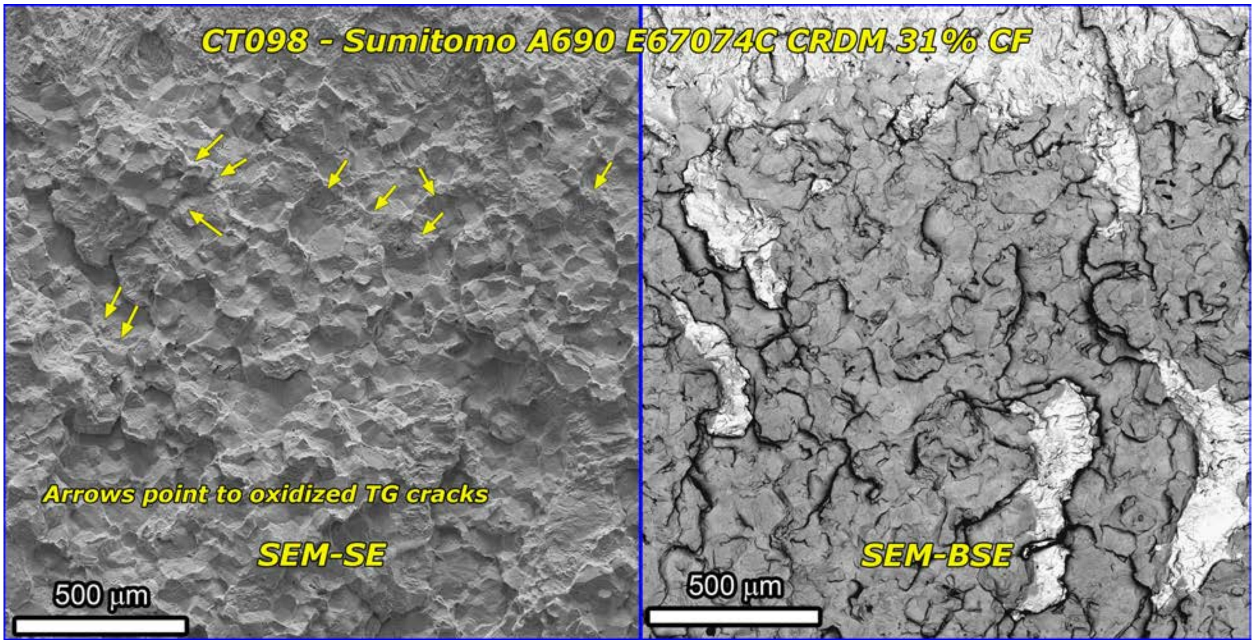

Figure 4.47 **Higher magnification side-by-side SEM-SE and BSE images of the cleaned crack growth surface of the 31%CF Sumitomo E67074C specimen CT098. Arrows point to oxidized TG cracks.**

4.3.4 Crack Growth Testing of the As-Received TK-VDM (Doosan) Bar 133454 Specimen - CT108

This specimen, also referred to as the Doosan CRDM material, was tested in series with an as-received (TT) TK-VDM plate specimen (CT107, described later in the report). A summary of test conditions and specimen response for the as-received TK-VDM specimen is given in **Table 4.11** while an overview plot of the entire test is provided in **Figure 4.48**. Four different assessments of constant K SCC CGRs were performed, two at 30 MPa√m, and then one each at 35 MPa√m and 39 MPa√m. The first constant K observation, which was preceded by a final transitioning step 980s/20s + 2.5-hour hold, resulted in an SCC CGR of <1x10^{-9} mm/s. As part of ongoing attempts to optimize SCC transitioning parameters for highly resistant materials, a 9980s/20s load cycle that produces a slower crack-tip strain rate was adopted for the remainder of the test and was typically combined with a 2.5-hour hold for the final transitioning step. The second constant K observation at 30 MPa√m again produced an SCC CGR of <1x10^{-9} mm/s, but a steady CGR of ~1x10^{-9} mm/s was attained at 35 MPa√m and a rate of ~2.5x10^{-9} mm/s was initially obtained for the 39 MPa√m assessment but eventually slowed to ~1x10^{-9} mm/s (**Figure 4.49**). Application of cycle+hold loading after each constant K observation revealed no indication of crack growth hidden by contact or ligament formation. Thus some general effect of stress intensity was observed, but SCC CGRs remained well below values of concern. Following completion of the test, the specimen was destructively examined.

Table 4.11 Test conditions and specimen response for the as-received TK-VDM (Doosan) alloy 690TT CRDM bar 133454 specimen CT108

								CT108 A690AR Doosan bar 133454		
Test Step	Start (h)	Duration (h)	R	Freq (Hz)	Hold (h)	Dissolved Hydrogen (cc/kg H_2)	Temp (°C)	Kmax (MPa√m)	CGR (mm/s)	Approx. Crack Extension (mm)
1	0	6	0.5	0.1	0	25	360	30	3.1E-06	0.063
2	6	40	0.5	0.01	0	25	360	30	5.9E-07	0.090
3	46	281	0.5	980s/20s	0	25	360	30	8.8E-08	0.090
4	327	457	0.5	980s/20s	2.5	25	360	30	1.2E-08	0.020
5	784	703	---	const K	---	25	360	30	4.5E-10	0.002
6	1487	305	0.5	980s/20s	2.5	25	360	30	1.9E-08	0.019
7	1792	647	0.5	9980s/20s	0	25	360	30	1.1E-08	0.026
8	2439	209	---	const K	---	25	360	30	NG	0.000
9	2648	484	0.35	9980s/20s	0	25	360	30	2.3E-08	0.041
10	3132	99	0.5	9980s/20s	0	25	360	30->35	NM	0.020
11	3231	235	0.5	9980s/20s	0	25	360	35	3.0E-08	0.027
12	3466	319	0.5	9980s/20s	1	25	360	35	2.3E-08	0.025
13	3785	184	0.5	9980s/20s	2.5	25	360	35	2.0E-08	0.014
14	3969	842	---	const K	---	25	360	35	8.9E-10	0.004
15	4811	197	0.5	9980s/20s	2.5	25	360	35	1.5E-08	0.010
16	5008	130	0.5	9980s/20s	2.5	25	360	35->39	NM	0.042
17	5138	270	0.5	9980s/20s	2.5	25	360	39	1.9E-08	0.026
18	5408	969	---	const K	---	25	360	39	1.1E-09	0.007
19	6377	115	0.5	9980s/20s	2.5	25	360	39	2.1E-08	0.006

NG = no growth
NM = not measured

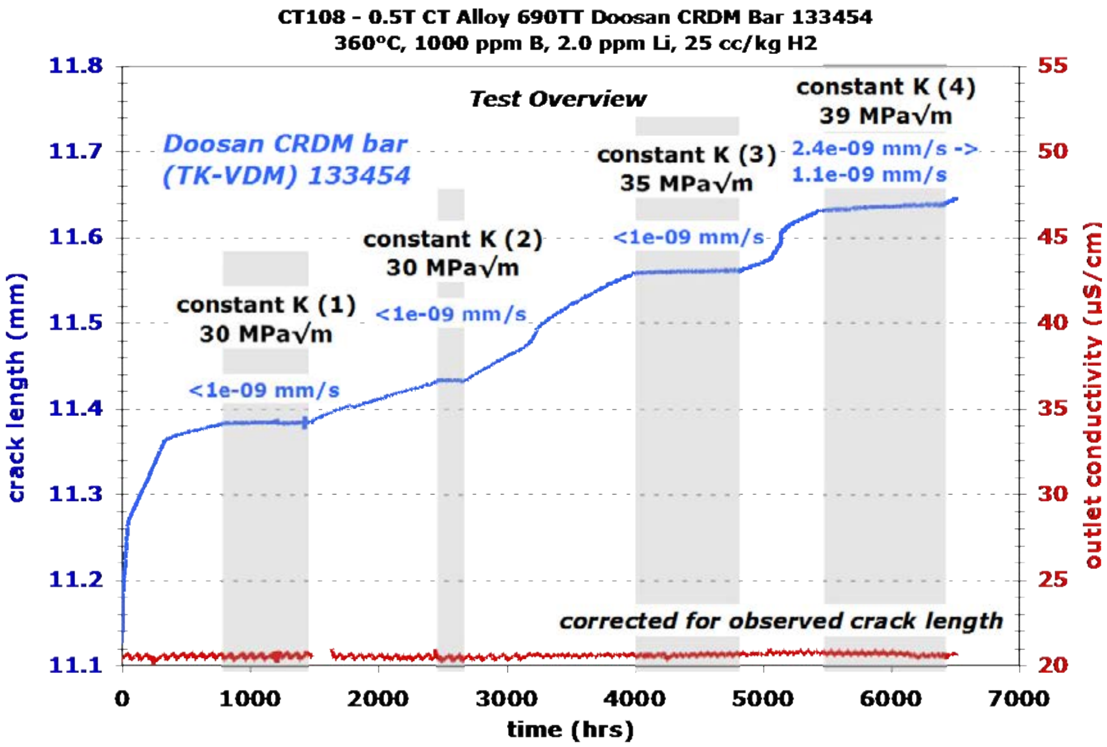

Figure 4.48 Overview of the entire SCC test on the as-received TK-VDM (Doosan) 133454 CRDM bar specimen CT108

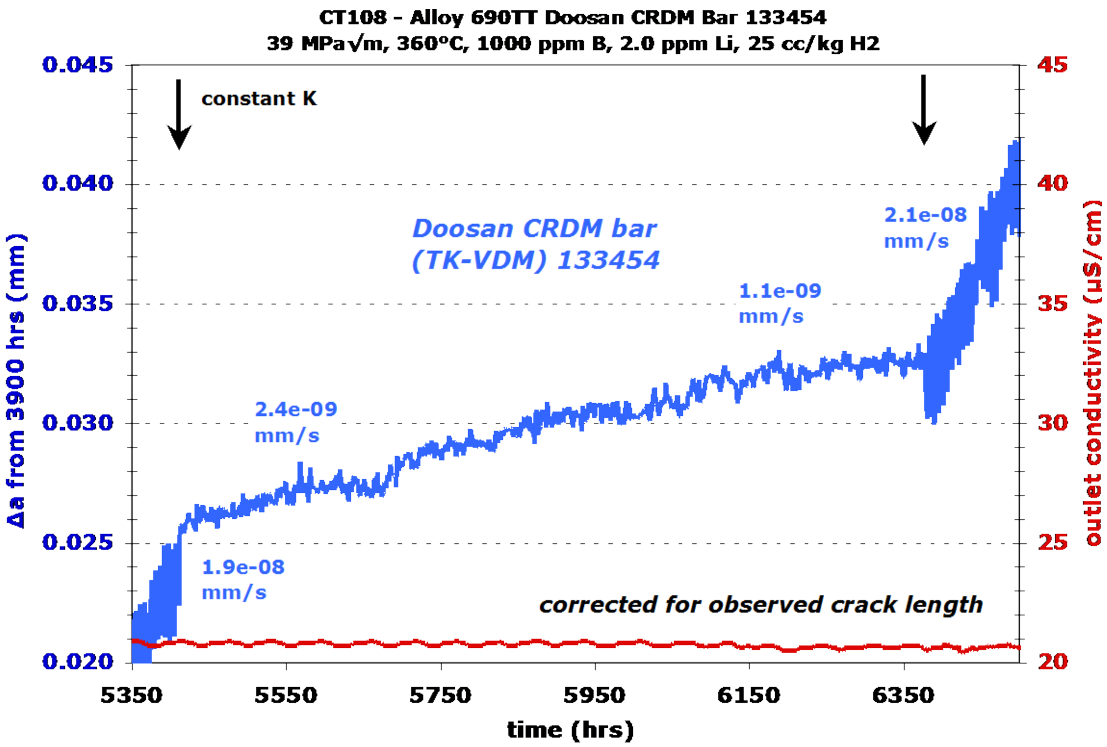

Figure 4.49 Constant K response of the as-received TK-VDM 133454 CRDM bar specimen CT108 at 38 MPa√m

An optical image of the crack surface of the as-received TK-VDM 133454 specimen is presented in Figure 4.50. The crack front is relatively straight from one side to the other but has a few protrusions suggestive of IG engagement. A few unbroken ligaments can be seen with one very close to the start of the in-situ testing. For the in-situ portion of the test, DCPD under predicted actual crack length by a very modest 10%. An SEM-SE image of the entire crack surface is presented in Figure 4.51, while a higher magnification image of a portion of the crack surface along the final crack front is presented in Figure 4.52.

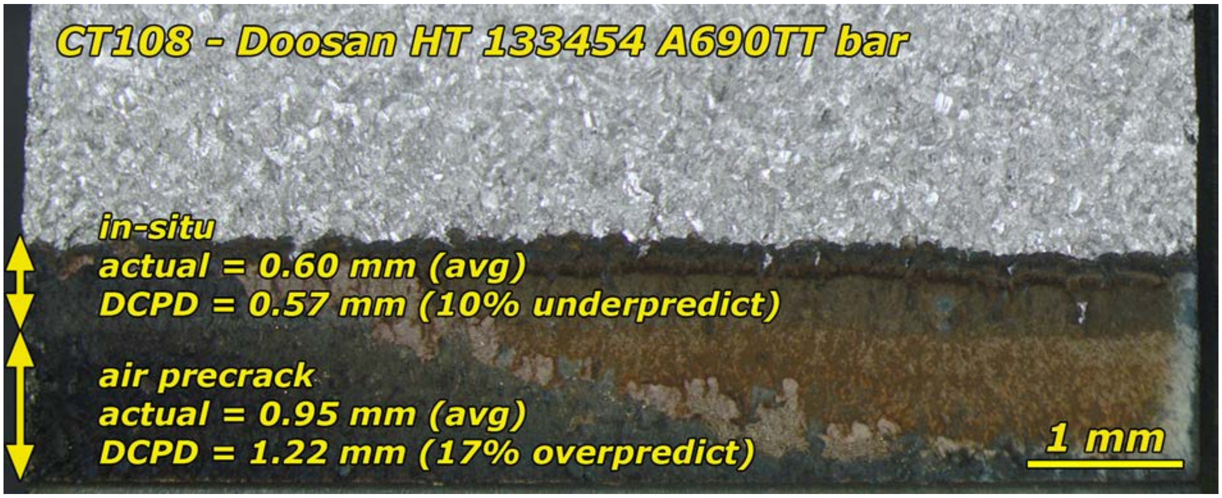

Figure 4.50 Optical image of the as-tested crack growth surface of the as-received TK-VDM 133454 CRDM bar specimen, CT108

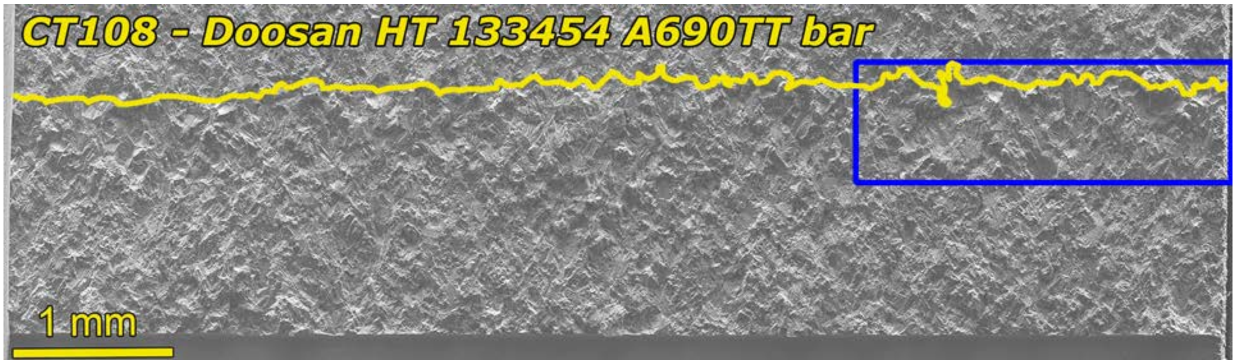

Figure 4.51 SEM-SE image of the cleaned crack growth surface of the as-received TK-VDM 133454 alloy 690TT CRDM bar specimen, CT108. Yellow line denotes the final crack front, and the blue box is a region of higher magnification shown in Figure 4.52.

Figure 4.52 **Higher magnification SEM BSE image of the cleaned crack growth surface of the as-received TK-VDM 133454 CRDM bar specimen, CT108. Only a few isolated IG facets were found along the final crack front.**

4.3.5 Crack Growth Testing of the 21.6%CF TK-VDM (Doosan) CRDM Bar 133454 Specimen - CT102

This 21.6%CF specimen was tested in series with a 21.4%CF Allvac plate specimen (CT101, described later in the report). A summary of test conditions and specimen response for the 22%CF Doosan specimen is given in **Table 4.12** while an overview plot of the entire test is provided in **Figure 4.53**.

Five different assessments of constant K SCC CGRs were performed, two at ~30 MPa√m, one at a corrected value of 39 MPa√m, and two at a corrected value of ~50 MPa√m. The ~30 MPa√m constant K observations had similar DCPD-based and adjusted values of ~2.4x10^{-8} mm/s, and ~4.3x10^{-8} mm/s, respectively. The first constant K observation is shown in Figure 4.54. The 39 MPa√m observation produced approximately the same response while the ~50 MPa√m observations produced ~1.3x higher DCPD-based values and ~1.7x higher adjusted values suggesting a very mild K dependence. It will be shown in Chapter 6 that on average, a very mild K dependence was observed for well-engaged specimens at K values of ≥30 MPa√m. The test was ended at constant K to get a clearer understanding of ligament or contact for formation under this condition.

Table 4.12 Test conditions and specimen response for the 21%CF TK-VDM (Doosan) alloy 690TT CRDM bar 133454 specimen CT102

								CT102 A690 CRDM Doosan 21.6% CF		
Test Phase	Start (h)	Duration (h)	R	Freq (Hz)	Hold (h)	Dissolved Hydrogen (cc/kg H_2)	Temp (°C)	Kmax (MPa√m)	CGR (mm/s)	Approx. Crack Extension (mm)
1	0	11	0.5	0.1	0	25	360	31	7.6E-06	0.303
2	11	35	0.5	0.01	0	25	360	30	1.7E-06	0.220
3	46	156	0.5	980s/20s	0	25	360	31	4.1E-07	0.182
4	202	552	0.5	980s/20s	2.5	25	360	31	6.0E-08	0.114
5	754	329	0.5	980s/20s	10	25	360	31	3.7E-08	0.042
6	1083	538	---	const K	---	25	360	31	2.1E-08	0.038
6*	1083	---	---	const K	---	25	360	31	3.5E-08	NA
7a	1621	193	0.5	980s/20s	2.5	25	360	31	1.3E-07	0.111
7b	1814	291	0.5	980s/20s	2.5	25	360	31	7.6E-08	0.100
8	2105	328	0.5	12s/12s	2.77	25	360	31	6.7E-08	0.079
9	2433	339	0.5	980s/20s	2.5	25	360	31	9.7E-08	0.110
10	2772	516	---	const K	---	25	360	32	2.8E-08	0.031
10*	2772	---	---	const K	---	25	360	32	4.3E-08	0.000
11	3288	308	0.5	980s/20s	2.5	25	360	32	1.0E-07	0.124
12	3596	137	0.5	980s/20s	2.5	25	360	32->40	Incr.	0.077
13	3733	124	0.5	980s/20s	2.5	25	360	40	2.1E-07	0.097
14	3857	522	---	const K	---	25	360	40	2.7E-08	0.040
14*	3857	---	---	const K	---	25	360	40	3.6E-08	0.000
15	4379	213	0.5	980s/20s	2.5	25	360	41	3.3E-07	0.278
16	4592	32	0.5	980s/20s	2.5	25	360	41->49	Incr.	0.054
17	4624	231	0.5	980s/20s	2.5	25	360	49	3.4E-07	0.343
18	4855	747	---	const K	---	25	360	49	4.0E-08	0.094
18*	4855	---	---	const K	---	25	360	49	5.7E-08	NA
19	5602	143	0.5	980s/20s	2.5	25	360	50	6.3E-07	0.386
20	5745	885	---	const K	---	25	360	51	4.0E-08	0.118

* CGR adjusted for contact/ligament formation
NA - Not applicable
Incr. - Increasing

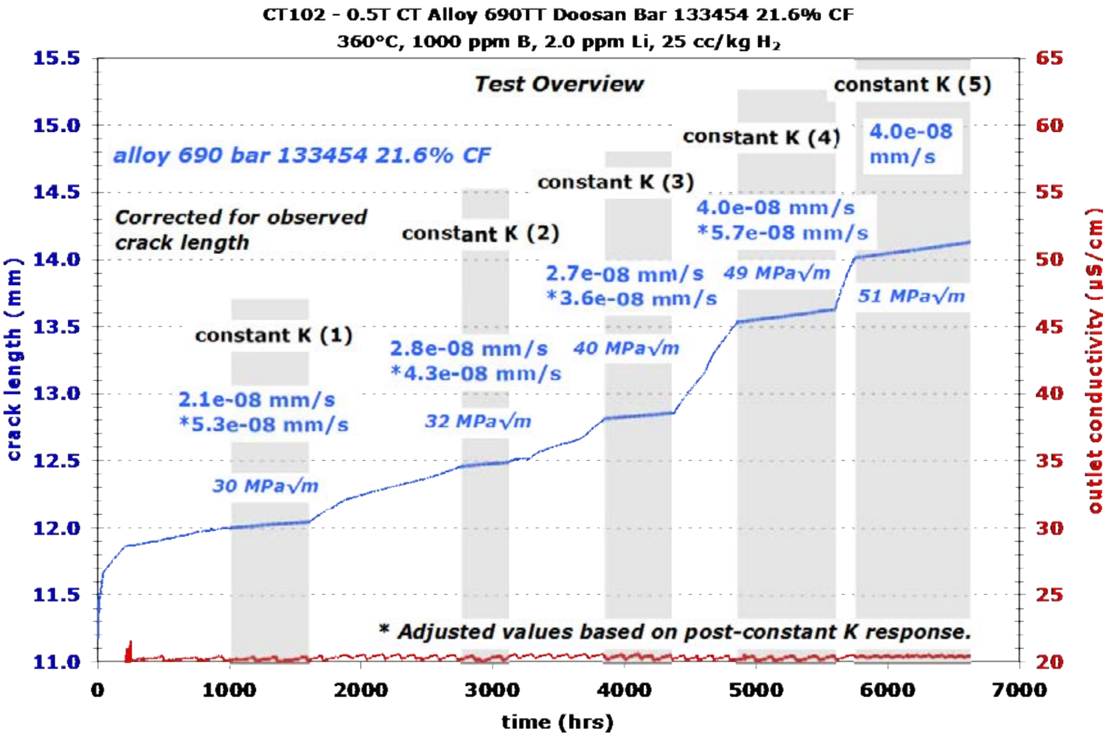

Figure 4.53 Overview of the entire SCC test on the 21%CF TK-VDM (Doosan) 133454 CRDM bar specimen CT102

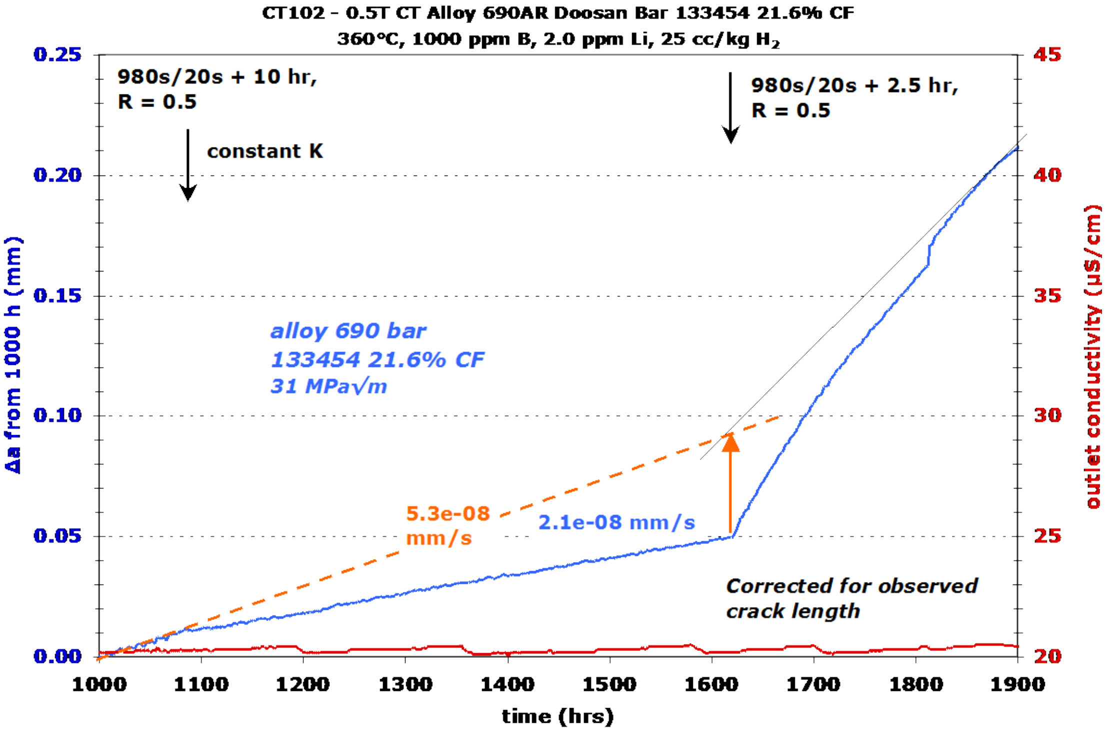

Figure 4.54 Constant K response of the 21%CF TK-VDM 133454 CRDM bar specimen CT102 at 30 MPa√m

An optical image of the crack surface of the 21%CF TK-VDM 133454 CRDM bar specimen is presented in Figure 4.55. Like other high SCC CGR materials that have been discussed thus far, there is substantial fingered growth along the final crack front and a large number of unbroken ligaments well behind the final crack front. Despite the fingered growth along the crack front suggesting partial IG engagement, SEM imaging (Figure 4.56) revealed that the final crack front was ≥95% IG. Moreover, the crack surface behind the crack front was ≥90% IG.

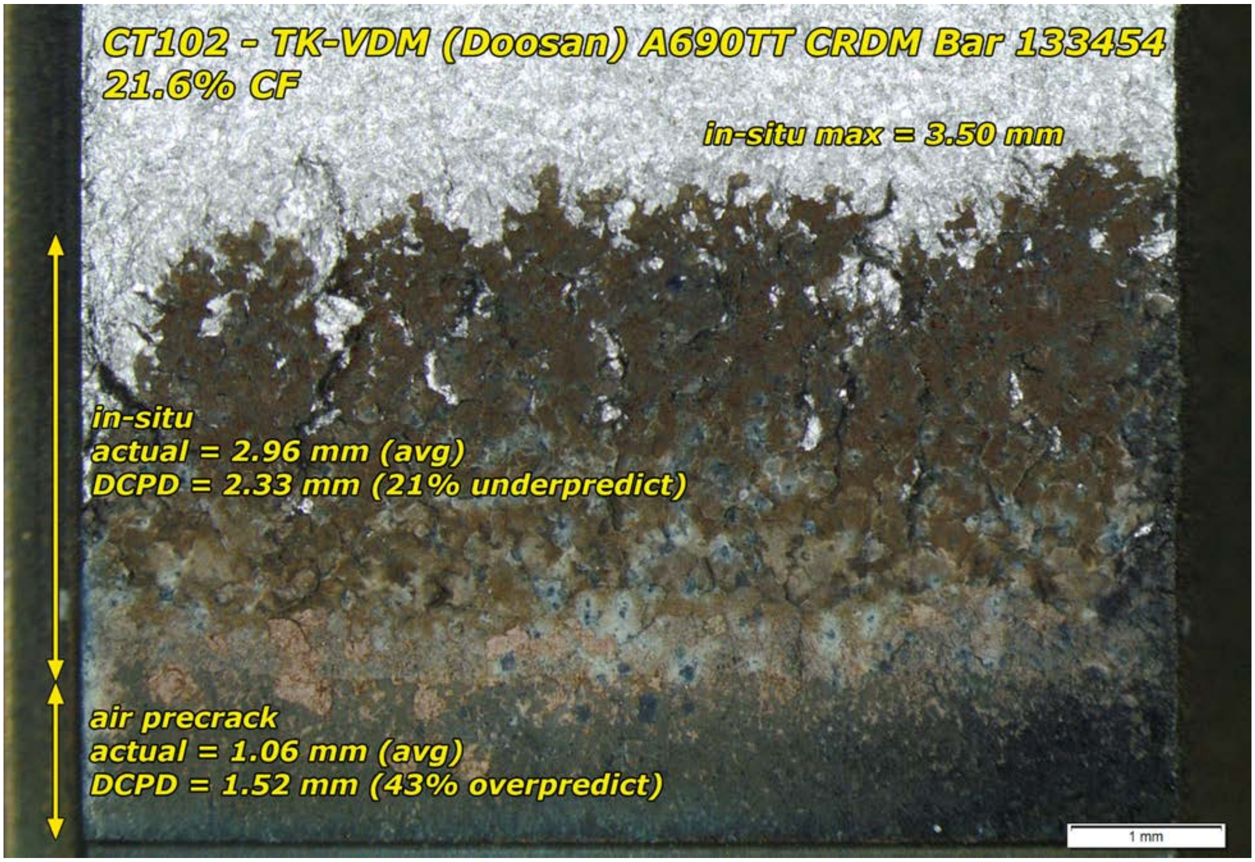

Figure 4.55 **Optical image of the as-tested crack growth surface of the 21%CF TK-VDM 133454 CRDM bar specimen CT102**

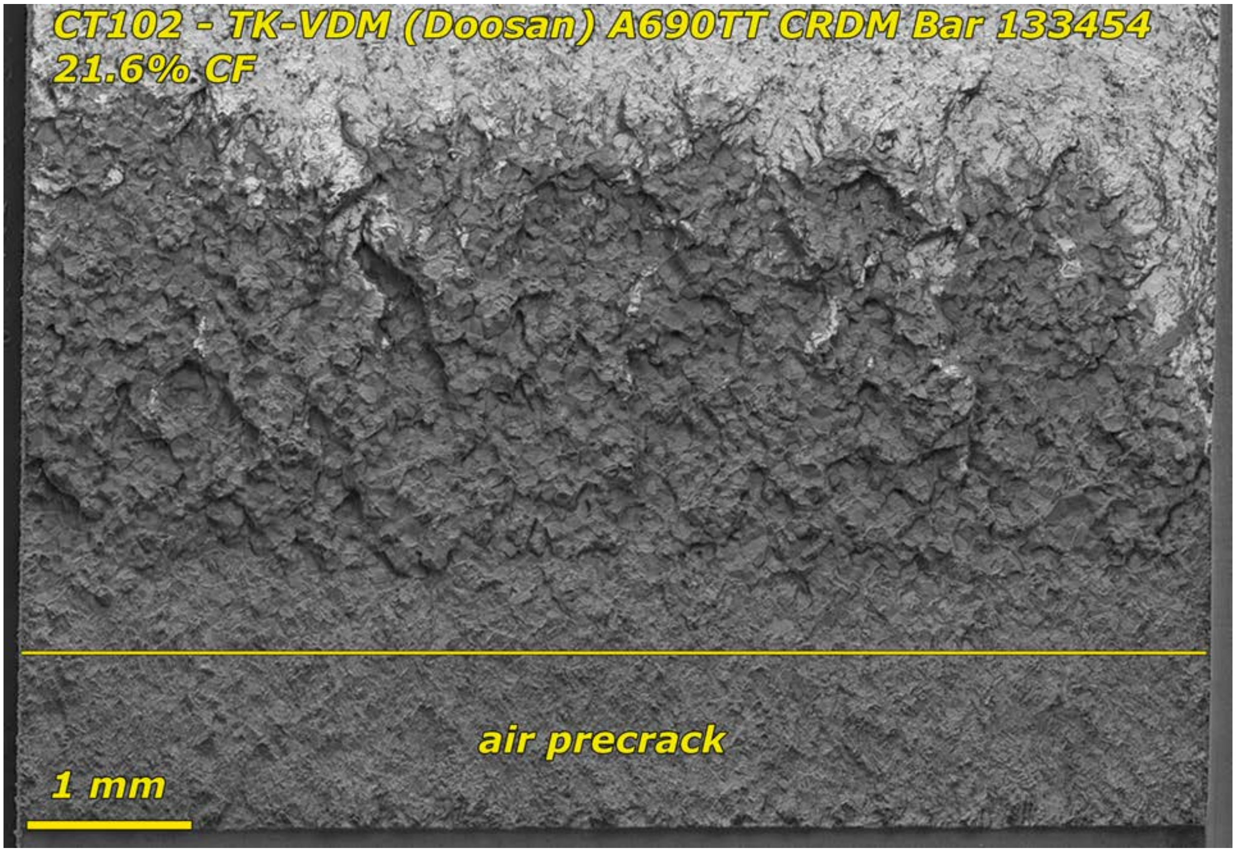

Figure 4.56 SEM BSE image of the cleaned crack growth surface of the 21%CF TK-VDM 133454 CRDM bar specimen CT102. The final crack front was found to be ≥95% IG despite the variable length crack front.

The presence of ligaments was studied more thoroughly for this specimen, in particular, there was an interest in determining whether there were oxidized TG cracks that could represent ligaments that had been broken during in-situ load cycling. Figure 4.57 presents SEM-SE and SEM-BSE images where yellow highlights represent TG ligaments that were broken by post-test fatigue cracking, and blue highlights represent TG cracks that formed during testing. Perhaps not surprisingly, there were many instances of oxidized TG cracks that formed in-situ. More interestingly, some of the post-test fatigue fractured ligaments were adjacent to oxidized TG cracks suggesting that ligaments were slowly being fractured in-situ by fatigue cycling. However as was demonstrated for CT099 where aggressive 0.1 Hz load cycling was applied in-situ, some ligaments can be difficult to remove even during aggressive cycling.

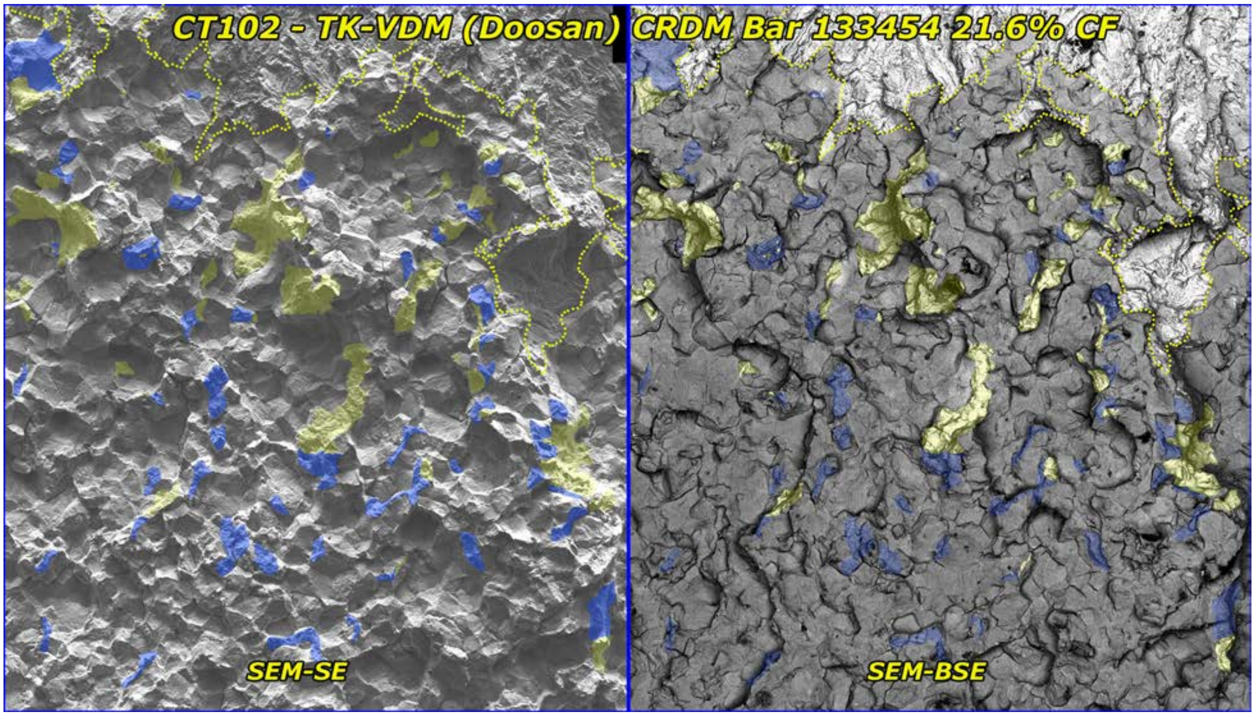

Figure 4.57 **Higher magnification SEM SE and BSE images of the crack growth surface of the 21%CF TK-VDM CRDM bar specimen CT102**

4.4 Summary of SCC Tests on CRDM Materials

This chapter has reviewed new SCC crack-growth tests at PNNL on alloy 690 CRDM materials in both as-received and cold worked conditions. The results presented remove any uncertainty with respect to the SCC susceptibility of alloy 690 and establishes that TT materials with excellent starting microstructures exhibit CGRs of concern at moderate-to-high levels of cold work (>20% reduction). All of the CRDM heats in the TT condition have equiaxed grain structures, a semi-continuous distribution of grain boundary Cr carbides, and no significant evidence for impurity stringers or inclusions. As a result, heat-to-heat microstructural differences are minimized, and the influence of cold work on SCC can be better established. SCC CGRs and percent engagement at ~30 MPa√m for these specimens along with prior tests are summarized in Table 4.13 for TT materials only, while Table 4.14 includes SA versus TT along with the response of the 31%CR specimen given a recovery treatment to better show the difference in response when given a solution anneal prior to cold working. Selected aspects of these results are presented here with a more detailed discussion delayed to Chapter 6 where the CRDM and plate material results can be efficiently discussed both individually and as a group.

Table 4.13 Summary of percent IG engagement and measurements of SCC CGRs (at ~30 MPa√m) for the alloy 690 TT CRDM specimens

ID	Producer	Heat #	Condition	% Engagement	SCC-CGR (mm/s) †
CT026	Valinox	WP142	TT*	3	5-9x10^{-10} [350°C]
CT027	Valinox	WP140	TT*	3	6-9x10^{-10} [350°C]
CT015	Valinox	RE243	TT*	3	3x10^{-10} [325°C]
CT104	Valinox	RE243	TT*+11.6%CF	37	1.7-4.2x10^{-9}
CT020	Valinox	RE243	TT*+17%CR	5	5x10^{-10} [325°C]
CT054	Valinox	RE243	TT*+17%CR	18	2.5x10^{-9}
CT100	Valinox	RE243	TT*+21%CF	85	1.6-2.1x10^{-8} (2.6-3.8x10^{-8})§
CT038	Valinox	RE243	TT*+31%CR	94	0.5-1.2x10^{-7}
CT099	Valinox	RE243	TT*+31%CF	95	3.0-6.4x10^{-8} (0.7-1.2x10^{-7})
CT093	Valinox	WP787	TT*+20%TS	90	3.1-4.9x10^{-9} (1.0-1.1x10^{-8})
CT103	Sumitomo	E67074C	TT*+12.7%CF	8	3-7x10^{-10}
CT098	Sumitomo	E67074C	TT*+31%CF	95	2.1-5.9x10^{-8} (0.8-1.7x10^{-7})
CT108	TK-VDM	133454	TT*	1	5x10^{-10}
CT102	TK-VDM	133454	TT*+21%CF	90	2.0-2.8x10^{-8} (4.2-4.4x10^{-8})

* As-received condition of the material

† Test temperature listed if other than 360°C

§ Values in parenthesis are adjusted for contact/ligament formation.

Table 4.14 Comparison of percent engagement and SCC CGR measurements (at ~30 MPa√m) for the alloy 690 TT and SA CRDM specimens

ID	Producer	Heat #	Condition	% Engagement	SCC-CGR (mm/s)†
CT015	Valinox	RE243	TT*	3	3x10^{-10} [325°C]
CT014	Valinox	RE243	TT+SA§	3	2x10^{-10} [325°C]
CT020	Valinox	RE243	TT+17%CR	5	5x10^{-10} [325°C]
CT019	Valinox	RE243	TT+SA+17%CR	3	2x10^{-10} [325°C]
CT054	Valinox	RE243	TT+17%CR	18	2.5x10^{-9}
CT068	Valinox	RE243	TT+SA+17%CR	5	1.7-2.2x10^{-9}
CT022	Valinox	RE243	TT+30%CR^{TL}	50	1.2x10^{-8} [350°C]
CT023	Valinox	RE243	TT+SA+30%CR^{TL}	10	1.0x10^{-9} [350°C]
CT038	Valinox	RE243	TT+31%CR	94	0.5-1.2x10^{-7}
CT039	Valinox	RE243	TT+SA+31%CR	65	5.8-9.7x10^{-9}
CT053	Valinox	RE243	TT+31%CR+RT‡	45	4.3x10^{-9}

* As-received condition of the material

† Test temperature listed if other than 360°C

§ 1100°C/1 h + Water Quench

^{TL} These specimens were tested in the T-L orientation, all others in the S-L orientation.

‡ Recovery Treatment (RT) - 700°C/1 h + Air Cool

When constant K SCC CGRs at 360°C and ~30 MPa√m are plotted as function of cold work (Figure 4.58), an approximate linear trend is observed for the RE243 TT data (left plot) where the most detailed analysis has been performed with tests on materials in the as- received, 11.6%CF, 17%CR, 21%CF, 31%CR and 31%CF conditions. As noted in the plot, additional transitioning performed on the 11.6%CF material did lead to a higher SCC CGR. For the 17%CR material, only a single transitioning sequence was performed, and it is thought that additional transitioning would have raised the SCC CGR for this material as well. Trend lines are drawn to bound the actual data or expected response for the RE243 TT. A continuous increase in SCC susceptibility with %CW can be seen with measured CGRs increasing by ~200X upon reaching 1×10^{-7} mm/s, a CGR that is comparable to the disposition curve for MA alloy 600. In the 11-17%CW range, the material has very limited susceptibility and extensive transitioning efforts may be required to achieve peak SCC CGRs.

The addition of the other three heats (middle plot) all in the TT condition does not alter the general correlation indicating that alloy 690 materials with excellent microstructures can become susceptible to IGSCC after ~10% cold work. One exception to this trend is the 12.7%CF Sumitomo material. This specimen was tested in tandem with the 11.6%CF RE243 where both underwent extensive transitioning sequences, and while the RE243 did exhibit susceptibility, the Sumitomo specimen was more resistant. This suggests that at these low CW levels, a 10x range in susceptibility may exist due to some materials being completely resistant with CGRs below 1×10^{-9} mm/s and others exhibiting low SCC susceptibility with rates of $\sim 5 \times 10^{-9}$ mm/s.

The SA RE243 and the recovery treatment RE243 materials (right plot) show similar response to the TT materials up to 17% CW where susceptibility is limited. However, at the highest CW level, they have a distinctly different response than the TT materials. It is worth noting that magnitude of the intergranular engagement for the cold worked SA materials was commensurate with their SCC CGRs.

For the series of correlations that are presented here, the lines drawn to bound the data were generated by hand rather than by a statistical fit and provide a visual marker of the data scatter. The presence of outliers indicates that a range of factors (e.g., material starting condition, efforts to fully transition a specimen, uncertainty in crack growth rate, IMD, or hardness, etc.) are causing the response of a specimen to not be captured by the correlations.

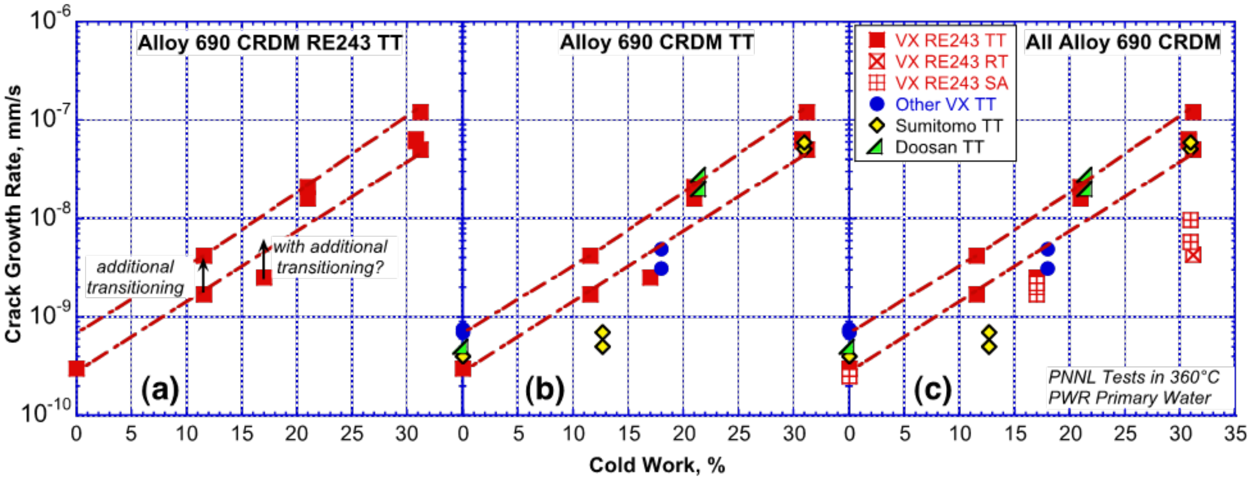

Figure 4.58 Effect of cold work on measured SCC CGRs at ~30 MPa√m for the CRDM heats: (a) RE243TT, (b) all CRDM TT, and (c) all CRDM

The SCC CGR response of all the CRDM materials is plotted in Figure 4.59 as a function of IG engagement, and not unexpectedly, shows an increasing trend. All the materials, both SA and TT, fall into the trend indicating that while the difference in starting microstructure affects the SCC CGR, the relationship between SCC CGR and IG engagement is more universal. The plot suggests that propagation rates of >1x10^{-8} mm/s are not exceeded until reaching ~60% IG engagement. None of the materials achieved 100% IG engagement. Even in the most highly cold worked materials, there was always a small percentage of TG cracking.

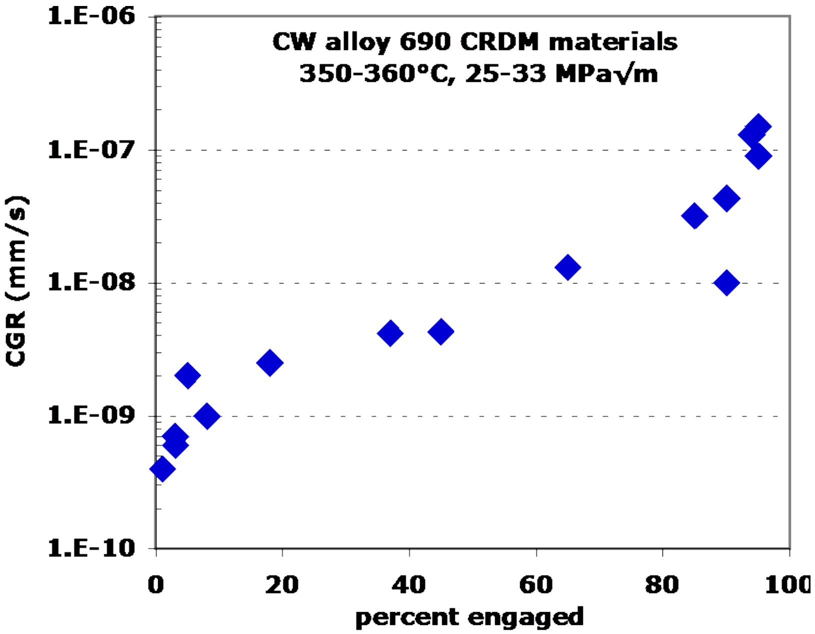

Figure 4.59 **Constant K CGR as a function of percent engagement for CRDM materials at 350-360°C and 25-33 MPa√m**

5 SCC CRACK-GROWTH-RATE TESTING OF ALLOY 690 PLATE AND BAR MATERIALS

5.1 Chapter Overview

Alloy 690 plate and bar products are applicable to selected reactor components, one example being the steam generator divider plate. These product forms can have a banded microstructure due to their fabrication method that often includes fewer remelt steps and undergoing a lower amount of warm or hot working that is useful in eliminating these unwanted microstructures. “Banded” microstructures have a high density of carbides or TiN as bands or sheets due to a non-uniform compositional distribution. These regions often have a finer grain size due to the second phases inhibiting grain growth during subcritical annealing processes while in regions away from these bands, the grain size is often larger resulting from a lack of carbides to pin the boundaries. The sheet or banded structures are aligned with the processing direction.

It has been suggested that accelerated SCC cracking may take place if the crack growth plane is in a banded plane. Early testing at PNNL [14], GE [15], and ANL [16] showed a range of crack growth rates, some very high, in a heat of alloy 690 plate obtained by ANL. Post-test examination performed at PNNL on a specimen tested at GE shows a crack growth surface that appears to have a mixed IG/TG cracking mode and is highly decorated with TiN particles (Figure 5.1). Because of this potential vulnerability to enhanced cracking and other possible issues associated with the reduced level of processing that sometimes occurs for plate or bar materials, there is significant interest in characterizing the SCC crack growth response of a variety of plate materials in the as-received and cold worked conditions.

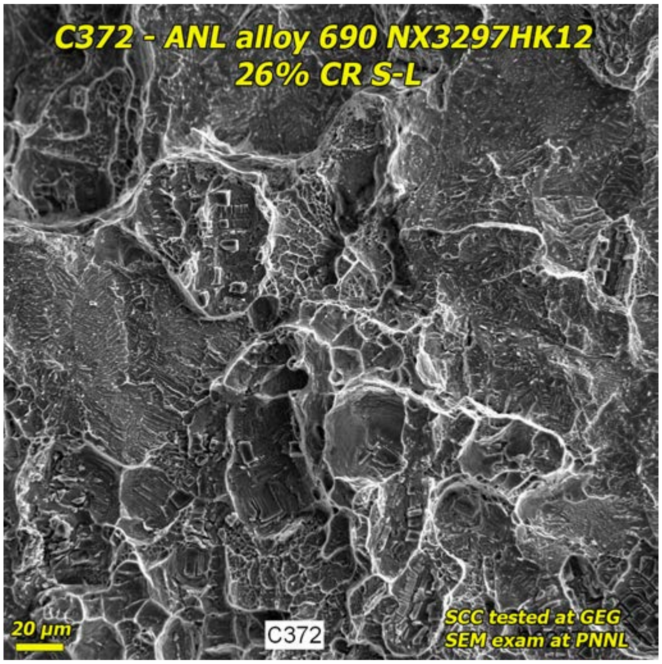

Figure 5.1 SCC crack growth surface of 26%CR alloy 690 NX3297HK12 obtained by ANL and tested at GE

Table 5.1 describes the materials covered in this chapter. There are six unique plate heats, three of which were tested in their as-received condition and in at least one cold worked condition. The effect of a high temperature anneal (HTA) on SCC CGR response was studied for two materials. In addition, a few tests were performed on alloy 690 heat affected zone (HAZ) regions. The general progression for presenting results in this chapter will be to cover results on a heat-by-heat basis. The exception is that the HAZ test results will be covered as a group at the end of the Chapter. Specimens listed in gray were covered prior NUREG in this series [6,7] and are not reported here.

Table 5.1 Table of Alloy 690 plate and bar crack growth specimens discussed in this report

ID	Source/Producer	Heat #	Form	Treatment
CT084	ANL/Special Metals	NX3297HK12	Plate	MA*
CT036	ANL/Special Metals	NX3297HK12	Plate	MA*+26%CR S-L
CT073	ANL-GE/Special Metals	NX3297HK12	Plate	MA*+30%CF S-L/S-T
CT074	ANL-GE/Special Metals	NX3297HK12	Plate	HTA§+30%CF S-L/S-T
CT085	GE/Allvac	B25K-2	Plate	MA*
CT037	GE/Allvac	B25K-2	Plate	MA*+20%CR S-L
CT070	GE/Allvac	B25K-2	Plate	HTA§+20%CR S-L
CT107	EPRI/TK-VDM	114092	Plate	TT*
CT094	GE/TK-VDM	114092	Plate	TT*+32%CF S-L/S-T
CT059	GE-ENSA/Aubert&Duval	WP547	Plate	TT*+32%CF S-L/S-T
CT060	GE-ENSA/Aubert&Duval	WP547	Plate	TT*+22%CR S-L
CT101	EPRI/Allvac	X87N-1	Billet	TT*+21%CF S-L/S-T
CT067	EPRI-ENSA/Aubert&Duval	WP547	Plate	TT* HAZ
CT086	ANL/Special Metals	NX3297HK12	Plate	MA* HAZ
CT087	KAPL/Unknown	Unknown	Plate	AR HAZ

* As-received condition of the material

§ High Temperature Anneal: 1100°C/1h + Water Quench (Higher carbon content in these materials resulted in only partial dissolution of the carbide population.)

5.2 SCC Tests on ANL/Special Metals Heat NX3297HK12

This material was obtained from ANL in a 26%CR S-L condition [16]. As reported in Chapter 3, this material has a high degree of carbide and TiN banding. SCC propagation rates of ~3x10^{-8} mm/s were reported by ANL for tests conducted at 320°C prompting an interest to have this material tested at other laboratories. Pieces of the 26%CR material were distributed to several other laboratories including PNNL along with as-received plate to PNNL. Testing has now been conducted on this heat in the as-received MA condition, the 26%CR S-L condition, and in a 30%CF condition with and without a prior HTA treatment.

5.2.1 ANL/Special Metals Heat NX3297HK12 - Mill Annealed Condition

A 0.5T CT specimen was extracted from the as-received MA plate so that the processing plane, i.e., the banding plane, was coplanar with the specimen crack growth plane. A summary of the test conditions and specimen response is provided in Table 5.2 while an overview of the entire test is shown in Figure 5.2. Two constant K observations were performed at 30 MPa√m and one at 35 MPa√m. For the first constant K, the final transitioning step was a 980s/20s load cycle at R

= 0.5 with a 2.5 h hold at K_{max}, while for the second two transitioning sequences, the final transitioning steps were a 9980s/20s continuous load cycle at R = 0.5 and then the same load cycle with a 2.5 h hold at K_{max}. Sustained growth at $\geq 1x10^{-9}$ mm/s could not be attained for any of the constant K observations, but at 35 MPa√m, an initial SCC CGR of $1.7x10^{-9}$ mm/s was observed as shown in Figure 5.3. Cycle+hold loading applied after constant K showed no evidence for contact or ligament formation that could mask the DCPD crack length estimate.

Table 5.2 Test conditions and specimen response for the as-received ANL alloy 690MA specimen (NX3297HK12), CT084

								CT084 ANL alloy 690MA specimen #1		
Test Phase	Start (h)	Duration (h)	R	Freq (Hz)	Hold (h)	Dissolved Hydrogen (cc/kg H_2)	Temp (°C)	Kmax (MPa√m)	CGR (mm/s)	Approx. Crack Extension (mm)
1	0	12	0.5	0.1	0	25	360	30	4.7E-06	0.202
2	12	93	0.5	0.01	0	25	360	30	8.7E-07	0.288
3	105	335	0.5	0.001	0	25	360	30	1.4E-07	0.153
4	440	714	0.5	980s/20s	2.5	25	360	30	1.4E-08	0.052
5	1154	597	---	const K	---	25	360	30	NG	0.000
6	1751	113	0.5	980s/20s	2.5	25	360	30	1.4E-08	0.005
7	1864	145	0.5	980s/20s	0	25	360	30	1.3E-07	0.055
8	2009	66	0.35	980s/20s	0	25	360	30	2.3E-07	0.055
9	2075	238	0.35	4980s/20s	0	25	360	30	6.1E-08	0.053
10	2313	357	0.35	9980s/20s	0	25	360	30	3.7E-08	0.047
11	2670	627	0.35	9980s/20s	2.5	25	360	30	2.3E-08	0.046
12	3297	519	0.35	9980s/20s	24	25	360	30	5.6E-09	0.010
13	3816	525	---	const K	---	25	360	30	7.9E-10	0.001
14	4341	146	0.5	980s/20s	2.5	25	360	30	1.6E-08	0.008
15	4487	76	0.5	980s/20s	0	11	360	30	1.3E-07	0.024
16	4563	30	0.4	0.1	0	25	360	30	7.2E-06	0.727
17	4593	49	0.5	0.01	0	25	360	30	7.3E-07	0.122
18	4642	190	0.5	980s/20s	0	25	360	30	1.5E-07	0.100
19	4832	392	0.5	980s/20s	2.5	25	360	30	1.6E-08	0.025
20	5224	552	0.35	9980s/20s	2.5	25	360	30	2.4E-08	0.046
21	5776	163	0.35	9980s/20s	2.5	25	360	30->35	Incr.	0.029
22	5939	185	0.35	9980s/20s	2.5	25	360	35	4.2E-08	0.030
23	6124	723	---	const K	---	25	360	35	5.3E-10	0.003
24	6847	143	0.5	980s/20s	2.5	25	360	35	2.3E-08	0.012

NG = No growth
Incr. = Increasing CGR

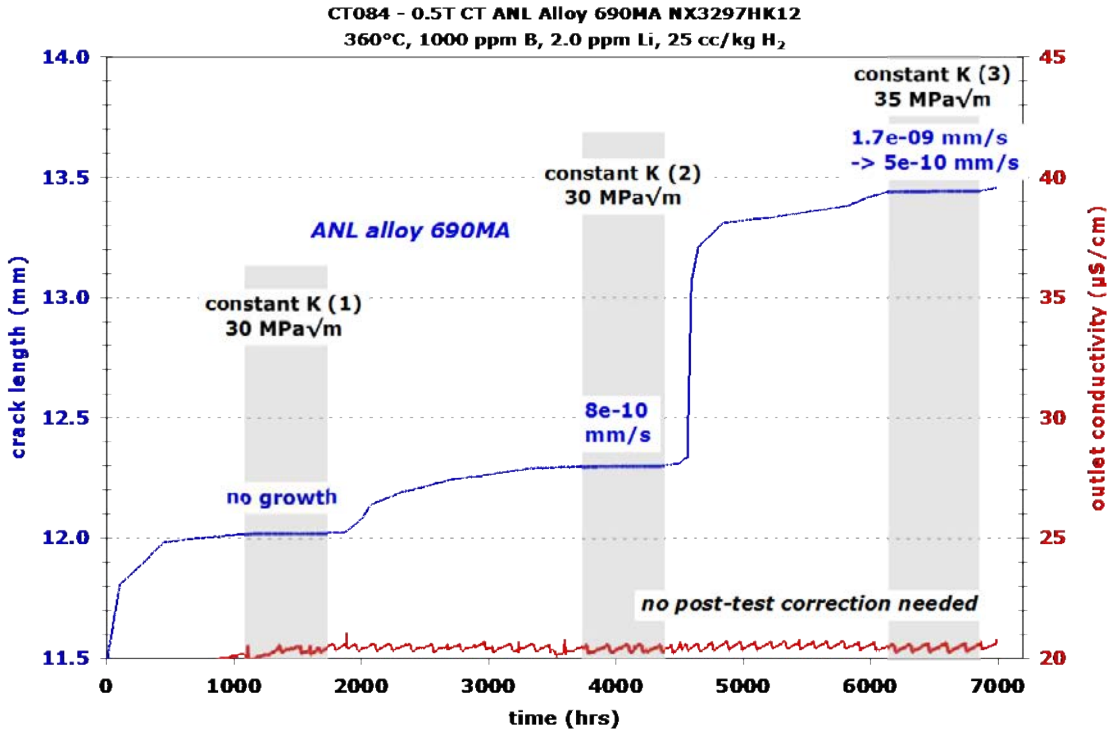

Figure 5.2 Overview of the entire SCC test on the as-received ANL alloy 690MA specimen (NX3297HK12), CT084

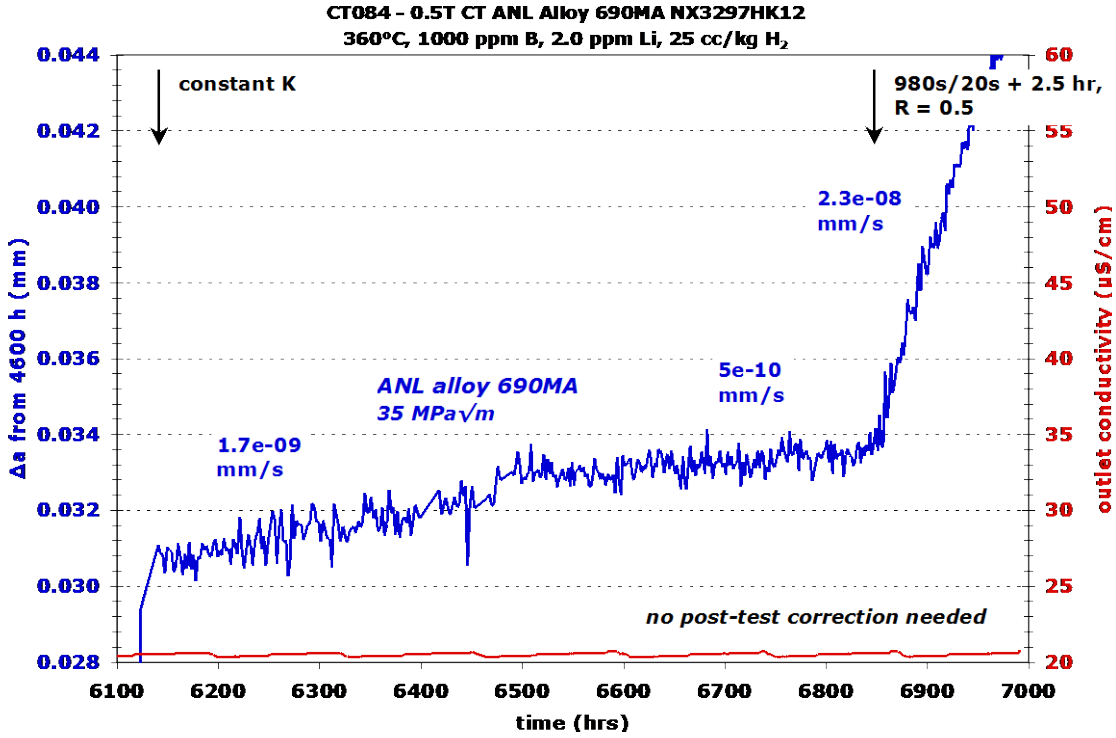

Figure 5.3 Crack growth response for the as-received ANL alloy 690MA specimen (NX3297HK12) CT084 during the final constant K observation at 35 MPa√m

After completing this 7000 h test, a slice of the specimen was removed for cross-section observation, and the remaining portion was fatigued open for crack surface observations. The optical image of the crack surface in Figure 5.4 shows a smooth crack front with a slight amount of lag at the side groove. As indicated, DCPD-estimated crack length was spot-on for both air precracking and in-situ testing. The sharp line running across the approximate middle of the in-situ portion of the test corresponds to the completion of the second constant K observation. A high resolution SEM image of the final ~1 mm of the crack surface is presented in Figure 5.5 while detail images of two locations along the final crack front are shown in Figure 5.6. No obvious IG cracking could be found in SEM examinations of the crack surface either along the final crack front or at other locations on the crack surface. The detail images do however show that there are occasional faceted features, however their morphology is not consistent with an IG crack. Interestingly, there were no crack surface ligaments for this specimen.

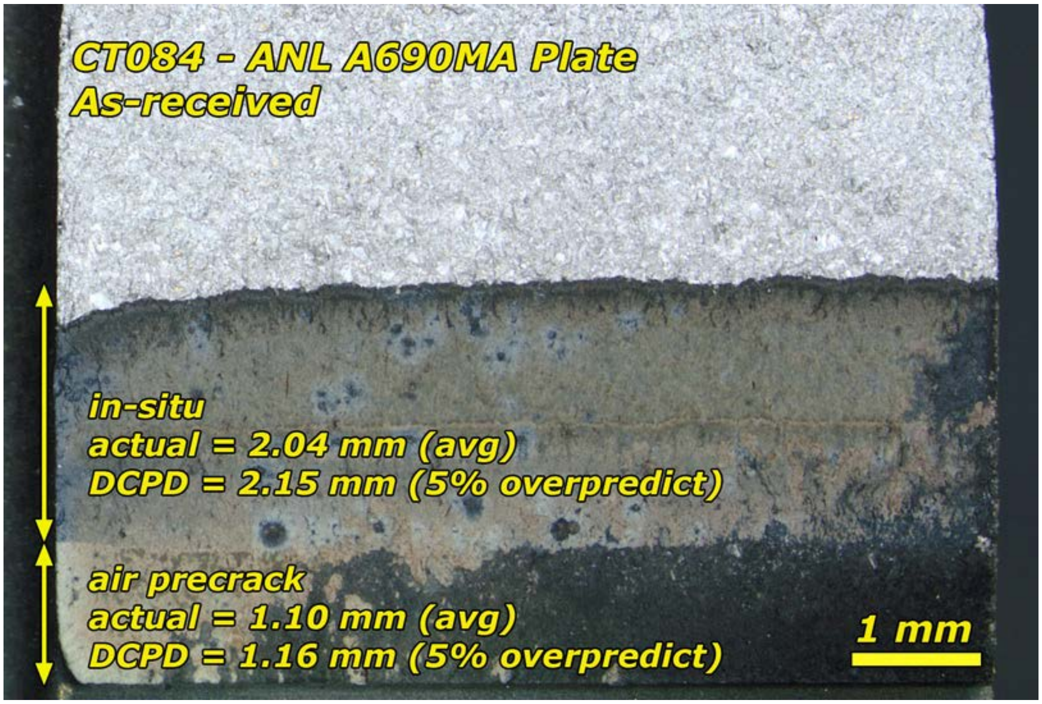

Figure 5.4 Optical image of the as-tested crack growth surface of the as-received ANL alloy 690MA CT specimen CT084

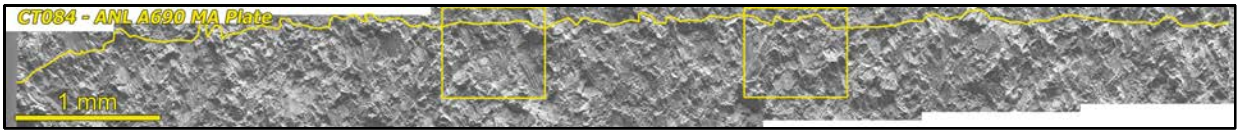

Figure 5.5 SEM-SE image of the final ~1 mm of crack growth for the as-received ANL alloy 690MA specimen, CT084. Yellow lines denote the final crack front and areas shown in Figure 5.6.

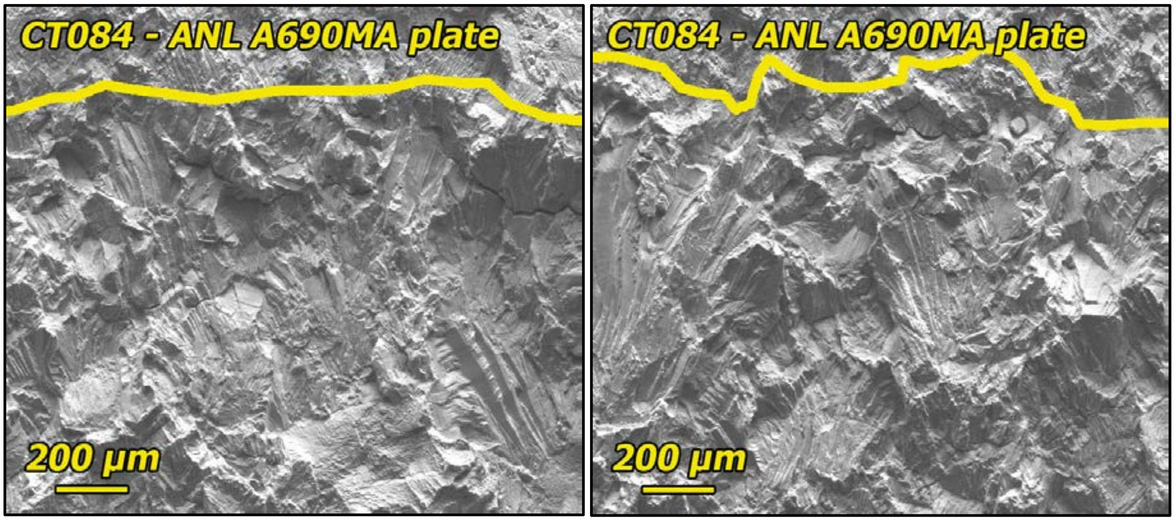

Figure 5.6 **Higher magnification SEM-SE images of the cleaned crack growth surface of the as-received ANL alloy 690MA specimen CT084**

5.2.2 ANL/Special Metals Heat NX3297HK12 - 30%CF Condition

This comparison between MA and HTA both with 30% cold forging represents a second assessment of the effect of initial material condition on the SCC resistance of CW alloy 690. In the first assessment which was performed on the Valinox RE243 CRDM heat, a HTA/SA treatment prior to 31% cold rolling resulted in a ~25x lower SCC cracking susceptibility. With such a strong effect, it was decided to examine the effect of the HTA treatment on several more materials. Like the tests on the Valinox heat, the ANL alloy 690MA heat NX3297HK12 material was given an 1100°C heat treat for 1 hour followed by a rapid water quench. Unlike the Valinox material, complete dissolution of the carbide population did not occur due to the higher carbon of this material. Prior experimentation by others [17] has shown that as the carbon content goes up in alloy 690, the annealing temperature must also be increased to cause complete dissolution. However, the grain boundary carbide microstructure was significantly changed by the HTA from a semi-continuous distribution of micrometer-sized IG carbides to a very low density of isolated nanometer-sized IG carbides as shown in Figure 3.3.

MA and HTA materials were cold forged to 30% reduction and 0.5T CT specimens were extracted. After air precracking, these specimens were paired together for SCC CGR testing. Stress intensity was set to be controlled to the MA + 30%CF specimen (CT073) because it was expected to exhibit higher CGRs. A summary of the test conditions and specimen response is provided in Table 5.3, while an overview of the entire test is shown in Figure 5.7. As shown in the overview plot, the 30%CF MA material exhibited SCC CGRs quite similar to other highly CW alloy 690 specimens, while the 30%CF HTA material exhibited low CGRs similar to the 31%CR SA alloy 690 CRDM. DCPD-indicated CGRs were 0.6-1.1x10^{-7} mm/s for the 30%CF MA material and 3-4x10^{-9} mm/s for the 30%CF HTA material. Examples are shown in Figure 5.8 and Figure 5.9. Evidence for ligament/contact formation was found for the 30%CF MA material (through cycle+hold loading response immediately after a constant K observation) with adjusted SCC CGRs of ~1.7x10^{-7} mm/s (Figure 5.10 and Figure 5.11). No evidence for ligament or contact formation was found for the 30%CF HTA materials. The 30%CF HTA material had 40-50x lower SCC CGRs than the 30%CF MA material, showing that the initial HTA treatment again dramatically reduced SCC susceptibility of highly cold worked alloy 690.

Table 5.3 Test conditions and specimen response for the 30%CF MA and the 30%CF HTA ANL alloy 690 specimens (NX3297HK12), CT073 and CT074

								CT073 30%CF ANL alloy 690MA			CT074 30%CF ANL alloy 690HTA		
Test Step	Start (h)	Dur-ation (h)	R	Freq (Hz)	Hold (h)	DH (cc/kg H_2)	Temp (°C)	Kmax (MPa√m)	CGR (mm/s)	Approx. Crack Ext. (mm)	Kmax (MPa√m)	CGR (mm/s)	Approx. Crack Ext. (mm)
1	0	6	0.5	0.1	0	25	360	32	2.1E-05	0.398	31	6.9E-06	0.086
2	6	24	0.5	0.01	0	25	360	33	3.3E-06	0.286	31	1.1E-06	0.106
3	30	112	0.5	0.001	0	25	360	33	7.9E-07	0.289	30	1.5E-07	0.063
4	142	332	0.5	980s/20s	2.5	25	360	33	2.8E-07	0.188	30	2.0E-08	0.028
5	474	56	---	const K	---	25	360	33	Insuff.	0.012	30	NG	0.002
6	530	107	---	const K	---	1	360	33	Insuff.	0.024	30	NG	0.001
7	637	446	---	const K	---	25	360	33	6.3E-08	0.087	30	3.1E-09	0.004
7*	637	---	---	const K	---	25	360	33	1.5E-07	---	30	NA	---
8	1083	671	---	const L	---	25	360	33	7.2E-08	0.067	30	3.1E-09	0.009
8*	1083	---	---	const L	---	25	360	33	1.7E-07	---	30	NA	---
9	1754	155	---	const K	---	25	360	33	6.3E-08	0.143	29	3.1E-09	0.003
9*	1754	---	---	const K	---	25	360	33	1.5E-07	---	29	NA	---
10	1909	356	0.5	12s/12s	2.77	25	360	35	2.9E-07	0.914	27	6.8E-09	0.007
11	2265	161	0.5	980s/20s	2.5	25	360	35	2.4E-07	0.164	27	8.5E-09	0.004
12	2426	210	---	const K	---	25	360	35	2.3E-08	0.028	27	1.5E-09	0.001
13	2636	18	0.5	12s/12s	2.77	25	360	35	NM	0.029	27	NM	0.001
14	2654	105	---	const K	---	25	360	35	2.3E-08	0.017	27	1.5E-09	0.001
15	2759	40	---	const K	---	25	360	35->41	Incr.	0.013	27->31	Incr.	0.002
16	2799	168	---	const L	---	25	360	41	5.9E-08	0.030	31	4.3E-09	0.003
16*	2799	---	---	const L	---	25	360	41	1.6E-07	---	31	NA	---
17	2967	203	0.5	980s/20s	2.5	25	360	43	8.1E-07	0.611	29	3.3E-08	0.022
18	3170	633	---	const L	---	25	360	43	1.1E-07	0.181	29	2.8E-09	0.006

* CGRs in these rows are adjusted for ligament/contact formation.
Insuff. = Insufficient crack extension to determine a CGR.
NG = No growth
NA = Not applicable
NM = Not measured
Incr. = Increasing

As part of this test, the effect of K on SCC CGR studied. For the 30%CF MA specimen, adjusted SCC CGRs were ~1.7x10^{-7} mm/s at both 33 MPa√m and at ~41 MPa√m. The lack of sensitivity of SCC CGRs to K levels above 30 MPa√m has been seen in tests at PNNL on other highly CW alloy 690 materials.

Another aspect considered for this test was the difference in SCC CGR response between constant K and constant load. During constant load testing at these moderate CGRs of ~5x10^{-8} mm/s for the 30%CF MA material, K increases slightly as crack length increases. Since it has been shown that a rising K does produce accelerated SCC CGRs [18], a concern arises that constant load may produce artificially high CGRs if dK/da is sufficiently high. After letting the propagation rate stabilize under constant K conditions during the first constant K observation, the test was set to constant load. A slight increase in CGR from 6.4x10^{-8} mm/s to 7.2x10^{-8} mm/s, well within the range of normal variability, was observed (Figure 5.8) suggesting a minimal dK/da effect for this particular set of conditions.

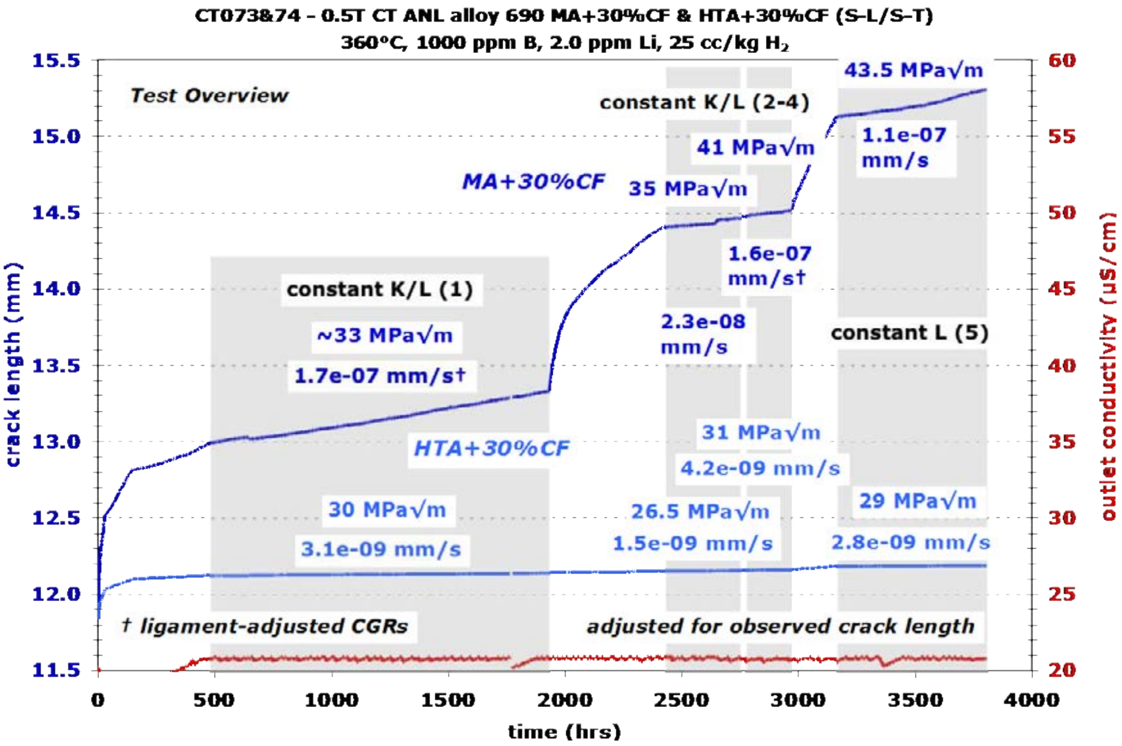

Figure 5.7 Overview of the entire test on the 30%CF MA and the 30%CF HTA ANL alloy 690 specimens (NX3297HK12), CT073 and CT074

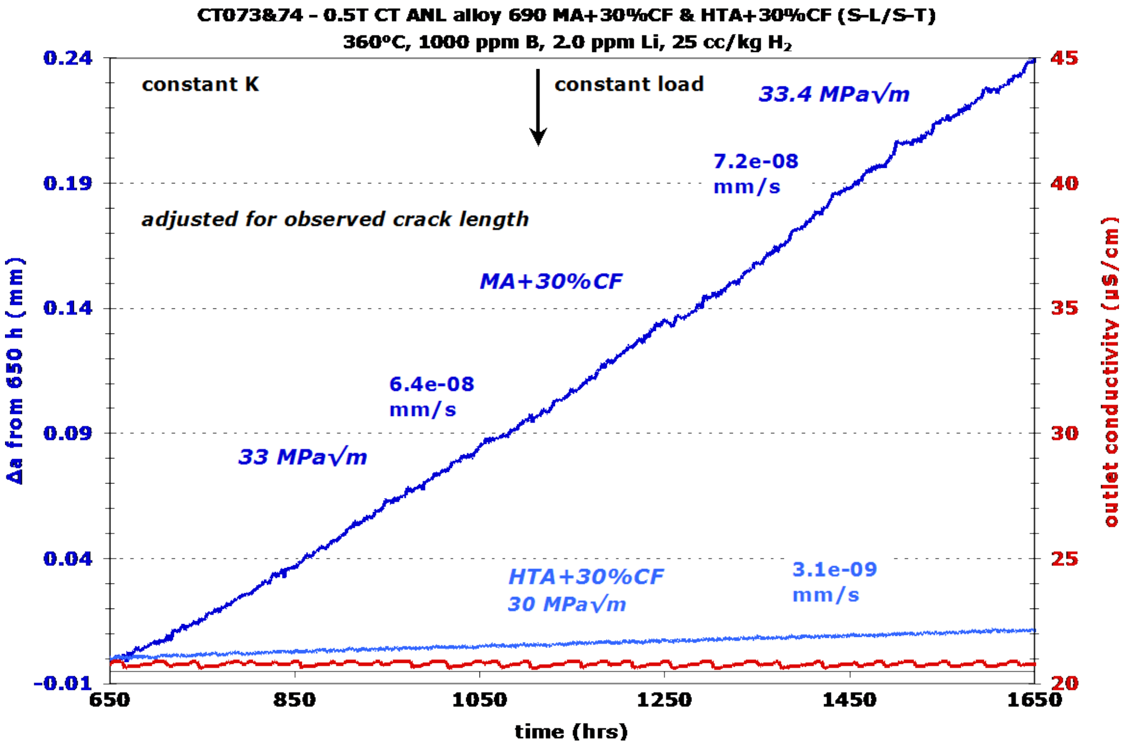

Figure 5.8 Constant K and constant load DCPD-based crack growth response for the 30%CF MA and the 30%CF HTA ANL alloy 690 specimens, CT073 and CT074, during the first observation period

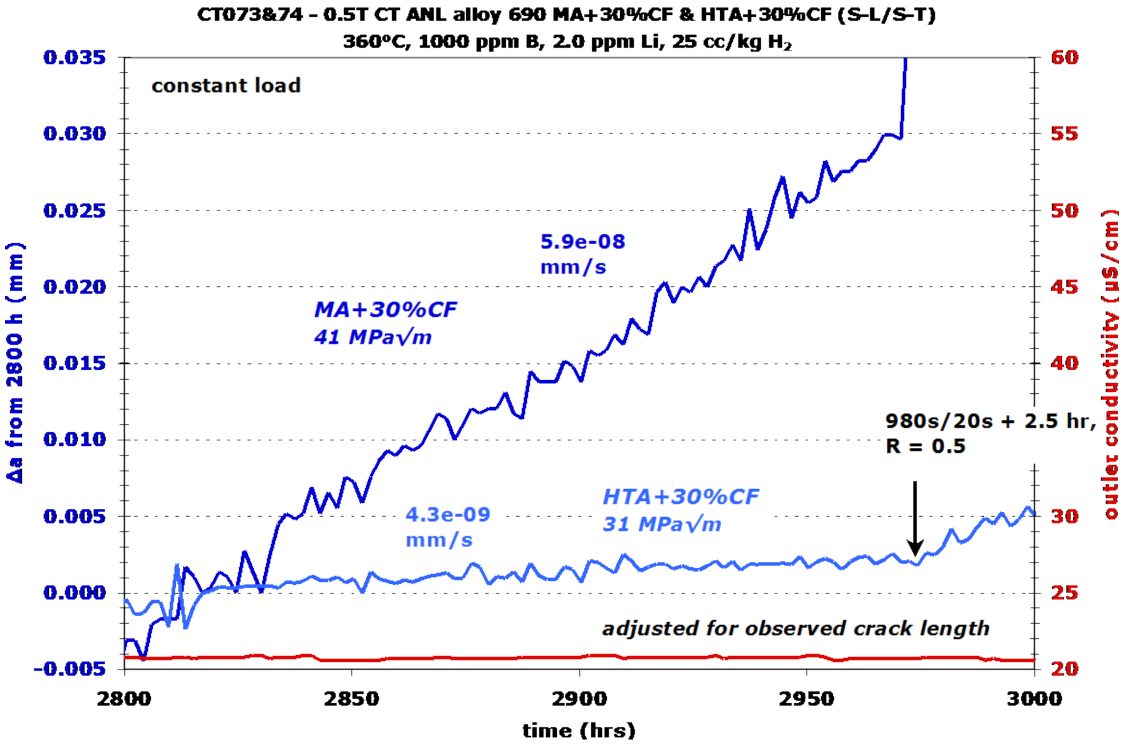

Figure 5.9 Constant load DCPD-based crack growth response for the 30%CF MA ANL alloy 690 specimens, CT073 and CT074, during the 4th observation period

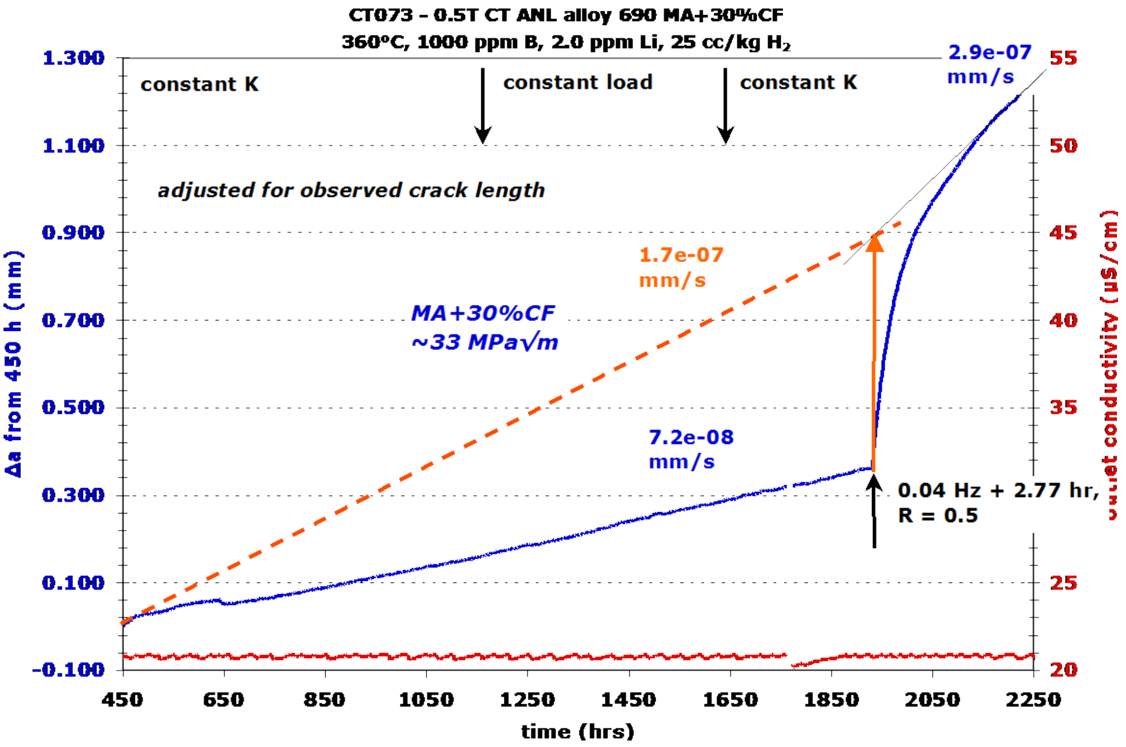

Figure 5.10 Ligament/contact-adjusted SCC CGR crack growth response for the 30%CF MA ANL alloy 690 specimen, CT073, during the first observation period

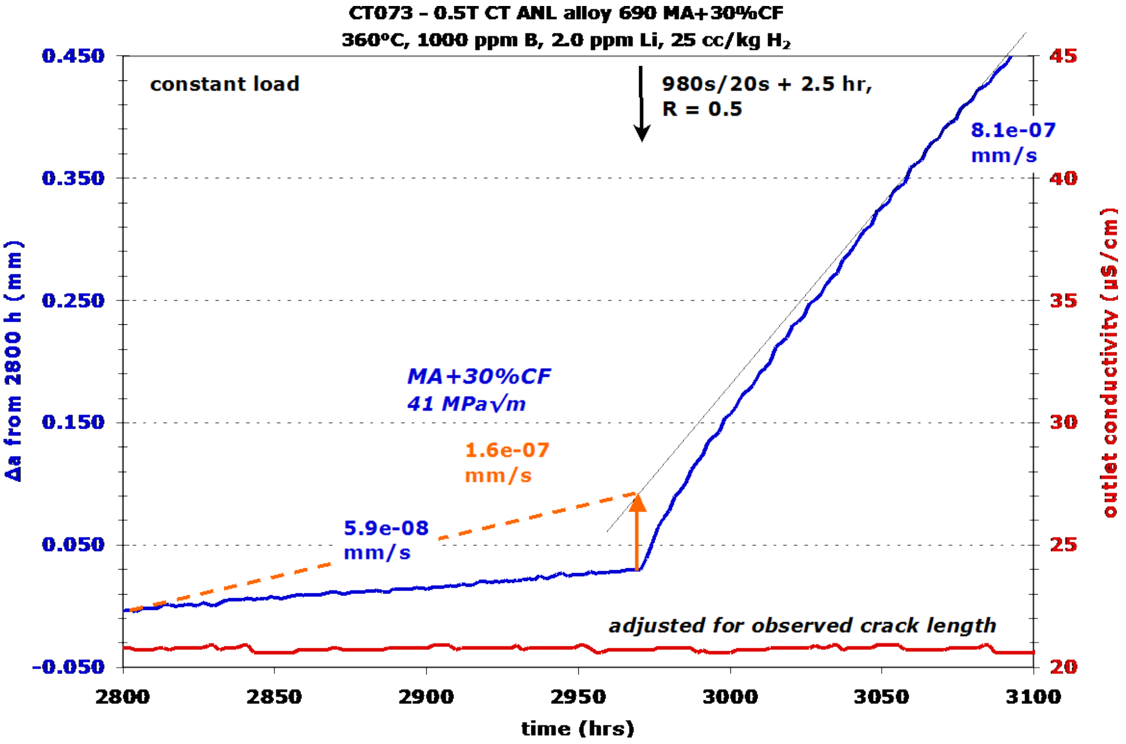

Figure 5.11 Ligament/contact-adjusted SCC CGR crack growth response for the 30%CF MA ANL alloy 690 specimen, CT073, during the fourth observation period

After completing the test, a slice was removed from each specimen for cross-section observation, and the remaining portion was fatigued open for crack surface observations. An optical image of the as-tested 30%CF MA crack surface in Figure 5.12 shows a relatively straight crack front in the central region, but near the side groove, lack of constraint reduced the K resulting in lower CGRs and a lower amount of crack extension. When using the central region of the crack front for determining the in-situ DCPD correction, it was found that DCPD underpredicted crack length by ~27%. This results in 27% higher CGRs while the increase in K varies with crack length. The in-situ portion of the crack surface shows the presence of ligaments as has been observed for other tests on CW materials. An optical image in Figure 5.13 of the as-tested crack growth surface of the 30%CF HTA specimen shows a much straighter crack front across the width of the specimen with no obvious ligaments. DCPD was found to underpredict crack length by 8% resulting in a proportionate increase in CGRs. Since K was not being controlled to this specimen, the corrected stress intensities are a function not only the DCPD correction to this specimen, but also the difference in crack length that developed between the two specimens during the test.

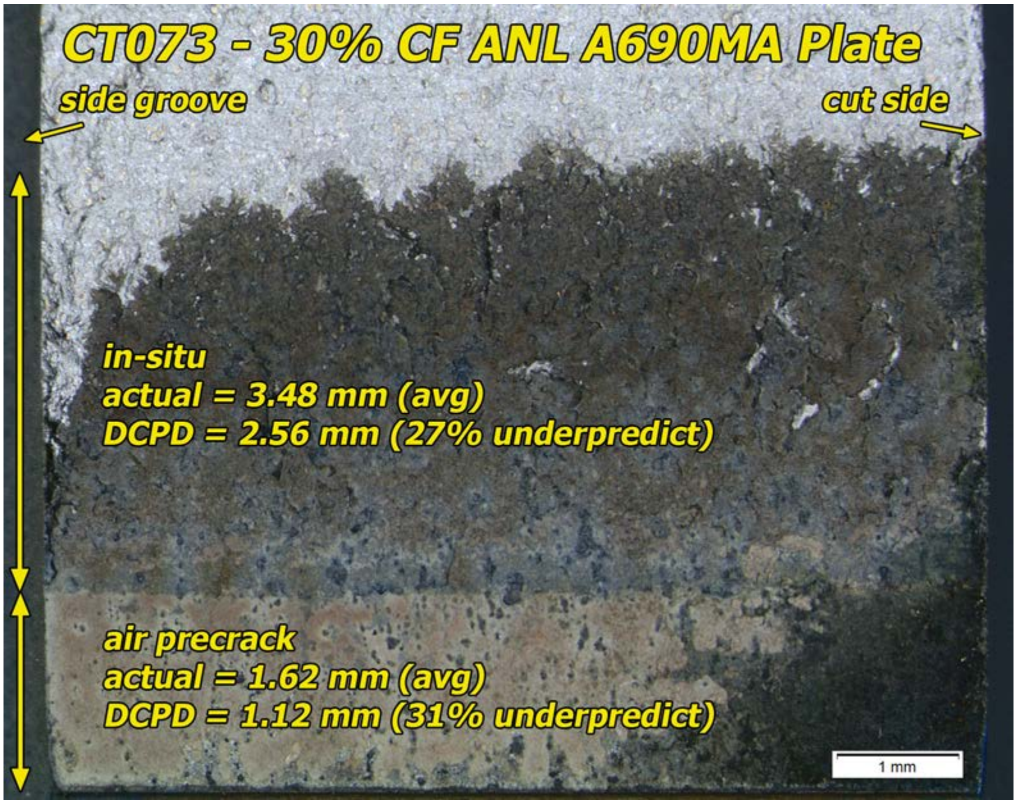

Figure 5.12 Optical image of the as-tested crack growth surface of the 30%CF ANL alloy 690MA CT specimen CT073

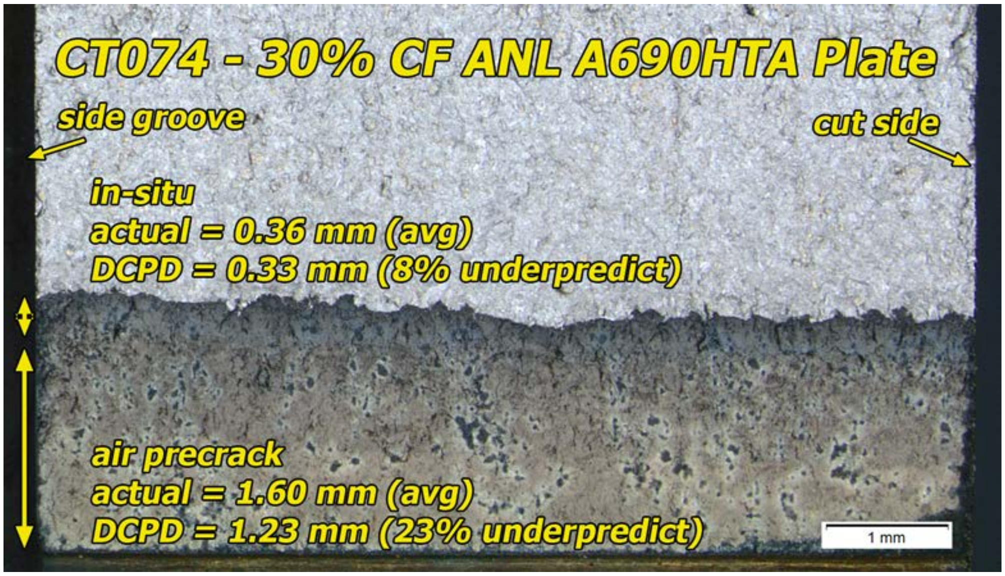

Figure 5.13 Optical image of the as-tested crack growth surface of the 30%CF ANL alloy 690HTA CT specimen CT074

SEM-SE and SEM-BSE examinations were used to study the degree of IG cracking and ligament formation. Example observations in Figure 5.14 (SEM-SE) and Figure 5.15 (SEM-BSE) for the 30%CF MA specimen show the final crack front region to be highly intergranular. Uncracked ligaments (bright regions in the SEM-BSE image, arrows in the SEM-SE image) and oxidized TG cracking were observed. Observations of these features provide another example that ligament formation does occur in these highly CW materials. It appears that some, but not all of these ligaments can be fatigue cracked with typical load cycling steps used by PNNL, some of which are quite aggressive. 85% IG cracking was determined from measurements of three different regions near the final crack front. Similar values are expected for other SCC CGR assessments earlier in the test. Unlike the 26%CR S-L specimen tested by GE (Figure 5.1), there were no obvious indications of cracked carbides or TiN particles on the crack growth surface. Thus it appears that relatively high CGRs were obtained in a non-banded region.

SEM-SE and SEM-BSE images are also provided for the 30%CF HTA specimen in Figure 5.16 and Figure 5.17, respectively. In regions of gentle cycling and constant K/L loading, an average of 44% IG was observed. Although there was significant TG cracking, very few uncracked ligaments were observed. These results mirror those for the 31%CR Valinox RE243 CRDM where a ~10x difference in SCC CGR was observed between the TT and SA materials. A similar result was obtained for the B25K-2 material as will be shown in the next section.

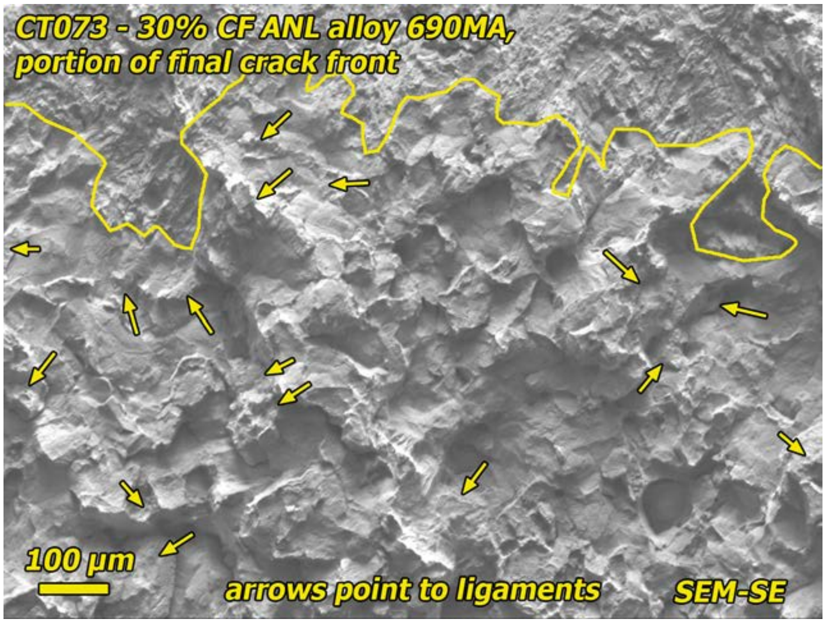

Figure 5.14 SEM-SE image of a portion of the final crack growth for the 30%CF ANL alloy 690MA specimen, CT073. Yellow line denotes the final crack front. Arrows point to TG patches.

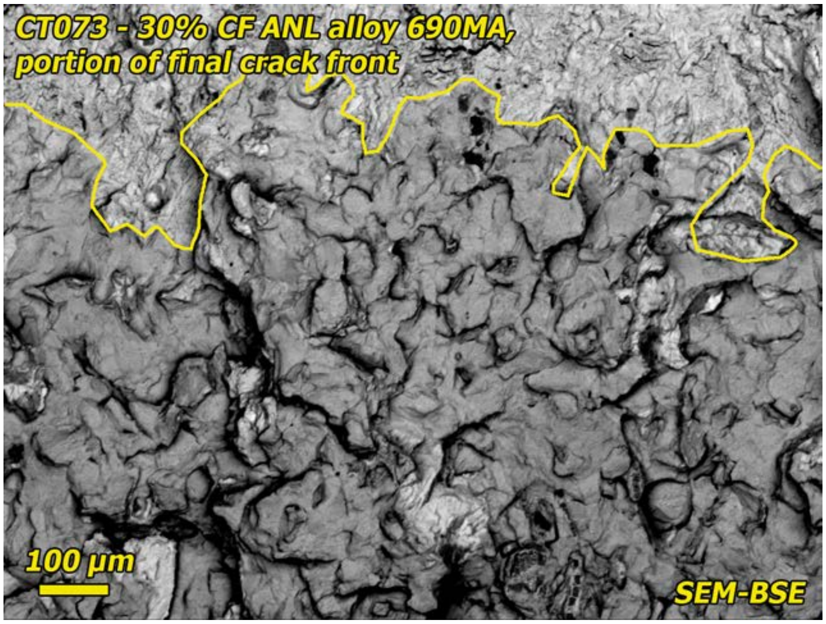

Figure 5.15 SEM-BSE image of a portion of the final crack growth for the 30%CF ANL alloy 690MA specimen, CT073. Yellow line denotes the final crack front.

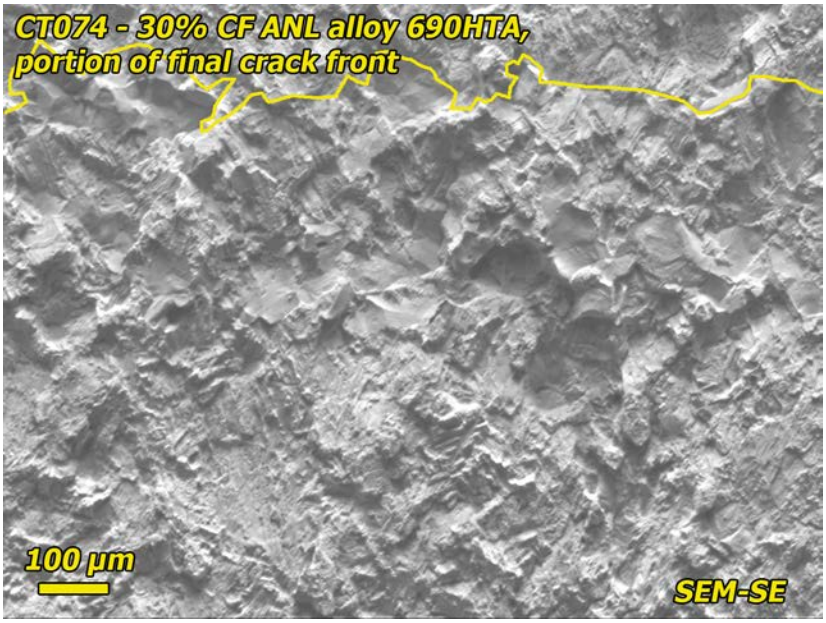

Figure 5.16 SEM-SE image of a portion of the final crack growth for the 30%CF ANL alloy 690HTA specimen, CT074. Yellow line denotes the final crack front.

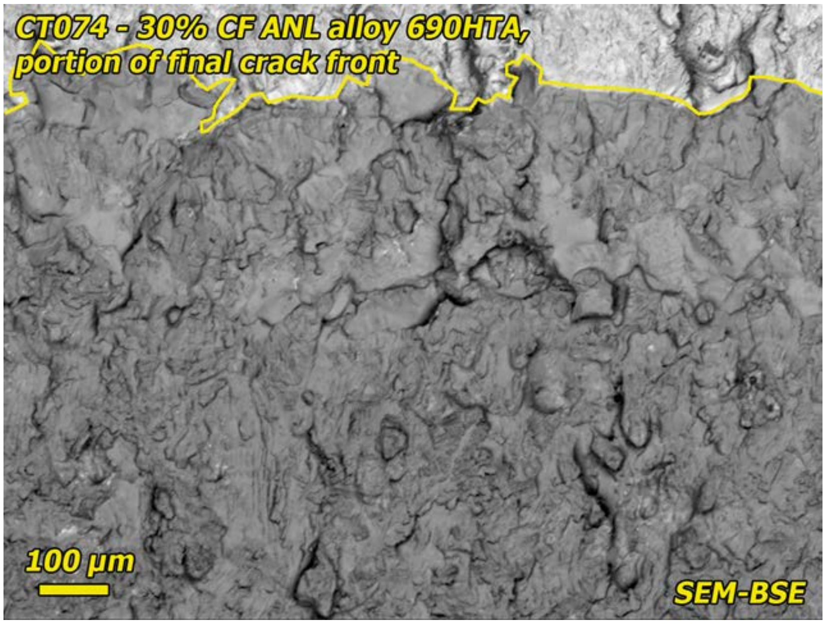

Figure 5.17 SEM-BSE image of a portion of the final crack growth for the 30%CF ANL alloy 690HTA specimen, CT074. Yellow line denotes the final crack front.

5.3 SCC Tests on GE/Allvac Heat B25K-2

This material was obtained from GE for testing. It was produced as thick plate with a 996°C mill anneal for 20 minutes. The first test performed by PNNL on this material was on a 20%CR S-L specimen obtained from GE. As reported in the previous NUREG in the series [7], higher than expected SCC CGRs of ~5x10^{-8} mm/s were obtained at this moderate level of cold work. Post-test examinations of the specimen revealed a very fine grain size, many twins, high hardness and a high IMD. However it had at best, only a sporadic distribution of IG carbides. Based on the microstructure, hardness and implied strain levels, this material should have exhibited lower SCC CGRs like the Valinox SA+CW or the ANL HTA+CW materials. Thus, the lack of IG carbides combined with the relatively high SCC CGR made this material especially interesting for further testing.

5.3.1 GE/Allvac Heat B25K-2 - Mill Annealed Condition

A 0.5T CT specimen was extracted from the MA plate so that the processing plane, i.e., the banding plane, was coplanar with the specimen crack growth plane. A summary of the test conditions and specimen response is provided in Table 5.4 while an overview of the entire test is shown in Figure 5.18. Two constant K observations were performed at ~30 MPa√m and one at 38 MPa√m. For the first constant K, the final transitioning step was a 980s/20s load cycle at R = 0.5 with a 2.5 h hold at K_{max}, while for the second two transitioning sequences, the final transitioning steps were a 9980s/20s continuous load cycle at R = 0.5 and then the same load cycle with a 2.5 h hold at K_{max}. Sustained growth at ≥1x10^{-9} mm/s could not be attained for either of the ~30 MPa√m constant K observations, but at 38 MPa√m, an initial SCC CGR of 2.1x10^{-9} mm/s that slowed to 1.3x10^{-9} mm/s was observed as shown in Figure 5.19. Cycle+hold loading applied after constant K showed no evidence for contact or ligament formation that could mask the DCPD crack length estimate.

Table 5.4 Test conditions and specimen response for the as-received GEG alloy 690MA specimen (B25K-2), CT085

								CT085 GE alloy 690MA specimen #1		
Test Phase	Start (h)	Duration (h)	R	Freq (Hz)	Hold (h)	Dissolved Hydrogen (cc/kg H_2)	Temp (°C)	Kmax ($MPa\sqrt{m}$)	CGR (mm/s)	Approx. Crack Extension (mm)
1	0	12	0.5	0.1	0	25	360	30	6.3E-06	0.250
2	12	93	0.5	0.01	0	25	360	30	1.4E-06	0.356
3	105	335	0.5	0.001	0	25	360	31	1.7E-07	0.208
4	440	714	0.5	980s/20s	2.5	25	360	31	1.8E-08	0.052
5	1154	597	---	const K	---	25	360	31	6.6E-10	0.001
6	1751	113	0.5	980s/20s	2.5	25	360	31	1.4E-08	0.006
7	1864	145	0.5	980s/20s	0	25	360	31	1.7E-07	0.072
8	2009	66	0.35	980s/20s	0	25	360	31	2.8E-07	0.068
9	2075	238	0.35	4980s/20s	0	25	360	31	7.6E-08	0.068
10	2313	357	0.35	9980s/20s	0	25	360	31	4.7E-08	0.060
11	2670	627	0.35	9980s/20s	2.5	25	360	31	2.4E-08	0.054
12	3297	519	0.35	9980s/20s	24	25	360	31	5.1E-09	0.009
13	3816	525	---	const K	---	25	360	31	NG	0.000
14	4341	146	0.5	980s/20s	2.5	25	360	31	1.6E-08	0.008
15	4487	76	0.5	980s/20s	0	11	360	31	1.3E-07	0.028
16	4563	30	0.4	0.1	0	25	360	31	8.1E-06	0.823
17	4593	49	0.5	0.01	0	25	360	32	1.1E-06	0.303
18	4642	190	0.5	980s/20s	0	25	360	32	1.9E-07	0.126
19	4832	392	0.5	980s/20s	2.5	25	360	32	2.2E-08	0.032
20	5224	552	0.35	9980s/20s	2.5	25	360	32	2.8E-08	0.055
21	5776	163	0.35	9980s/20s	2.5	25	360	32->38	Incr.	0.040
22	5939	185	0.35	9980s/20s	2.5	25	360	38	4.2E-08	0.030
23	6124	723	---	const K	---	25	360	38	1.3E-09	0.005
24	6847	143	0.5	980s/20s	2.5	25	360	38	3.5E-08	0.019

NG = No growth
Incr. = Increasing CGR

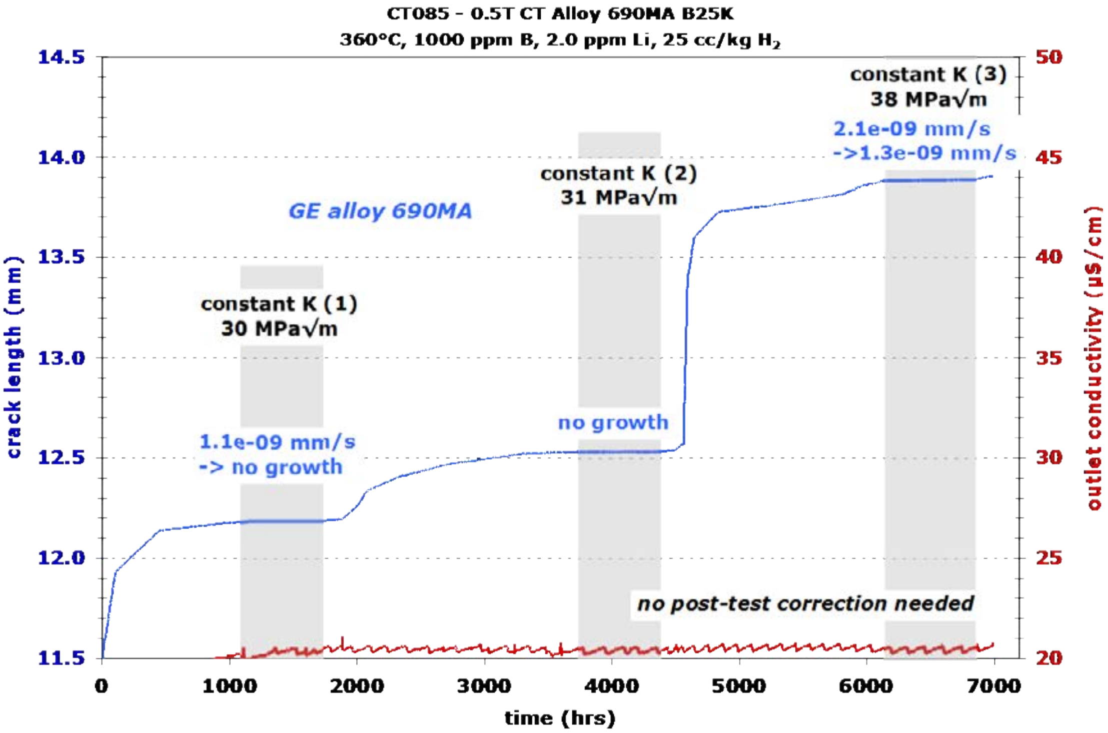

Figure 5.18 Overview of the entire SCC test on the as-received GEG alloy 690MA specimen (B25K-2), CT085.

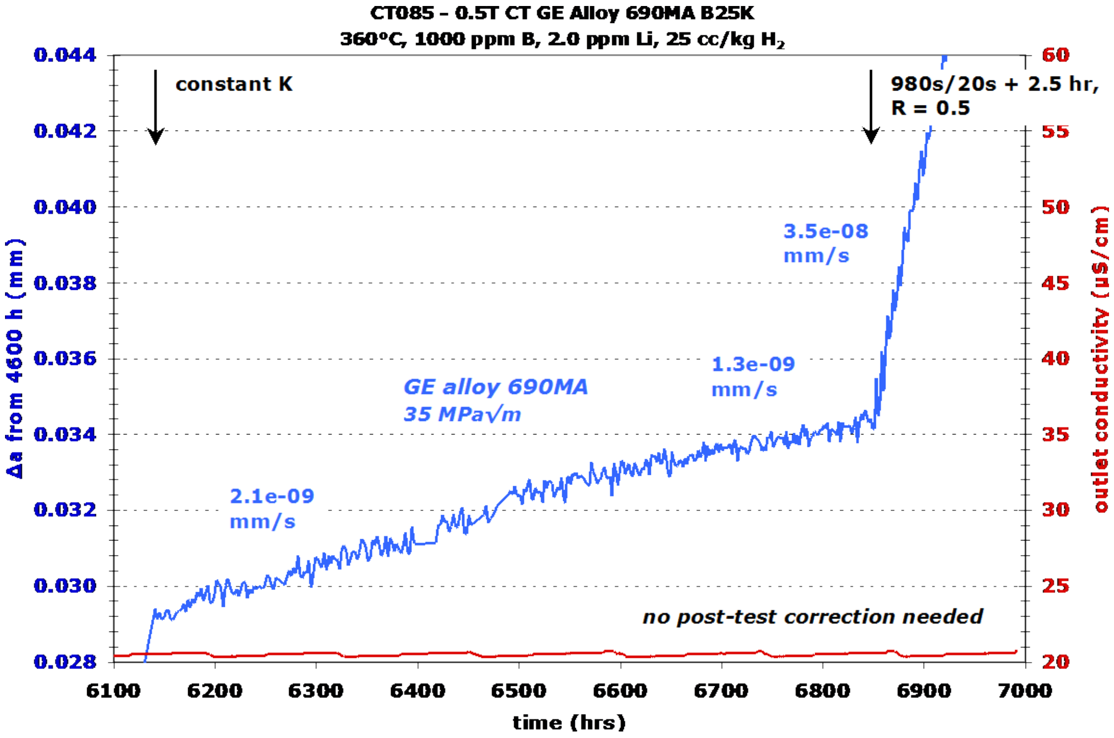

Figure 5.19 Crack growth response for the as-received GEG alloy 690MA specimen (B25K-2) CT085 during the final constant K observation at 35 MPa√m.

After completing this 7000 h test, a slice of the specimen was removed for cross-section observation, and the remaining portion was fatigued open for crack surface observations. The optical image of the crack surface in Figure 5.20 shows a smooth crack front with a slight amount of lag in crack length at the side groove. As indicated, DCPD-estimated crack length was spot-on for both air precracking and in-situ testing. The sharp line running across the approximate middle of the in-situ portion of the test corresponds to the completion of the second constant K observation. A high resolution SEM image of the final ~1 mm of the crack surface is presented in Figure 5.21 while detail images of two locations along the final crack front are shown in Figure 5.22. Arrows point to regions of IG cracking. Approximately 22% IG cracking was measured along the final crack front and at the location corresponding to the second constant K observation. No attempt was made to identify IG cracking at the first constant K location. There were no crack surface ligaments for this specimen. Side surface observations as shown in Figure 5.23 confirm that the crack growth plane was nearly parallel to the banding. The banding consisted predominantly of TG carbides and a small amount of TiN.

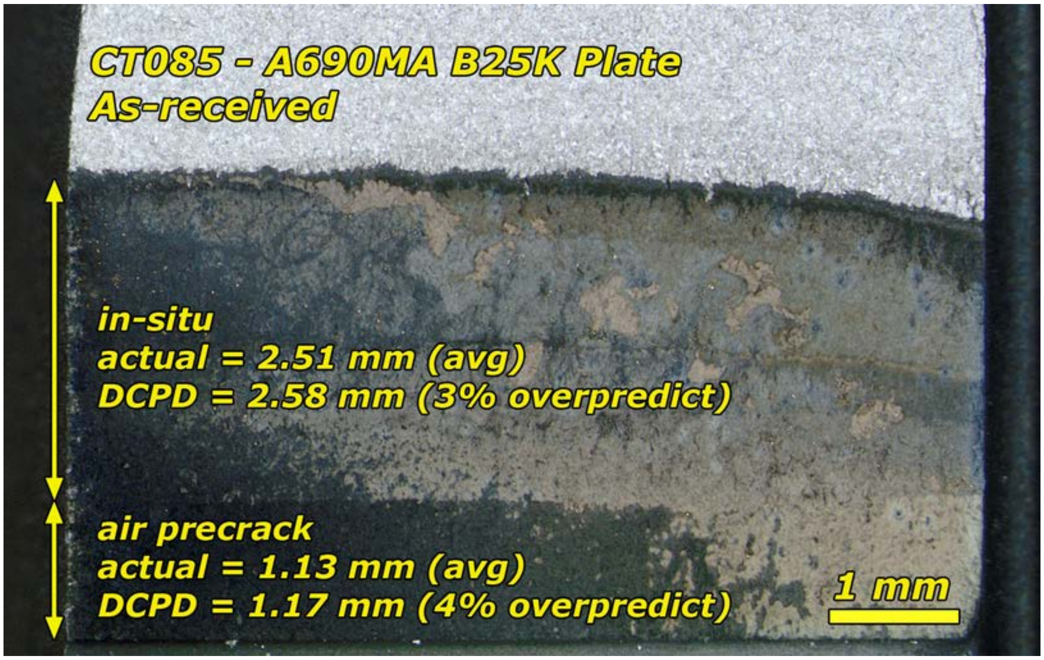

Figure 5.20 **Optical image of the as-tested crack growth surface of the as-received GEG alloy 690MA (B25K-2) specimen CT085.**

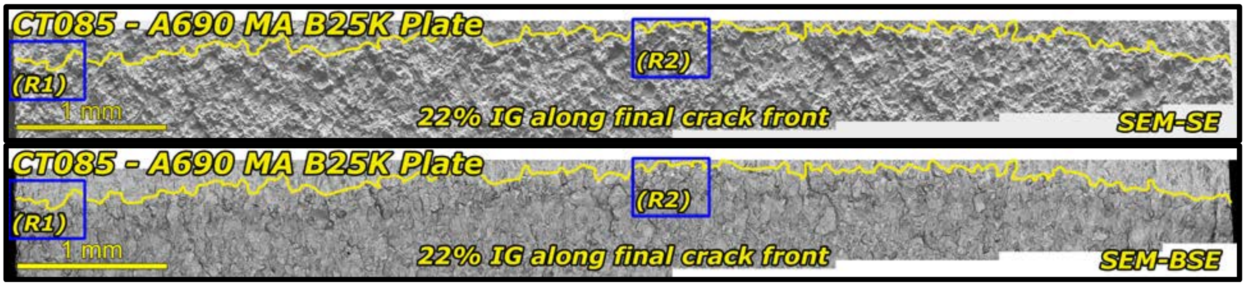

Figure 5.21 **SEM-SE and SEM-BSE images of the final ~1 mm of crack growth for the as-received GEG alloy 690MA specimen, CT085. Yellow lines denote the final crack front and blue boxes denote the location of SEM-SE images shown in Figure 5.22.**

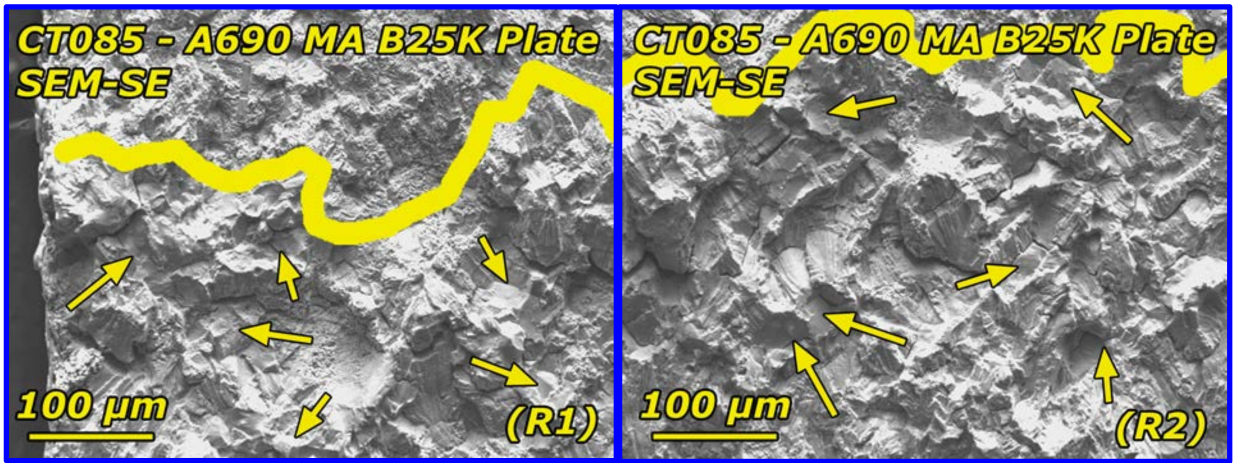

Figure 5.22 **Higher magnification SEM-SE images of the cleaned crack growth surface of the as-received GEG alloy 690MA specimen, CT085.**

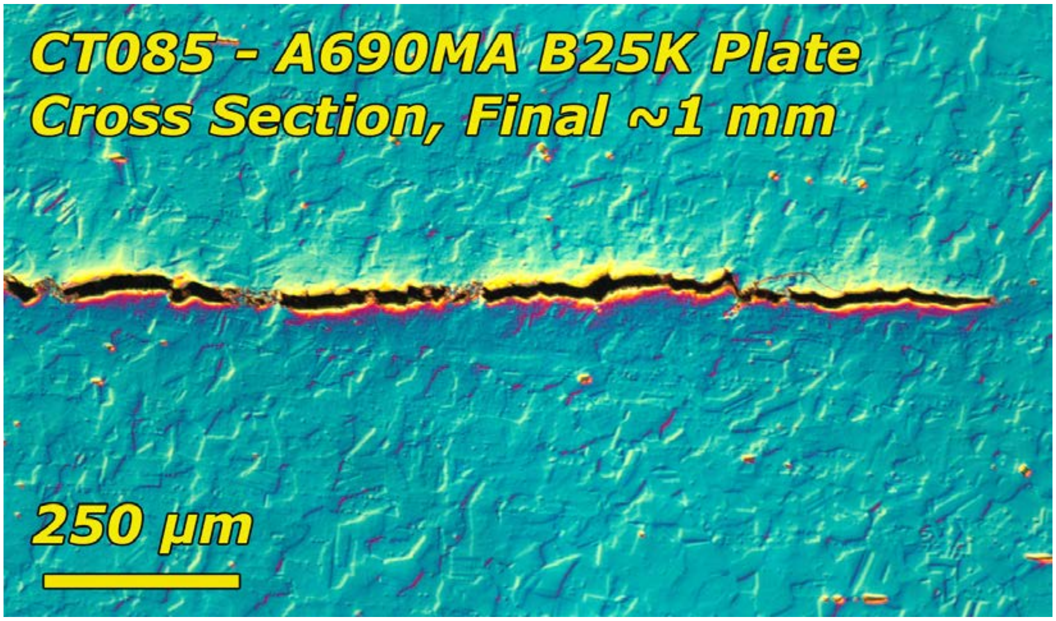

Figure 5.23 **Side surface observation of the as-received GEG alloy 690MA specimen, CT085, showing fine banding nearly parallel to the crack growth plane. Banding was a combination of TG carbides and TiN.**

5.3.2 GE/Allvac Heat B25K-2 - HTA+20%CR S-L - CT070

The GE/Allvac B25K-2 material was unique in its SCC response in that it exhibited relatively high SCC CGRs of ~5x10^{-8} mm/s in a MA+20%CR S-L condition where there were no significant amount of grain boundary carbides. SCC CGRs of other CW materials without GB carbides, e.g., the SA+31%CR S-L Valinox RE243 CRDM and the HTA+30%CF ANL plate, were below 5x10^{-9} mm/s. In order to better understand the SCC susceptibility of the GE/Allvac material, a piece was also given an HTA treatment of 1100°C for 1 h followed by a water quench. Due to its relatively high 0.034 wt% carbon content, a small number of plate-like carbides were found on the grain boundaries after the heat treatment, therefore not quite attaining a complete solution anneal. After the HTA treatment, the material was cold rolled to a 20% reduction, matching the value used for the SCC testing on the original CR MA material. A specimen was cut out in the S-L orientation relative to the cold rolling. This orientation was also parallel with the banding orientation of the original plate material.

A summary of the test conditions and specimen response is provided in Table 5.5, while an overview of the entire test is shown in Figure 5.24. Three constant K observations were performed, all at 30 MPa√m. DCPD noise issues plagued much of this test resulting in too much noise during the first two constant K observations to determine an SCC CGR. The cause of the noise was eventually determined, and for the third constant K observation, a steady SCC CGR of $1.8x10^{-9}$ mm/s was observed as shown in Figure 5.25. Cycle+hold loading applied after constant K showed no evidence for contact or ligament formation that could mask the DCPD crack length estimate.

Table 5.5 Test conditions and specimen response for the HTA+20%CR S-L GEG alloy 690 specimen (B25K-2), CT070

								CT070 GE B25K SA+20%CR S-L		
Test Phase	Start (h)	Duration (h)	R	Freq (Hz)	Hold (h)	Dissolved Hydrogen (cc/kg H_2)	Temp (°C)	Kmax (MPa√m)	CGR (mm/s)	Approx. Crack Extension (mm)
1	0	12	0.5	0.1	0	25	360	31	4.7E-06	0.220
2	12	108	0.5	0.01	0	25	360	31	8.7E-07	0.336
3	120	195	0.5	0.001	0	25	360	31	1.4E-07	0.102
4	315	763	0.5	0.001	2.5	25	360	31	1.2E-08	0.051
5	1078	1103	---	const K	---	25	360	31	ND	ND
6	2181	58	0.5	980s/20s	2.5	25	360	31	ND	ND
7	2239	67	0.5	0.1	0	25	360	31	4.9E-06	1.193
8	2306	73	0.5	0.01	0	25	360	32	8.1E-07	0.213
9	2379	137	0.5	0.001	0	25	360	32	1.3E-07	0.068
10	2516	391	0.5	0.001	2.5	25	360	32	1.7E-08	0.020
11	2907	596	---	const K	---	25	360	30	ND	ND
12	3503	100	0.5	980s/20s	0	25	360	30	1.5E-07	0.045
13	3603	259	0.5	980s/20s	2.5	25	360	30	2.0E-08	0.019
14	3862	838	---	const K	---	25	360	30	1.8E-09	0.005
15	4700	283	0.5	12s/12s	2.77	25	360	30	9.2E-09	0.013
16	4983	120	0.5	980s/20s	2.5	25	360	30	1.6E-08	0.006

ND = No Data

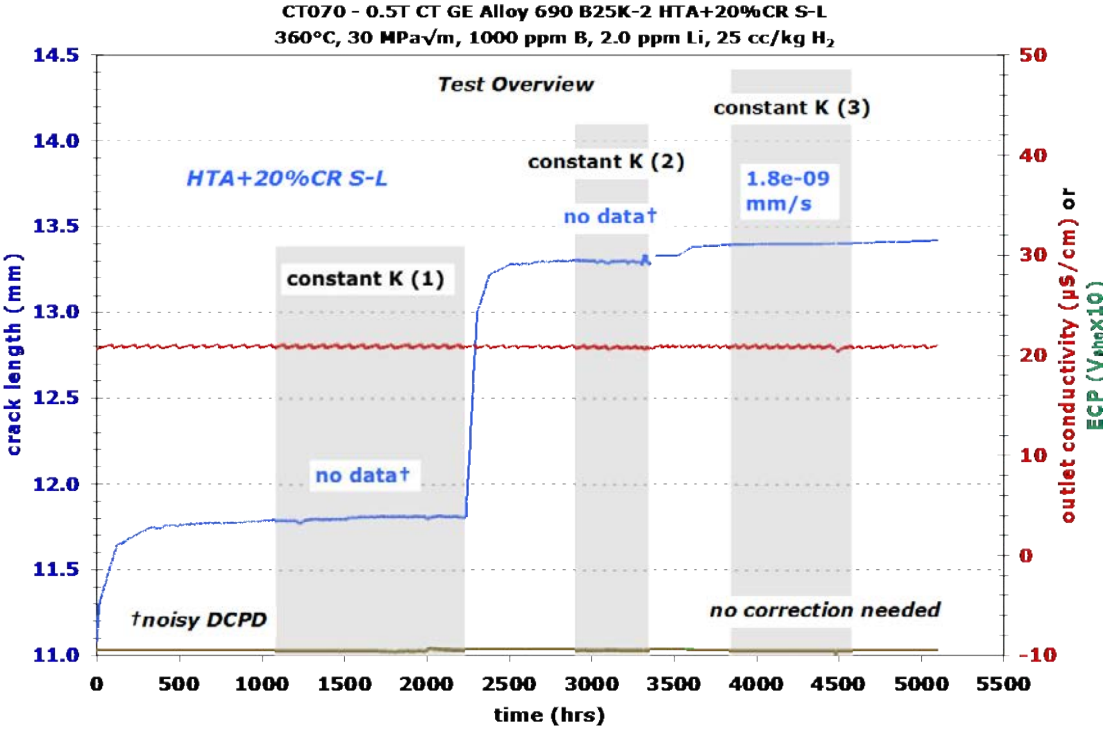

Figure 5.24 Overview of the entire SCC test on the HTA+20%CR S- GEG alloy 690 specimen (B25K-2), CT070

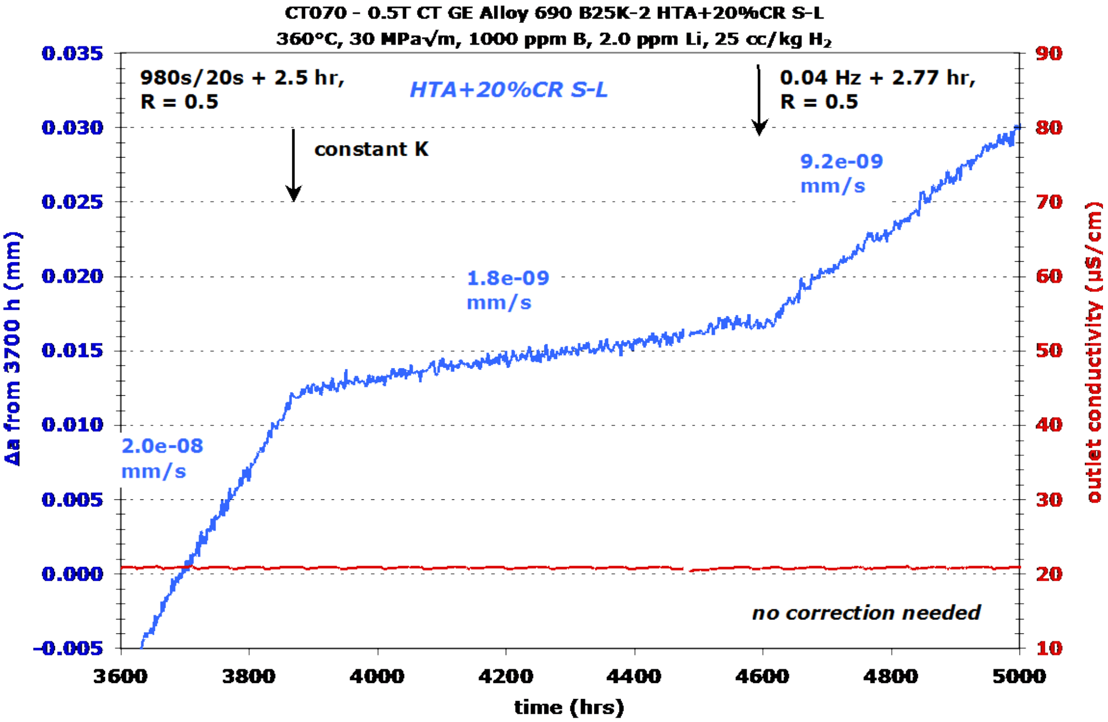

Figure 5.25 Crack growth response for the HTA+20%CR S-L GEG alloy 690 specimen (B25K-2) CT070 during the final constant K observation

After completing this ~5100 h test, a slice of the specimen was removed for cross-section observation, and the remaining portion was fatigued open for crack surface observations. The optical image of the crack surface in Figure 5.26 shows a smooth crack front with some lag in crack length at the side groove. As indicated, DCPD-estimated crack length somewhat underpredicted the precrack length, but was nearly spot-on for the in-situ testing. The step changes in texture are due to substantial changes in test condition. The first is due to the change from air precracking to in-situ testing, while the second and third present the change from gentle to aggressive load cycling and then back to gentle load cycling, respectively.

An overview SEM-SE image the entire crack surface is presented in Figure 5.27 while a higher resolution image along the final crack front is shown in Figure 5.28. Arrows point to regions of IG cracking. Approximately 18% IG cracking was measured along the final crack front. This degree of IG cracking persisted for up to ~500 µm from the final crack front. Side surface optical image shown in Figure 5.29 confirms the occasional IG cracking. The remnant TiN banding from the original plate processing can be seen and is parallel to the crack.

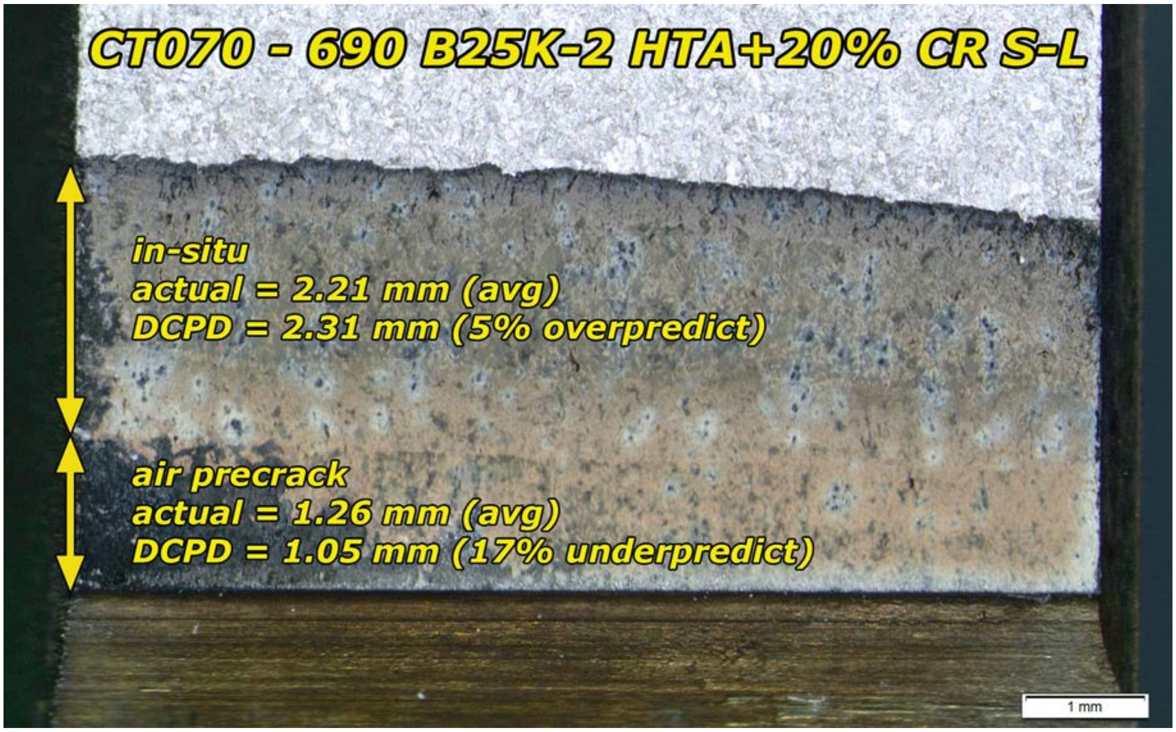

Figure 5.26 Optical image of the crack growth surface of the HTA+20%CR S-L GEG alloy 690 (B25K-2) CT specimen CT070

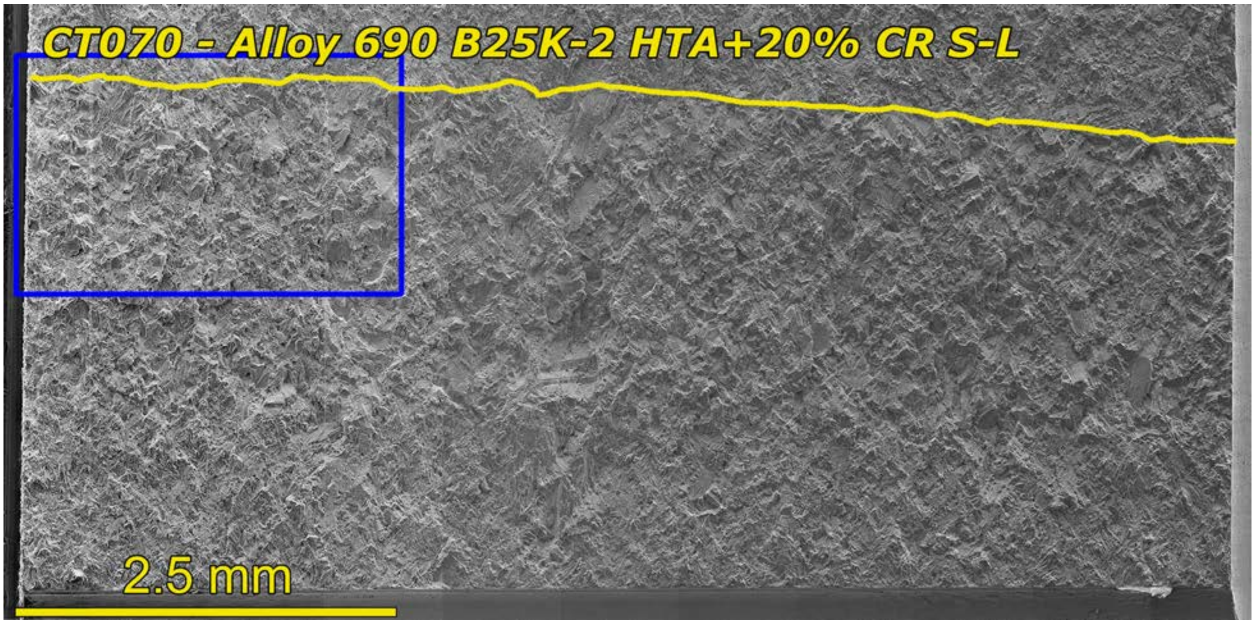

Figure 5.27 SEM-SE image of the final ~1 mm of crack growth for the HTA+20%CR S-L GEG alloy 690 specimen, CT070. Yellow lines denote the final crack front and the blue box denotes the location of the image shown in Figure 5.28.

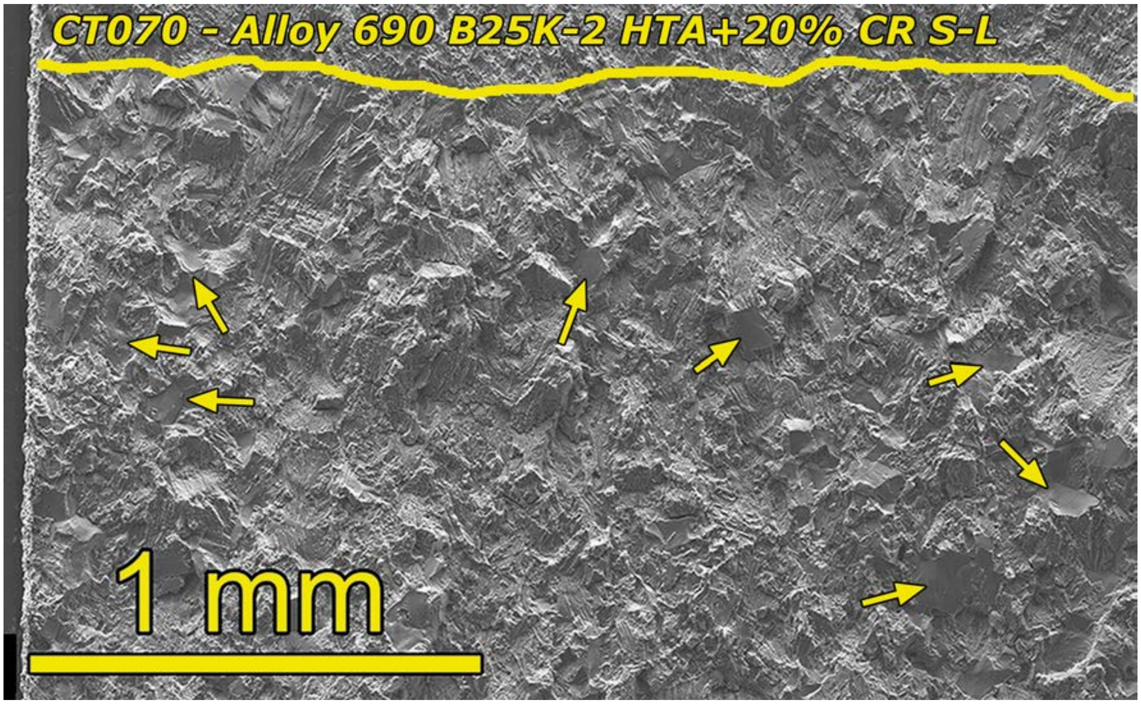

Figure 5.28 Higher magnification SEM-SE image of the cleaned crack growth surface of the HTA+20%CR S-L GEG alloy 690 specimen, CT070. Arrows point to IG facets.

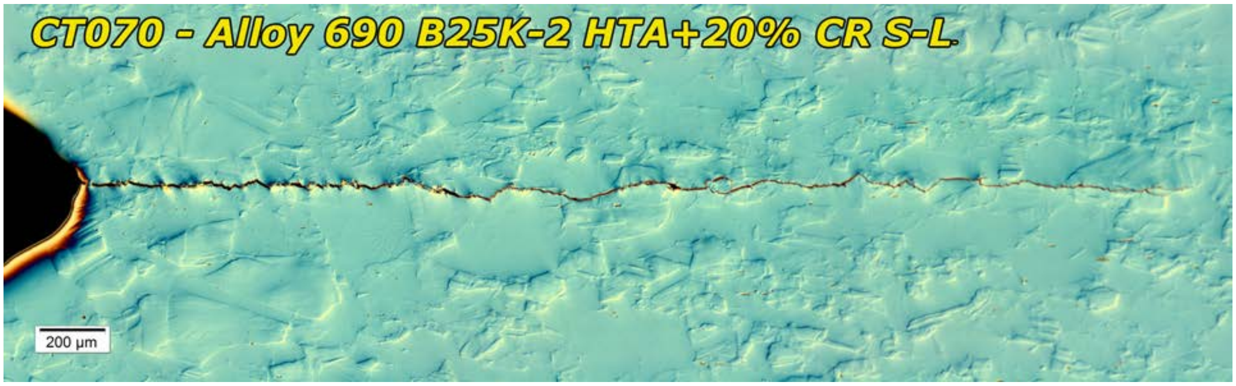

Figure 5.29 **Side surface observation of the as-received GEG alloy 690 HTA+20%CR S-L specimen, CT070, showing banding (small TG features) nearly parallel to the crack growth plane**

5.4 SCC Tests on EPRI/TK-VDM Heat 114092

5.4.1 EPRI/TK-VDM Heat 114092 - As-received TT Condition - CT107

This plate material was of interest primarily because it was in the TT condition. As noted in Chapter 3, it has a continuous distribution of grain boundary carbides, a semi-continuous distribution of TG carbides on prior (ghost) boundaries and a banded structure consisting of alternate regions of fine and coarse grains. The banding is in the plate fabrication plane.

A summary of the test conditions and specimen response is provided in Table 5.6, while an overview of the entire test is shown in Figure 5.30. Four constant K observations were performed, two at 30 MPa√m, one at 35 MPa√m, and one at 39 MPa√m. Transitioning using 980s/20s load cycling with a 2.5-h hold at K_{max} for the final step was initially employed, but constant K propagation rates were $<1x10^{-9}$ mm/s. More gentle transitioning using a 9980s/20s load cycle was applied, and K was also raised (by dK/da), but the material continued to exhibit strong resistance to SCC growth with the final constant K observations eventually resulting in propagation rates of $<1x10^{-9}$ mm/s. The final constant K observation with an initial SCC CGR of $1.5x10^{-9}$ mm/s is shown in Figure 5.31.

Table 5.6 Test conditions and specimen response for the as-received TK-VDM heat 114092 alloy 690TT specimen, CT107

								CT107 A690TT TK-VDM 114092		
Test Step	Start (h)	Duration (h)	R	Freq (Hz)	Hold (h)	Dissolved Hydrogen (cc/kg H_2)	Temp (°C)	Kmax (MPa√m)	CGR (mm/s)	Approx. Crack Extension (mm)
1	0	6	0.5	0.1	0	25	360	30	4.5E-06	0.080
2	6	40	0.5	0.01	0	25	360	30	7.2E-07	0.100
3	46	281	0.5	980s/20s	0	25	360	30	1.3E-07	0.120
4	327	457	0.5	980s/20s	2.5	25	360	30	1.5E-08	0.021
5	784	703	---	const K	---	25	360	30	2.8E-10	0.001
6	1487	305	0.5	980s/20s	2.5	25	360	30	2.0E-08	0.010
7	1792	647	0.5	9980s/20s	0	25	360	30	1.7E-08	0.032
8	2439	209	---	const K	---	25	360	30	NG	0.000
9	2648	484	0.35	9980s/20s	0	25	360	30	2.9E-08	0.046
10	3132	99	0.5	9980s/20s	0	25	360	30->35	NM	0.021
11	3231	235	0.5	9980s/20s	0	25	360	35	4.1E-08	0.031
12	3466	319	0.5	9980s/20s	1	25	360	35	2.8E-08	0.029
13	3785	184	0.5	9980s/20s	2.5	25	360	35	2.2E-08	0.012
14	3969	842	---	const K	---	25	360	35	2.5E-10	0.001
15	4811	197	0.5	9980s/20s	2.5	25	360	35	1.6E-08	0.009
16	5008	130	0.5	9980s/20s	2.5	25	360	35->39	NM	0.022
17	5138	270	0.5	9980s/20s	2.5	25	360	39	2.3E-08	0.027
18	5408	969	---	const K	---	25	360	39	4.0E-10	0.003
19	6377	115	0.5	9980s/20s	2.5	25	360	39	2.5E-08	0.007

NG = no growth
NM = not measured

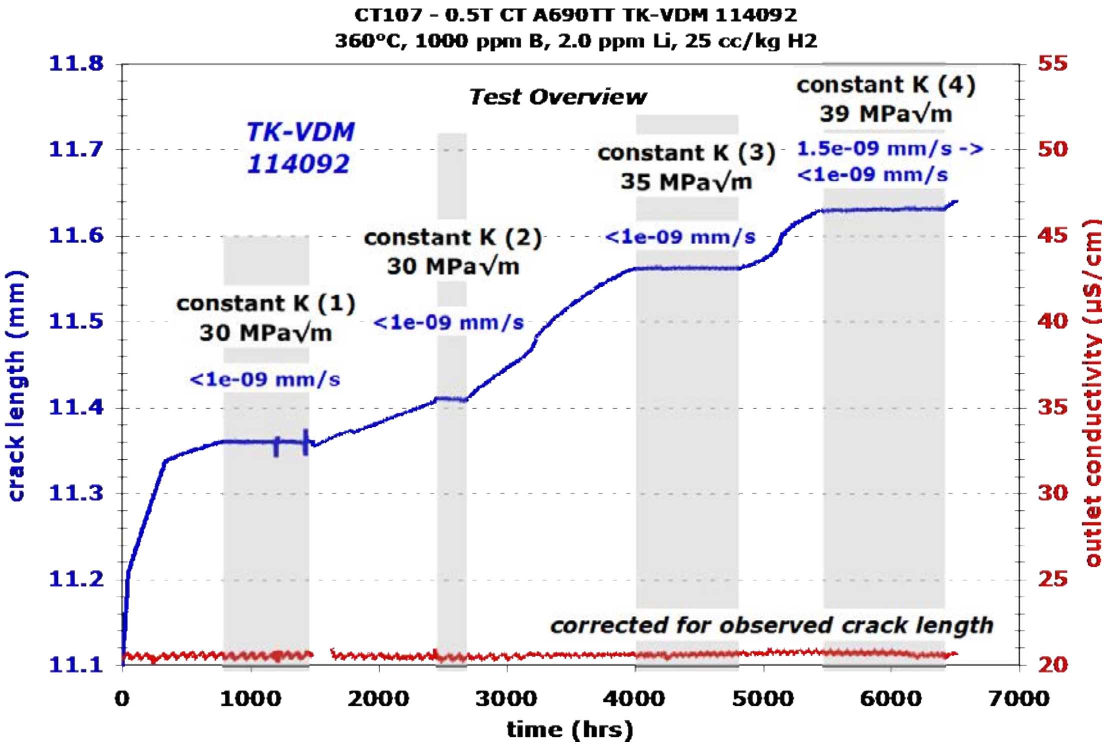

Figure 5.30 Overview of the entire SCC test on as-received TK-VDM heat 114092 alloy 690TT specimen, CT107

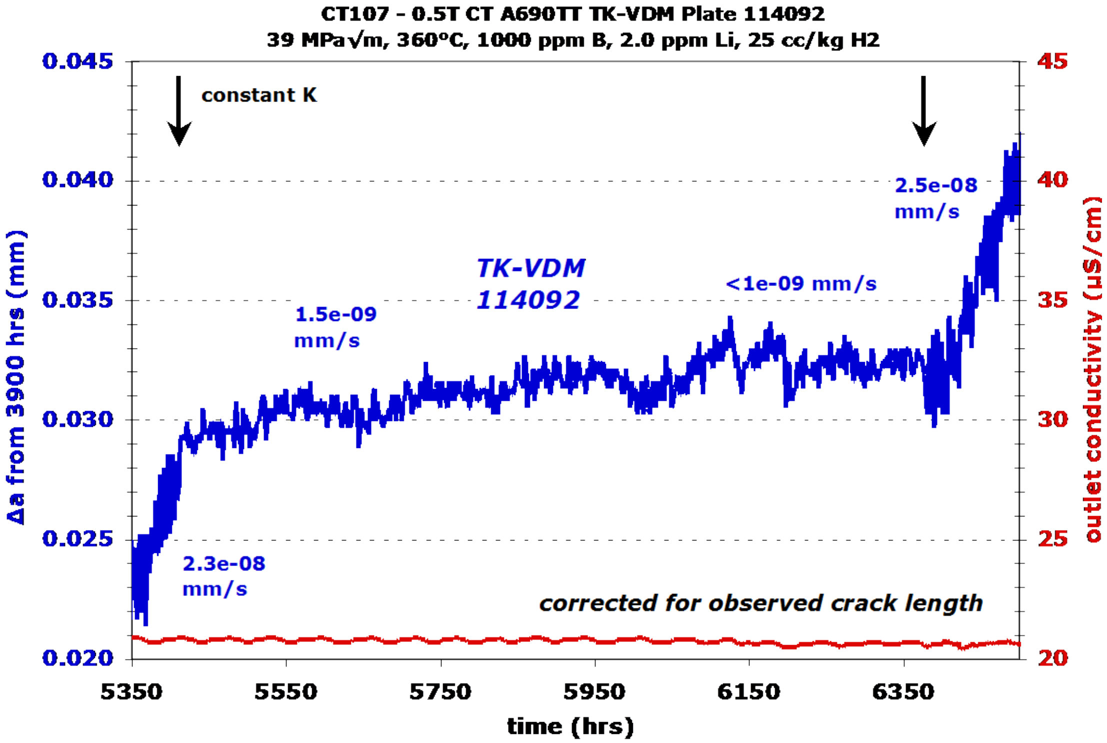

Figure 5.31 Crack growth response for as-received TK-VDM heat 114092 alloy 690TT specimen CT107 during the final constant K observation

After completing this ~6500 h test, a slice of the specimen was removed for cross-section observation, and the remaining portion was fatigued open for crack surface observations. The optical image of the crack surface in Figure 5.32 shows relatively straight final crack front. As indicated, DCPD-estimated crack length somewhat overpredicted the precrack length, but underpredicted the in-situ portion. SEM imaging of the surface revealed no obvious IG cracking with an example shown in Figure 5.33 for the final crack front. Side surface examinations also showed 100% TG cracking.

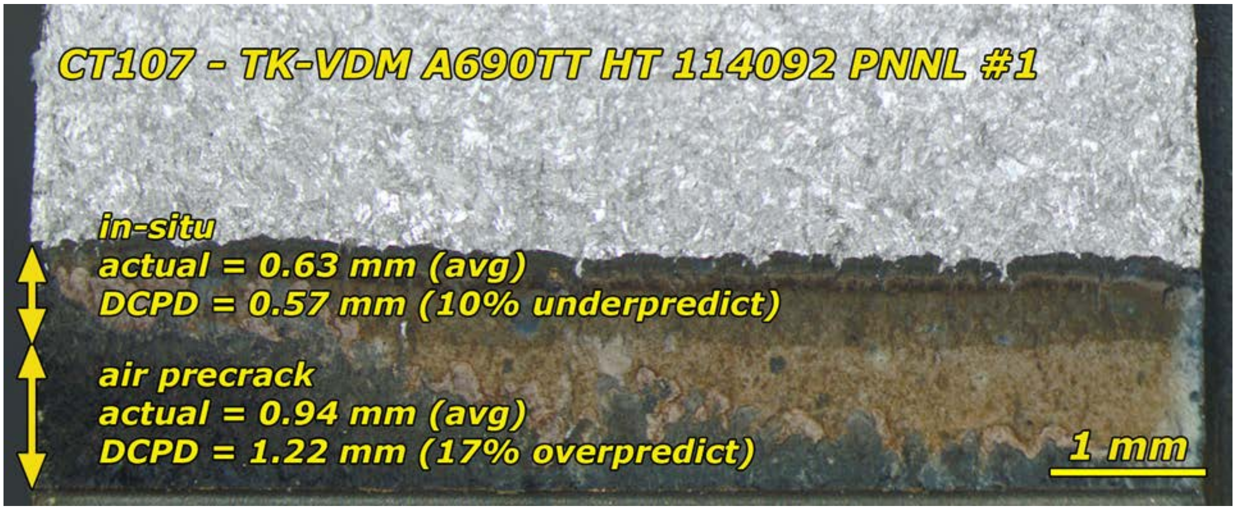

Figure 5.32 **Optical image of the crack growth surface of the as-received TK-VDM heat 114092 alloy 690TT specimen, CT107**

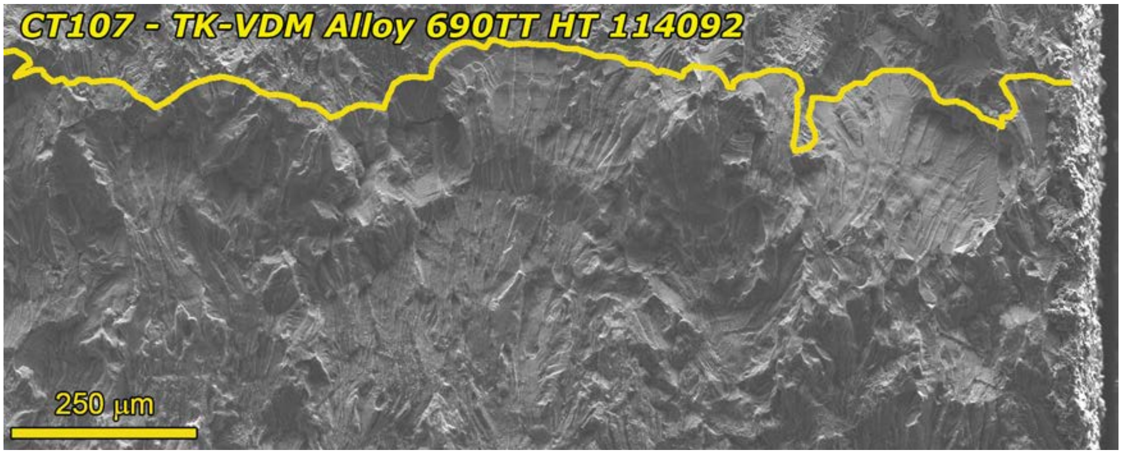

Figure 5.33 **SEM-SE image of a portion of the final crack front (yellow line) for the as-received TK-VDM heat 114092 alloy 690TT specimen, CT107**

5.4.2 EPRI/TK-VDM Heat 114092 - 32%CF Condition - CT094

The material was cold forged by, and obtained from, GE. A summary of the test conditions and specimen response is provided in Table 5.7, while an overview plot of the entire test is shown in Figure 5.34. Final transitioning steps before constant K observations included 980s/20s and 980s/20s+2.5 h hold load cycling. Two constant K observations were performed, both at a corrected value of ~31.5 MPa√m. Relatively low DCPD-indicated SCC CGRs of 2.3-3.1x10^{-8} mm/s were measured, but cycle+hold loading after constant K exhibited high initial CGRs indicating untracked crack growth due to ligament/contact formation. An example of the response for the first constant K observation is shown in Figure 5.35, and adjusted SCC CGRs for the two constant K observations were found to be 0.8-1.5x10^{-7} mm/s. Because of the indication of significant ligament/contact formation, SCC response was also assessed using extended hold times. The response during a cycle+hold loading with a 24-h hold and then a 10-h hold is presented in Figure 5.36. For both hold times, a staircase shaped data trend was observed indicating ligament/contact formation during these longer hold periods. Propagation rates for both of these test steps are similar to that for the constant K observations, but the stair-steps for 10 h hold data suggest that the actual SCC CGR could be higher than 1.5x10^{-7} mm/s.

Table 5.7 Test conditions and specimen response for the TT+32%CF TK-VDM heat 114092 alloy 690 specimen, CT094

								TK-VDM HT 114092 A690TT 32%CF S-L/S-T		
Test Phase	Start (h)	Duration (h)	R	Freq (Hz)	Hold (h)	Dissolved Hydrogen (cc/kg H_2)	Temp (°C)	Kmax (MPa√m)	CGR (mm/s)	Approx. Crack Extension (mm)
1	0	8	0.5	0.1	0	25	360	30	9.2E-06	0.200
2	8	34	0.5	0.01	0	25	360	31	1.7E-06	0.250
3	42	142	0.5	980s/20s	0	25	360	31	3.7E-07	0.220
4	184	244	0.5	980s/20s	2.5	25	360	31	2.6E-07	0.178
5	428	0	---	const K	---	25	360	31	3.3E-08	0.011
5*	428	573	---	const K	---	25	360	32	9.2E-08	0.000
6	1001	163	0.5	980s/20s	2.5	25	360	31	3.7E-07	0.364
7	1164	0	---	const K	---	25	360	31	2.2E-08	0.023
7*	1164	271	---	const K	---	25	360	32	1.5E-07	0.023
8	1435	281	0.5	980s/20s	2.5	25	360	31	2.6E-07	0.458
9	1716	291	0.5	980s/20s	24	25	360	31	6.4E-08	0.063
10	2007	123	0.5	980s/20s	10	25	360	31	1.3E-07	0.067
11	2130	185	0.5	980s/20s	0	25	360	31	4.1E-07	0.640

* Ligament/contact adjusted CGR listed in this row.

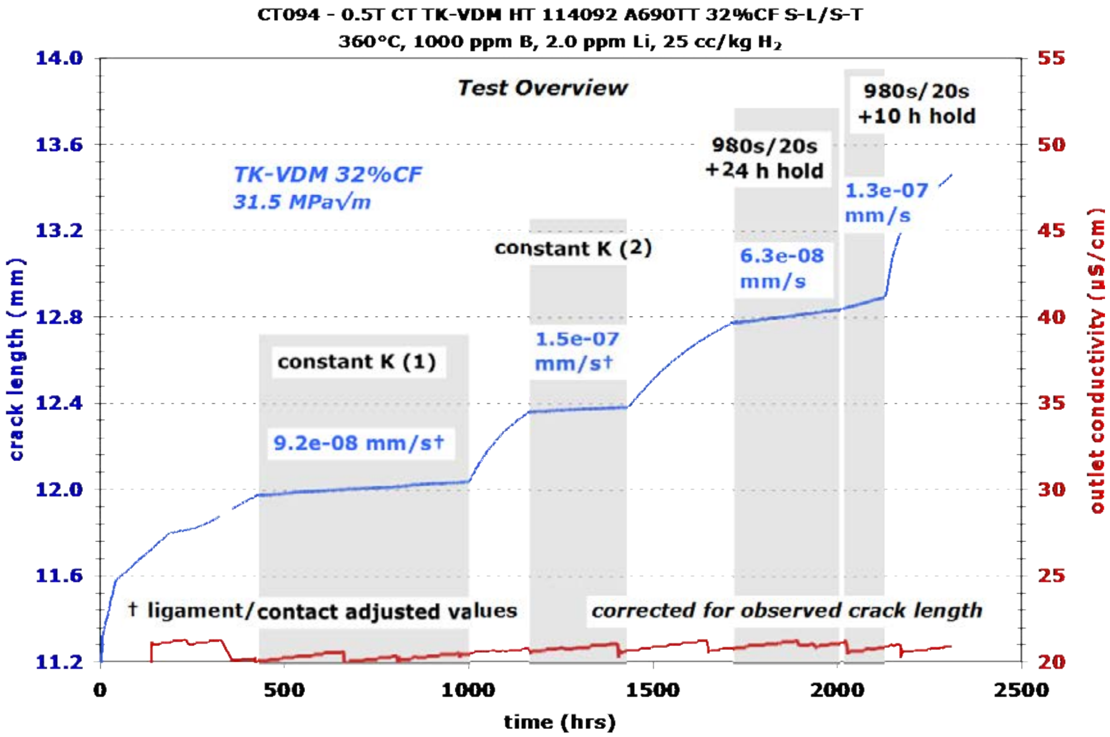

Figure 5.34 Overview of the entire SCC test on the TT+32%CF TK-VDM heat 114092 alloy 690 specimen, CT094

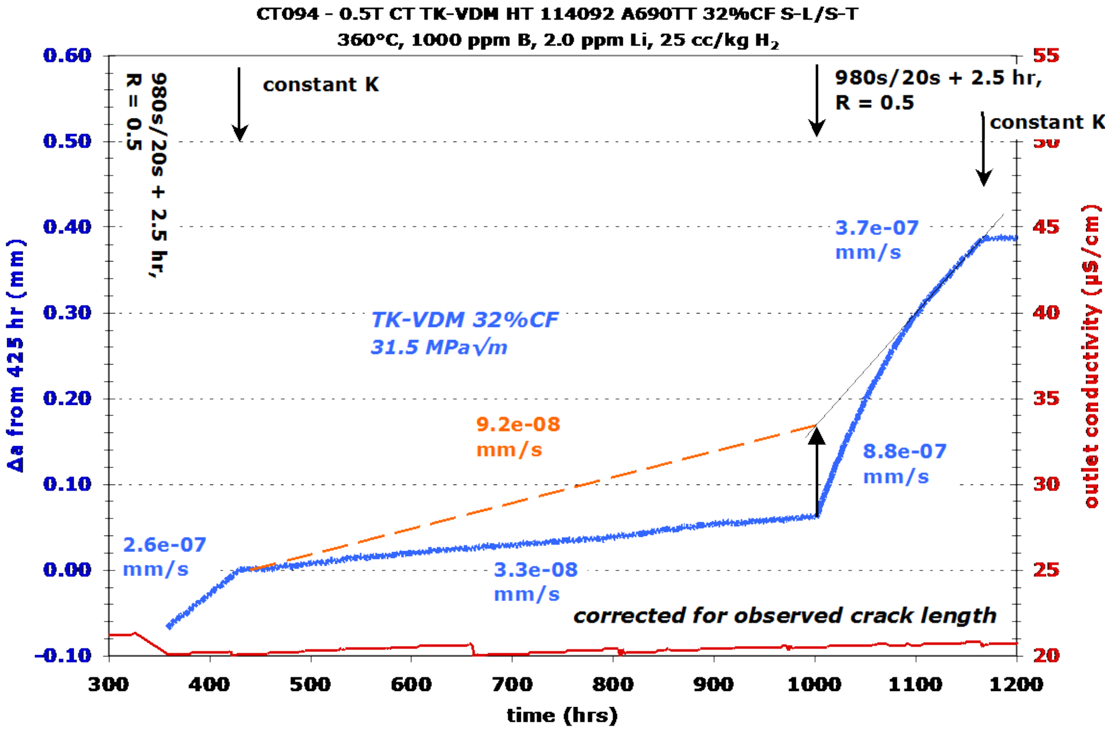

Figure 5.35 Crack growth response for the TT+32%CF TK-VDM heat 114092 alloy 690 specimen CT094 during the first constant K observation

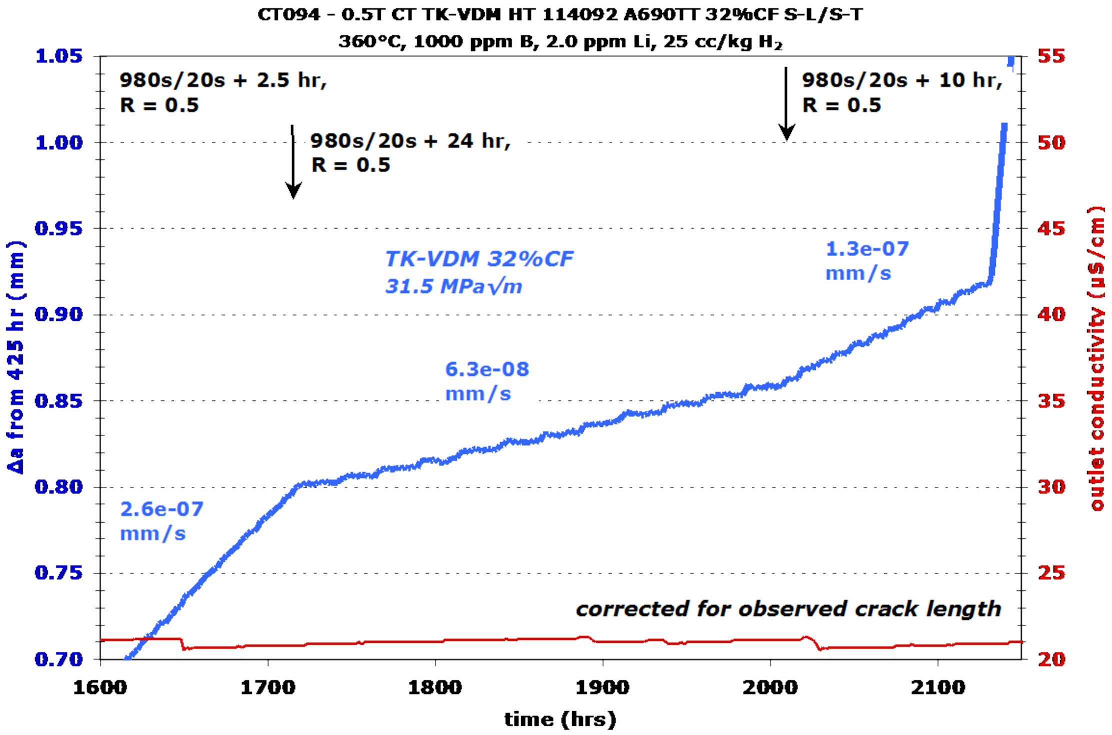

Figure 5.36 Crack growth response for the TT+32%CF TK-VDM heat 114092 alloy 690 specimen CT094 during cycle+hold loading

After completing this ~2300 h test, a slice of the specimen was removed for cross-section observation, and the remaining portion was fatigued open for crack surface observations. The optical image of the crack surface in Figure 5.37 shows a variable length crack suggestive of varying degrees of engagement, however there were no obvious unbroken ligaments. DCPD overpredicted both the precrack length and the in-situ portion by modest values of 9 and 14%, respectively. An SEM-SE image of the entire crack front in Figure 5.38 indicates a high degree of IG engagement, but some TG cracking is evident as shown in the detail images in Figure 5.39. In the vicinity of the constant K observations, the crack was determined to be ~83% engaged.

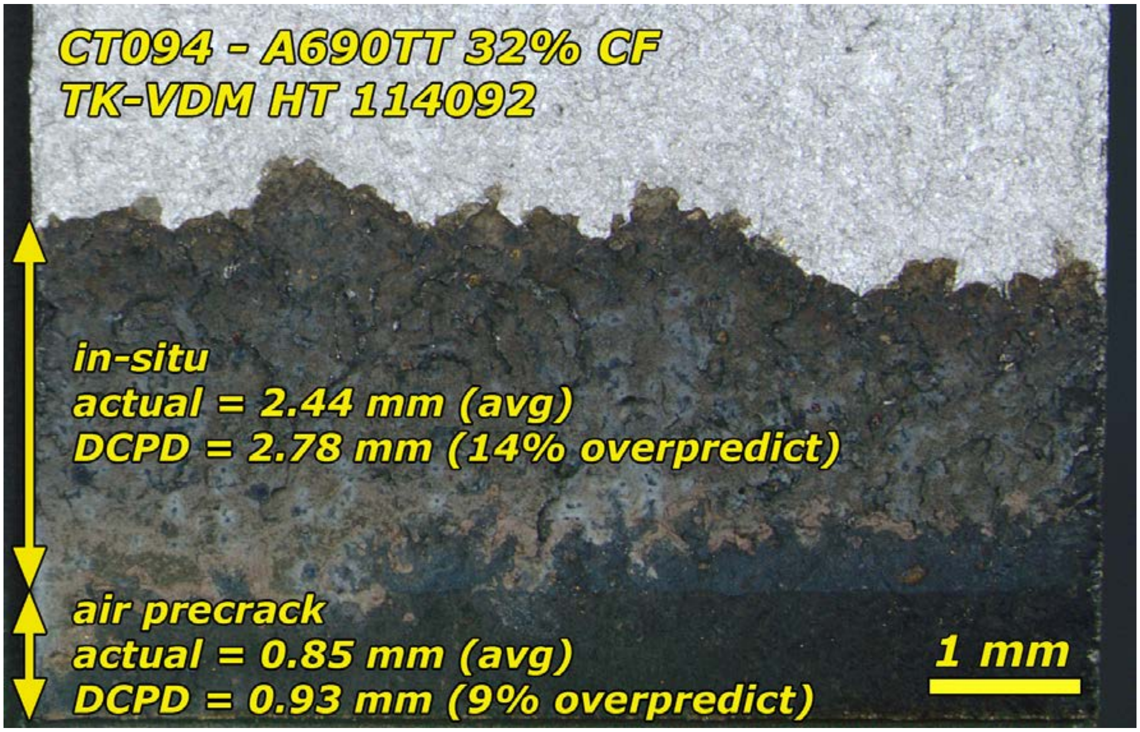

Figure 5.37 Optical image of the crack growth surface of the TT+32%CF TK-VDM heat 114092 alloy 690 specimen CT094

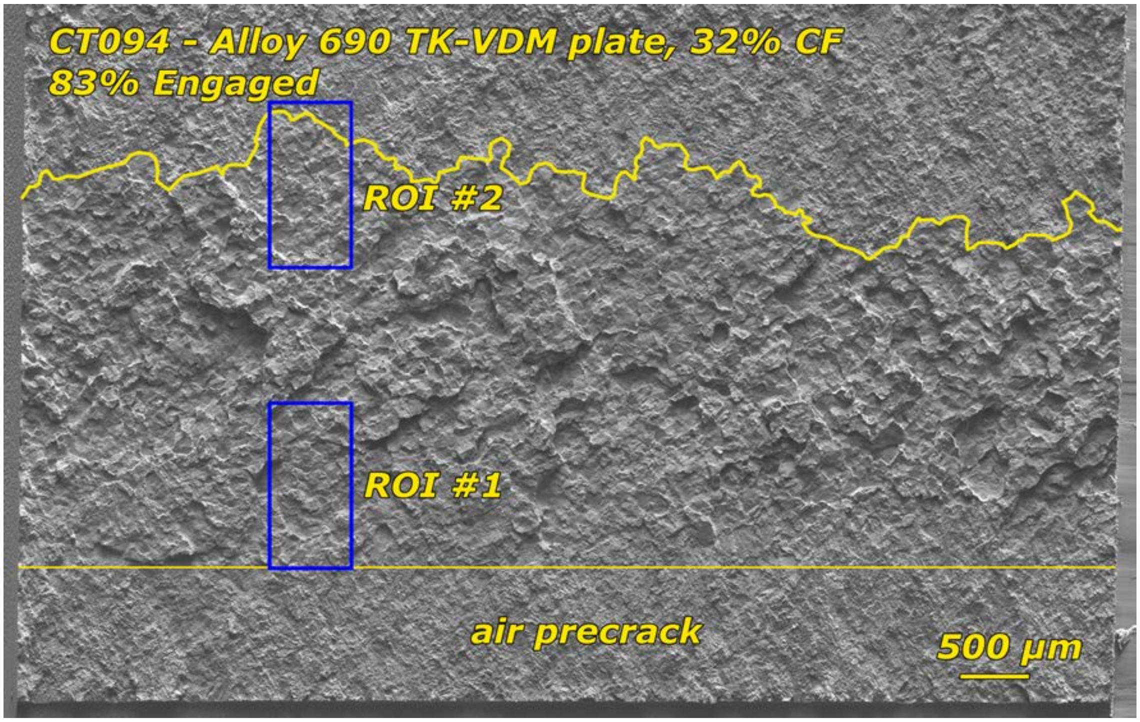

Figure 5.38 SEM-SE overview image of the entire crack growth surface for the TT+32%CF TK-VDM heat 114092 alloy 690 specimen, CT094. Yellow line denotes the final crack front, and the blue boxes are higher magnification regions shown in Figure 5.39.

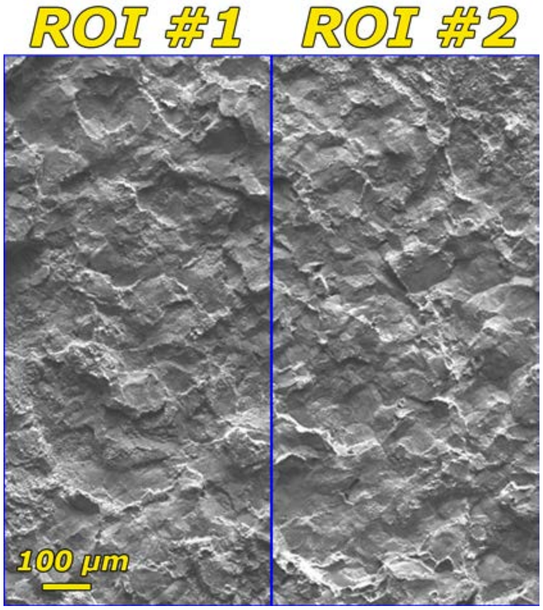

Figure 5.39 **SEM-SE image of a region near the initial transitioning region (ROI #1) and of a portion near the final crack front (ROI #2) for the TT+32%CF TK-VDM heat 114092 alloy 690 specimen, CT094**

5.5 SCC Tests on ENSA/Aubert&Duval Heat WP547 - 32%CF and 22%CR S-L Conditions

These two specimens were tested as a pair making it convenient to present the results for both at the same time. These materials were donated to the EPRI materials stockpile and acquired by GE where some material was 32%CF and other material was 22%CR. Specimens were cut so that the deformation plane is parallel to the geometric crack growth plane. These specimens were used to study the effect of dissolved hydrogen on SCC crack growth. The specimen identifications are CT059 for the 32%CF and CT060 for the 22%CR. A summary of the test conditions and specimen response is provided in **Table 5.8**, while an overview plot of the entire test is shown in **Figure 5.40**. Final transitioning steps before constant K observations included 980s/20s and 980s/20s+2.5 h hold load cycling. Two constant K observations were performed. The corrected stress intensities for the first constant K observation were 34.5 and 30.3 MPa√m for the 32% CF and 22% CR respectively, and for the second constant K observation, the values were 36.3 and 29.5 MPa√m.

Table 5.8 Test conditions and specimen response for the TT+32%CF and TT+22%CR ENSA/A&D alloy 690 specimens, CT059 & CT060

								CT059 ENSA A690 TT+32%CF			CT060 ENSA A690 TT+22%CR S-L		
Test Step	Start (h)	Dur-ation (h)	R	Freq (Hz)	Hold (h)	DH (cc/kg H^2)	Temp (°C)	Kmax (MPa√m)	CGR (mm/s)	Approx. Crack Ext. (mm)	Kmax (MPa√m)	CGR (mm/s)	Approx. Crack Ext. (mm)
1		16	0.5	0.1	0	25	360	31	1.1E-05	0.606	30	6.8E-06	0.363
2		68	0.5	0.01	0	25	360	32	2.4E-06	0.587	30	1.1E-06	0.289
3		159	0.5	0.001	0	25	360	33	5.4E-07	0.301	30	1.9E-07	0.110
4		23	0.5	0.01	0	25	360	33	2.5E-06	0.202	30	1.3E-06	0.112
5		79	0.5	0.001	0	25	360	33	4.1E-07	0.124	30	2.1E-07	0.059
6		237	0.5	0.001	2.5	25	360	33	1.6E-07	0.108	30	3.5E-08	0.035
7		315	---	const K	---	25	360	34	4.7E-08	0.047	30	1.8E-08	0.017
8		379	---	const K	---	5	360	34	2.4E-08	0.041	30	1.0E-08	0.014
9		382	---	const K	---	1	360	34	1.7E-08	0.027	30	1.0E-08	0.016
10		246	---	const K	---	15	360	34	3.3E-08	0.025	30	1.2E-08	0.011
11		187	---	const K	---	25	360	34	3.6E-08	0.026	30	1.8E-08	0.010
12		392	---	const K	---	60	360	34	4.4E-08	0.065	30	2.5E-08	0.028
13		262	---	const K	---	25	360	34	3.2E-08	0.031	30	1.8E-08	0.020
14		318	---	const K	---	10.5	325	34	6.5E-09	0.026	30	6.6E-09	0.007
15		166	0.5	0.001	2.5	10.5	325	35	4.8E-07	0.549	29	1.2E-07	0.112
16		235	---	const K	---	10.5	325	35	1.1E-08	0.008	29	4.2E-09	0.004
17		336	---	const K	---	60	325	35	1.3E-08	0.017	29	5.6E-09	0.005
18		338	---	const K	---	10.5	325	36	1.4E-08	0.013	29	8.2E-09	0.005
19		316	---	const K	---	30	325	36	1.5E-08	0.016	29	7.4E-09	0.008
20		357	---	const K	---	4	325	36	5.7E-09	0.006	29	5.3E-09	0.004
21		315	---	const K	---	1	325	36	5.3E-09	0.005	29	5.1E-09	0.005
22		200	---	const K	---	10.5	325	36	1.6E-08	0.010	29	9.3E-09	0.003
23		106	---	const K	---	25	360	36	3.1E-08	0.007	29	1.8E-08	0.005
24		368	---	const K	---	1	360	36	1.8E-08	0.027	29	1.0E-08	0.015

The first dissolved hydrogen (DH) effects study was performed at 360°C as presented in Figure 5.41. SCC response was assessed at the Ni/NiO stability line, and then the DH was reduced into the NiO stability region. SCC CGRs were observed to decrease with decreasing DH. The test was brought back to the Ni/NiO stability line to compare to the initial observation at the Ni/NiO stability line and then increased into the Ni-metal stability regime. For testing at 325°C (Figure 5.42), a similar approach was used except that Ni-metal stable was assessed before NiO stable conditions. SCC CGR plotted as a function of DH is shown in Figure 5.43 for both the 360°C and 325°C runs. The data at 360°C where propagation rates were ≥1.0x10^{-8} mm/s show a decreasing CGR as conditions change from the Ni/NiO stability line to NiO stable, similar to that for alloy 600. However as DH is increased beyond the Ni/NiO stability line, instead of a decreasing CGR like for alloy 600, the alloy 690 CGR appears to either hold steady or increase slightly. At 325°C for the 32%CF material where propagation rates are still predominantly ≥1x10^{-8} mm/s, a similar trend is observed. For the 22%CR material where propagation rates are <1x10^{-8} mm/s, the trend is less clear. The tendency for decreased CGRs remains under NiO stable conditions, but CGRs were either similar or slightly lower at Ni-metal stable conditions as measured at the Ni/NiO stability line.

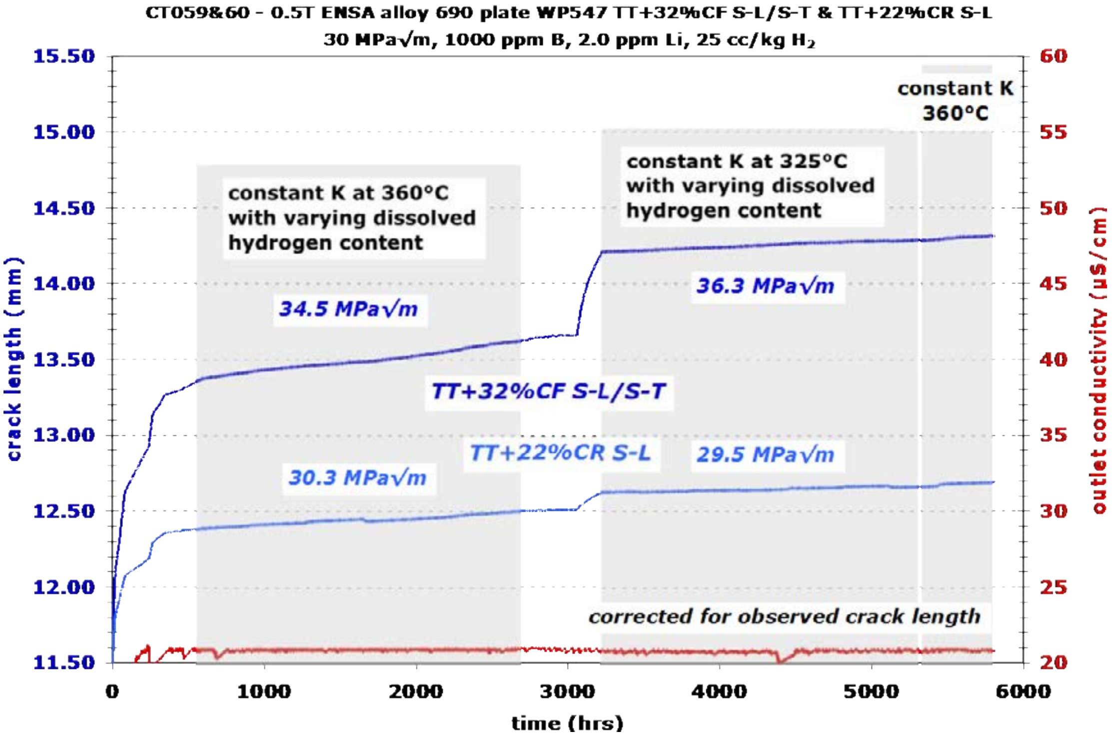

Figure 5.40 **Overview of the entire SCC test for the TT+32%CF and TT+22%CR ENSA/A&D alloy 690 specimens, CT059 & CT060**

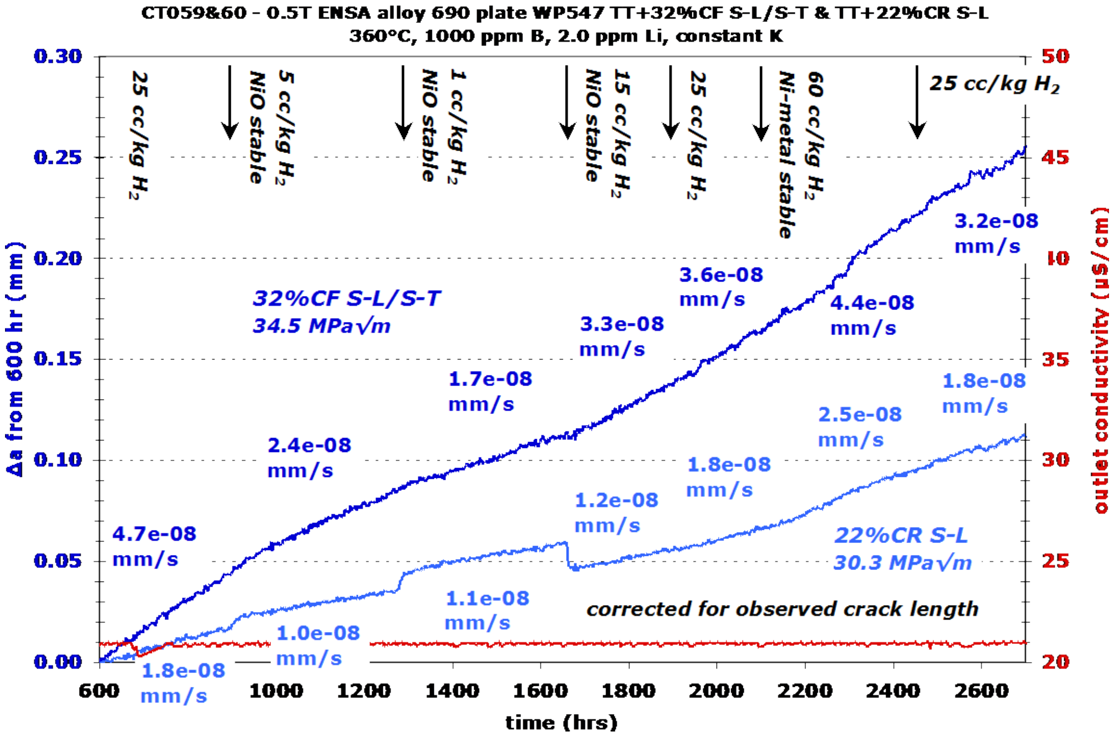

Figure 5.41 Crack growth response for the TT+32%CF and TT+22%CR ENSA/A&D alloy 690 specimens, CT059 & CT060, at 360°C with varying dissolved H_2

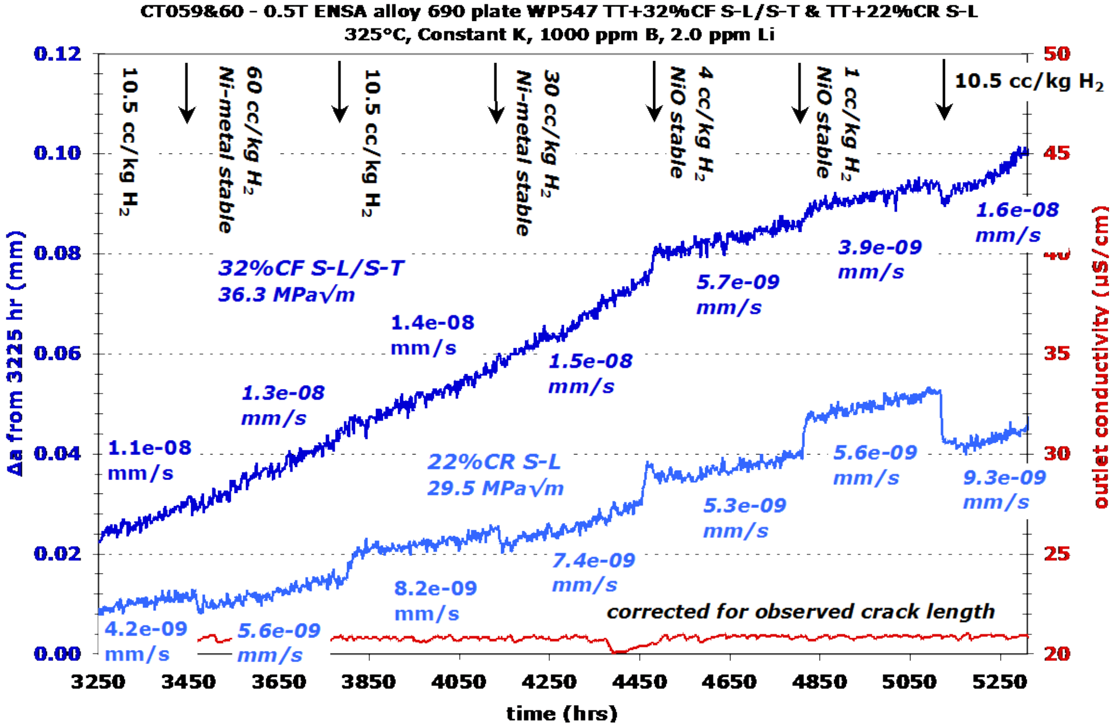

Figure 5.42 Crack growth response for the TT+32%CF and TT+22%CR ENSA/A&D alloy 690 specimens, CT059 & CT060, at 325°C with varying dissolved H_2

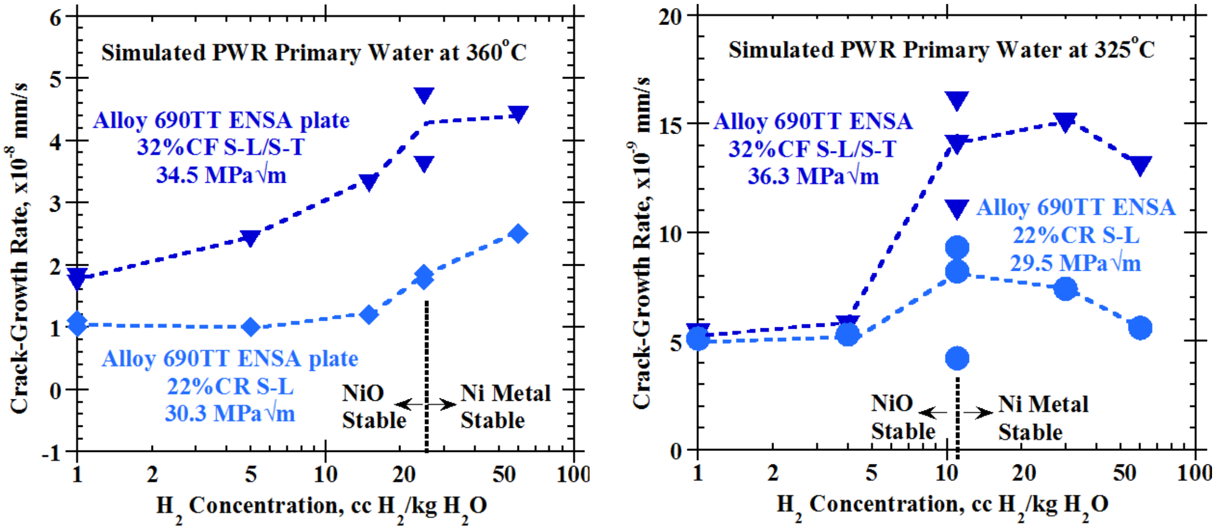

Figure 5.43 **Constant K SCC crack growth rate versus dissolved hydrogen for the TT+32%CF and TT+22%CR ENSA/A&D alloy 690 specimens, CT059 & CT060, at 360°C and at 325°C**

After completing this ~5,800 h test, a slice of the specimen was removed for cross-section observation, and the remaining portion was fatigued open for crack surface observations. A machining mishap occurred for the 32%CF specimen (CT059) resulting in the specimen being cut into three slices rather than two. The optical image of the crack surface for this specimen is shown in Figure 5.44. The overall crack front is relatively straight from one side to the other, but there are a number of undulations, and some evidence for unbroken ligaments behind the crack front can be seen. As noted in the text of the image, DCPD significantly underpredicted the actual crack length. This is primarily due to the choice of calibration factor that was used for this test. An SEM-SE overview image of the final crack front is provided in Figure 5.45 while a higher magnification portion is shown in Figure 5.46. The grains had a very flattened appearance, and measurements near the final crack front indicated ~92% IG engagement. Examples of TG cracking are indicated by the yellow arrows.

Results for the 22%CR material are shown in Figure 5.47, Figure 5.48, and Figure 5.49. In this case, the grains had a more typical (not flattened) appearance, and slightly less IG engagement of 87% was measured.

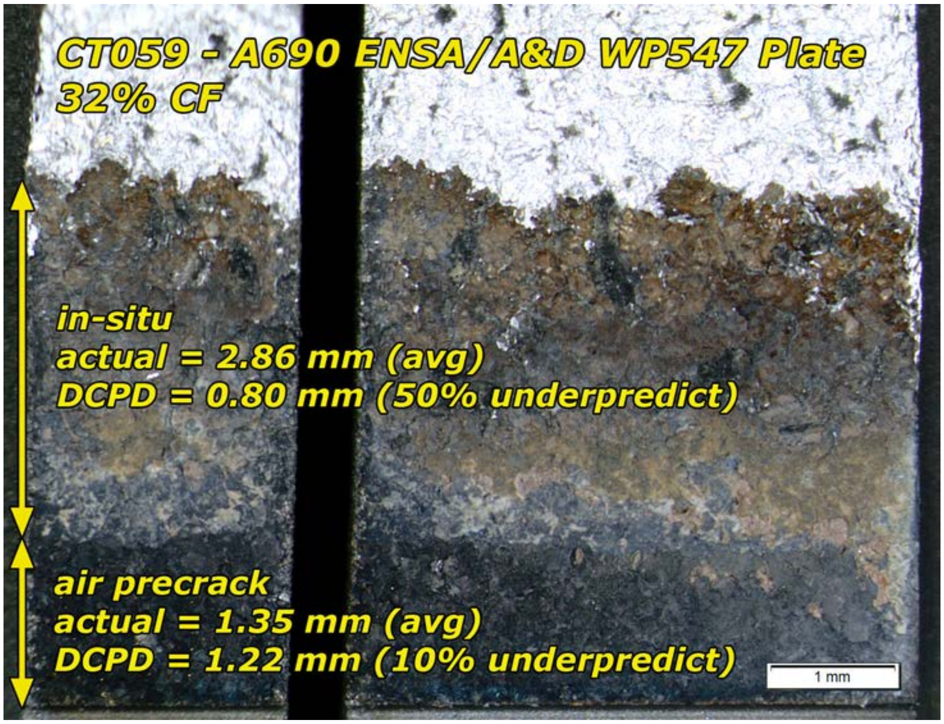

Figure 5.44 Optical image of the crack growth surface of the TT+32%CF ENSA/A&D alloy 690 specimen, CT059

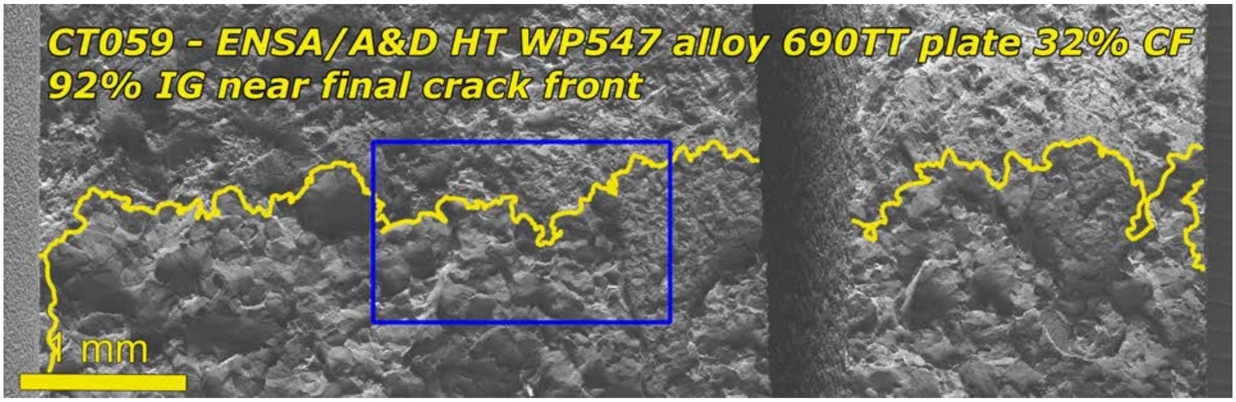

Figure 5.45 SEM-SE overview image near the final crack front for the 32%CF ENSA/A&D alloy 690TT specimen, CT059. Yellow line denotes the final crack front, and the blue box is a higher magnification region shown in Figure 5.46.

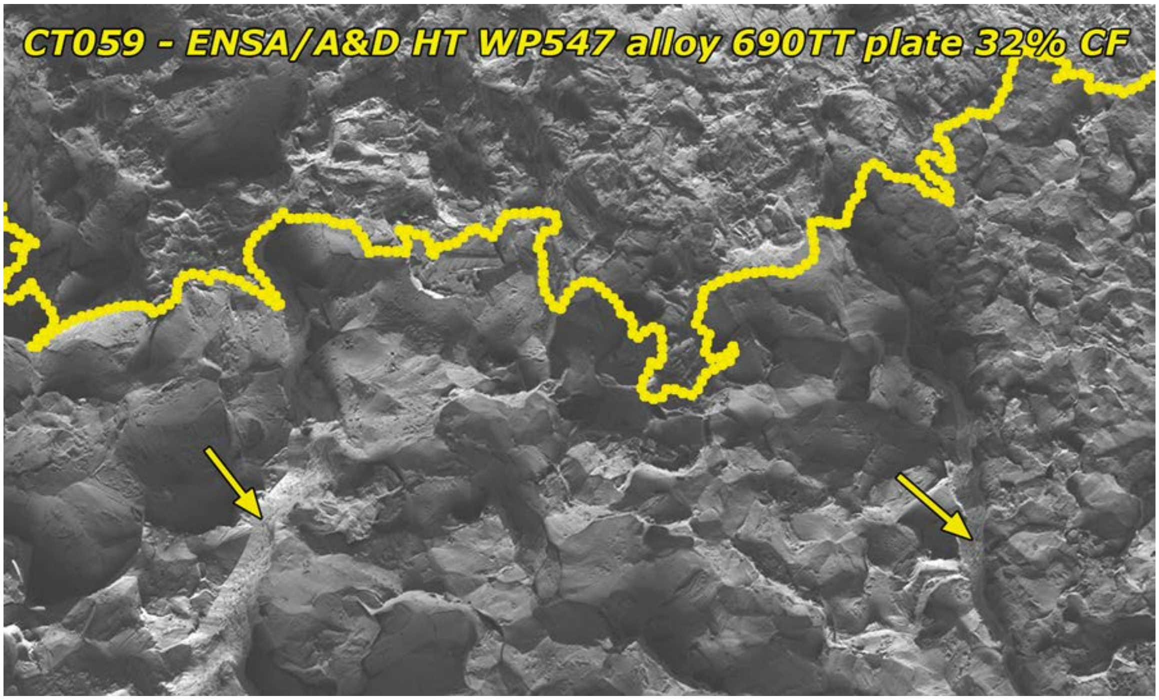

Figure 5.46 SEM-SE image of a portion of the final crack front for the 32%CF ENSA/A&D alloy 690TT specimen, CT059. Patches of TG cracking are denoted by the arrows.

Figure 5.47 Optical image of the crack growth surface of the 22%CR ENSA/A&D alloy 690TT specimen, CT060

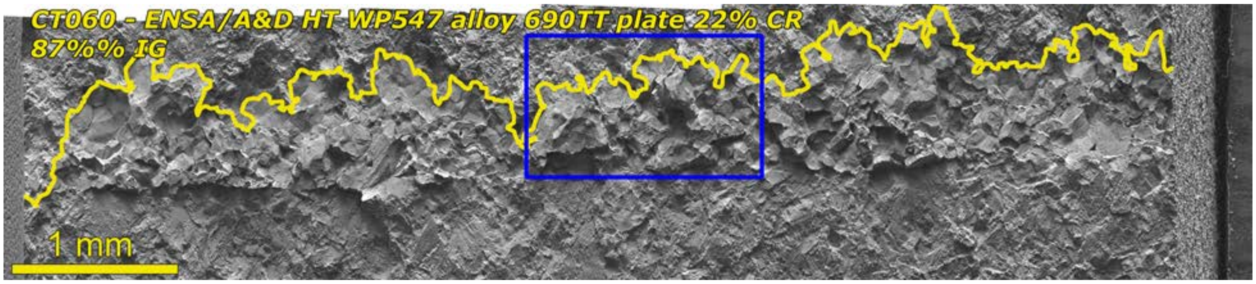

Figure 5.48 SEM-SE overview image for the 22%CR ENSA/A&D alloy 690TT specimen, CT060. Yellow line denotes the final crack front, and the blue box is a higher magnification region shown in Figure 5.49.

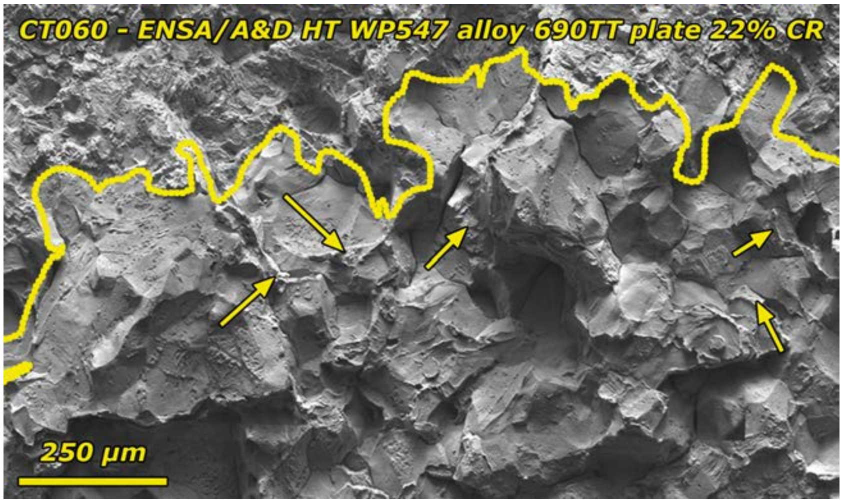

Figure 5.49 SEM-SE image of a portion of the final crack front for the 22%CR ENSA/A&D alloy 690TT specimen, CT060. Patches of TG cracking are denoted by the arrows.

5.6 SCC Tests on EPRI/Allvac Heat X87N-1 - 21%CF Condition

Only one specimen of this material, obtained from the EPRI materials stockpile, has been tested. Cold forging of the material was again performed by GEG. A summary of the test conditions and specimen response is provided in **Table 5.9**, while an overview plot of the entire test is shown in **Figure 5.50**. Final transitioning steps before constant K observations included 980s/20s and 980s/20s+2.5 hr hold load cycling. Five constant K observations were performed at stress intensities ranging from 30 to 43 MPa√m. The observed SCC CGRs of 2.8-7.3x10^{-9} mm/s were very low for a 20% CW, and there was almost no indication of ligaments or contacts causing any untracked crack extension. There was a clear correlation between SCC propagation rate and stress intensity, however the influence was relatively mild. An example of the SCC response for the first constant K observation is shown in **Figure 5.51**.

Table 5.9 Test conditions and specimen response for the 21%CF Allvac X87N-1 alloy 690TT specimen, CT101

								CT101 A690 Billet X87N-1 21.4 % CF		
Test Phase	Start (h)	Duration (h)	R	Freq (Hz)	Hold (h)	Dissolved Hydrogen (cc/kg H_2)	Temp (°C)	Kmax (MPa√m)	CGR (mm/s)	Approx. Crack Extension (mm)
1	0	11	0.5	0.1	0	25	360	30	3.4E-06	0.155
2	11	35	0.5	0.01	0	25	360	30	7.6E-07	0.101
3	46	156	0.5	980s/20s	0	25	360	30	1.6E-07	0.100
4	202	552	0.5	980s/20s	2.5	25	360	30	2.4E-08	0.050
5	754	329	0.5	980s/20s	10	25	360	30	7.9E-09	0.011
6	1083	538	---	const K	---	25	360	30	2.8E-09	0.006
6*	1083	---	---	const K	---	25	360	30	NO	NA
7a	1621	193	0.5	980s/20s	2.5	25	360	30	2.3E-08	0.025
7b	1814	291	0.5	980s/20s	2.5	25	360	30	2.4E-08	0.031
8	2105	328	0.5	12s/12s	2.77	25	360	30	1.6E-08	0.022
9	2433	339	0.5	980s/20s	2.5	25	360	30	2.9E-08	0.036
10	2772	516	---	const K	---	25	360	30	2.1E-09	0.002
10*	2772	---	---	const K	---	25	360	30	5.1E-09	0.000
11	3288	308	0.5	980s/20s	2.5	25	360	30	2.4E-08	0.029
12	3596	137	0.5	980s/20s	2.5	25	360	30->37	Incr.	0.025
13	3733	124	0.5	980s/20s	2.5	25	360	37	5.9E-08	0.030
14	3857	522	---	const K	---	25	360	37	3.2E-09	0.006
14*	3857	---	---	const K	---	25	360	37	NO	0.000
15	4379	213	0.5	980s/20s	2.5	25	360	37	7.4E-08	0.064
16	4592	32	0.5	980s/20s	2.5	25	360	37->43	Incr.	0.021
17	4624	231	0.5	980s/20s	2.5	25	360	43	8.4E-08	0.093
18	4855	747	---	const K	---	25	360	43	7.3E-09	0.018
18*	4855	---	---	const K	---	25	360	43	NO	NA
19	5602	143	0.5	980s/20s	2.5	25	360	43	1.6E-07	0.099
20	5745	885	---	const K	---	25	360	43	6.3E-09	0.019

* CGR adjusted for contact/ligament formation
NO - Not Observed
NA - Not Applicable
Incr. - Increasing CGR

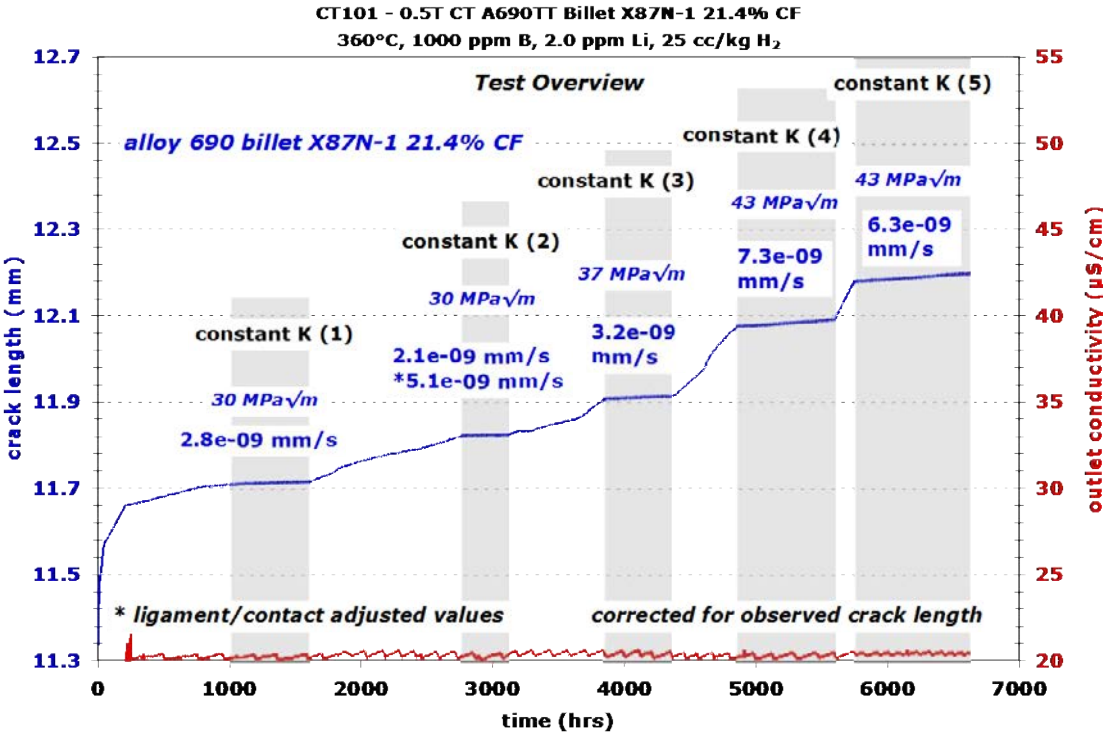

Figure 5.50 Overview of the entire SCC test on the 21%CF Allvac X87N-1 alloy 690TT specimen, CT101

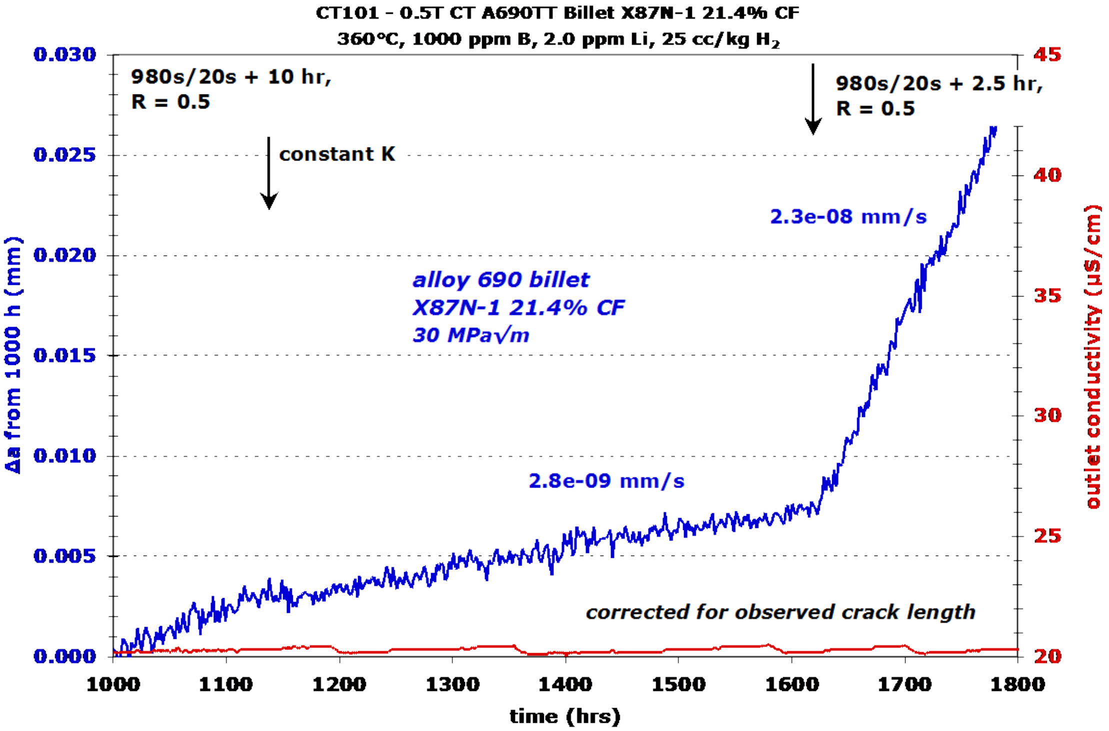

Figure 5.51 Crack growth response for the 21%CF Allvac X87N-1 alloy 690TT specimen, CT101 during the first constant K observation

After completing this ~6700 h test, a slice of the specimen was removed for cross-section observation, and the remaining portion was fatigued open for crack surface observations. The optical image of the as-tested crack surface in Figure 5.52 shows an overall straight crack front with local variability in crack length. There are a few minor indications of unbroken ligaments behind the crack front. DCPD overpredicted both the precrack length and the in-situ portion by modest values of 33 and 11%, respectively. An SEM-SE image of the entire crack front in Figure 5.53 indicates a high degree of IG engagement, but some TG cracking is evident as shown in the detail images in Figure 5.54. Since this material exhibited low SCC CGRs, there was an expectation that there would be a low degree of IG engagement, however, in the vicinity of the constant K observations, the crack was determined to have a relatively high ~76% engagement.

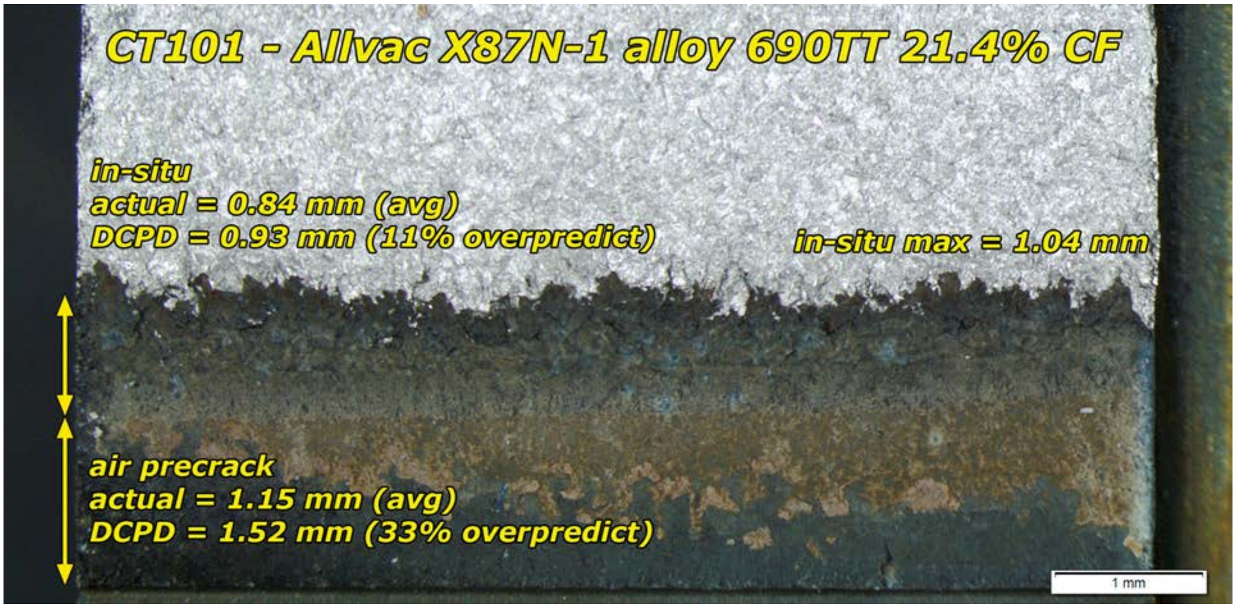

Figure 5.52 **Optical image of the as-test 21%CF Allvac X87N-1 alloy 690TT specimen, CT101**

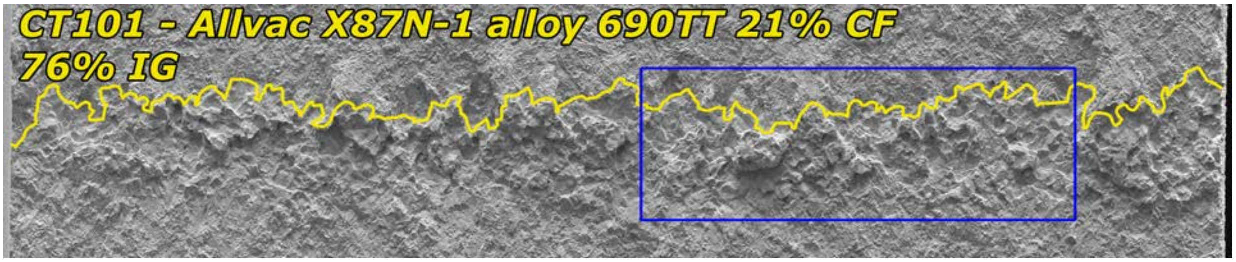

Figure 5.53 **SEM-SE image of the SCC crack growth region of the 21%CF Allvac X87N-1 alloy 690TT specimen, CT101. Yellow line denotes the final crack front, and the blue box is a higher magnification region shown in Figure 5.54.**

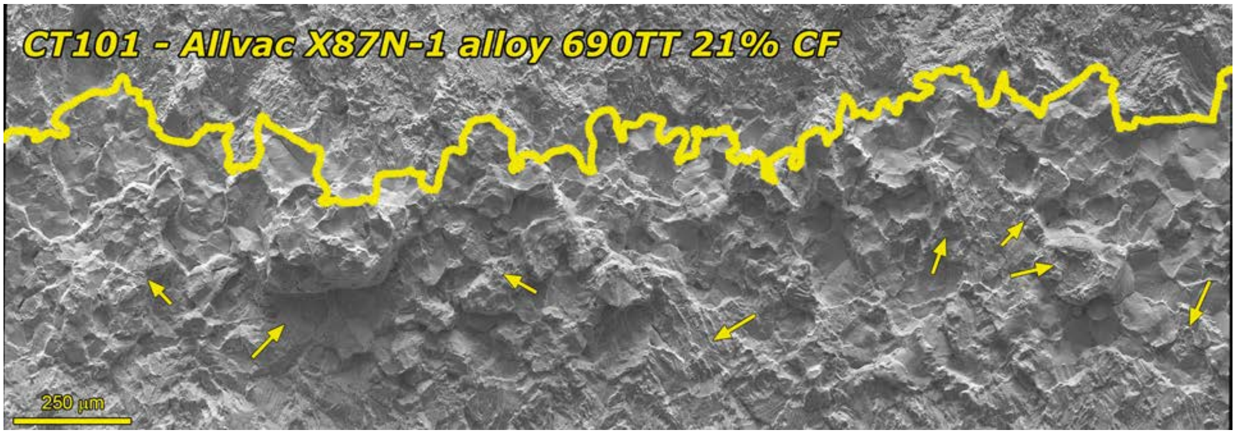

Figure 5.54 **SEM-SE image of a portion of the final crack front (yellow line) for the 21%CF Allvac X87N-1 alloy 690TT specimen, CT101. Yellow arrows point to isolated areas of TG cracking.**

5.7 SCC Tests on HAZ Materials

5.7.1 Ciemat/Aubert&Duval WP547 TT Plate HAZ

This specimen was cut from an alloy 52 weldment prepared by Ciemat. A summary of the test conditions and specimen response is provided in **Table 5.10**, while an overview plot of the entire test is shown in **Figure 5.55**. Final transitioning steps before constant K observations included 980s/20s and 980s/20s+2.5 hr hold load cycling. Five constant K observations were performed at stress intensities ranging from 30 to 40 MPa√m. Microstructural locations for SCC CGR testing were selected based on the location of the fusion line relative to the geometric crack growth plane as shown in **Figure 5.56**. All five observations were intended to be relatively close to the fusion line, but the 4th one was planned to be closest. The observed sustained SCC CGRs of 1.4-2.1x10^{-9} mm/s are slightly higher than that for as-received alloy 690 but were still quite low. An example of the SCC response for the first constant K observation is shown in **Figure 5.57**.

Table 5.10 Test conditions and specimen response for the Ciemat WP547 alloy 690TT HAZ specimen, CT067

							CT067 Ciemat A52/690 HAZ		
Test Phase	Duration (h)	R	Freq (Hz)	Hold (h)	Dissolved Hydrogen (cc/kg H_2)	Temp (°C)	Kmax (MPa√m)	CGR (mm/s)	Approx. Crack Extension (mm)
1	12	0.5	0.1	0	25	360	30	6.0E-06	0.223
2	63	0.5	0.01	0	25	360	30	9.8E-07	0.218
3	185	0.5	0.001	0	25	360	30	1.7E-07	0.125
4	315	0.5	0.001	2.5	25	360	30	2.0E-08	0.025
5	170	0.5	980s/20s	2.5	25	360	30	2.0E-08	0.014
6	885	---	const K	---	25	360	30	1.7E-09	0.011
7	145	0.5	980s/20s	0	25	360	30	1.7E-07	0.086
8	365	0.5	980s/20s	1	25	360	30	4.1E-08	0.055
9	183	0.5	980s/20s	2.5	25	360	30	2.0E-08	0.013
10	318	---	const K	---	25	360	30	1.4E-09	0.003
11	117	0.5	980s/20s	2.5	25	360	30->35	6.7E-08	0.022
12	245	0.5	980s/20s	2.5	25	360	35	2.9E-08	0.027
13	593	---	const K	---	25	360	35	1.7E-09	0.005
14	92	0.5	0.01	0	25	360	36	1.4E-06	0.451
15	133	0.5	0.001	0	25	360	36	1.9E-07	0.043
16	259	0.5	0.001	2.5	25	360	36	2.4E-08	0.022
17	1236	---	const K	---	25	360	36	1.9E-09	0.005
18	30	0.5	0.1	0	25	360	36	9.1E-06	0.824
19	104	0.5	0.01	0	25	360	37	1.2E-06	0.439
20	169	0.5	980s/20s	0	25	360	37	1.9E-07	0.116
21	116	0.5	980s/20s	0	25	360	37->40	2.9E-07	0.109
22	229	0.5	980s/20s	2.5	25	360	40	3.7E-08	0.027
23	490	---	const K	---	25	360	40	7.0E-10	0.004
24	181	0.5	0.04	2.77	25	360	40	1.8E-08	0.011

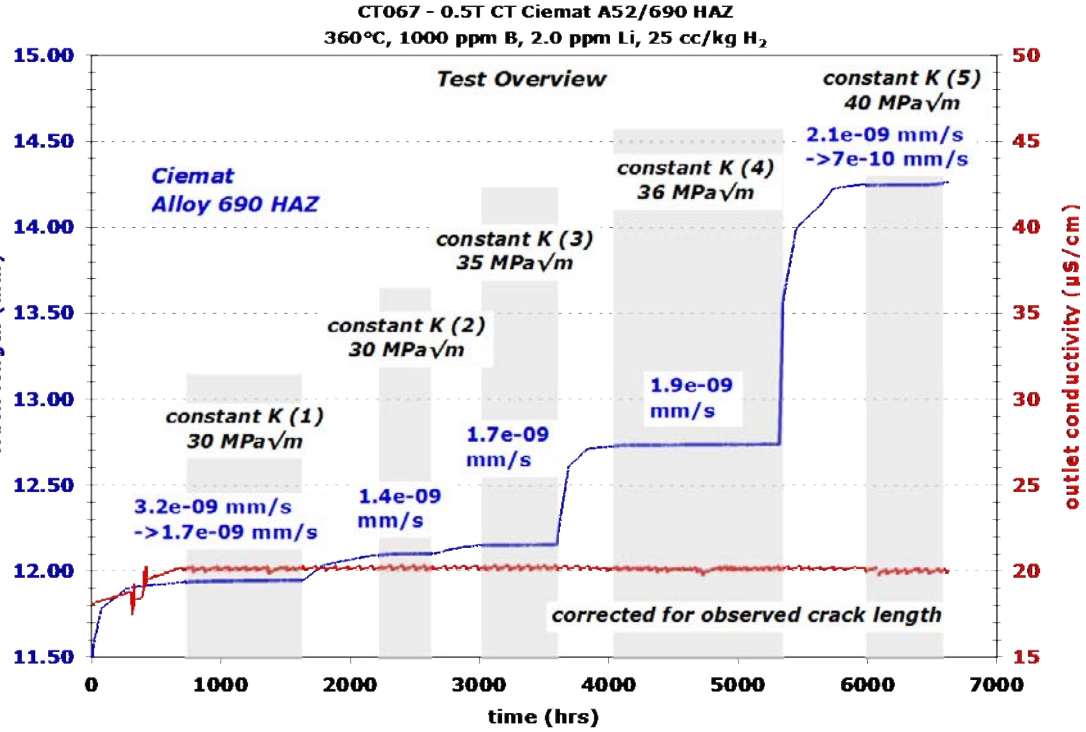

Figure 5.55 Overview of the entire SCC test on the Ciemat WP547 alloy 690TT HAZ specimen, CT067

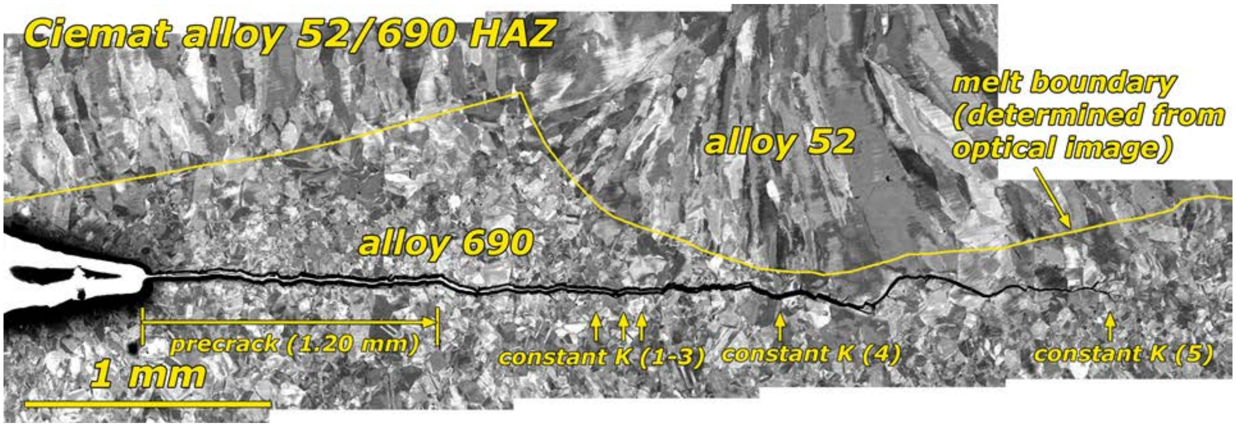

Figure 5.56 SEM-BSE side surface image of the Ciemat WP547 alloy 690TT HAZ specimen, CT067 showing where the constant K observations were performed

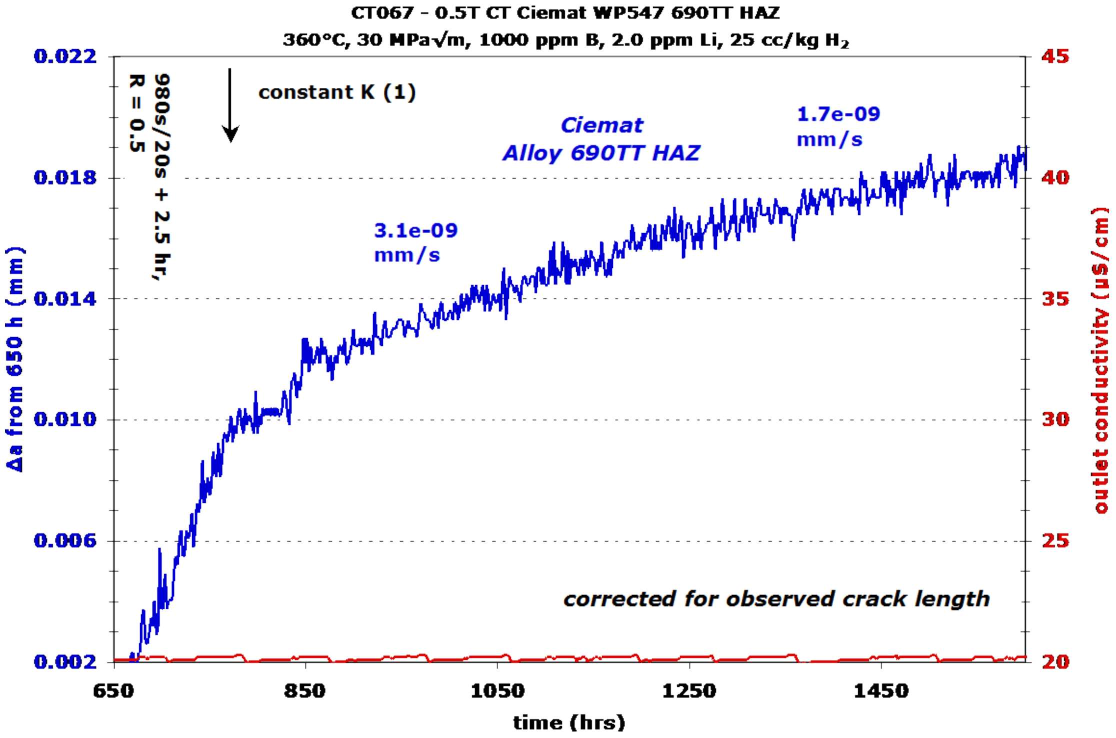

Figure 5.57 Crack growth response for the Ciemat WP547 alloy 690TT HAZ specimen, CT067 during the first constant K observation

After completing this ~6800 h test, a slice of the specimen was removed for cross-section observation, and the remaining portion was fatigued open for crack surface observations. The optical image of the cleaned crack surface in Figure 5.58 shows a slightly peaked crack front that is relatively smooth. No unbroken ligaments behind the crack front were observed. DCPD underpredicted both the precrack length and the in-situ portion of the test by modest values of 5 and 11%, respectively. An SEM-SE image of the entire crack growth surface is shown in Figure 5.59. A difference in texture is apparent for the portion of the crack surface that was closest to the fusion line, but no IG cracking was observed anywhere, consistent with the low SCC CGRs.

Figure 5.58 Optical image of the crack growth surface of the Ciemat WP547 alloy 690TT HAZ specimen, CT067

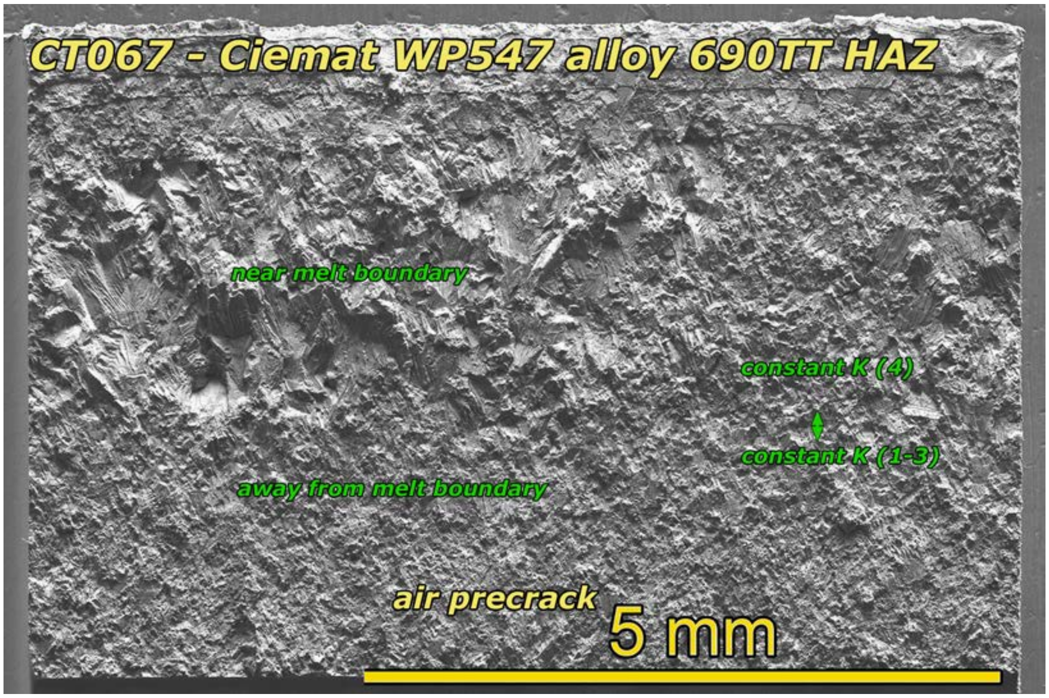

Figure 5.59 SEM-SE image of the SCC crack growth surface of the Ciemat WP547 alloy 690TT HAZ specimen, CT067

5.7.2 ANL NX3297HK12 Alloy 690MA HAZ and KAPL Alloy 690 HAZ

These two specimens were tested as a pair making it convenient to present the results for both at the same time. The ANL NX3297HK-12 material is the same heat the exhibited high SCC CGRs in the 26%CR S-L and in the 30%CF condition. It was cut from a piece of the ANL alloy 152v2 weld at PNNL. The KAPL material had not previously been tested. It was cut from an alloy 52M narrow gap weldment produced by KAPL. The heat number for this alloy 690 has not yet been determined. Specimens were cut with the intent of having the geometric crack growth plane within ~200 µm of the fusion line. The actual result for the specimens is shown in **Figure 5.60** and **Figure 5.61** for the ANL and KAPL HAZ specimen respectively. For the ANL HAZ (CT086), the geometric crack plane came within ~500 µm of the fusion line on one side and within ~800 µm on the other side. Better alignment was achieved for the KAPL HAZ with the distance being ~500 µm on one side and as close as ~300 µm on the other side.

Figure 5.60 Location of fusion line relative to the CT specimen centerline for the ANL NX3297HK12 alloy 690MA HAZ specimen, CT086

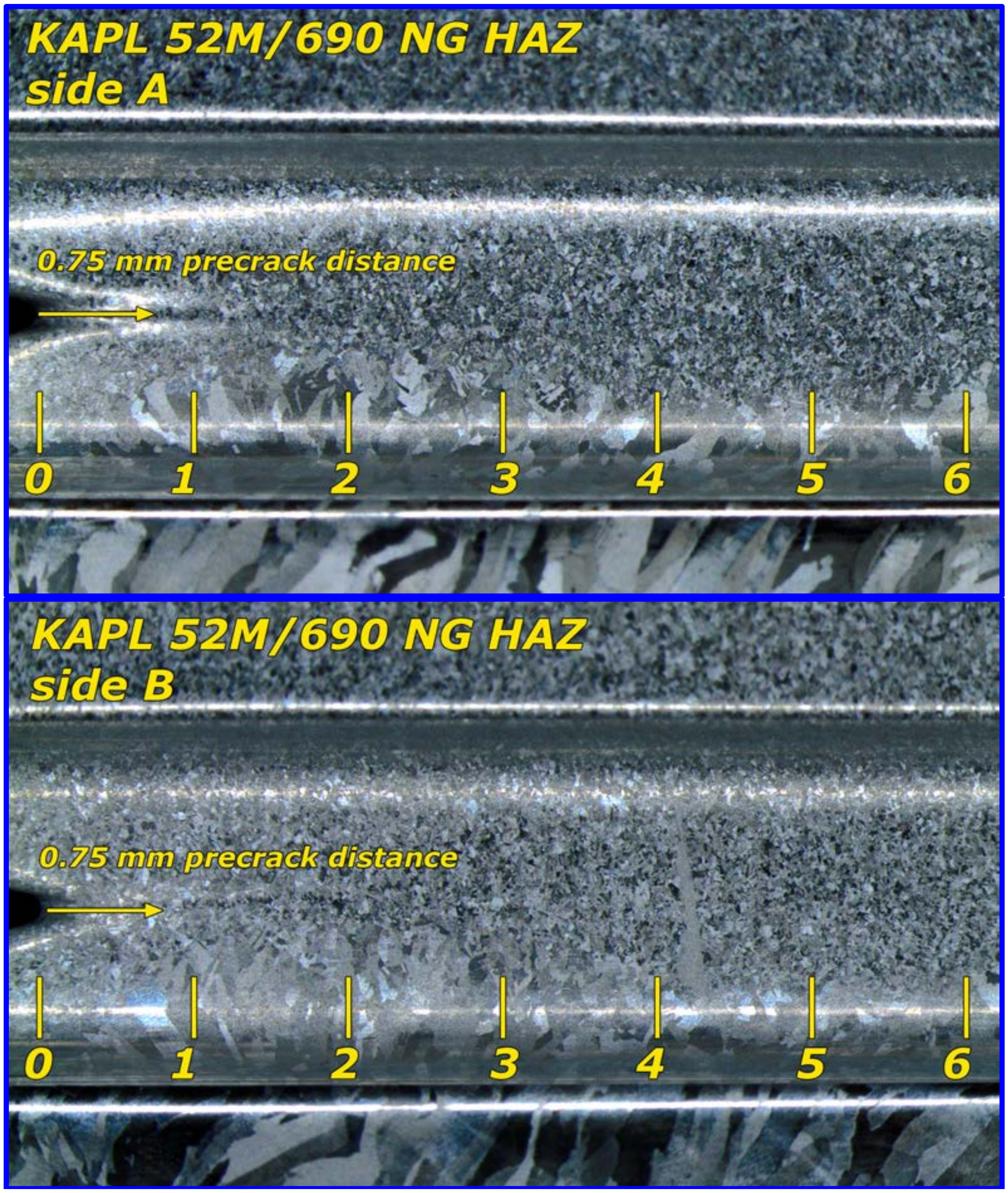

Figure 5.61 **Location of fusion line relative to the CT specimen centerline for the KAPL alloy 690 HAZ specimen, CT087**

A summary of the test conditions and specimen response is provided in Table 5.11, while an overview plot of the entire test is shown in Figure 5.62. Final transitioning steps before constant K observations included 980s/20s and 980s/20s+2.5 hr hold load cycling. The 9980s/20s with R=0.35 and 24980s/20s with R=0.35 load cycles were also used for some transitioning steps. Four constant K observations were performed. Since the closest the crack would come to the fusion line was for a crack length of 1-1.5 mm from the notch for both specimens, air precracking was set to be only 0.8 mm, and the first and second constant K observations were set to take place at 1-1.5 mm from the notch. The third constant K observation was performed at a location that would be close to the fusion line for the KAPL HAZ specimen, and the fourth was for a location as close as possible to the fusion line for the ANL HAZ specimen. Stress intensity was set to 30 MPa√m for the first two constant K observations and then 35 MPa√m for the second two. For all the constant K observations, SCC CGRs were $\leq 1\text{x}10^{-9}$ mm/s with an example shown in Figure 5.63 for the second constant K observation. Cycle+hold loading applied after constant K produced typical propagation rates for the loading condition showing that there were no contacts or ligaments forming during constant K that were causing untracked crack growth.

Table 5.11 Test conditions and specimen response for the ANL NX3297HK-12 and KAPL alloy 690 HAZ specimens, CT086 & CT087

								CT086 ANL A152v2 HAZ #1			CT087 KAPL A52M NG HAZ #1		
Test Step	Start (h)	Duration (h)	R	Freq (Hz)	Hold (h)	DH (cc/kg H^2)	Temp (°C)	Kmax (MPa$\sqrt{m}$)	CGR (mm/s)	Approx. Crack Ext. (mm)	Kmax (MPa$\sqrt{m}$)	CGR (mm/s)	Approx. Crack Ext. (mm)
1	0	11	0.5	0.1	0	25	360	30	5.5E-06	0.142	30	4.8E-06	0.176
2	11	53	0.5	0.01	0	25	360	30	9.8E-07	0.144	30	8.6E-07	0.169
3	64	248	0.5	0.001	0	25	360	30	1.7E-07	0.111	30	1.6E-07	0.148
4	312	788	0.5	980s/20s	2.5	25	360	30	1.9E-08	0.037	30	2.1E-08	0.050
5	1100	824	---	const K	---	25	360	30	NG	0.000	30	NG	0.000
6	1924	258	0.35	9980s/20s	0	25	360	30	5.2E-08	0.029	30	4.8E-08	0.036
7	2182	724	0.35	24980s/20s	0	25	360	30	2.4E-08	0.045	30	2.1E-08	0.057
8	2906	503	---	const K	---	25	360	30	NG	0.000	30	NG	0.000
9	3409	147	0.5	980s/20s	2.5	25	360	30	2.0E-08	0.007	30	1.4E-08	0.007
10	3556	74	0.5	980s/20s	0	11	360	30	Insuff.	0.028	30	Insuff.	0.036
11	3630	13	0.4	0.1	0	25	360	30	9.4E-06	0.293	30	8.1E-06	0.337
12	3643	37	0.5	0.01	0	25	360	30	1.1E-06	0.109	30	9.8E-07	0.130
13	3680	91	0.5	980s/20s	0	25	360	30	1.9E-07	0.047	30	1.9E-07	0.059
14	3771	521	0.5	980s/20s	2.5	25	360	30	1.8E-08	0.034	30	1.7E-08	0.034
15	4292	557	0.35	9980s/20s	2.5	25	360	30	2.9E-08	0.040	30	2.3E-08	0.044
16	4849	133	0.35	9980s/20s	2.5	25	360	30->35	Incr.	0.022	30->35	Incr.	0.023
17	4982	189	0.35	9980s/20s	2.5	25	360	35	4.1E-08	0.024	35	3.8E-08	0.025
18	5171	537	---	const K	---	25	360	35	NG	0.000	35	NG	0.000
19	5708	120	0.5	0.05	0	25	360	37	4.4E-06	1.393	37	3.8E-08	1.720
20	5828	65	0.5	0.01	0	25	360	35	1.1E-06	0.197	35	1.0E-06	0.236
21	5893	173	0.5	980s/20s	0	25	360	35	2.1E-07	0.096	35	2.0E-07	0.128
22	6066	222	0.5	980s/20s	2.5	25	360	35	2.6E-08	0.017	35	2.0E-07	0.020
23	6288	1122	---	const K	---	25	360	35	2.7E-10	0.013	35	NG	0.000
24	7410	161	0.5	980s/20s	0	25	50	35	Insuff.	0.000	35	Insuff.	0.004
25	7571	366	0.5	480s/20s	0	25	50	35	5.8E-08	0.058	35	1.2E-07	0.135
26	7937	120	0.5	0.01	0	25	50	35	3.8E-07	0.162	36	6.7E-07	0.301
27	8057	470	0.5	0.001	0	25	50	35	4.4E-08	0.047	36	6.8E-08	0.096
28	8527	555	0.35	9980s/20s	0	25	50	35	6.5E-09	0.012	36	1.1E-08	0.022

NG = No Growth

Insuff. = Insufficient data to determine a CGR

Incr. = Increasing CGR

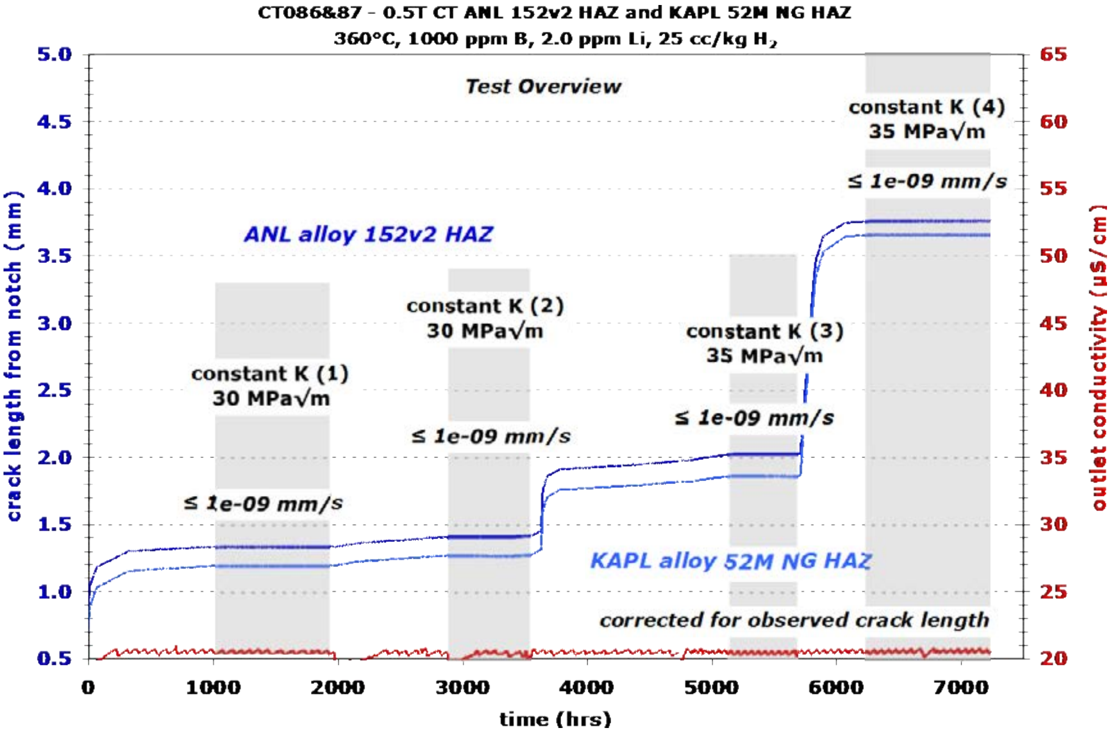

Figure 5.62 Overview of the entire SCC test for the ANL NX3297HK-12 and KAPL alloy 690 HAZ specimens, CT086 & CT087

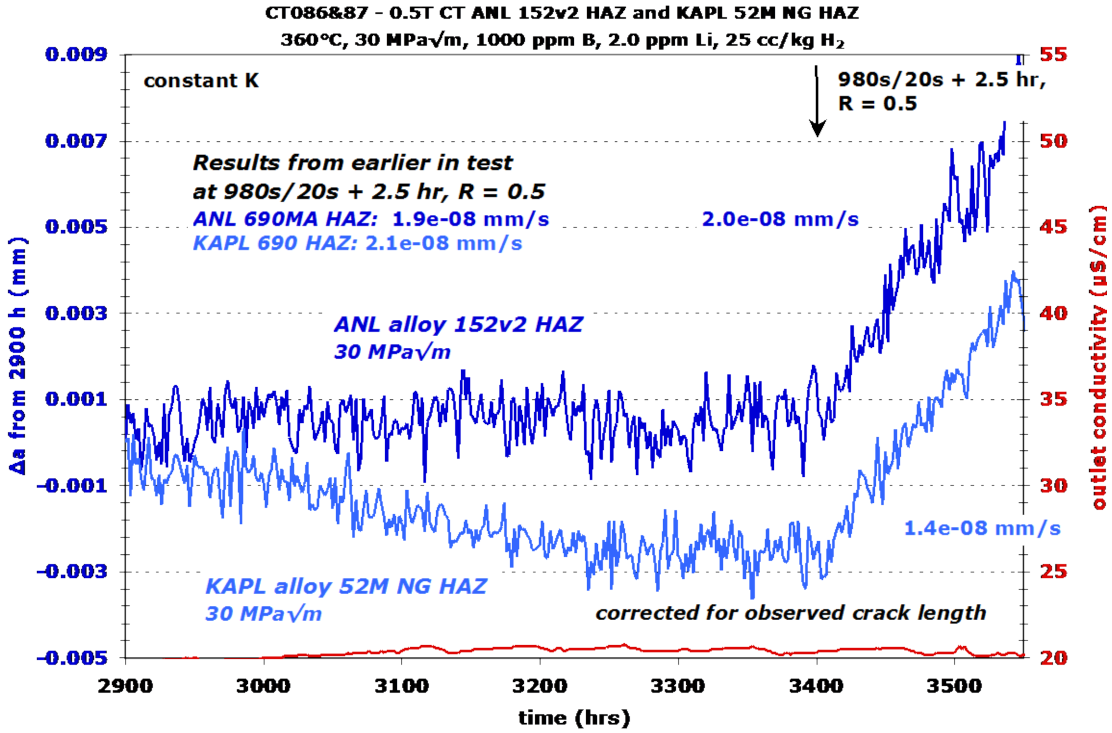

Figure 5.63 Crack growth response during the second constant K observation for the ANL NX3297HK-12 and KAPL alloy 690 HAZ specimens, CT086 & CT087

After completing this ~7200 h test, a slice of each specimen was removed for cross-section observation, and the remaining portions were fatigued open for crack surface observations. An optical image of the crack surface of the ANL HAZ specimen (CT086) is shown in Figure 5.64. The overall crack front is relatively straight from one side to the other with no significant protrusions. Some evidence of small ligaments can be seen towards the left side of the specimen. In the SEM-SE image of the entire crack surface in Figure 5.65, no indications of IG engagement could be found anywhere. The KAPL HAZ specimen was similar in appearance with optical and SEM-SE images shown in Figure 5.66 and Figure 5.67. For both specimens, DCPD accurately tracked actual crack length.

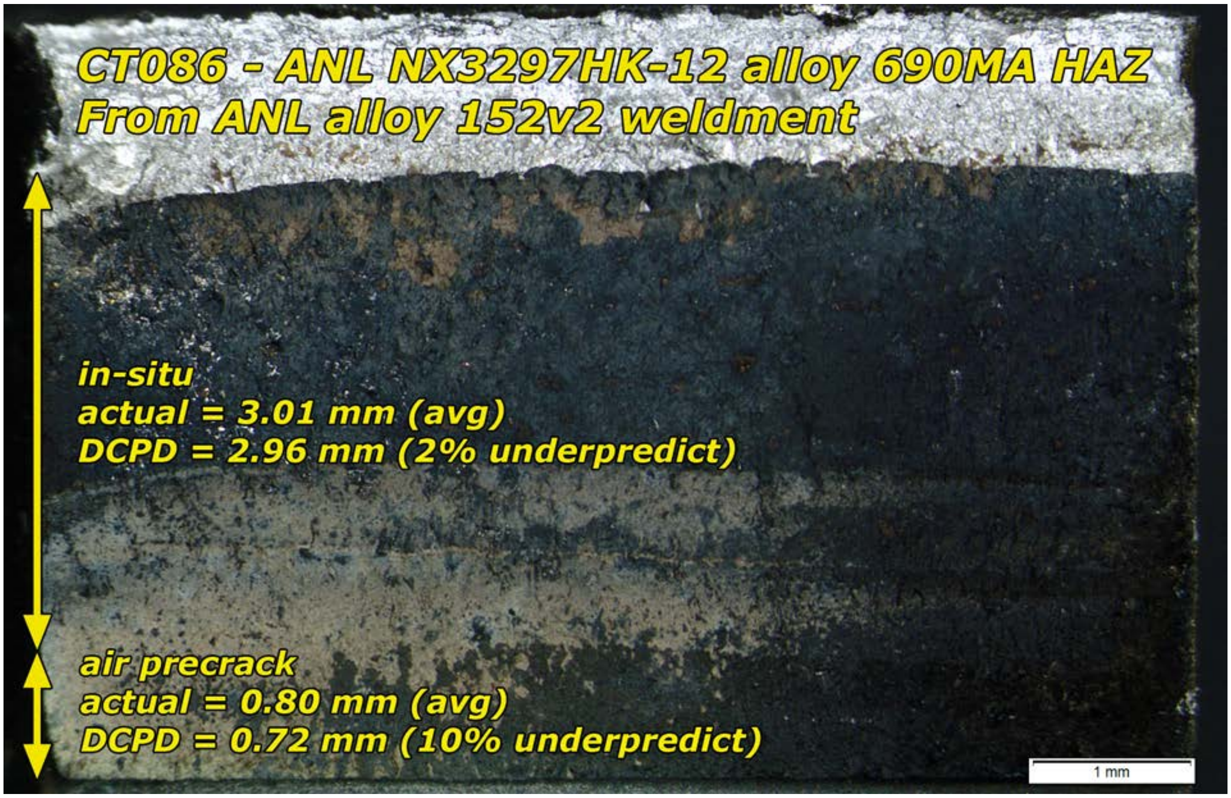

Figure 5.64 Optical image of the crack growth surface of the ANL alloy 690MA HAZ specimen, CT086

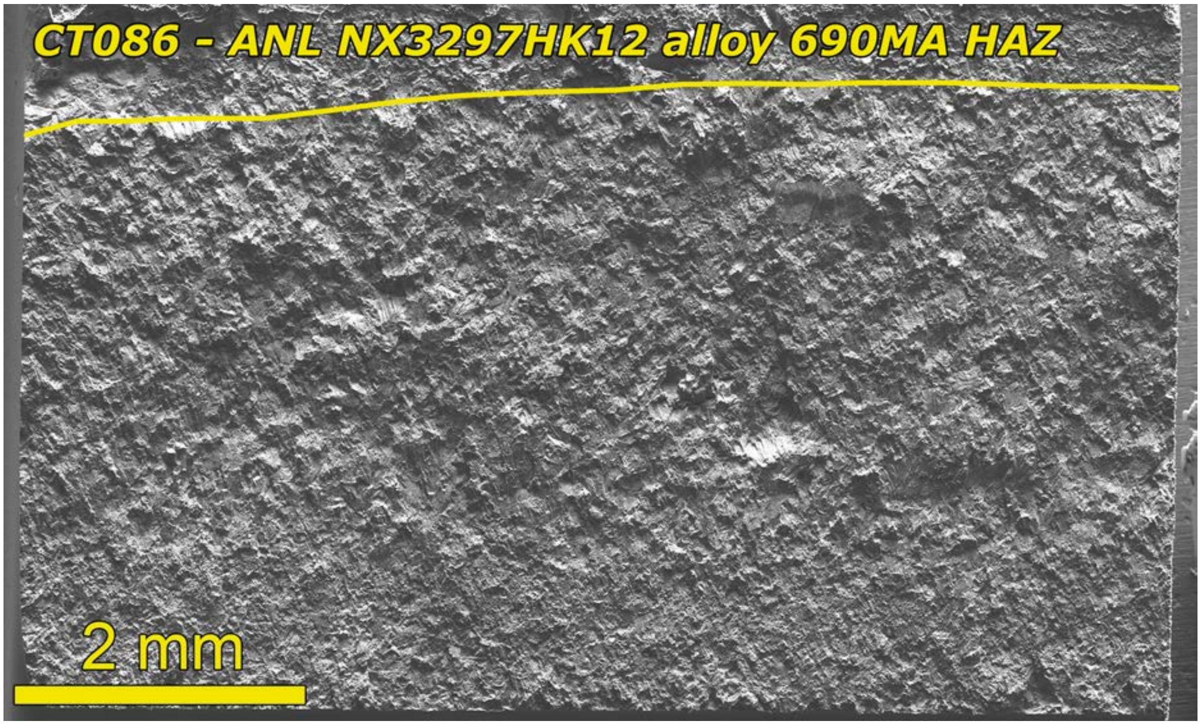

Figure 5.65 SEM-SE image of the entire crack growth surface for the ANL alloy 690MA HAZ specimen, CT086. Yellow line denotes the final crack front.

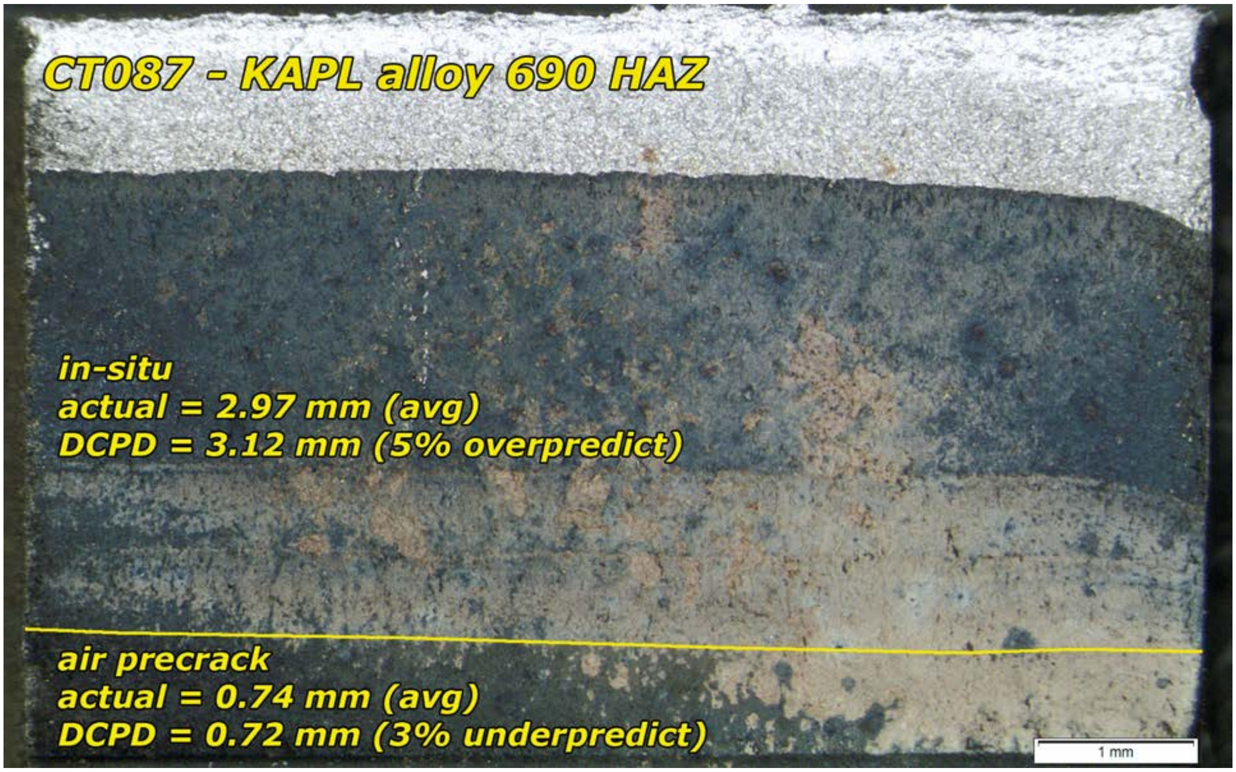

Figure 5.66 Optical image of the crack growth surface of the KAPL alloy 690 HAZ specimen, CT087

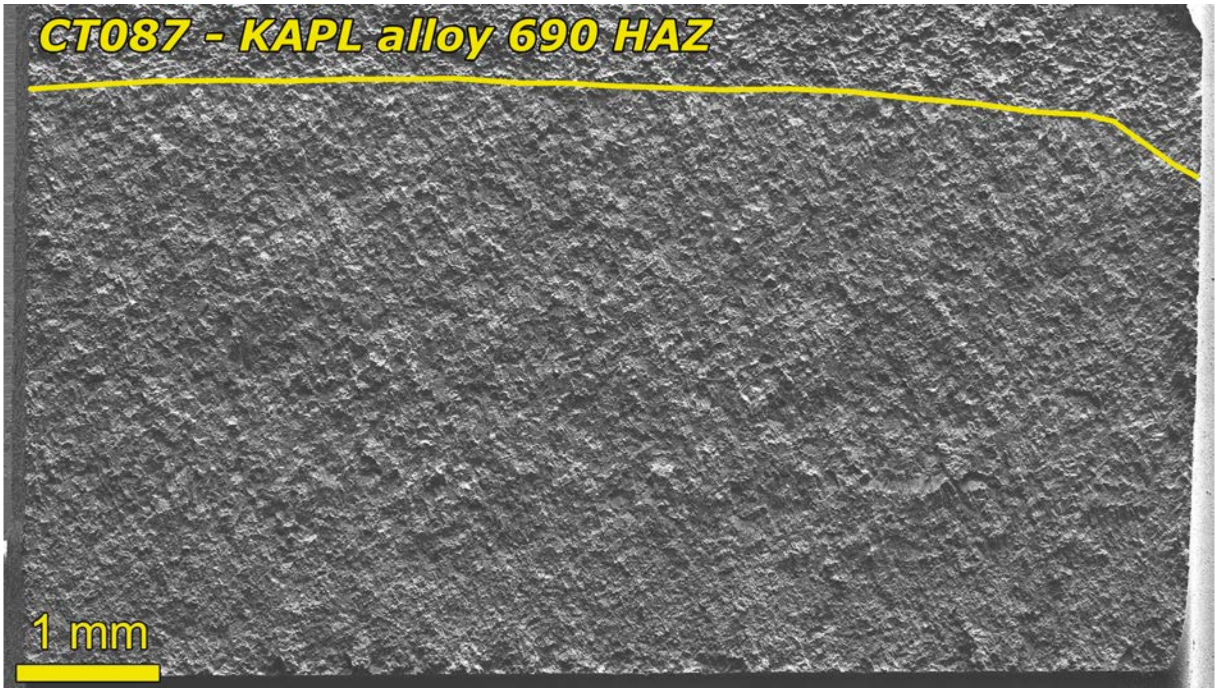

Figure 5.67 **SEM-SE image of the entire crack surface for the KAPL alloy 690 HAZ specimen, CT087. Yellow line denotes the final crack front.**

5.8 Summary of SCC Tests on Plate and Bar Materials

Constant K crack growth rates and percent IG engagement for the plate, bar and HAZ specimens are summarized in Table 5.12. As with the CRDM materials, the plate and bar alloy 690 materials exhibited a strong dependence of cold work on SCC response. CGR as a function of cold work is shown in Figure 5.68 where it is compared to the response of the Valinox RE243 TT alloy 690. For the non-CW condition, a slightly higher SCC response was observed for the B25K-2 specimen where 18% engagement and a sustained SCC CGR of >1x10^{-9} mm/s was observed. This same material showed high SCC CGRs in the 20%CR condition, and these two data points set the high side of the trend band for the non-CRDM materials. The remaining materials generally fall along the same magnitude of response as for the Valinox RE243 TT. GE has reported higher SCC CGRs in some of the same plate materials [15] where it has been proposed that the accelerated growth occurred due to cracking occurring in a banding plane. Examinations of the specimens tested at PNNL do not show any clear indication of cracking in a banding plane. Figure 5.68(c) that includes the response of the HTA materials shows that just as with the Valinox RE243 CRDM material, plate materials given an HTA treatment prior to cold working exhibit lower CGRs for a given amount of cold work.

CGR as a function of IG engagement is shown in Figure 5.69 where it can be seen that the same trend is observed as for the CRDM materials and that SCC CGRs of greater than 1x10^{-8} mm/s are not observed until reaching ~80% IG engagement.

Table 5.12 Summary of alloy 690 plate and bar SCC response for testing at ~30 MPa√m and 360°C

ID	Producer	Heat #	Condition	% Engagement	SCC-CGR (mm/s)†
CT084	Special Metals	NX3297HK12	MA*	3	2-8x10^{-10}
CT036	Special Metals	NX3297HK12	MA*+26%CR	94	6.3x10^{-8}
CT073	Special Metals	NX3297HK12	MA*+30%CF	85	7.2x10^{-8} (1.7x10^{-7})*
CT074	Special Metals	NX3297HK12	HTA§+30%CF	44	3.1x10^{-9}
CT085	Allvac	B25K-2	MA*	22	0.5-1.1x10^{-9}
CT037	Allvac	B25K-2	MA*+20%CR	89	4.5x10^{-8}
CT070	Allvac	B25K-2	HTA§+20%CR	18	1.7x10^{-9}
CT107	TK-VDM	114092	TT*	1	2x10^{-10}
CT094	TK-VDM	114092	TT*+32%CF	83	2.3-3.1x10^{-8} (0.8-1.5x10^{-7})
CT059	Aubert&Duval	WP547	TT*+32%CF	92	3.2-4.7x10^{-8}
CT060	Aubert&Duval	WP547	TT*+22%CR	87	1.8x10^{-8}
CT101	Allvac	X87N-1	TT*+21%CF	76	2.1-2.8x10^{-9} (5.1x10^{-9})
CT067	Aubert&Duval	WP547	TT* HAZ	1	1.4-1.7x10^{-9}
CT086	Special Metals	NX3297HK12	MA* HAZ	1	1.5x10^{-10}
CT087	Unknown	Unknown	AR HAZ	1	1x10^{-10}

* As-received condition of the material.

† Values in parenthesis are ligament/contact adjusted.

§ High temperature anneal that left a low density of small plate-like grain boundary carbides.

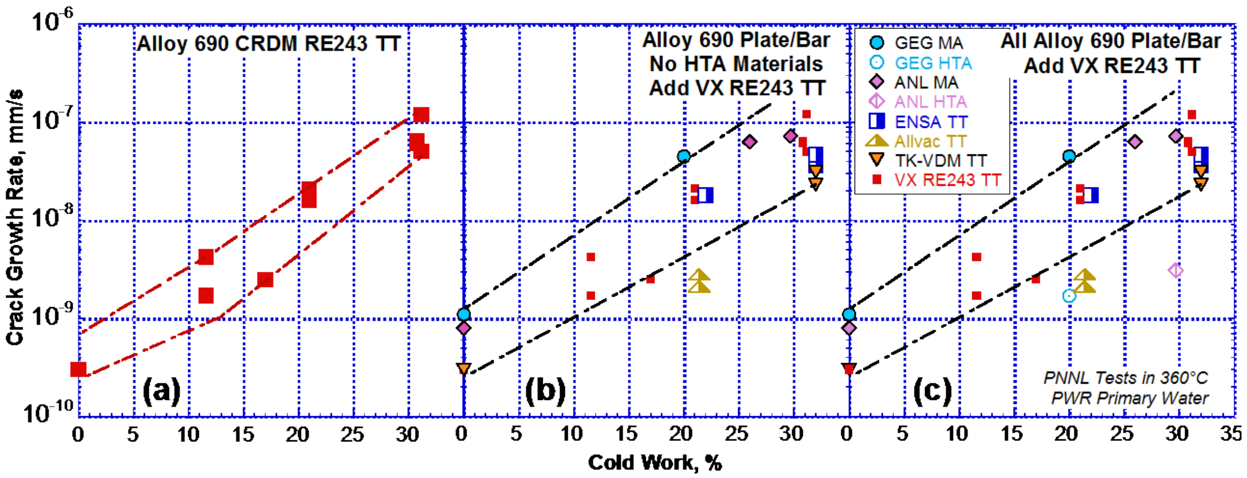

Figure 5.68 Crack growth rate versus cold work for a) alloy 690TT RE243 Valinox, and b), c) for alloy 690 plate materials

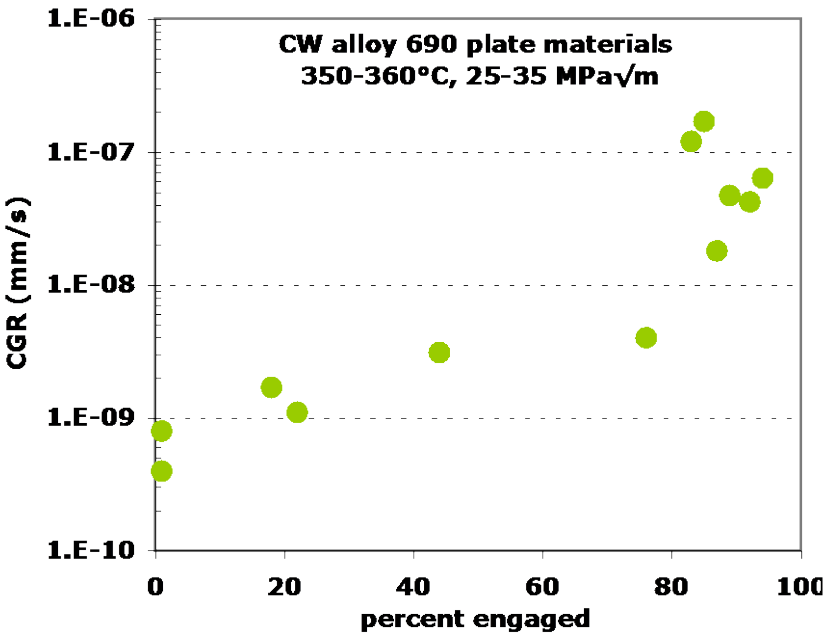

Figure 5.69 Constant K CGR versus IG engagement for the plate and bar materials. HAZ are not included

6 DISCUSSION OF COLD WORK EFFECTS ON SCC FOR ALLOY 690 MATERIALS

6.1 Overview

It is known that the SCC susceptibility typically increases as the strength of a material is increased, particularly by cold work [19,20]. As seen in Chapters 4 and 5, there is a clear correlation between SCC susceptibility and the degree of cold work for the 12 heats of alloy 690 with cold work levels ranging from 0-32%. The correlation, however, has a fair amount of scatter when comparing multiple heats of material. This is perhaps not surprising considering that cold work is only a rough indication of the amount of deformation or material strength in the region of crack growth, and the level of cold work does not indicate anything about the strain or strength of the material prior to being cold worked. The IMD and hardness measurements performed on the specimens are a more direct measurement of strain and strength respectively, and can potentially provide more insight into the consistency of the effect of cold work on the SCC response of this material. The next section will present correlations between SCC CGR and IMD or hardness. Results will be considered with respect to the observed microstructures of the materials.

For the series of correlations that are presented here, the lines drawn to bound the data were generated by hand rather than by a statistical fit and provide a visual marker of the data scatter. The judgment of straight line or curved fits to the data is based partly on the power law relationship established between hardness and IMD in Section 3.8. The presence of data scatter and some outliers indicates that all heat-to-heat differences are not effectively captured by the correlations and highlight the significant effect of the initial material condition.

6.2 Correlations Among SCC, Cold Work, Hardness, and Strain

It was shown in Chapter 3 that hardness and IMD provide information about strength and the level of plastic strain in a material. When hardness was plotted as a function of IMD (Figure 3.40), a power law relationship was found to accurately correlate the two parameters, just as is often observed when plotting stress versus plastic strain for a tensile test. The observed power law exponent was found to be ~0.4, consistent with the uniform elongation for a tensile test on non-cold worked alloy 690. Since these values are more representative of bulk properties than the level of applied cold work, there is an expectation that there will be reduced data scatter for SCC susceptibility as a function of these variables. However, since there is a non-linear relationship between hardness and IMD, it is expected that the correlation between SCC CGR and IMD will be different than that between SCC CGR and hardness. These comparisons will be made here, starting first with the Valinox RE243 TT material.

SCC CGR as a function of cold work, hardness, and IMD for the Valinox RE243 TT material is shown in Figure 6.1. As previously discussed in Chapter 4, additional transitioning resulted in a higher SCC CGR for the 11.6%CF material and might have resulted in a higher SCC CGR for the 17%CF material that underwent only a single transitioning sequence. The arrows for these two cold work levels indicate this. For all three datasets, a straight line trend band representative of an exponential fit have been added by hand. Using the hand fit trend band, the correlation between SCC CGR and cold work appears to be well represented an exponential relationship. When SCC CGR is plotted as a function of hardness, the correlation tightens up further and becomes even more linear. The poorest <u>exponential</u> correlation is to the IMD results where the SCC CGRs run high for IMD values of ~0.05 and ~0.09 rads/pixel. This suggests that there should also be a non-exponential relationship between SCC CGR and IMD. Since cold work is a representation of applied strain, a non-exponential relationship should apply here as well. The possibility of a non-exponential fit to SCC CGR vs cold work and IMD is presented in in Figure 6.2. While subjective, SCC CGR versus cold work, and in particular, IMD appear to be better represented by the curved lines drawn to bound the data.

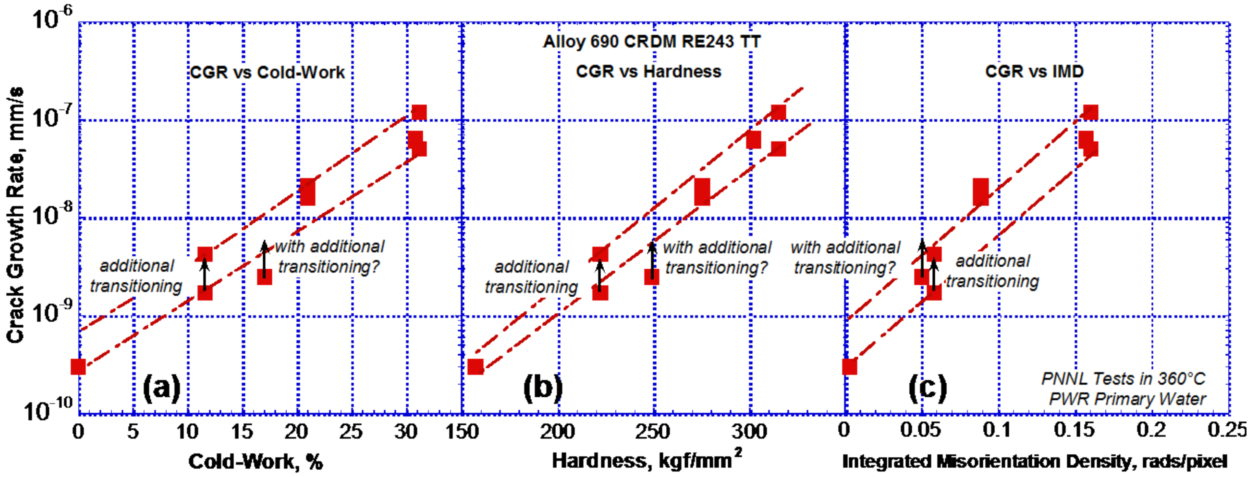

Figure 6.1 SCC CGR as a function of either (a) cold work, (b) hardness, or (c) IMD for Valinox RE243 TT tested at ~30 MPa√m at 360°C

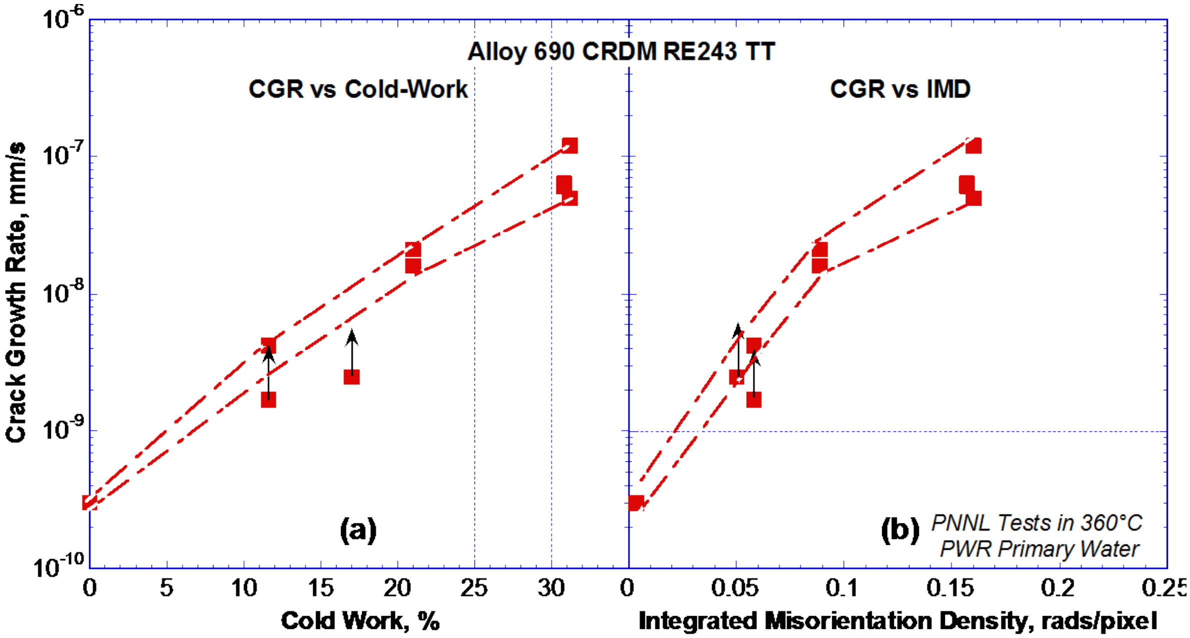

Figure 6.2 SCC CGR as a function of (a) cold work and (b) IMD for Valinox RE243 TT tests performed at ~30 MPa√m at 360°C

Attempts to fit SCC CGR to the IMD data revealed that the best fit was obtained for a power law dependence given by:

$$(SCCCGR - SCCCGR_o) = K \bullet IMD^n \tag{6.1}$$

The difference in the quality of the curve fits can be seen in Figure 6.3. This apparent difference in dependence of SCC CGR on hardness (strength) and IMD (strain) is tied to the nonlinear, power law relationship that exists between hardness and strain that was shown in Chapter 3 (Figure 3.40). This nonlinear dependence between hardness and strain precludes SCC CGR having the same dependence on hardness and strain. While the RE243TT data indicate that SCC CGR fits well to either parameter, it is perhaps easier to visually assess the quality of the fit for the exponential dependence on hardness.

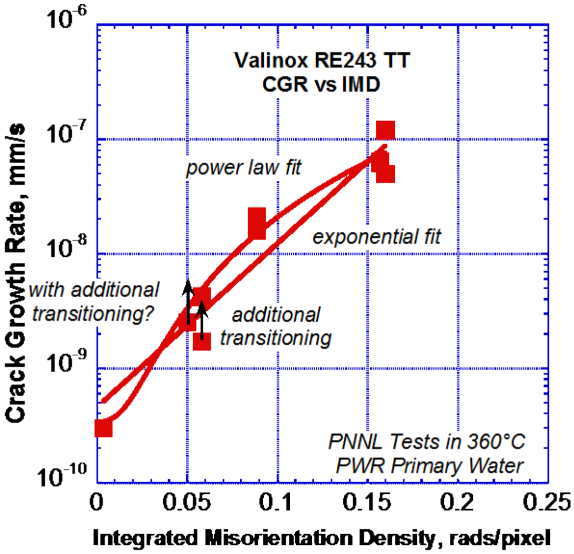

Figure 6.3 Exponential and power law curve fits to the SCC CGR as a function of IMD for the Valinox RE243TT results at ~30 MPa√m at 360°C

SCC CGR comparisons for all TT CRDM materials tested at PNNL are shown in Figure 6.4. Trend lines are copied from the RE243TT plots. The correlation to hardness is reasonably consistent among the different CRDM heats. The only significant outlier is the Sumitomo (STO) tested in the 12.7%CF condition. This Sumitomo specimen was tested in tandem with the 11.6%CF Valinox and was quite resistant to SCC crack growth. When plotted as a function of IMD, the scatter is reduced compared to the RE243TT trend band, perhaps suggesting a better relationship between SCC CGR and strain rather than strength. However, the 12.7%CF Sumitomo continues to be an outlier for the correlation to IMD as well.

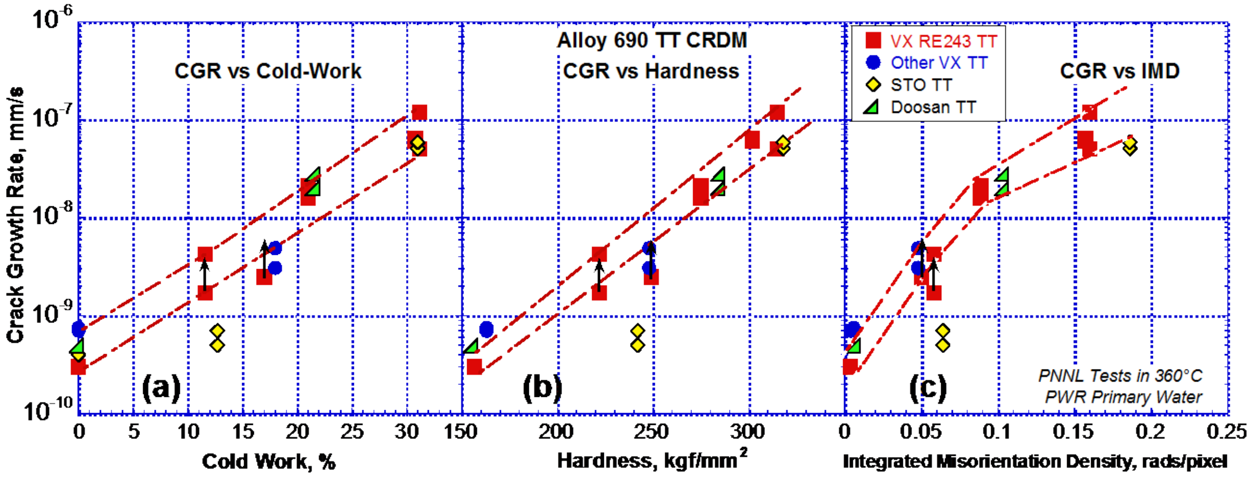

Figure 6.4 SCC CGR as a function of either (a) cold work, (b) hardness, or (c) IMD for all TT CRDM tested at ~30 MPa√m at 360°C

Plots combining the CRDM and plate materials in the TT or MA starting condition are shown in Figure 6.5. With the addition of the plate material, trend bands drawn by hand to capture the majority of the data are larger, and there is still a new outlier - the Allvac X87N-1 20%CF specimen. Without regard to the Allvac and Sumitomo data, the correlation to CW appears to have the most variability, especially when considering that the trend band should have a curved shape like the correlation to IMD. The correlation to hardness is slightly better, and perhaps the correlation to IMD is the tightest overall.

From the perspective of specimen response, these hardness and IMD correlations further confirm that the SCC susceptibility of the tested CRDM and plate materials have similar dependence on cold work induced microstructural changes. This is perhaps not surprising considering that the majority of the materials have broadly similar starting microstructures, i.e., solution strengthening with either semi-continuous or continuous grain boundary carbide distributions with average grain size ranging from ~30-100 µm. Perhaps surprisingly, nothing microstructurally unique about the Allvac X87N-1 or the Sumitomo E67074C outliers has been identified. One material that is microstructurally unique and yet falls cleanly within the trend bands is the GE/Allvac B25K-2 material. It has a smaller grain size, a higher density of twins, and was nearly free of any grain boundary carbides. As noted previously, it appears that all of the specimens tested at PNNL did not undergo growth on banding planes. GE has noted SCC CGRs approaching 1x10^{-6} mm/s when encountering banding planes in 26%CR ANL NX3297HK12 material [15]. Such a data point would lie above the trend bands shown in these plots. Hardness, IMD, and SCC CGR values for the tests that have been discussed thus far are listed in Table 6.1 for the TT CRDM materials and Table 6.2 for the TT/MA plate/bar (non-CRDM) materials.

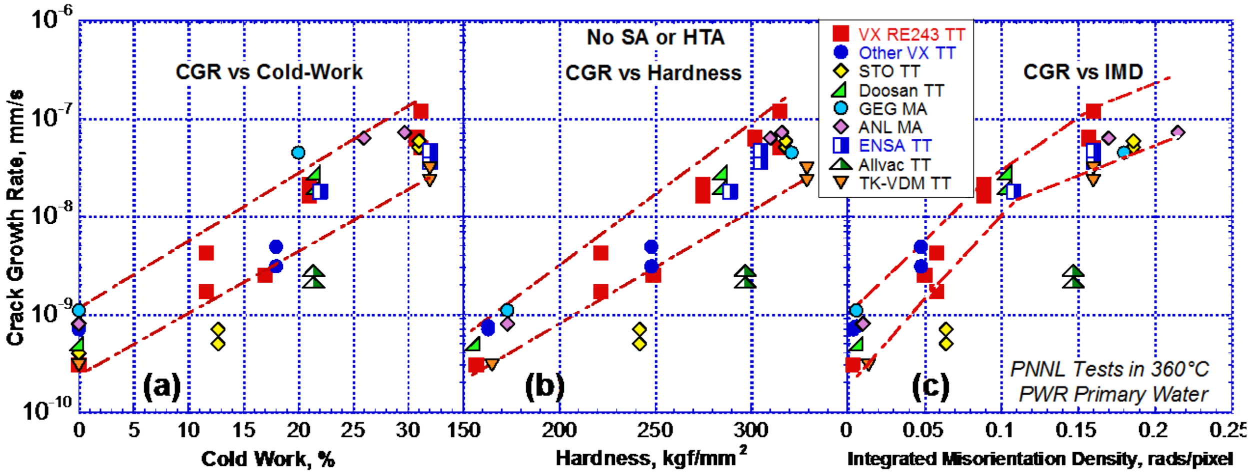

Figure 6.5 SCC CGR versus (a) cold work, (b) hardness, or (c) IMD for all alloy 690 TT/MA materials. Tests were ~30 MPa√m at 360°C.

Table 6.1 Summary of hardness, misorientation density, and SCC CGR measurements (at ~30 MPa√m) for the alloy 690 TT CRDM specimens

ID	Producer	Heat #	Condition	HV (kgf/mm^2)	Average IMD	SCC-CGR (mm/s)†
CT026	Valinox	WP142	TT*	163	0.0039	5-9x10^{-10} [350°C]
CT027	Valinox	WP140	TT	163	0.0057	6-9x10^{-10} [350°C]
CT014	Valinox	RE243	TT	157	0.0036	3x10^{-10} [325°C]
CT104	Valinox	RE243	TT+11.6%CF	222	0.0583	1.7-4.2x10^{-9}
CT020	Valinox	RE243	TT+17%CR	249	0.0500	5x10^{-10} [325°C]
CT054	Valinox	RE243	TT+17%CR	249	0.0500	2.5x10^{-9}
CT100	Valinox	RE243	TT+21%CF	275	0.0887	1.6-2.1x10^{-8} (2.6-3.8x10^{-8})**
CT038	Valinox	RE243	TT+31%CR	315	0.160	0.5-1.2x10^{-7}
CT099	Valinox	RE243	TT+31%CF	302	0.157	3.0-6.4x10^{-8} (0.7-1.2x10^{-7})
CT093	Valinox	WP787	TT+20%TS	248	0.0477	3.1-4.9x10^{-9} (1.0-1.1x10^{-8})
CT103	Sumitomo	E67074C	TT+12.7%CF	242	0.064	3-7x10^{-10}
CT098	Sumitomo	E67074C	TT+31%CF	318	0.186	2.1-5.9x10^{-8} (0.8-1.7x10^{-7})
CT108	TK-VDM	133454	TT	156	0.0071	5x10^{-10}
CT102	TK-VDM	133454	TT+21%CF	285	0.104	2.0-2.8x10^{-8} (4.2-4.4x10^{-8})

† Tested at 360°C and ~30 MPa√m unless otherwise noted.
* TT is the as-received condition for all the materials in this table.
** Values in parenthesis are adjusted for contact/ligament formation.

Table 6.2 Summary of hardness, misorientation density, and SCC CGR measurements (at ~30 MPa$\sqrt{\text{m}}$) for the alloy 690 plate specimens

ID	Producer	Heat #	Condition	HV (kgf/mm^2)	Average IMD	SCC-CGR (mm/s)†
CT084	Special Metals	NX3297HK12	MA*	173‡	0.0100‡	2-8x10^{-10}
CT036	Special Metals	NX3297HK12	MA*+26%CR	310	0.170	6.3x10^{-8}
CT073	Special Metals	NX3297HK12	MA*+30%CF	316	0.215	7.2x10^{-8} (1.7x10^{-7})**
CT085	Allvac	B25K-2	MA*	173‡	0.0056‡	0.5-1.1x10^{-9}
CT037	Allvac	B25K-2	MA*+20%CR	321	0.1800	4.5x10^{-8}
CT107	TK-VDM	114092	TT*	165	0.0137	2x10^{-10}
CT094	TK-VDM	114092	TT*+32%CF	329	0.1600	2.3-3.1x10^{-8} (0.8-1.5x10^{-7})
CT059	Aubert&Duval	WP547	TT*+32%CF	305	0.160	3.2-4.7x10^{-8}
CT060	Aubert&Duval	WP547	TT*+22%CR	289	0.108	1.8x10^{-8}
CT101	Allvac	X87N-1	TT*+21%CF	297	0.147	2.1-2.8x10^{-9} (5.1x10^{-9})

* As-received condition

† Tested at 360°C and ~30 MPa$\sqrt{\text{m}}$ unless otherwise noted.

‡ Measured from coupons not taken from the CT specimen.

** Values in parenthesis are ligament/contact adjusted.

§ High temperature anneal that left a low density of small plate-like grain boundary carbides.

Another important aspect of this study is the effect of applying an SA or HTA treatment and water quench prior to cold working. This effect was studied in depth for the Valinox RE243 CRDM material with SCC CGR comparisons as a function of CW, hardness and IMD shown in Figure 6.6. No differences in SCC CGRs were observed between TT and SA conditions for the non-cold worked and the 17%CR materials where SCC CGRs were already quite low for both conditions. However, a very significant effect was seen for the highly cold worked material. The 31%CR SA specimen revealed a ~10X lower SCC propagation rate. It is important to note that after cold rolling, the hardness and IMD levels were similar between the TT and SA, and as a result, these data points do not collapse onto the RE243 TT trend band for the plots as a function of hardness and IMD. The most obvious difference between the TT and SA materials is the continuous distribution of $Cr_{23}C_6$ carbides in the TT condition and essentially no IG carbides in the SA condition. One additional change that occurs due to solution annealing is the removal of the preexisting grain boundary Cr depletion in the TT materials (measured at ~22-25 wt% versus 30 wt% in the matrix). The same relative response was obtained for comparison tests between MA and HTA plate material as shown in Figure 6.7. The response of the GEG B25K specimen is particularly important for this comparison because unlike the RE243 TT material, the GEG B25K MA material had a limited distribution of IG carbides and only local regions of any Cr depletion, therefore, questioning the role of these microstructural/microchemical features on SCC susceptibility of high cold worked alloy 690.

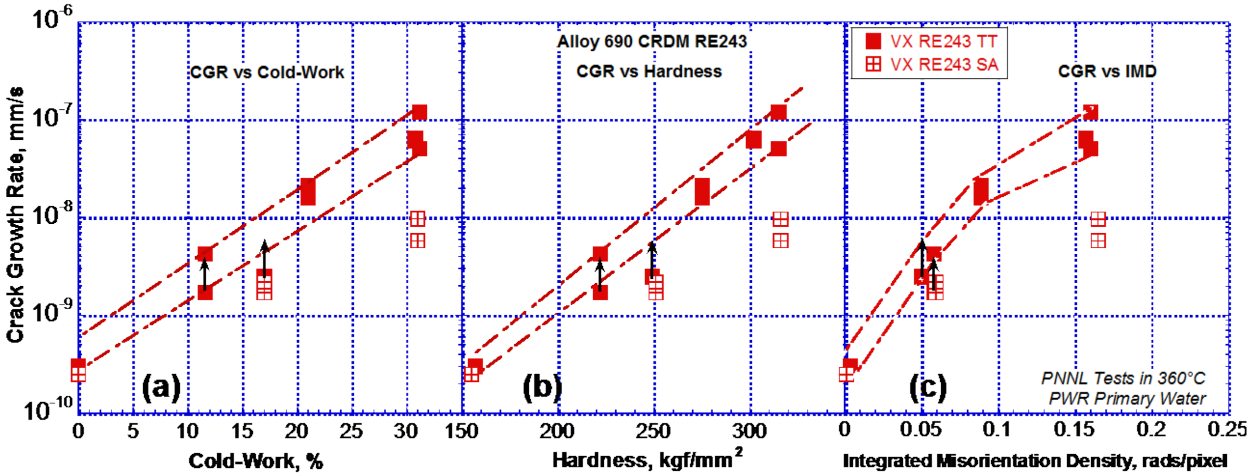

Figure 6.6 SCC CGR versus (a) cold work, (b) hardness, or (c) IMD for Valinox RE243 comparing TT and SA starting conditions. Tests were at ~30 MPa√m and 360°C.

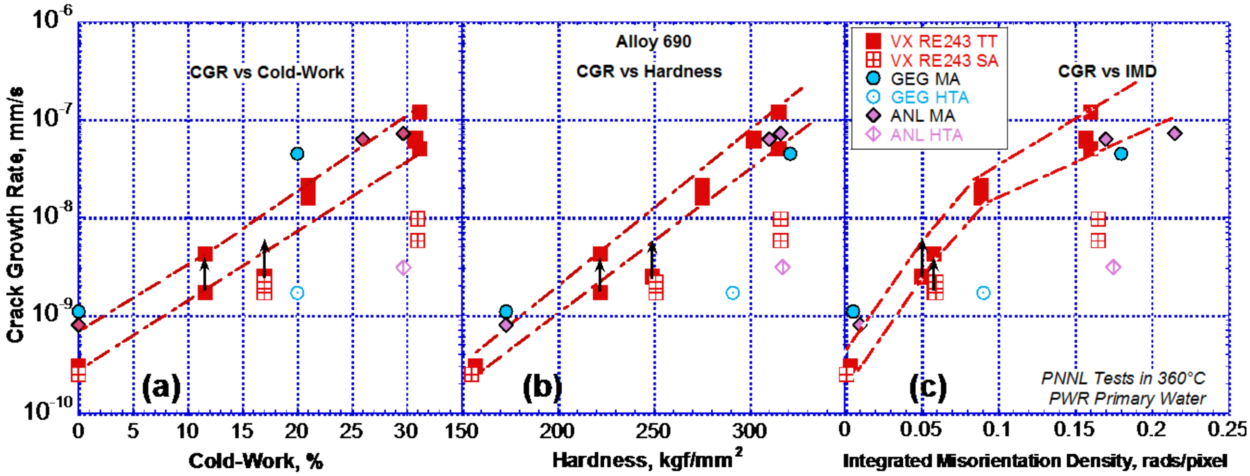

Figure 6.7 SCC CGR as a function of (a) cold work, (b) hardness, or (c) IMD for all materials with either a TT or SA/HTA starting condition. Tests were at ~30 MPa√m and 360°C.

Microstructure observations offer a possible explanation for the difference in response between TT/MA and SA/HTA materials. The 17%CR and 31%CR Valinox RE243 were heavily deformed as documented by high strain contrast in SEM and EBSD images and had extremely high dislocation densities in TEM images. Qualitatively, these observations also indicated enhanced deformation localized at grain boundaries particularly for the alloy TT material. This is thought to be due to the GB carbides causing constraint that drove additional localized deformation. Consistent with this apparent higher grain boundary damage for the TT material is the formation of low density of small voids adjacent to IG Cr carbides along with isolated cracked Cr carbides after ~30%CW. No permanent damage of this type was seen in the 30%CW SA/HTA materials. One possibility is that the cracked carbides and voids act as precursor sites for accelerated SCC crack growth, but detailed SEM and TEM observations of crack tips have never revealed any evidence to suggest any cracks extending out from these damage areas. Additional evidence of the role of voids and cracked carbides can be inferred from the test on the 20%CR

GE MA material. As mentioned previously, the GEG MA had no GB carbides and yet exhibited high SCC CGRs in the CW condition. In addition, no correlation between the IG void/crack distribution and SCC CGRs was discovered. This shows that voids and cracked carbides are not a requisite for high SCC CGRs in cold worked materials.

In order to further evaluate cold work effects, a “recovery” heat treatment was applied to a 31%CR alloy 690TT RE243 specimen. Multiple heat treatments at or near 700°C were examined to modify the dislocation structure in the cold worked material without promoting local recrystallization. The 700°C/1h/AC recovery treatment dropped measured hardness from 315 to 274 kgf/mm^2 while the IMD values changed only slightly from 0.16 to 0.15. No obvious changes were produced in the carbide microstructure or the matrix dislocation density by the recovery anneal and no regions of local recrystallization were discovered. Qualitatively, the most significant change appeared to be in the dislocation structures associated with grain boundaries. The recovery heat treatment did alter the susceptibility to IGSCC showing a ~20X lower CGR that dropped from ~8x10^{-8} mm/s to ~4x10^{-9} mm/s (Figure 6.8). As with the SA/HTA material, the response of this specimen did not collapse on the TT trend band for CGR as a function of either hardness or IMD. This result for the recovery treatment specimen supports the idea that cold work induced damage at grain boundaries that plays a key role in SCC response. A tabulated summary comparing the response of TT/MA and SA/HTA materials is listed in Table 6.3.

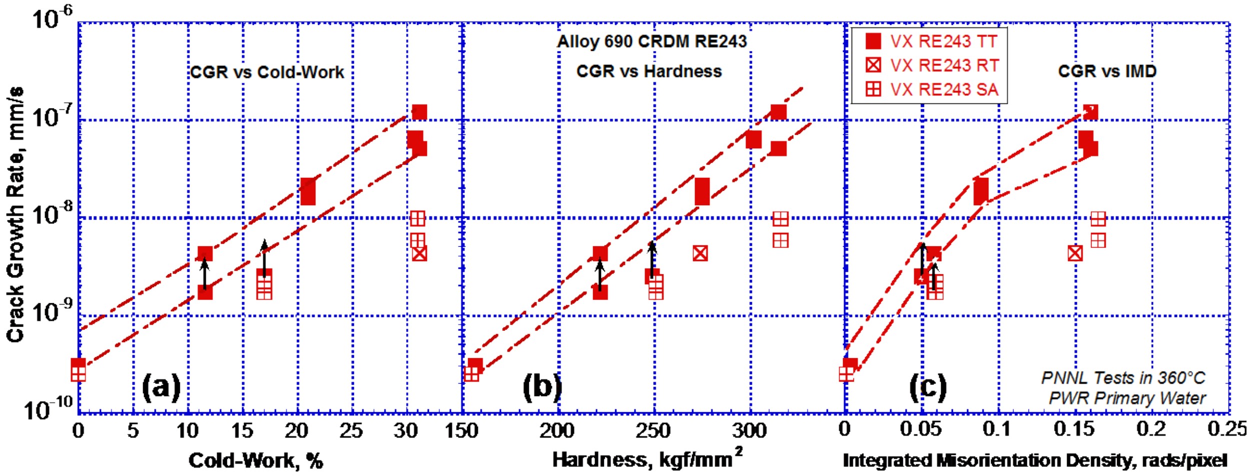

Figure 6.8 **SCC CGR as a function of (a) cold work, (b) hardness, or (c) IMD for Valinox RE243 CRDM showing the effect of the recovery treatment. Tests were at ~30 MPa√m and 360°C.**

Table 6.3 Comparison of the response between TT/MA, SA/HTA, and CW+RT materials.

ID	Producer	Heat #	Condition	HV (kgf/mm^2)	Avg. IMD	SCC-CGR (mm/s)†
CT014	Valinox	RE243	TT	157	0.0036	3x10^{-10} [325°C]
CT015	Valinox	RE243	TT+SA*	155	0.0013	2x10^{-10} [325°C]
CT020	Valinox	RE243	TT+17%CR	249	0.0500	5x10^{-10} [325°C]
CT019	Valinox	RE243	TT+SA+17%CR	251	0.0595	2x10^{-10} [325°C]
CT054	Valinox	RE243	TT+17%CR	249	0.0500	2.5x10^{-9}
CT068	Valinox	RE243	TT+SA+17%CR	251	0.0595	1.7-2.2x10^{-9}
CT022	Valinox	RE243	TT+30%CR^{TL}	300	N.M.	1.2x10^{-8} [350°C]
CT023	Valinox	RE243	TT+SA+30%CR^{TL}	290	N.M.	1.0x10^{-9} [350°C]
CT038	Valinox	RE243	TT+31%CR	315	0.160	0.5-1.2x10^{-7}
CT039	Valinox	RE243	TT+SA+31%CR	316	0.165	5.8-9.7x10^{-9}
CT053	Valinox	RE243	TT+ 31%CR+RT#	274	0.150	4.3x10^{-9}
CT073	Sp Met	NX3297HK12	MA*+30%CF	316	0.215	7.2x10^{-8} (1.7x10^{-7})**
CT074	Sp Met	NX3297HK12	HTA*§+30%CF	317	0.175	3.1x10^{-9}
CT037	Allvac	B25K-2	MA*+20%CR	321	0.1800	4.5x10^{-8}
CT070	Allvac	B25K-2	HTA§+20%CR	291	0.0905	1.7x10^{-9}

† Tested at 360°C and ~30 MPa√m unless otherwise noted.
* 1100°C/1 hr/WQ
# Recovery Treatment (RT) - 700°C/1 hr + Air Cool
** Values in parenthesis are ligament/contact adjusted.
§ High temperature anneal that left a low density of small plate-like grain boundary carbides.

In summary, this section has shown that SCC response can be related to both strength (hardness) and plastic strain (IMD). For a single starting condition, i.e., the Valinox RE243 TT material, a tight trend band is produced as a function of either hardness or IMD. The relationship to hardness appears to be purely exponential while for IMD, a non-exponential trend was observed. The different dependencies are consistent with the power law strain hardening relationship that exists between stress and strain. When additional CRDM and plate materials were added to the comparison plots, these trends were preserved, but with slightly more scatter. SCC CGR correlated better to hardness and IMD than percent cold work due to the fact that percent cold work is an average value across the thickness of a material and it does not contain any information about the starting strength or plastic strain of a material. In comparison, hardness and IMD provided more localized measurements associated with the crack-growth plane and will contain information about material starting condition.

Highly cold worked SA/HTA materials were found to fall off the hardness and IMD trend bands established by TT/MA materials. Microstructure comparisons between SA/HTA and TT/MA materials revealed several differences. Careful consideration of these differences indicates that a key factor controlling SCC susceptibility is level of plastic deformation adjacent to grain boundaries. No evidence was found to support the idea that voids near carbides or cracked carbides are a requisite for high SCC CGRs. Limited evidence also suggests that reduced grain boundary Cr concentration in TT/MA materials is not a key factor in the enhanced susceptibility of the cold worked TT/MA materials.

6.3 Crack Growth Rate as a Function of Stress Intensity

Crack growth rate as a function of K for the CRDM materials is presented in Figure 6.9. A wide range of SCC CGRs due to the different levels of cold work is apparent in this summary plot. However for any given material, the effect of K on CGR is minimal for values of 30 MPa√m or higher. The one exception to this is the 11.6%CF RE243 material that did exhibit an ~10x increase in SCC CGR between 30 and 42 MPa√m. Figure 6.9 also shows the effect of K below 30 MPa√m for 31%CF Valinox and Sumitomo CRDM materials. A strong dependence is seen here with SCC CGRs dropping down to 2-4x10^{-9} mm/s as K was decreased down to 18-20 MPa√m, mirroring the general trend of the MRP-55 disposition curve for alloy 600. The response of the plate and bar (non-CRDM) materials in Figure 6.10 is generally similar to that of the CRDM materials with minimal effect of K on SCC CGR for K values of 30 MPa√m or higher.

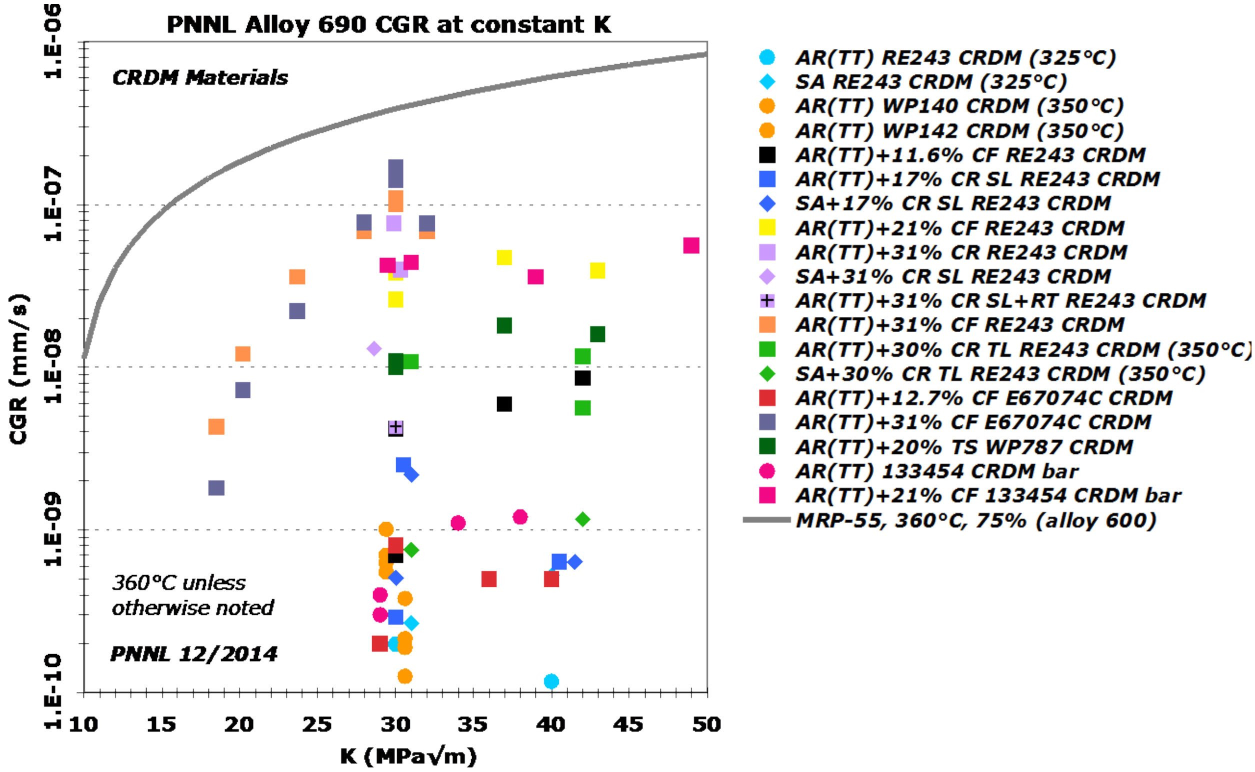

Figure 6.9 Measured SCC CGRs versus K for alloy 690 CRDM materials.

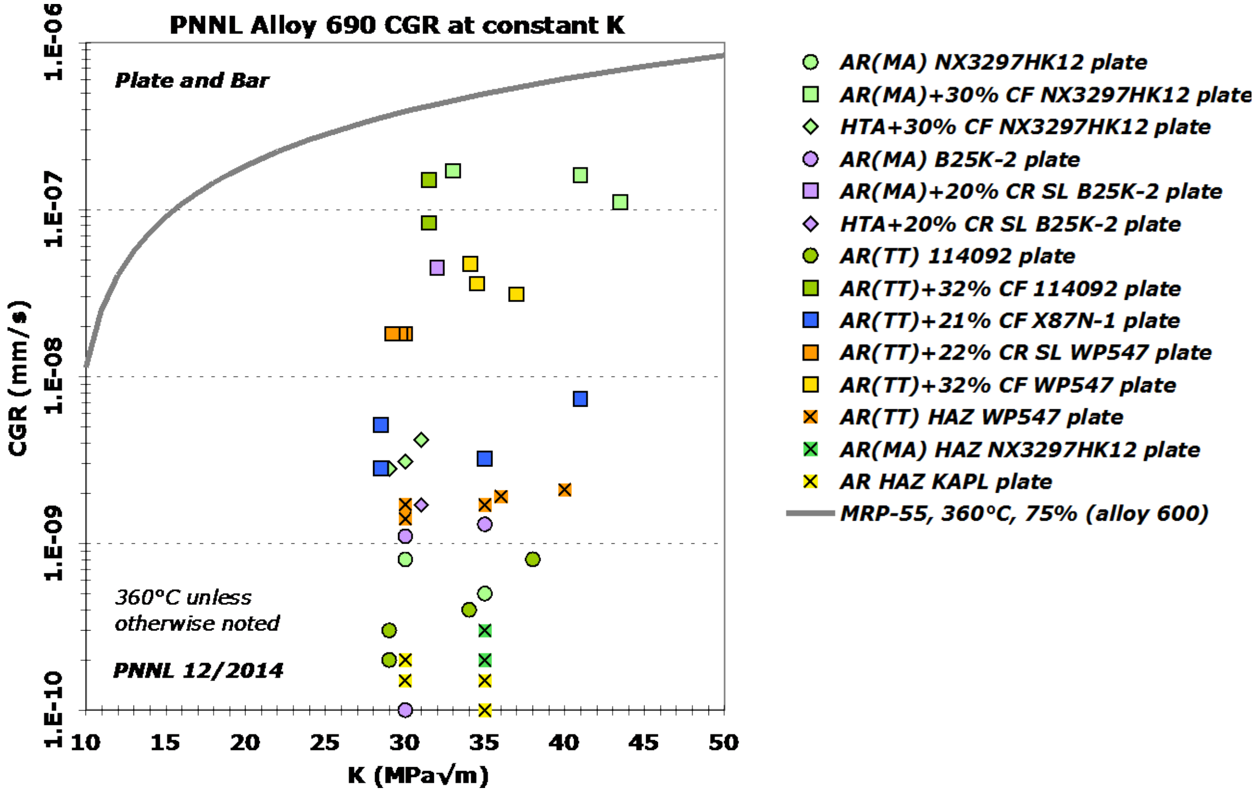

Figure 6.10 Measured SCC CGRs versus K for alloy 690 plate and bar materials.

6.4 SCC Susceptibility of HAZ Materials

A summary of the response of the three HAZ tests that were completed for this report is listed in Table 6.4. As noted in Chapter 5, the IMD values are similar to that for non-CW material, but the hardness values are somewhat higher than as-received alloy 690 heats evaluated. However, there was no indication of a local hardness increase within the HAZ in comparison to the base metal for these specimens. The higher hardness suggests some possibility of SCC susceptibility, but extensive transitioning efforts resulted in no SCC engagement and very low CGRs. Based on these limited tests, the current outlook is that alloy 690 HAZ materials have at best only a slightly higher chance of SCC growth compared to base material response. Additional tests are recommended on well-characterized weld HAZ regions where local strain has been identified. Based on EBSD measurements, Morra [21] has reported equivalent plastic strains of 10-12% in the HAZ for selected alloy 690 welds.

Table 6.4 Summary of hardness, IMD, and SCC response of the tested HAZ materials

ID	Producer	Heat #	Condition	HV (kgf/mm^2)	Average IMD	SCC-CGR (mm/s)
CT067	Aubert&Duval	WP547	TT* HAZ	200-220	0.0091-0.018	$1.4\text{-}1.7 \times 10^{-9}$
CT086	Special Metals	NX3297HK12	MA* HAZ	210-230	0.012-0.023	1.5×10^{-10}
CT087	Unknown	Unknown	AR† HAZ	200-220	0.0089-0.013	1×10^{-10}

* As-received condition of the material.

† As-received condition is not known.

6.5 Other Aspects of Alloy 690 SCC Behavior

Testing of cold worked alloy 690 has allowed assessing the effect of two key parameters on SCC crack growth, namely temperature and dissolved hydrogen. The effect of both parameters was assessed on a smaller range of materials in the prior NUREG in this series [7]. The new data serve to confirm the observed prior response.

6.5.1 Effect of Temperature on SCC Crack Growth

Preliminary data obtained for the prior NUREG on 31%CR alloy 690TT gave an activation energy of ~110 kJ/mol over the temperature range from 290-360°C for tests conducted at the Ni/NiO stability line. The final data for that test and for several other additional tests are shown in Figure 6.11. New data include measurements on the 17%CR Valinox, SA+31%CR Valinox RE243, and for the ENSA (Aubert&Duval) WP547 plate heat in the 32%CF and 22%CR conditions. The revised activation energy for the 31%CR alloy 690TT is slightly higher at 130 kJ/mol. The 17%CR TT and the 31%CR SA Valinox were 150 and 164 kJ/mol, respectively, while both of the cold worked ENSA materials were just slightly below 100 kJ/mol. In aggregate, this covers a wide range of values, but the average of all these values, ~130 kJ/mol, matches the accepted value for alloy 600 of ~130 kJ/mol [5,22,23].

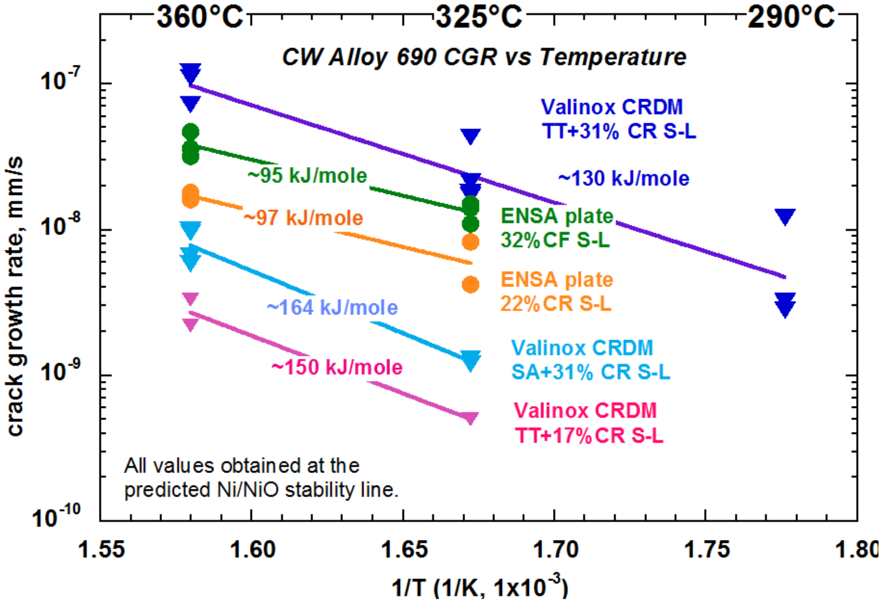

Figure 6.11 Arrhenius plot for SCC CGR as a function of temperature for cold worked alloy 690 materials.

6.5.2 Effect of Dissolved Hydrogen on SCC Crack Growth

Preliminary data obtained for the prior NUREG indicated that cold worked alloy 690 tested at 325°C had a reduced SCC susceptibility for dissolved hydrogen contents corresponding to the NiO stable regime, similar to that for alloy 600/182 [9,10]. However in the Ni-metal stable regime, SCC CGRs remained approximately the same as the value obtained at the Ni/Ni-metal stability line. Both alloy 600 and alloy 182 have reduced susceptibility in the Ni-metal stable regime. The final data for this response of the 31%CF alloy 690TT material are shown in Figure

6.12. New data, shown in Chapter 5, were obtained for the ENSA plate heat in the 22% and 32% CW condition and is reproduced here in Figure 6.13 for convenience. Testing of the ENSA material at 360°C produced the same dependence on dissolved hydrogen as observed for the RE243 CRDM at 325°C. Testing of the ENSA plate material at 325°C again shows reduced susceptibility in the NiO stable regime, but the response in the Ni-metal stable regime suggests perhaps some slight reduction in susceptibility at higher hydrogen concentrations. The datasets as a whole still suggest that cold worked alloy 690 acts similarly to alloy 600/182 in the NiO stable regime, but it maintains high susceptibility in the Ni-metal stable regime.

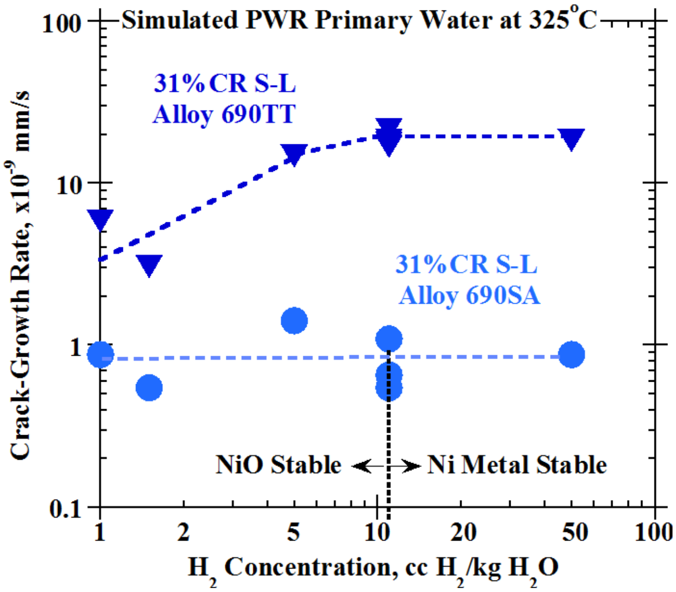

Figure 6.12 SCC CGR as a function of dissolved hydrogen for 31%CF alloy 690.

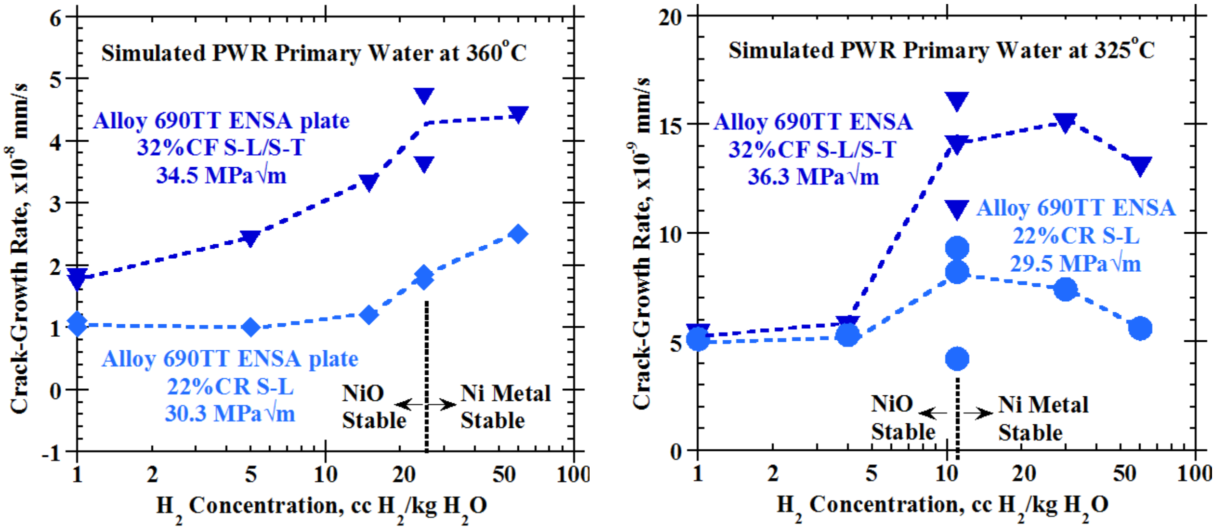

Figure 6.13 Constant K SCC crack growth rate versus dissolved hydrogen for the TT+32%CF and TT+22%CR ENSA/A&D alloy 690 specimens, CT059 & CT060, at 360°C and 325°C.

7 SUMMARY

The results from more than five years of SCC research on alloy 690 materials have been presented here. The data clearly show that alloy 690 becomes susceptible to SCC when it is cold worked. Thermally treated materials are quite sensitive to the degree of cold work with the data suggesting that SCC CGRs of up to ~1x10^{-8} mm/s are possible with only ~12% CW when tested at 360°C. The SCC susceptibility of alloy 690 in the SA condition, however, is not nearly as sensitive to cold work. Highly cold worked (30-31%) alloy 690 CRDM materials in the SA condition exhibited an order of magnitude lower SCC CGRs than the same heat in the TT condition after identical cold work.

It has been found that SCC CGRs correlate better hardness and EBSD IMD measurements performed on the tested CT specimens well ahead of the final crack tip than to the applied cold work level. This is because hardness and IMD are more direct measurements than percent cold work and are sensitive to the condition of the material prior to cold working. Despite the better sensitivity to material condition, not all the SCC data correlate to a single trend line. In particular, the SA materials do not fall on the same trend line as the TT/MA materials. Microstructure and EBSD observations indicate that higher strains occur at the grain boundaries when a high density of carbides is present. It is thought that IGSCC susceptibility is dependent on these grain boundary strains along with matrix strength. The available data do not suggest that voids at carbide interfaces or cracked carbides have a significant effect on SCC susceptibility. These assessments are substantiated by the 31%CR alloy 690TT that was given a recovery treatment. As with the alloy 690SA materials, this recovery treatment specimen fell well below the alloy 690TT trend band. SEM observations showed no change in the number of voids and cracked carbides, but EBSD suggested slightly reduced strains in the vicinity of the grain boundaries. Indirect evidence also indicates that grain boundary Cr depletion does not play an important role in SCC susceptibility for the alloy 690 materials examined in this research.

Additional data were produced during tests on alloy 690 materials that provide information on weld HAZs and the influence of test temperature and dissolved hydrogen concentrations. Alloy 690 HAZs were found to have essentially the same susceptibility as non-cold worked alloy 690 despite having IMD values that are on the high end of non-cold worked material and somewhat higher hardness values. Test temperature effects studies indicate an ~5x reduction in SCC CGR of highly cold worked alloy 690 when decreasing temperature from 360°C to 325°C, while the dissolved hydrogen studies suggest similar CGRs at the Ni/NiO and Ni metal stable concentrations but lower CGRs at NiO-stable concentrations.

8 REFERENCES

[1] H. Xu, S. Fyfitch, P. Scott, M. Foucault, R. Killian and M. Winters, *Materials Reliability Program: Resistance to Primary Water Stress Corrosion Cracking of Alloys 690, 52 and 152 in Pressurized Water Reactors (MRP-111),* EPRI, Palo Alto, CA: 2004, 1009801.

[2] "Materials Reliability Program: Resistance of Alloys 690, 152, and 52 to Primary Water Stress Corrosion Cracking (MRP-237, Rev. 1) ", Product ID 1018130, Electric Power Research Institute, August 2008.

[3] "Materials Reliability Program: Resistance of Alloys 690, 152, and 52 to Primary Water Stress Corrosion Cracking (MRP-237, Rev. 2) Summary of Findings Between 2008 and 2012 from Completed and Ongoing Tests", Product ID 3002000190, Electric Power Research Institute, April 2013.

[4] D. J. Paraventi and W. C. Moshier, "Alloy 690 SCC Growth Rate Testing," *Workshop on Cold Work in Iron- and Nickel-Base Alloys,* Ed. R.W. Staehle and J. Gorman, EPRI, Palo Alto, CA, June 2007. Also *Proc. EPRI Alloy 690 Workshop,* EPRI, Palo Alto, CA, October 2007.

[5] "Materials Reliability Program (MRP) Crack Growth Rates for Evaluating Primary Water Stress Corrosion Cracking (PWSCC) of Thick-Wall Alloy 600 Materials", MRP-55 Revision 1, Document 1006695, November 2002.

[6] S.M. Bruemmer and M.B. Toloczko, "Pacific Northwest National Laboratory Investigation of Stress Corrosion Cracking in Nickel Base Alloys, Volume 1", NUREG/CR-7103, Vol. 1, ML11277A230 and ML11294A228, U.S. NRC, September 2011.

[7] S.M. Bruemmer, M.B. Toloczko, M.J. Olszta, "Pacific Northwest National Laboratory Investigation of Stress Corrosion Cracking in Nickel Base Alloys, Volume 2", NUREG/CR-7103, Vol. 2, ML12114A011, U.S. NRC, April 2012.

[8] "Standard Test Method for Determining Threshold Stress Intensity Factor for Environment-Assisted Cracking of Metallic Materials", ASTM E 1681-03, ASTM International, 2003.

[9] S.A. Attanasio and D.S. Morton, "Measurement of the Ni/NiO Transition in Ni-Cr-Fe Alloys and Updated Data and Correlation to Quantify the Effect of Aqueous Hydrogen on Primary Water SCC", *Proc. 11th Int. Symp. on Environmental Degradation of Materials in Nuclear Power Systems*, ANS, 2003.

[10] D.S. Morton, S.A. Attanasio and G.A. Young, "Primary Water SCC Understanding and Characterization Through Fundamental Understanding in the Vicinity of the Ni / NiO Phase Transition", *Proc. 10th Int. Symp. on Environmental Degradation of Materials in Nuclear Power Systems – Water Reactors*, NACE, 2001.

[11] "Standard Test Method for Knoop and Vickers Hardness of Materials" ASTM Standard E-384, ASTM International, 2007.

[12] "Metallic Materials - Vickers Hardness Test - Part 1: Test Method" ISO 6507-1, International Organization for Standardization, 2005.

[13] A. J. Schwartz, Kuman, M., Adams, B.L., *Electron Backscatter in Materials Science*, 1st, Edition, Kluer, N.Y., 2000, pp. 247-263.

[14] M. B. Toloczko and S. M. Bruemmer, “Crack Growth Response of Alloy 690 in Simulated PWR Primary Water,” *Proc. 14th Int. Conf. on Environmental Degradation of Materials in Nuclear Power Systems - Water Reactors,* American Nuclear Society, 2009, p. 706.

[15] P. L. Andresen, M. M. Morra, K. S. Ahluwalia and J. Wilson, “Effect of Deformation and Orientation on SCC of Alloy 690,” *Proc. 14th Int. Conf. on Environmental Degradation of Materials in Nuclear Power Systems - Water Reactors,* American Nuclear Society, 2009, p. 846.

[16] B. Alexandreanu, “The Stress Corrosion Cracking Behavior of Alloys 690 and 152 Weld in a PWR Environment,” *Proc. 14th Int. Conf. on Environmental Degradation of Materials in Nuclear Power Systems - Water Reactors,* American Nuclear Society, 2009, p. 239.

[17] J.M. Sarver, J.E. Crum, and W.L. Mankins, "Carbide Precipitation and the Effect of Thermal Treatments on the SCC Behavior of Inconel Alloy 690", *Proc. Conf. on Environmental Degradation of Materials in Nuclear Power Systems - Water Reactors*, The Metallurgical Society, 1988. p. 581.

[18] P.L. Andresen and M.M. Morra, "Effects of Positive and Negative dK/da on SCC Growth Rates", *Proc. 12th Int. Conf. on Environmental Degradation of Materials in Nuclear Power Systems - Water Reactors,* The Minerals, Metals and Materials Society, 2005, p. 167.

[19] P.L. Andresen, P.W. Emigh, M.M. Morra and R.M. Horn, "Effects of Yield Strength, Corrosion Potential, Stress Intensity Factor, Silicon and Grain Boundary Character on the SCC of Stainless Steels", 11th Int. Conf. on Environmental Degradation of Materials in Nuclear Power Systems, Stevenson, WA, August 2003, p. 816.

[20] D.J. Paraventi and W.C. Moshier, "Assessment of the Interaction of Variables in the Intergranular Stress Corrosion Crack Growth Rate Behavior of Alloys 600, 82, and 182", *13th Int. Conf. on Environmental Degradation of Materials in Nuclear Power Systems*, Whistler, British Columbia, August 2007.

[21] P.L. Andresen, M.M. Morra, and K. Ahluwalia, "SCC of Alloy 690 and Its Weld Metals", *15th Int. Conf. on Environmental Degradation,* The Minerals, Metals and Materials Society, 2011, p. 161.

[22] D.S. Morton, S.A. Attanasio, E. Richey, and G.A. Young, "In Search of the True Temperature Dependence and Stress Intensity Factor Dependencies for PWSCC", *Proc. 12th Int. Conf. on Environmental Degradation of Materials in Nuclear Power Systems - Water Reactors,* The Minerals, Metals and Materials Society, 2005, p. 977.

[23] F. Vaillant, P. Moulart, J.M. Boursier, C. Amzallag, J. Daret, "Crack Growth Rates in Thick Materials of Alloy 600 and Weld Metals of Alloy 182 in Laboratory Primary Water Comparison with Field Experience", *Proc. of 5th International Symposium on Contribution of Materials Investigation to the Resolution of Problems Encountered in Pressurized Water Reactors (Fontevraud 5)*, Fontevraud, France, 23-27 September (2002), CD-ROM

NRC FORM 335
(12-2010)
NRCMD 3.7

U.S. NUCLEAR REGULATORY COMMISSION

BIBLIOGRAPHIC DATA SHEET

(See instructions on the reverse)

1. REPORT NUMBER
(Assigned by NRC, Add Vol., Supp., Rev., and Addendum Numbers, if any.)
NUREG/CR-7103
Volume 3

2. TITLE AND SUBTITLE
Stress Corrosion Cracking of Cold Worked Alloy 690

3. DATE REPORT PUBLISHED

MONTH	YEAR
July	2016

4. FIN OR GRANT NUMBER

5. AUTHOR(S)
M.B. Toloczko, N.R. Overman, M.J. Olszta, S.M. Bruemmer

6. TYPE OF REPORT
Technical

7. PERIOD COVERED (Inclusive Dates)

8. PERFORMING ORGANIZATION - NAME AND ADDRESS (If NRC, provide Division, Office or Region, U. S. Nuclear Regulatory Commission, and mailing address; if contractor, provide name and mailing address.)
Pacific Northwest National Laboratory
902 Battelle Boulevard
Richland, WA 99352

9. SPONSORING ORGANIZATION - NAME AND ADDRESS (If NRC, type "Same as above", if contractor, provide NRC Division, Office or Region, U. S. Nuclear Regulatory Commission, and mailing address.)
Office of Nuclear Regulatory Research
Division of Engineering
U.S. Nuclear Regulatory Commission
Washington, DC 20555

10. SUPPLEMENTARY NOTES

11. ABSTRACT (200 words or less)

The report summarizes the results of a testing program to evaluate the effects of cold work, including rolling, forging, and tensile straining, on the primary water stress corrosion cracking (PWSCC) susceptibility of alloy 690. Alloy 690 is a high-chromium, nickel base material used in reactor pressure vessel head penetration nozzles, steam generator divider plates, and other components. PWSCC growth rates were measured for a total of 37 different alloy 690 specimens in simulated primary water reactor environments. The alloy 690 test materials included six different heats of extruded control-rod-drive mechanism (CRDM) tubing and five plate/bar heats with variations in the degree of cold work, from no cold work to cold work greater than 30%. In addition, different thermo-mechanical treatments were applied to some heats of material before cold working, thereby altering properties such as the grain boundary carbide morphology, to assess how this would affect the PWSCC response. Materials were examined by optical microscopy, electron microscopy, electron backscatter diffraction, and other characterization techniques to devise a mechanistic explanation for the test results and to identify the key parameters that control the PWSCC susceptibility.

12. KEY WORDS/DESCRIPTORS (List words or phrases that will assist researchers in locating the report.)
Alloy 690
Nickel alloys
Cold work
Stress corrosion cracking

13. AVAILABILITY STATEMENT
unlimited

14. SECURITY CLASSIFICATION
(This Page)
unclassified
(This Report)
unclassified

15. NUMBER OF PAGES

16. PRICE

UNITED STATES
NUCLEAR REGULATORY COMMISSION
WASHINGTON, DC 20555-0001

OFFICIAL BUSINESS

@NRCgov

NUREG/CR-7103, Vol. 3

Pacific Northwest National Laboratory Investigation of
Stress Corrosion Cracking in Nickel-Base Alloys:
Stress Corrosion Cracking of Cold Worked Alloy 690

July 2016